

**Synthesis, Structure and Catalysis of Polyoxo-
Noble-Metalates (Pt, Au, Pd) and Noble Metal
(Pt, Rh)-Containing Polyoxometalates**

by

Jiayao Zhang

a Thesis submitted in partial fulfillment of the requirements for the degree of

Doctor of Philosophy in Chemistry

Approved Dissertation Committee

Prof. Dr. Ulrich Kortz – Constructor University (Mentor)

Prof. Dr. Nikolai Kuhnert – Constructor University

Dr. Bassem S. Bassil – Constructor University

Prof. Dr. Jens Beckmann – University of Bremen

Date of Defense: 25th May 2023

School of Science

Statutory Declaration

Family Name, Given/First Name	Zhang, Jiayao
Matriculationnumber	20332369
What kind of thesis are you submitting: Bachelor-, Master- or PhD-Thesis	PhD-Thesis

English: Declaration of Authorship

I hereby declare that the thesis submitted was created and written solely by myself without any external support. Any sources, direct or indirect, are marked as such. I am aware of the fact that the contents of the thesis in digital form may be revised with regard to usage of unauthorized aid as well as whether the whole or parts of it may be identified as plagiarism. I do agree my work to be entered into a database for it to be compared with existing sources, where it will remain in order to enable further comparisons with future theses. This does not grant any rights of reproduction and usage, however.

The Thesis has been written independently and has not been submitted at any other university for the conferral of a PhD degree; neither has the thesis been previously published in full.

German: Erklärung der Autorenschaft (Urheberschaft)

Ich erkläre hiermit, dass die vorliegende Arbeit ohne fremde Hilfe ausschließlich von mir erstellt und geschrieben worden ist. Jedwede verwendeten Quellen, direkter oder indirekter Art, sind als solche kenntlich gemacht worden. Mir ist die Tatsache bewusst, dass der Inhalt der Thesis in digitaler Form geprüft werden kann im Hinblick darauf, ob es sich ganz oder in Teilen um ein Plagiat handelt. Ich bin damit einverstanden, dass meine Arbeit in einer Datenbank eingegeben werden kann, um mit bereits bestehenden Quellen verglichen zu werden und dort auch verbleibt, um mit zukünftigen Arbeiten verglichen werden zu können. Dies berechtigt jedoch nicht zur Verwendung oder Vervielfältigung.

Diese Arbeit wurde in der vorliegenden Form weder einer anderen Prüfungsbehörde vorgelegt noch wurde das Gesamtdokument bisher veröffentlicht.

22/06/2023 *Jiayao*
Date, Signature

Acknowledgements

This work has been carried out under the guidance of Prof. Ulrich Kortz at Constructor University. First of all, I would like to express my deep gratitude and appreciation to my mentor, Prof. Kortz, for his unwavering support, guidance, and encouragement throughout my PhD studies. His expertise, insights, and feedback were invaluable to the success of my research. I would also like to thank Prof. Nikolai Kuhnert, Dr. Bassem S. Bassil and Prof. Dr. Jens Beckmann for their precious time and agreement to be committee members of my PhD defense. I gratefully appreciate Dr. Saurav Bhattacharya for XRD support and productive discussions, Dr. Xiang Ma and Dr. Anusree Sundar for their patient instructions on instruments and for being so helpful in many ways, Dr. Ali S. Mougharbel and Dr. Ananthu Rajan for lab and work assistance, Mahmoud Elcheikh Mahmoud and Bahaa Eddin Khsara for catalysis experiments. Great acknowledgements go to Dr. Xiang Ma for his great help during my early days in the lab. I am, of course, thankful to all of my lab fellows who have provided a stimulating and supportive academic environment for their countless assistance during the time of research. I would also like to convey thanks to Sihana Ahmedi for being part of my research project as undergraduate student with hard work.

I sincerely acknowledge the following collaborators: (i) Prof. Nikolai Kuhnert, Mrs. Anja B. Müller for ESI-MS analysis (Constructor University, Germany); (ii) Prof. Veit Wagner, Dr. Talha Nisar for XPS analysis (Constructor University, Germany).

I am delighted to extend my great gratitude to China Scholarship Council (CSC) for a doctoral fellowship. A special note of my appreciation goes to Prof. Xiao-Ming Liu

(Jiaxing University, P.R. China) and Prof. Ming-Xing Li (Shanghai University, P.R. China) for their all-time support. My warm gratitude also goes to the support given by my friends in both Germany and China.

Last but not least, my whole hearted thanks go to my family members especially my parents for their love, encouragement and support throughout my academic journey, and to my boyfriend Shengquan Lu for his constant encouragement and loving company during my PhD education. Their patience, understanding, and belief in me have been the foundation of my success.

Abstract

Polyoxometalates (POMs) are discrete, anionic, soluble polynuclear metal-oxygen clusters forming a distinct class of compounds which can be finely tuned at the molecular level. POMs can be subdivided in isopoly- and heteropolyanions and are usually comprised of (distorted) octahedral MO_6 building blocks, where M is tungsten, molybdenum, or vanadium, and less frequently niobium or tantalum in high (d^0 , d^1) oxidation states. The large number of POM structures and compositions result in many different physicochemical properties (fine tuning of compositional, structural, electronic, magnetic, redox, photochemical, and thermal properties is possible) which can result in applications ranging from catalysis and material science to bio-medicine. Noble metal-containing POMs including palladium, platinum, rhodium and iridium are of distinct interest as catalysts for organic transformations, including industrially relevant processes. Examples include the activation of readily available “green” oxidants O_2 and H_2O_2 , as well as (selective) hydrogenations and C–C coupling reactions.

This thesis is divided into six chapters. Chapter I generally introduces the historical background, structural aspects, properties, and applications of POMs, the state of the art of polyoxo-noble-metalates, noble-metal-containing POMs and arsenic compound, as well as the motivation to perform this work. Chapter II includes the information of applied analytical techniques and synthetic procedures for the used POM and organorhodium(III) precursors.

Chapter III is devoted to polyoxoplatinate, polyoxopalladate and mixed polyoxo-noble-metalates, and 7 novel polyoxo-noble-metalates have been obtained with the following highlights: (i) The first Pt^{IV} -containing discrete polyoxoplatinate(II)

[Pt^{IV}Pt^{II}₆O₆(AsO₂(CH₃)₂)₆]²⁻ (**Pt7**) and polyoxopalladate(II) [Pt^{IV}Pd^{II}₆O₆(AsO₂(CH₃)₂)₆]²⁻ (**PtPd6**) have been prepared and characterized in the solid-state, in solution, and in the gas phase; (ii) The first discrete mixed platinum(IV)-gold(III) oxoanion [Pt^{IV}₂Au^{III}₃O₆((CH₃)₂AsO₂)₆]⁻ (**Pt2Au3**) was structurally characterized in the solid state by single-crystal XRD and TGA, and in solution by multinuclear (¹H, ¹³C, ¹⁹⁵Pt) NMR, indicating that polyanion **Pt2Au3** is stable in solution, which was confirmed by ESI-MS studies. The sodium salt of **Pt2Au3** undergoes a clean single-crystal-to-single-crystal (SCSC) structural transformation upon rehydration and dehydration; (iii) the mixed noble metal gold(III)-palladium(II)-oxo nanocluster [Pd^{II}₁₀Au^{III}₄O₁₂(AsO₂(CH₃)₂)₁₀]²⁻ (**Au4Pd10**) with a central cube shaped [Pd₄O₄((CH₃)₂AsO₂)₂] unit, connected to two tetrameric bowl shaped [AuPd₃O₄((CH₃)₂AsO₂)₄] units by two square-planar coordinated gold atoms on each side; (iv) Two **M·(Pd₁₆)₄** type palladium oxo clusters incorporating 3d Sc^{III} and Zn^{II} as guest metal M have been prepared.

Chapter IV presents 3 novel Platinum(II/III)-containing isopolytungstates. The polyoxoanion [Pt₃W₁₁O₄₁]¹⁰⁻ (**Pt3W11**) consists of three {W₃O₁₃} and one {W₂O₁₀} fragments connected by three Pt(II) atoms forming linear {Pt₃O₁₂} triad involved in direct Pt–Pt bonding (2.64 to 2.68 Å). The polyoxoanion [Pt^{II}₂W₅O₁₈((CH₃)₂AsO₂)₂]⁴⁺ (**Pt^{II}2W5**) and [Pt^{III}₂W₅O₁₈((CH₃)₂AsO₂)₄]⁴⁺ (**Pt^{III}2W5**) both consists of one lacunary Lindqvist fragments {W₅O₁₈}⁶⁻ coordinated by two Pt(II) in square planar coordination and two Pt(III) in square-pyramidal coordination with direct Pt–Pt bonding (2.64 Å), respectively. Chapter V describes the synthesis of three all-inorganic platinum arsenate(III) compound. The first two full inorganic discrete platinum arsenate(III) clusters: [Pt^{IV}(As₃O₆)₂]²⁻ (**PtAs6**) and [Pt^{II}₄(H₂AsO₃)₆(HAsO₃)₂]²⁻ (**Pt4Ass**), have been synthesized in aqua media. In

PtAs₆, one Pt atom is coordinated by two [As₃O₆]³⁻ units via O atoms, in which PtAs₃O₆ rings are formed. In **Pt₄As₈**, Each Pt atom is coordinated by two O atoms and two As atoms from AsO₃ group forming square-planar PtO₂As₂ involved in direct bonding between As^{III} *E* and Pt^{II} orbitals (Pt–As = 2.31 Å), resulting an open cage structure. And a platinum arsenate(III) heteropolytungstate [Pt₂As₆W₄O₂₈]¹⁰⁻ (**Pt₂As₆W₄**) has been synthesized in aqua media and characterized by ¹⁹⁵Pt NMR. Each Pt atom is coordinated by one μ₃-O atom and three As atoms from AsO₃ group forming square-planar PtOAs₃ with Pt–As bonding.

Chapter VI deals with the synthesis and characterization of two RhCp*-containing heteropolytungstates, [Na(Rh^{III}C₅Me₅)₄As₂W₁₀O₄₂]⁵⁻ and [Na(Rh^{III}C₅Me₅)₄P₂W₁₀O₄₂]⁵⁻, which are composed of two equivalent AsW₅O₂₂ or PW₅O₂₂ fragments linked *via* corners and a Na⁺ templating ion, and capped by four RhCp* units.

Table of Contents

Acknowledgements	III
Abstract	V
List of Figures	XII
List of Tables	XIX
List of Compounds Obtained with Codes	XXI
Chapter I Introduction	1
1.1 Polyoxometalates (POMs).....	1
1.2 Polyoxo-noble-metalates	4
1.3 Platinum-containing POMs	7
1.4 Arsenic(III) Compounds.....	8
1.5 The RhCp*- and IrCp*-Containing POMs.....	10
1.6 Catalysis	12
Chapter II Experimental Details	13
2.1 Instrumentations	13
2.1.1 Single-Crystal X-Ray Diffraction	13
2.1.2 Fourier Transform Infrared (FT-IR) Spectroscopy	14
2.1.3 Elemental and Thermogravimetric Analyses	14
2.1.4 Nuclear Magnetic Resonance (NMR) Spectroscopy	14
2.1.5 Electrospray-Ionization Mass Spectrometry (ESI-MS).....	15
2.1.6 X-ray photoelectron spectroscopy (XPS)	15
2.1.7 Powder X-ray diffraction (PXRD).....	16
2.1.8 Sorption Measurements	16

2.1.9	Batch Reactor.....	16
2.1.10	Gas chromatography (GC).....	17
2.1.11	Bond Valence Sum (BVS) Calculations	17
2.2	Synthesis of $(\text{RhC}_5\text{Me}_5\text{Cl}_2)_2$ and POM Precursors.....	18
2.2.1	Synthesis of $(\text{RhCp}^*\text{Cl}_2)_2$	18
2.2.2	$\text{Na}_9[\text{A-}\alpha\text{-As}^{\text{V}}\text{W}_9\text{O}_{34}] \cdot 18\text{H}_2\text{O}$	18
2.3	Synthesis of Mesoporous Supports	19
2.3.1	Synthesis of SBA15	19
2.3.2	Synthesis of Aminopropyl-Modified SBA15 (SBA15-apts)	19
Chapter III Polyoxo-noble-metalates		20
3.1	Pt^{IV} -Containing hexaplatinate(II) and hexapalladate(II).....	20
3.1.1	Synthesis	21
3.1.2	Single-Crystal XRD Data	23
3.1.3	Bond Valence Sum Calculations.....	24
3.1.4	Results and Discussion	25
3.1.5	Conclusions.....	45
3.2	Au(III)-containing noble metal-oxo clusters.....	46
3.2.1	Synthesis	46
3.2.2	Single-Crystal XRD Data	50
3.2.3	Bond Valence Sum Calculations.....	52
3.2.4	Results and Discussion	53
3.2.5	Conclusions.....	69
3.3	Sc(III) and Zn(II)-containing 16-palladium(II)-oxo cluster.....	71
3.3.1	Synthesis	71

3.3.2	Single-Crystal XRD Data	72
3.3.3	Bond Valence Sum Calculations	73
3.3.4	Results and Discussion	75
3.3.5	Conclusions.....	77
Chapter IV	Platinum(II/III) Isopolytungstates	78
4.1	Synthesis.....	78
4.2	Single-Crystal XRD Data	82
4.3	Bond Valence Sum Calculations	83
4.4	Results and Discussion	83
4.4.1	Solid-State Structure	83
4.4.2	Multinuclear NMR Study	90
4.5	Conclusions	92
Chapter V	Platinum(II/IV) Arsenate(III) Clusters	94
5.1	Synthesis.....	94
5.2	Single-Crystal XRD Data	97
5.3	Bond valence sum calculations.	98
5.4	Results and Discussion	99
5.4.1	Solid-State Structure	99
5.4.2	¹⁹⁵ Pt NMR Study.....	108
5.4.3	Powder XRD Study.....	108
5.4.4	XPS Study.....	112
5.4.5	Infrared Spectroscopy Study.....	113
5.4.6	Conclusions.....	114
Chapter VI	Organorhodium(III)-containing POMs	115

6.1	Synthesis.....	115
6.2	Single-Crystal XRD Data.....	117
6.3	Results and Discussion.....	118
6.3.1	Solid-State Structure.....	118
6.3.2	Multinuclear NMR Study.....	120
6.4	Conclusions.....	121
Chapter VII	Summery and Outlook.....	123
Appendix.....		126
References.....		127

List of Figures

- Figure 1.1.** POM structural types: Keggin, Wells-Dawson, Strandberg (edge-shared and corner-shared); Lindqvist, Anderson, Allman-Waugh, Weakley-Yamase (edge-shared) and Dexter-Silverton (face-shared and corner-shared). 2
- Figure 1.2.** View of 5 isomers of Keggin type polyanions. Color codes: original $\{M_3O_{13}\}$ polyhedrons, blue; after rotating $\{M_3O_{13}\}$ polyhedrons, green. 3
- Figure 1.3.** Combined polyhedral/ball-and-stick representation of $[Pd^{II}_{13}As^V_8O_{34}(OH)_6]^{8-}$ (a), $[NaCPd^{II}_{15}O_{40}(P^VO)_{10}]^{19-}$ (b) and $[Cu^{II}_2Pd^{II}_{22}P^V_{12}O_{60}(OH)_8]^{20-}$ (c). Color code, balls: Pd (pale blue), Cu (sky blue), Na (blue), O (red); polyhedra: $\{AsO_4\}$ (green), $\{PO_4\}$ (light blue). 5
- Figure 1.4.** Combined polyhedral/ball-and-stick representation of $[Pt^{III}_{12}O_8(S^{VI}O_4)_{12}]^{4-}$. Color code, balls: Pt (orange), O (red); polyhedra: $\{SO_4\}$ (yellow). 6
- Figure 1.5.** Ball-and-stick representation of (a) $[Au^{III}_4As^V_4O_{20}]^{8-}$ and (b) $\{Cl_4Na_5[Au^{III}_4As^V_4O_{20}H_{2.5}]_2\}^{10-}$ dimeric fragment. Color code: Au, yellow; As, light blue; O, red; Na, blue. Chlorides and solvent molecules have been omitted for clarity. 6
- Figure 1.6.** Combined polyhedral/ball-and-stick representation of $[Pt^{IV}W_6O_{24}]^{8-}$ (left), $[H_2Pt^{IV}V_9O_{28}]^{5-}$ (middle) and $[Pt^{IV}(Nb_6O_{19})_2]^{12-}$ (right). Color code: Pt (orange), O (red), H (green), $\{WO_6\}$ (blue), $\{VO_6\}$ (sky blue), $\{NbO_6\}$ (green). 7
- Figure 3.1.** FT-IR spectrum of **KNa-Pt₇** (red) and **Na-PtPd₆** (blue). 22
- Figure 3.2.** Thermograms of **KNa-Pt₇** (left) and **Na-PtPd₆** (right) from room temperature to 500 °C under N₂ atmosphere. 23
- Figure 3.3.** The symmetry unit of solid-state interaction of polyanions with Na⁺ and K⁺ counter cations in **Pt₇** (left) and Na⁺ counter cations in **PtPd₆** (right), respectively (50% probability ellipsoids). 26
- Figure 3.4.** Structural representation of **Pt₇** (left) and **PtPd₆** (right). Color code: Pt (orange), Pd (dark red), O (red), C (gray), $\{(CH_3)_2AsO_2\}$ (blue tetrahedra), hydrogens omitted for clarity. 27
- Figure 3.5.** ¹H (a) and ¹³C (b) NMR spectra (D₂O) of **Pt₇** and **PtPd₆** compared to spectra of the references cacodylic acid (H-cac) and sodium cacodylate (Na-cac). The * represents free cacodylate ions. 28
- Figure 3.6.** Enlarged ¹H spectrum (D₂O) of **KNa-Pt₇**. 29

Figure 3.7. Time dependent ^1H spectra (D_2O) of Na-PtPd₆	29
Figure 3.8. ^1H spectrum (D_2O) of KNa-Pt₇ after 2 months.....	30
Figure 3.9. ^{195}Pt NMR spectra of KNa-Pt₇ (left) and Na-PtPd₆ (right).....	30
Figure 3.10. ESI-MS spectrum (full scan) of an aqueous solution of KNa-Pt₇ in the negative-ion mode.....	31
Figure 3.11. Left: Simulated (bottom panel) and experimental ESI-MS spectrum (top panel) of a doubly charged $[\text{Pt}_7\text{O}_6((\text{CH}_3)_2\text{AsO}_2)_6]^{2-}$ ion (expanded view); right: Simulated (bottom panel) and experimental ESI-MS spectrum (top panel) of a singly charged $[\text{HPt}_7\text{O}_6((\text{CH}_3)_2\text{AsO}_2)_6]^-$ ion (expanded view).....	32
Figure 3.12. Left: ESI-MS spectrum (full scan) of an aqueous solution of Na-PtPd₆ in the negative-ion mode; Right: Simulated (bottom panel) and experimental ESI-MS spectrum (top panel) of a doubly charged $[\text{PtPd}_6\text{O}_6((\text{CH}_3)_2\text{AsO}_2)_6]^{2-}$ ion (expanded view).....	33
Figure 3.13. X-ray photoelectron spectra and fits for Pt $4f_{7/2}$ and $4f_{5/2}$ doublet of KNa-Pt₇	34
Figure 3.14. X-ray photoelectron spectra and fits for Pt $4f_{7/2}$ and $4f_{5/2}$ doublet of Na-PtPd₆ (top), and Pd $3d_{5/2}$ and $3d_{3/2}$ doublet of Na-PtPd₆ (bottom).....	34
Figure 3.15. Schematic representation of the catalytic hydrogenation of <i>o</i> -xylene using the catalyst KNa-Pt₇@SBA15-apt	41
Figure 3.16. N_2 sorption isotherms of the SBA15 support before and after modification, after immobilization with KNa-Pt₇ and after calcination and catalysis.	44
Figure 3.17. ^1H spectrum of the filtrate obtained after immobilizing KNa-Pt₇ on the modified SBA15 support.	44
Figure 3.18. FT-IR spectra of Na-Pt₂Au₃ (red) and K-Pt₂Au₃ (blue).	48
Figure 3.19. Thermograms of Na-Pt₂Au₃ (red) and K-Pt₂Au₃ (blue) from room temperature to 500 °C under N_2	48
Figure 3.20. FT-IR spectrum of Pd₇ from 400–4000 cm^{-1} on KBr pellets.	49
Figure 3.21. FT-IR spectrum of Na-Au₄Pd₁₀ from 400–4000 cm^{-1} on KBr pellets.	49

Figure 3.22. Thermograms of **Na-Au₄Pd₁₀** from room temperature to 500 °C under N₂.50

Figure 3.23. Combined ball-and-stick/polyhedral representation and Ball-and-stick representation (side view) of **Pt₂Au₃**. Color code: {PtO₆} orange octahedra, {(CH₃)₂AsO₂} blue tetrahedra, Au yellow, Pt orange, As sky blue, O red, C grey. Hydrogen atoms omitted for clarity. 54

Figure 3.24. The symmetry unit of solid-state interaction of polyanion **1** with Na⁺ counter cations in **Na-Pt₂Au₃** (top left) and **Na-Pt₂Au₃(a)** (top right), as well as K⁺ counter cations in **K-Pt₂Au₃** (bottom), respectively (50% probability ellipsoids). Hydrogen atoms omitted for clarity. 55

Figure 3.25. Solid state structure of **Na-Pt₂Au₃** highlighting the supramolecular 2D layered plane. 56

Figure 3.26. Combined ball-and-stick/polyhedral representation and Ball-and-stick representation (side view) of **Au₄Pd₁₀**. Color code: {(CH₃)₂AsO₂} blue tetrahedra, Pd green, Au yellow. Hydrogen atoms omitted for clarity. 57

Figure 3.27. The symmetry unit of solid-state interaction of polyanion **Au₄Pd₁₀** with Na⁺ counter cations in **Na-Au₄Pd₁₀** (50% probability ellipsoids). Hydrogen atoms omitted for clarity. 58

Figure 3.28. ¹H (left) and ¹³C (right) NMR spectra of **Na-Pt₂Au₃** and **K-Pt₂Au₃** dissolved in H₂O/D₂O compared to spectra of the sodium cacodylate reference. 59

Figure 3.29. pH-dependent ¹H NMR spectra (D₂O/H₂O) of **Na-Pt₂Au₃**. 59

Figure 3.30. ¹⁹⁵Pt NMR spectra of **Na-Pt₂Au₃** and **K-Pt₂Au₃** dissolved in H₂O/D₂O. 61

Figure 3.31. ¹⁹⁵Pt NMR spectra of fresh synthesis solutions of **Na-Pt₂Au₃** after stirring at room temperature for 10 min (top left, 4510 scans) and for 40 min (top right, 3018 scans), as well as at 40 °C for 30 min (bottom left, 3052 scans) and the same solution after a longer measurement time (bottom right, 126693 scans). 61

Figure 3.32. ESI-MS spectrum (full scan) for aqueous solutions of **Na-Pt₂Au₃** in the negative-ion mode (identical result for **K-Pt₂Au₃**). 62

Figure 3.33. Simulated ESI-MS spectrum of **Na-Pt₂Au₃** and **K-Pt₂Au₃** in negative-ion mode (top) and experimental ESI-MS spectrum (bottom) of the singly-charged polyanion **Pt₂Au₃** (expanded view). 63

- Figure 3.34.** Simulated ESI-MS spectrum of **Na-Pt₂Au₃** in positive-ion mode (bottom) and experimental ESI-MS spectrum (top) of the doubly-charged $[\text{Na}_3\text{Pt}_2\text{Au}_3\text{O}_6(\text{AsO}_2(\text{CH}_3)_2)_6]^{2+}$ ion (expanded view). 63
- Figure 3.35.** The fully reversible SCSC transition of **Na-Pt₂Au₃** to **Na-Pt₂Au₃**. Left: ball-and-stick representation; right: packing diagrams for **Na-Pt₂Au₃** (AA mode) and **Na-Pt₂Au₃(a)** (AB mode). Color code: Au yellow, Pt orange, O red, C grey, N blue, As light blue, Cl light green, Na pink, H light grey..... 65
- Figure 3.36.** Experimental and simulated PXRD patterns of **Na-Pt₂Au₃(a)** and **Na-Pt₂Au₃** during a dehydration process by air drying (simulated diffraction patterns derived from single-crystal data). 66
- Figure 3.37.** PXRD patterns for **Na-Pt₂Au₃** in the presence of water vapor for different periods of time at RT..... 67
- Figure 3.38.** Thermograms of air-dried and partially rehydrated (several hours) **Na-Pt₂Au₃** from room temperature to 500 °C under N₂ atmosphere. Complete rehydration of the bulk material **Na-Pt₂Au₃** results in partial dissolution. 67
- Figure 3.39.** FT-IR spectra of air-dried and rehydrated **Na-Pt₂Au₃** from 400–4000 cm⁻¹ on KBr pellets. 68
- Figure 3.40.** Time-dependent PXRD spectra of **Na-Pt₂Au₃** under blue light irradiation. 69
- Figure 3.41.** Time-dependent ¹H NMR spectra of **Na-Pt₂Au₃** without (left) and with (right) blue light irradiation..... 69
- Figure 3.42.** FT-IR spectra of **Sc-Pd₁₆** (red) and **Zn-Pd₁₆** (blue) from 400–4000 cm⁻¹ on KBr pellets. 72
- Figure 3.43.** Structural representation of the disk-shaped **Pd₁₆** (top left), view of H-bond interaction in **Sc-Pd₁₆** (top right (along *b* axis) and bottom left (along *c* axis) and **Zn-Pd₁₆** (bottom right (along *c* axis)). Color code: Pd green, O (red), H grey, {(CH₃)₂AsO₂} blue tetrahedra, {ScO₆} green octahedra, {ZnO₄} orange tetrahedron. 76
- Figure 4.1.** FT-IR spectra of **KNa-Pt₃W₁₁** (orange), **KNa-Pt^{II}₂W₅** (blue) and **KNa-Pt^{III}₂W₅** (purple). 81
- Figure 4.2.** Thermograms of **KNa-Pt₃W₁₁** (top), **KNa-Pt^{II}₂W₅** (bottom left) and **KNa-Pt^{III}₂W₅** (bottom right) from room temperature to 500 °C under N₂ atmosphere. 81

Figure 4.3. Crystal shape of KNa-Pt₃W₁₁ , KNa-Pt^{II}₂W₅ and KNa-Pt^{III}₂W₅ (small cube crystals) from left to right.	84
Figure 4.4. The symmetry unit of solid-state interaction of polyanion with Na ⁺ and K ⁺ counter cations in KNa-Pt^{II}₂W₅ (top) and KNa-Pt^{III}₂W₅ (bottom). (50% probability ellipsoids).....	84
Figure 4.5. The symmetry unit of solid-state interaction of polyanion with Na ⁺ and K ⁺ counter cations in KNa-Pt₃W₁₁ (top), Na ⁺ and Cl ⁻ counter ions in Pt₂ (bottom). (50% probability ellipsoids).	85
Figure 4.6. Combined polyhedral/ball-and-stick representation of [Pt ₃ W ₁₁ O ₄₁] ¹⁰⁻ polyanion. Pt red, {WO ₆ } blue and green octahedra, {WO ₅ } orange square-pyramids...	86
Figure 4.7. Combined polyhedral/ball-and-stick representation of {[Pt ₃ W ₁₁ O ₄₁] ¹⁰⁻ } _n chain. Pt red, {WO ₆ } and {WO ₅ } blue octahedra.	87
Figure 4.8. Combined polyhedral/ball-and-stick representation of [Pt ^{II} ₂ W ₅ O ₁₈ ((CH ₃) ₂ AsO ₂) ₂] ⁴⁻ anion (left) and [Pt ^{III} ₂ W ₅ O ₁₈ ((CH ₃) ₂ AsO ₂) ₄] ⁴⁻ anion (right). Pt red, {WO ₆ } blue octahedra, {(CH ₃) ₂ AsO ₂ } green tetrahedra.	88
Figure 4.9. Combined polyhedral/ball-and-stick representation of {[Pt ^{III} ₂ ((CH ₃) ₂ AsO ₂) ₅] ⁺ } _n chain. Pt red, {(CH ₃) ₂ AsO ₂ } green tetrahedra.	90
Figure 4.10. Simulated and experimental PXRD patterns of KNa-Pt^{II}₂W₅ upon dehydration and rehydration. (simulated diffraction pattern derived from single-crystal data).....	90
Figure 4.11. Time-dependent ¹ H (left) and ¹³ C (right) NMR spectra (H ₂ O/D ₂ O) of Pt^{II}₂W₅ compared to spectra of the reference sodium cacodylate (Na-Cac).	91
Figure 4.12. ¹⁹⁵ Pt NMR spectrum (H ₂ O/D ₂ O) of Pt^{II}₂W₅	92
Figure 5.1. FT-IR spectrum of Na-PtAs₆	96
Figure 5.2. FT-IR spectrum of Na-Pt₂As₆W₄	96
Figure 5.3. Thermograms of Na-PtAs₆ (left) and Na-Pt₂As₆W₄ (right) from room temperature to 500 °C under N ₂ atmosphere.	97
Figure 5.4. The symmetry unit of solid-state interaction of polyanion with Na ⁺ counter cations in Na-PtAs₆ (top left) and Na-Pt₂As₆W₄ (top right), as well as K ⁺ counter cations	

in **K-Pt₄As₈** (bottom left) and **K-Pt₄As₈ (dehy)** (bottom right), respectively (50% probability ellipsoids). 100

Figure 5.5. Ball-and-stick representation of [Pt^{IV}(As₃O₆)₂]²⁻ polyanion. Pt orange, As light blue, O red..... 101

Figure 5.6. Crystal packing diagram of **PtAs₆**, showing the layered structure (left) and 3D framework (right) self-assembled by the [Pt(As₃O₆)₂]²⁻ moieties via Na⁺ ions. {PtO₆} orange octahedra, {NaO₇} pink polyhedra, As light blue, O red..... 101

Figure 5.7. Ball-and-stick representation of [Pt₂As₆W₄O₂₈]¹⁰⁻ polyanion. Pt orange, W green, As light blue, O red. 102

Figure 5.8. Ball-and-stick representation of [Pt^{II}₄(H₂AsO₃)₆(HAsO₃)₂]²⁻ polyanion (left) and the [K₂(Pt^{II}₄(H₂AsO₃)₆(HAsO₃)₂)₄]⁶⁻ fragment (middle). 3D lattice structure of **K-Pt₄As₈** (right). Color code: Pt orange, As light blue, K violet, O red, H sky blue..... 103

Figure 5.9. H-bond interactions (orange dotted bonds) within the **K₂(Pt₄As₈)₄** fragment. Pt orange, As light blue, K violet, O red, H sky blue..... 105

Figure 5.10. H-bond interactions (orange dotted bonds) in the **K-Pt₄As₈** crystal packing along *b* and *c* axis..... 105

Figure 5.11. Crystal packing diagram of **Pt₄As₈**, Pt orange, As light blue, O red. H atoms are not shown. 106

Figure 5.12. Pt···Pt distance in **K₂(Pt₄As₈)₄** fragment. {AsO₃} sky blue tetrahedra, {KO₈} purple polyhedral, Pt orange..... 106

Figure 5.13. ¹⁹⁵Pt (D₂O) NMR spectra of **Na-Pt₂As₆W₄**..... 108

Figure 5.14. Top: Packing diagrams for **K-Pt₄As₈** (top) along *b* and *c* axis. Bottom: the {K(Pt^{II}₄(AsO₃)₈)₈} fragment (left) and packing diagram (right) along *c* axis of **K-Pt₄As₈ (dehy)**. {KO₈} purple polyhedron. 109

Figure 5.15. Simulated and experimental PXRD patterns (left) of **K-Pt₄As₈** and **K-Pt₄As₈ (dehy)** upon dehydration and rehydration. (simulated diffraction patterns derived from single-crystal data). 110

Figure 5.16. PXRD patterns **K-Pt₄As₈** upon dehydration by air drying and heating..... 111

Figure 5.17. TGA curves of freshly prepared, dehydrated, and rehydrated compound **K-Pt₄As₈**..... 111

Figure 5.18. FT-IR spectrums of freshly synthesized and dehydrated K-Pt₄As₈	112
Figure 5.19. X-ray photoelectron spectra and fits for Pt d _{3/2} and d _{5/2} doublet (left) and As 3p doublet (right) of Pt₄As₈	113
Figure 5.20. FT-IR spectrums of K-Pt₄As₈	114
Figure 6.1. FT-IR spectra of Na-Rh₄As₂W₁₀ (red) and Na- Rh₄P₂W₁₀ (blue).	116
Figure 6.2. Thermograms of Na-Rh₄As₂W₁₀ (red) and Na-Rh₄P₂W₁₀ (blue) from room temperature to 500 °C under N ₂ atmosphere.	117
Figure 6.3. Polyhedral representation of the structure of Rh₄As₂W₁₀ (left) and Rh₄P₂W₁₀ (right). Color code: Rh (dark red), As (yellow), P (purple), Na (green), O (red), C (grey), WO ₆ (blue octahedra).	120
Figure 6.4. ¹³ C NMR spectra (H ₂ O/D ₂ O) of Rh₄As₂W₁₀ (top) and Rh₄P₂W₁₀ (bottom).	121
Figure 6.5. ³¹ P NMR spectra (H ₂ O/D ₂ O) of Rh₄P₂W₁₀	121

List of Tables

Table 3.1. Crystal data and structure refinement for KNa-Pt₇ and Na-PtPd₆	23
Table 3.2. BVS values for μ_3 -bridging oxygen atoms in KNa-Pt₇ and Na-PtPd₆	25
Table 3.3. Computationally predicted NMR chemical shifts (δ_{calc}) in ppm for Pt₇ and PtPd₆ using different methods.....	36
Table 3.4. Cartesian Coordinates of computationally optimized structures for Pt₇ and PtPd₆ anions (Ångström, Å).....	36
Table 3.5. <i>o</i> -xylene hydrogenation at 300 °C and 90 bar H ₂ pressure using different supported catalyst materials (support = SBA15-apts).	42
Table 3.6. Variation of the surface area and pore size of the prepared materials after modification, Pt₇ immobilization, calcination and after catalysis.	43
Table 3.7. Crystal data and structure refinement for Na-Pt₂Au₃ , Na-Pt₂Au₃(a) , K-Pt₂Au₃ and Na-Au₄Pd₁₀	51
Table 3.8. BVS values for μ_2 -bridging oxygen atoms in Na-Pt₂Au₃ , Na-Pt₂Au₃(a) , and K-Pt₂Au₃	53
Table 3.9. BVS values for μ_3 -bridging oxygen atoms in Na- Au₄Pd₁₀	53
Table 3.10. Peak assignments of the ESI-MS spectra of Na-Pt₂Au₃ and K-Pt₂Au₃	64
Table 3.11. Crystal data and structure refinement for Sc-Pd₁₆ and Zn-Pd₁₆	72
Table 3.12. BVS values for μ_2 - and μ_4 -bridging oxygen atoms in Sc-Pd₁₆ and Zn-Pd₁₆	73
Table 4.1. Crystal data and structure refinement for KNa-Pt₃W₁₁ , KNa-Pt^{II}₂W₅ , KNa-Pt^{III}₂W₅ and Pt₂	82
Table 5.1. Crystal data and structure refinement for Na-PtAs₆ , K-Pt₄As₈ , K-Pt₄As₈ (dehy) and Na-Pt₂As₆W₄	97
Table 5.2. Bond valence sum values for different types of bridging oxygen atoms and terminal oxygen atoms for K-Pt₄As₈ and Na-Pt₂As₆W₄	98

Table 5.3. Bond valence sum values for Pt and As atoms for **K-Pt₄As₈**..... 107

Table 6.1. Crystal data and structure refinement for **Na-Rh₄As₂W₁₀** and **Na-Rh₄P₂W₁₀**.
.....117

List of Compounds Obtained with Codes

1	$\text{KNa}[\text{Pt}^{\text{IV}}\text{Pt}^{\text{II}}_6\text{O}_6(\text{AsO}_2(\text{CH}_3)_2)_6] \cdot \text{NaNO}_3 \cdot \text{NaAsO}_2(\text{CH}_3)_2 \cdot 21\text{H}_2\text{O}$	KNa-Pt₇
2	$\text{Na}_2[\text{Pt}^{\text{IV}}\text{Pd}^{\text{II}}_6\text{O}_6(\text{AsO}_2(\text{CH}_3)_2)_6] \cdot 2\text{NaNO}_3 \cdot 9\text{H}_2\text{O}$	Na-PtPd₆
3	$\text{Na}[\text{Pt}^{\text{IV}}_2\text{Au}^{\text{III}}_3\text{O}_6(\text{AsO}_2(\text{CH}_3)_2)_6] \cdot \text{NaCl} \cdot \text{NaNO}_3 \cdot 6\text{H}_2\text{O}$	Na-Pt₂Au₃
4	$\text{K}[\text{Pt}^{\text{IV}}_2\text{Au}^{\text{III}}_3\text{O}_6(\text{AsO}_2(\text{CH}_3)_2)_6] \cdot \text{KCl} \cdot \text{KAsO}_2(\text{CH}_3)_2 \cdot 18\text{H}_2\text{O}$	K-Pt₂Au₃
5	$\text{Na}_2[\text{Pd}^{\text{II}}_{10}\text{Au}^{\text{III}}_4\text{O}_{12}(\text{AsO}_2(\text{CH}_3)_2)_{10}] \cdot 17\text{H}_2\text{O}$	Na-Au₄Pd₁₀
6	$4[\text{Pd}_{16}\text{O}_{24}(\text{OH})_8((\text{CH}_3)_2\text{As})_8] \cdot \text{NaSc}((\text{CH}_3)_2\text{As})_4(\text{H}_2\text{O})_2 \cdot x\text{H}_2\text{O}$	Sc-Pd₁₆
7	$4[\text{Pd}_{16}\text{O}_{24}(\text{OH})_8((\text{CH}_3)_2\text{As})_8] \cdot \text{Na}_2\text{Zn}((\text{CH}_3)_2\text{As})_4 \cdot x\text{H}_2\text{O}$	Zn-Pd₁₆
8	$\text{K}_3\text{Na}_7[\text{Pt}_3\text{W}_{11}\text{O}_{41}] \cdot 16\text{H}_2\text{O}$	KNa-Pt₃W₁₁
9	$\text{Na}_2\text{K}_2[\text{Pt}^{\text{II}}_2\text{W}_5\text{O}_{18}((\text{CH}_3)_2\text{AsO}_2)_2] \cdot 9\text{H}_2\text{O}$	KNa-Pt^{II}₂W₅
10	$\text{Na}_2\text{K}_2[\text{Pt}^{\text{III}}_2\text{W}_5\text{O}_{18}((\text{CH}_3)_2\text{AsO}_2)_4] \cdot x\text{H}_2\text{O}$	KNa-Pt^{III}₂W₅
11	$4[\text{Pt}^{\text{III}}_2((\text{CH}_3)_2\text{AsO}_2)_5] \cdot 2[\text{PtCl}_4] \cdot \text{Na}_2[\text{PtCl}_4] \cdot x\text{H}_2\text{O}$	Pt₂
12	$\text{Na}_2[\text{Pt}(\text{As}_3\text{O}_6)_2] \cdot 7\text{H}_2\text{O}$	Na-PtAs₆
13	$\text{K}_2[\text{Pt}_4(\text{H}_2\text{AsO}_3)_6(\text{HAsO}_3)_2] \cdot 5\text{H}_2\text{O}$	K-Pt₄As₈
14	$\text{Na}_{10}[\text{Pt}_2\text{As}_6\text{W}_4\text{O}_{28}] \cdot 18\text{H}_2\text{O}$	Na-Pt₂As₆W₄
15	$\text{Na}_5[\text{Na}(\text{Rh}^{\text{III}}\text{C}_5\text{Me}_5)_4(\textit{cis}\text{-As}^{\text{V}}_2\text{W}_{10}\text{O}_{42})] \cdot 12\text{H}_2\text{O}$	Na-Rh₄As₂W₁₀
16	$\text{Na}_5[\text{Na}(\text{Rh}^{\text{III}}\text{C}_5\text{Me}_5)_4(\textit{trans}\text{-P}^{\text{V}}_2\text{W}_{10}\text{O}_{42})] \cdot 12\text{H}_2\text{O}$	Na-Rh₄P₂W₁₀

Chapter I Introduction

1.1 Polyoxometalates (POMs)

Polyoxometalates (POMs), often described as discrete and soluble polynuclear metal-oxygen cluster anions, which contain highly symmetrical core assemblies of MO_x units, where M is usually tungsten or molybdenum, less frequently vanadium, niobium or tantalum, or mixtures of these elements, at high (d^0 , d^1) oxidation states.¹ POMs include two families of isopolyanions ($[\text{M}_y\text{O}_z]^{n-}$) and heteropolyanions ($[\text{X}_x\text{M}_y\text{O}_z]^{m-}$) (X = heteroatom, e.g. As, P, Si and M = metallic elements in their high oxidation numbers). The structure of POMs is defined primarily by either corner sharing (one bridging μ_2 -oxo group) or edge sharing (two bridging μ_2 -oxo groups) of MO_6 octahedra. Occasionally it can be also defined by sharing of three bridging μ_2 -oxo groups (face sharing).² Eventually connection of polyhedra in different fashions leads to various structures (Figure 1.1), for example, Keggin type,³ Wells-Dawson type,⁴ Anderson-Evans type,⁵ Lindqvist type,⁶ Allmann-Waugh type (1:9),⁷ Strandberg,⁸ Dexter-Silverton type (1:12),⁹ and Weakley-Yamase.¹⁰

POMs show great promise in terms of their applications, including in catalysis, biotechnology, medicine, electrochemistry, material sciences and molecular magnetism etc.¹¹ These applications stem from the noticeable features of POMs, such as: (1) possessing high solubility in various media, thermal and oxidative stability; (2) displaying a wide variety of well-defined sizes and shapes, usually with highly symmetric topologies; (3) having interesting redox properties (e.g. recognized as electron reservoirs because of their high capacity to bear and release electrons) that can be tuned to great extent by the

POM skeletons modifications; and (4) containing sufficient charge density at their surface oxygens to incorporate either functional organic moieties or additional metallic centers from the d and f blocks.¹²

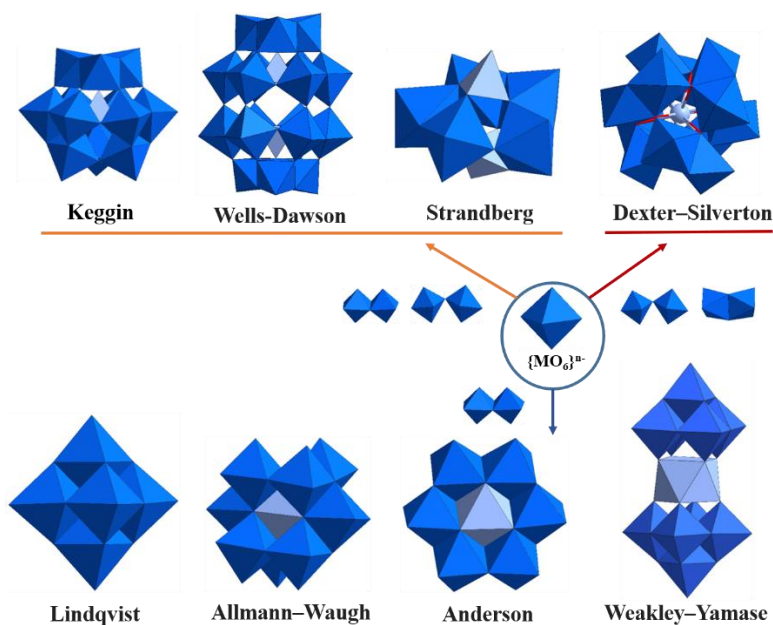


Figure 1.1. POM structural types: Keggin, Wells-Dawson, Strandberg (edge-shared and corner-shared); Lindqvist, Anderson, Allman-Waugh, Weakley-Yamase (edge-shared) and Dexter-Silverton (face-shared and corner-shared).

The Keggin anion, first to be reported was 12-tungstophosphoric acid [H₃PW₁₂O₄₀] in 1933.^{3c} Ever since that, Keggin structure motif has become the archetypical polyoxometalate (POM) and one to which the majority of POM-related publications are devoted. The Keggin structure consists of four {M₃O₁₃} triads of edge-sharing octahedra, surrounding a central tetrahedral oxoanion XO₄ with a charge that can range from 2- (X = S^{VI})¹³ to 7- (X = Cu^I).¹⁴ The original (α) Keggin anions isomer can undergo 60° rotations of one, two, three and four {M₃O₁₃} units to respectively give the β , γ , δ , and ϵ isomers (see the Figure 1.2).¹⁵ The rearrangement of the triads affects not only the overall electronic and atomic structure but also the electrostatic repulsion between these units. The Keggin anions

are preferred to adopt α and β forms, especially the most stable α one ($\alpha > \beta$), whereas the γ , δ , and ε frameworks are thermodynamically unstable.¹⁶ And the δ and ε isomers can only be obtained in a reduced state when bound to a transition metal ion. The energy grows as well as the number of rotated triads of the metal-oxide core in the order $\alpha < \beta < \gamma < \delta < \varepsilon$, a trend that does not hold for the reduced clusters.¹⁷ Indeed, some V^{IV} -containing Keggin-based anions have been used as qubits for molecular spintronics¹⁸ or as molecular magnets.¹⁹

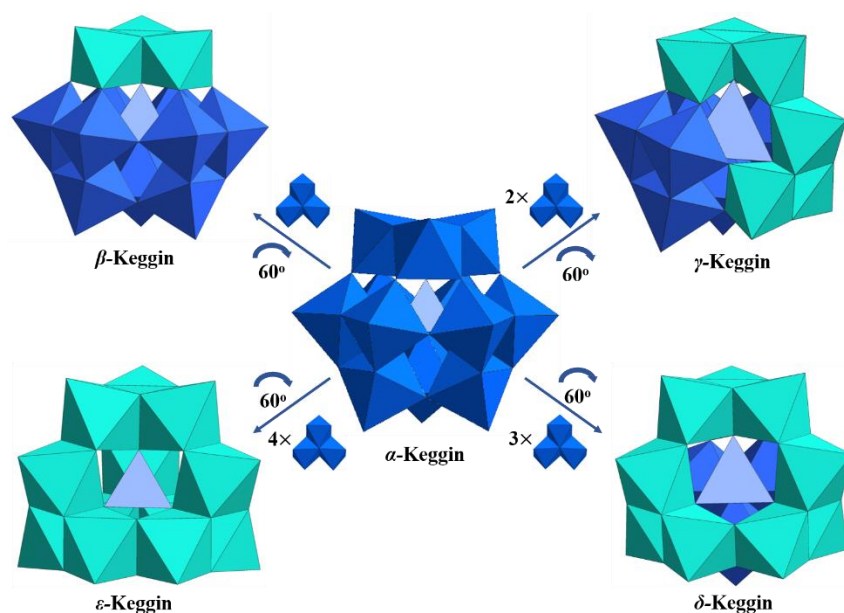


Figure 1.2. View of 5 isomers of Keggin type polyanions. Color codes: original $\{M_3O_{13}\}$ polyhedrons, blue; after rotating $\{M_3O_{13}\}$ polyhedrons, green.

Primitively, POMs have been prepared and isolated from conventional aqueous and nonaqueous solutions and hydrothermal synthesis. Based on the information obtained over the years, chemists are making efforts to re-evaluate their synthetic approach and employ new approaches, such as “superheating” microwave synthesis, ionothermal method, and solid-phase synthetic protocol.²⁰ Generally, a small number of steps, or even just one step (one-pot synthesis) are required to produce POM-based clusters, during which the

acidification is a main factor that drives the condensation reaction. There are some crucial experimental variables for the formation of specific molecular species, and need to be taken into consideration during the synthesis, such as: (1) concentration/type of metal oxide anion, (2) pH, (3) ionic strength, (4) heteroatom type/concentration, (5) presence of additional ligands, (6) reducing environment, (7) temperature and pressure of reaction (e.g., microwave, hydrothermal, refluxing), (8) counter-ion and metal-ion effect and (9) processing methodology (one-pot, continuous flow conditions, 3D printed reactors).²¹

1.2 Polyoxo-noble-metalates

Recently, an entirely new family of POM clusters which are based on non-traditional metal centers, is the family of palladates. Like all the other noble metals, Pt and Au, discussed in this section, the square-planar Pd^{II} ions can assemble into POM-like molecular structures bridged with oxygen ligands, containing heteroatom capping groups or both ligand and heteroatom capping groups. To date, more than 80 polyoxopalladates(II) with a large compositional and structural variety (e.g. cube, star, bowl, dumbbell, wheel, and open-shell archetypes) have been prepared by using various external capping groups RXO_3^{n-} ($\text{X} = \text{P}^{\text{V}}$, As^{V} , Se^{IV} , V^{V} ; $\text{R} = \text{O}$, Ph, lone pair) and many different central metal ion guests M ($\text{M} = s$, p , d or f element).²² There have been a series of $\{\text{Pd}_x\}$ species which are first examples of polyoxopalladate(II) reported by Kortz group of different nuclearities, such as $\{\text{Pd}_{13}\}$,²³ $\{\text{Pd}_{15}\}$ ²⁴ and $\{\text{Pd}_{22}\}$ ²⁵ (Figure 1.3). Recently, the same group demonstrated the ability of $[\text{Pd}^{\text{II}}_{13}\text{As}^{\text{V}}_8\text{O}_{34}(\text{OH})_6]^{8-}$ to be used as secondary building blocks for the formation of the first stable heterogeneous noble metal-based metal-organic framework exhibiting interesting sorption and catalytic properties.²⁶ In 2021, Kortz group reported the first

examples of neutral palladium(II)-oxo clusters (POCs), $[\text{Pd}_{16}\text{O}_8(\text{OH})_8((\text{CH}_3)_2\text{AsO}_2)_8]$ (**Pd₁₆**), $[\text{Pd}_{16}\text{O}_8(\text{OH})_5\text{Cl}_3((\text{CH}_3)_2\text{AsO}_2)_8]$ (**Pd₁₆Cl**), $[\text{Pd}_{24}\text{O}_{12}(\text{OH})_8((\text{CH}_3)_2\text{AsO}_2)_{16}]$ (**Pd₂₄**), and $[\text{Pd}_{40}\text{O}_{24}(\text{OH})_{16}(\text{CH}_3)_2\text{AsO}_2)_{16}]$ (**Pd₄₀**), by using dimethylarsinate as capping group.²⁷ Later, the first two examples of cationic palladium(II)-oxo clusters (POCs) by incorporating *f*-metal ions, $[\text{Pd}^{\text{II}}_6\text{O}_{12}\text{M}_8\{(\text{CH}_3)_2\text{AsO}_2\}_{16}(\text{H}_2\text{O})_8]^{4+}$ ($\text{M} = \text{Ce}^{\text{IV}}, \text{Th}^{\text{IV}}$),²⁸ as well as the mixed-valent palladium(IV/II)-oxoanion $[\text{Pd}^{\text{IV}}\text{O}_6\text{Pd}^{\text{II}}_6((\text{CH}_3)_2\text{AsO}_2)_6]^{2-}$ were also synthesized by Kortz group.²⁹ When reacting Pd^{II} and Au^{III} ions at the same time with the arsenate capping group, the first fully inorganic, mixed gold-palladium-oxoanion $[\text{NaAu}^{\text{III}}_4\text{Pd}^{\text{II}}_8\text{O}_8(\text{AsO}_4)_8]^{11-}$ (**Au₄Pd₈**) could be obtained.³⁰ In 2016, Kortz group reported on the rational synthesis of the first examples of noble metal-capped bimetallic silver(I)-palladium(II)-oxo nanoclusters $\{\text{Ag}_4\text{Pd}_{13}\}$ and $\{\text{Ag}_5\text{Pd}_{15}\}$ in a fully inorganic assembly, featuring an unprecedented host-guest mode.³¹

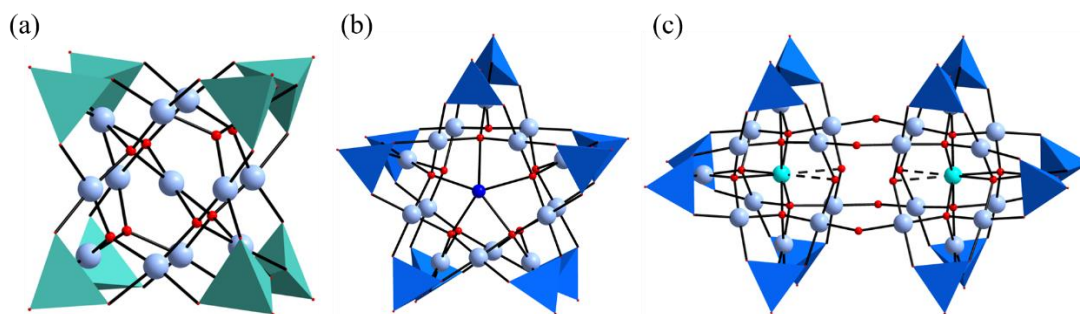


Figure 1.3. Combined polyhedral/ball-and-stick representation of $[\text{Pd}^{\text{II}}_{13}\text{As}^{\text{V}}_8\text{O}_{34}(\text{OH})_6]^{8-}$ (a), $[\text{Na}\text{C}\text{Pd}^{\text{II}}_{15}\text{O}_{40}(\text{P}^{\text{V}}\text{O})_{10}]^{19-}$ (b) and $[\text{Cu}^{\text{II}}_2\text{Pd}^{\text{II}}_{22}\text{P}^{\text{V}}_{12}\text{O}_{60}(\text{OH})_8]^{20-}$ (c). Color code, balls: Pd (pale blue), Cu (sky blue), Na (blue), O (red); polyhedra: $\{\text{AsO}_4\}$ (green), $\{\text{PO}_4\}$ (light blue).

Moving to the larger and more kinetically inert Pt, the reported examples are limited to the structure published by Wickleder group in 2004 with the formula $[\text{Pt}^{\text{III}}_{12}\text{O}_8(\text{S}^{\text{VI}}\text{O}_4)_{12}]^{4-}$ (Figure 1.4) where the Pt atoms lie on the corners of an icosahedron formed by six dumbbell-shaped $\{\text{Pt}_2\}^{6+}$ units.³² Obviously, the reactivity of Au with comparable ionic

radius proved to be more diverse. In 2010 Kortz group successfully synthesized the first ever members of polyoxoaurate $[\text{Au}^{\text{III}}_4\text{As}^{\text{V}}_4\text{O}_{20}]^{8-}$ and its dimeric adducts $\{\text{Cl}_4\text{Na}_5[\text{Au}^{\text{III}}_4\text{As}^{\text{V}}_4\text{O}_{20}\text{H}_{2.5}]_2\}^{10-}$ and $\{(\text{NO}_3)_4\text{Na}_5[\text{Au}^{\text{III}}_4\text{As}^{\text{V}}_4\text{O}_{20}\text{H}_{2.5}]_2\}^{10-}$ are shown in Figure 1.5.³³ The main polyanionic skeleton consists of a tetrameric structure with four square-planar coordinated Au^{III} ions linked by four oxo and arsenate/selenite bridging ligands.³⁴

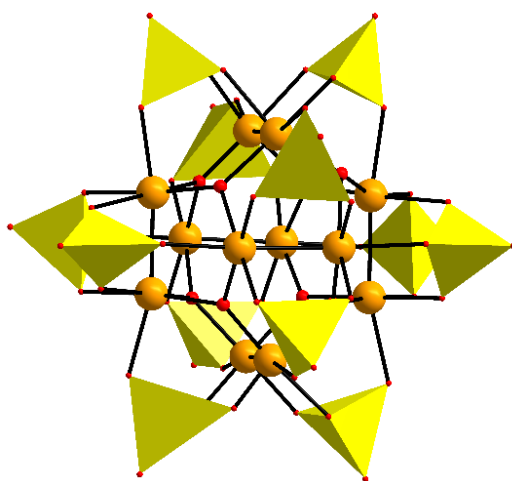


Figure 1.4. Combined polyhedral/ball-and-stick representation of $[\text{Pt}^{\text{III}}_{12}\text{O}_8(\text{S}^{\text{VI}}\text{O}_4)_{12}]^{4-}$. Color code, balls: Pt (orange), O (red); polyhedra: $\{\text{SO}_4\}$ (yellow).

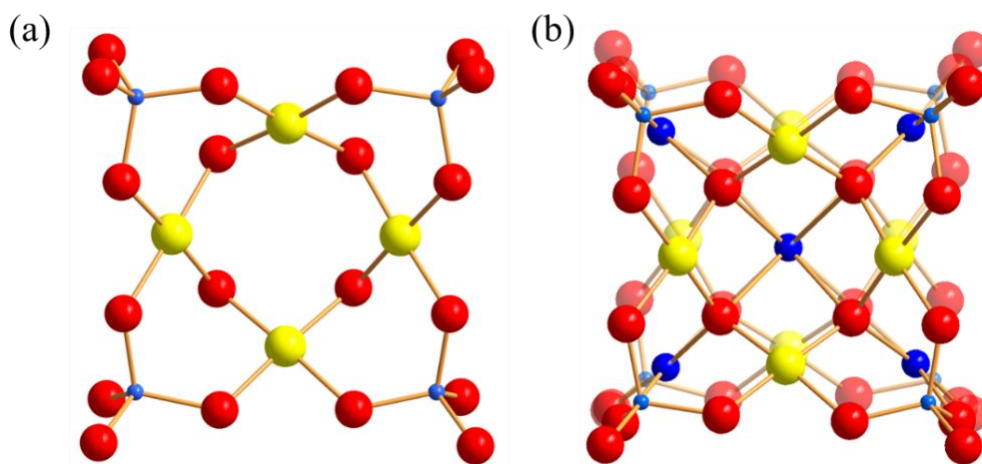


Figure 1.5. Ball-and-stick representation of (a) $[\text{Au}^{\text{III}}_4\text{As}^{\text{V}}_4\text{O}_{20}]^{8-}$ and (b) $\{\text{Cl}_4\text{Na}_5[\text{Au}^{\text{III}}_4\text{As}^{\text{V}}_4\text{O}_{20}\text{H}_{2.5}]_2\}^{10-}$ dimeric fragment. Color code: Au, yellow; As, light blue; O, red; Na, blue. Chlorides and solvent molecules have been omitted for clarity.

1.3 Platinum-containing POMs

The coordination chemistry of platinum has a long history and can be regarded as classics, but surprisingly little is known about incorporation of Pt(IV) or Pt(II) to polyoxometalates (POM). Moreover, some reports on supposedly Pt-coordinated POM remain controversial. In terms of platinum-containing POMs, well established examples of Pt containing POM are sparse and are essentially restricted to a series of Pt(IV)-containing Anderson-type clusters with various degrees of protonation reported in the course of years, such as $[\text{H}_3\text{Pt}^{\text{IV}}\text{W}_6\text{O}_{24}]^{5-}$,³⁵ and $[\text{Pt}^{\text{IV}}\text{Mo}_6\text{O}_{24}]^{8-}$ (Figure 1.6).³⁶ In 2003, the Lee group also reported a double Pt-substituted silicotungstate $(\text{C}(\text{NH}_2)_3)_8[\text{SiPt}^{\text{IV}}_2\text{W}_{10}\text{O}_{40}]\cdot 6\text{H}_2\text{O}$.³⁷ Later it was, however, suggested that this formulation was incorrect, the product being instead the guanidinium salt of monolacunary $[\text{SiW}_{11}\text{O}_{39}]^{8-}$.³⁸ In 2011, a Pt^{IV}-containing Keggin-type tungstophosphate anion $\alpha\text{-}[\text{PW}_{11}\text{O}_{39}\{\text{Pt}(\text{NH}_3)_2\}_2]^{3-}$ was proposed, based on ¹H and ¹⁸³W NMR spectra.³⁹ This suggestion was confirmed very recently by single-crystal XRD on $\text{Cs}_3[\alpha\text{-PW}_{11}\text{O}_{39}\{\text{cis-Pt}(\text{NH}_3)_2\}_2]\cdot 8\text{H}_2\text{O}$, which demonstrated that the $\{\text{cis-Pt}(\text{NH}_3)_2\}$ groups are attached to the lacunary polyanion.⁴⁰ Platinum-containing $[\text{ZnWPt}^{\text{II}}_2(\text{ZnW}_9\text{O}_{34})_2]^{12-}$ complexes are represented but not yet fully characterized.⁴¹

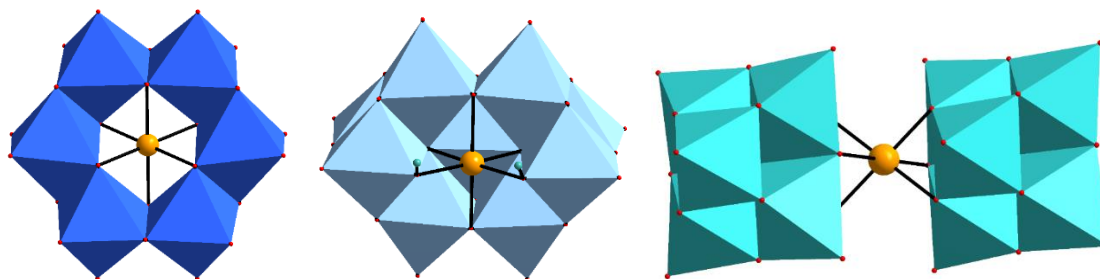


Figure 1.6. Combined polyhedral/ball-and-stick representation of $[\text{Pt}^{\text{IV}}\text{W}_6\text{O}_{24}]^{8-}$ (left), $[\text{H}_2\text{Pt}^{\text{IV}}\text{V}_9\text{O}_{28}]^{5-}$ (middle) and $[\text{Pt}^{\text{IV}}(\text{Nb}_6\text{O}_{19})_2]^{12-}$ (right). Color code: Pt (orange), O (red), H (green), $\{\text{WO}_6\}$ (blue), $\{\text{VO}_6\}$ (sky blue), $\{\text{NbO}_6\}$ (green).

In 2012, Pt(II)-containing dimeric POM complex $[\text{Pt}_2(\text{W}_5\text{O}_{18})_2]^{8-}$ was reported, containing two lacunary Lindqvist isopoly fragments $[\text{W}_5\text{O}_{18}]^{6-}$ linked by two square planar Pt(II) centers.⁴² In the family of group 5 POM the only example of a Pt-containing complex is $\text{Na}_5[\text{H}_2\text{Pt}^{\text{IV}}\text{V}_9\text{O}_{28}] \cdot 21\text{H}_2\text{O}$ (Figure 1.6).⁴³ The ^{51}V and ^{195}Pt NMR chemical shifts for $[\text{H}_2\text{Pt}^{\text{IV}}\text{V}_9\text{O}_{28}]^{5-}$ were successfully modeled by DFT methods.⁴⁴ In 2015, the first platinum polyniobates was characterized by Abramov and Sokolov groups.⁴⁵ Reaction of $[\text{Nb}_6\text{O}_{19}]^{8-}$ with $[\text{Pt}(\text{OH})_4(\text{H}_2\text{O})_2]$ in a 1:1 molar ratio upon heating yielded a dimeric complex $[\text{Nb}_6\text{O}_{19}\{\text{Pt}^{\text{IV}}(\text{OH})_2\}]_2^{12-}$. Increasing the Pt/Nb₆ molar ratio to 1:2 yielded a mixture of $[\text{Nb}_6\text{O}_{19}\{\text{Pt}^{\text{IV}}(\text{OH})_2\}]_2^{12-}$ and a sandwich type complex $[\text{Pt}^{\text{IV}}(\text{Nb}_6\text{O}_{19})_2]^{12-}$ (Figure 1.6). The first examples of dimeric, di-Pt^{II}-containing heteropolytungstates are reported, the two isomeric diplatinum(II)-containing 22-tungsto-2-phosphates anti- and syn- $[\text{Pt}^{\text{II}}_2(\alpha\text{-PW}_{11}\text{O}_{39})_2]^{10-}$.⁴⁶ Another Pt(II)-containing POM also has been reported, $[\alpha\text{-PW}_{11}\text{O}_{39}\{\text{cis-Pt}^{\text{II}}(\text{Me}_2\text{ppz})\}]^{5-}$ ($\text{Me}_2\text{ppz} = N,N'$ -dimethylpiperazine).⁴⁷ Later, there are several reports describing very interesting electrocatalytic activity of single-atom Pt-containing POM and $[\text{Pt}_2(\text{W}_5\text{O}_{18})_2]^{8-}$ in the hydrogen evolution reaction (HER).⁴⁸ Hence the preparation and reliable characterization of Pt-containing POM (this is also more or less true for other noble metals) still remains a considerable challenge.

1.4 Arsenic(III) Compounds

Transition metal oxoarsenates(III) are of interest due to the presence of the $4s^2$ electron lone pair E situated at the As^{III} atom. The spatial arrangement of corresponding ψ -tetrahedral AsO_3^{3-} groups may result in compounds with non-centrosymmetric crystal structures exhibiting interesting physical properties like pyroelectricity, piezoelectricity,

ferroelectricity, or non-linear optical (NLO) properties.⁴⁹ Moreover, oxoarsenates(III) are possible sources or intermediates of natural arsenic compounds in the lithosphere. In particular, arsenic(III) compounds are considered as the main and most toxic pollutants in drinking or ground waters with high arsenic concentrations in some areas of the earth.⁵⁰ Finally, a large number of water-containing and anhydrous oxoarsenates is known from nature as minerals.⁵¹ In combination with the different valence states of the transition metals, it exists a variety of ternary compounds. Representatives of oxoarsenates(V) are well known. However, representatives of oxoarsenates(III) are comparatively scarce. Although, the classical coordination chemistry of platinum has a long history and is replete with interesting compounds, only limited work has been reported on the cluster of Pt^{IV} or Pt^{II}. For example, in the 1990s oxonitro-complexes comprising di- and/or tetravalent platinum ions (e.g. [Pt^{IV}Pt^{II}₃O₃(NO₂)₉]⁵⁻, [Pt^{IV}Pt^{II}₆O₆(NO₂)₁₂]⁸⁻) were reported.⁵² In 1988, a mixed-valence tetranuclear platinum(I,II) complex ([Pt^I₂Pt^{II}₂(μ ₃-O)₂(DMSO)₆Cl₂]) with a Pt(I)-Pt(I) bond was reported.⁵³ In 2015 polynuclear hydroxy-bridged platinum(IV) nitrate complexes, [Pt^{IV}₄(OH)₆(NO₃)₁₀] and [Pt^{IV}₆(OH)₁₀(NO₃)₁₂], were reported.⁵⁴ An important milestone in the area of polyoxo-noble-metalates was the discovery of polyoxo-12-platinate(III) (POPt), [Pt^{III}₁₂O₈(SO₄)₁₂]⁴⁻, by Wickleder and co-workers in 2004 (using rather extreme experimental conditions), which is the only polyoxoplatinate known till date, as mentioned above. In 2022, the first polythioplattinate(II), [Pt^{II}₃S₂(SO₃)₆]¹⁰⁻ was synthesized by Kortz group.⁵⁵

Besides, it is very rare that lone pair electron (*E*) containing cations bond directly to transition-metal cations as ligands. A few examples known so far involve the As³⁺ ions of pyramidal *E*AsO₃ groups, which are bonded to Cu⁺ (d¹⁰) ions to form tetrahedral clusters

with short Cu–As bonds, and to low-spin Fe^{2+} (d^6) ions to form octahedral clusters with short As–Fe bonds; such as the tetrahedral CuAs_4 cluster of dixenite with As–Cu = 2.240 and 2.336 Å,⁵⁶ the tetrahedral CuAs_2Cl_2 cluster of freedite with Cu–As = 2.32 Å, and the tetrahedral CuCl_3As cluster of $\text{Pb}_6\text{Cu}(\text{AsO}_3)_2\text{Cl}_7$ with As–Cu = 2.34 Å.⁵⁷ In the octahedral FeAs_6 clusters of nanlingite,⁵⁸ the low-spin Fe^{2+} (d^6) ion is surrounded by six As^{3+} ions with As–Fe = 2.40 Å. To the best of our knowledge, although many oxide compounds that contain AsO_3^{3-} ions have been prepared, and most metal ions in such types of compounds are transition- and rare-earth-metal ions, nearly nothing is known about the platinum. In particular, the only known compound is the arsenoplatin, $[\text{Pt}(\mu\text{-NHC}(\text{CH}_3)\text{O})_2\text{ClAs}(\text{OH})_2]$ with Pt–As = 2.27 Å.⁵⁹

1.5 The RhCp*- and IrCp*-Containing POMs

In recent years there has been a growing interest in the chemistry of organometallic oxides, not least the organometallic clusters derived from polyoxometalates, a field which has been developed by W. G. Klemperer, W. Knoth, and R. G. Finke.^{1b, 60} Various organometallic groups, for example, $[\text{M}(\text{Cp}^*)]^{2+}$ ($\text{M} = \text{Rh}, \text{Ir}$; $\text{Cp}^* = \eta^5\text{-C}_5\text{Me}_5$), $[\text{M}(\text{CO})_3]^+$ ($\text{M} = \text{Mn}, \text{Re}$), $[\text{M}(\text{CO})_2]^+$ ($\text{M} = \text{Rh}, \text{Ir}$), $[\text{Ru}(\text{C}_6\text{H}_6)]^+$, $[\text{Rh}(\text{C}_7\text{H}_8)]^+$, and $[\text{Ir}(\text{C}_8\text{H}_{12})]^+$, have been employed to assemble the oxide clusters. The derivatives can serve as models for metal oxide surfaces and thus help to provide a basic understanding of catalyst-to-support interactions in heterogeneous catalytic processes. Recent in situ EXAFS⁶¹ and FT-IR⁶² studies show that RhCp* derivatives supported on inorganic oxide surface are more active and selective for hydroformylation than classical impregnation catalysts. However, and despite such potential, the chemistry (e.g. catalysis) of RhCp*- and IrCp*-containing POMs has not

been extensively investigated.

At an early stage, most of these studies have employed niobium incorporated heteropolytungstates as the support system, namely Klemperer and Day's $[\text{RhCp}^*(\text{cis-Nb}_2\text{W}_4\text{O}_{19})]^{2-}$ (the first RhCp^* -containing POMs in 1984),⁶³ in which the *cis*- $\text{Nb}_2\text{W}_4\text{O}_{19}^{4-}$ ion behaves as a tridentate ligand utilizing a triangle of bridging oxygen atoms for the rhodium binding site, and Finke's Keggin $\text{SiW}_9\text{Nb}_3\text{O}_{40}^{7-}$ and Dawson $\text{P}_2\text{W}_{15}\text{Nb}_3\text{O}_{62}^{9-}$ systems.^{60b, 63-64} Finke's work was followed up in 1996 by Nomiya with the synthesis of $\text{Na}_5[\text{RhCp}^*\text{SiW}_9\text{Nb}_3\text{O}_{40}]\cdot 3\text{DMSO}\cdot 2\text{H}_2\text{O}$.⁶⁵ The report of $(\text{MCp}^*)_4\text{V}_6\text{O}_{19}$ ($\text{M} = \text{Rh}, \text{Ir}$) constituted the first example of a vanadium-substituted polyoxoanion-supported organometallic groups $[\text{M}(\text{Cp}^*)]^{2+}$,⁶⁶ and only three other examples of trivanadium polyoxoanion-supported organometallics group $[\text{RhCp}^*]^{2+}$, $(\text{Bu}^n_4\text{N})_5[(\text{RhCp}^*)_2\text{P}_2\text{W}_{15}\text{V}_3\text{O}_{62}]$, $[(\text{RhCp}^*)(\alpha\text{-}1,4,9\text{-PW}_9\text{V}_3\text{O}_{40})]^{4-}$ and $(\text{NBu}_4)_6[(\text{RhCp}^*)(\alpha\text{-}1,2\text{-P}_2\text{W}_{16}\text{V}_2\text{O}_{62})]$, have since reported by Nomiya group.⁶⁷ In 1993, five organorhodium $[\text{RhCp}^*]^{2+}$ oxomolybdenum complexes had been reported by Gouzerh group, the $[\text{Mo}_5\text{O}_{13}(\text{OCH}_3)_4(\text{NO})]^{3-}$ anion of which can be viewed as a lacunary Lindqvist-type species. In 2017, Jin had introduced two noble metal-containing POMs, the $\text{H}_3[(\text{RhCp}^*)_4\text{PMo}_8\text{O}_{32}]\cdot 14\text{H}_2\text{O}$ and the $\text{H}_5[\text{Na}_2(\text{IrCp}^*)_4\text{PMo}_8\text{O}_{34}]\cdot 13\text{H}_2\text{O}$.⁶⁸ They were chemically adsorbed and successfully nanostructured on the nanofiber surface and proved to be active electrocatalytic materials. In 2003, Nishikawa reported the triple cubane- and windmill-type isomers of an organorhodium tungsten oxide clusters $[(\text{Cp}^*\text{Rh})_4\text{W}_4\text{O}_{16}]$.⁶⁹ Later, the $[\text{H}_8\{\text{Rh}(\text{Cp}^*)\}_4\text{W}_8\text{O}_{32}]\cdot 23\text{H}_2\text{O}$ and its iridium analogue the $[\text{H}_4\{\text{Ir}(\text{Cp}^*)\}_4\text{W}_8\text{O}_{32}]\cdot 17.33\text{H}_2\text{O}$ were synthesized by Niu group.⁷⁰ In 2015, two new hybrid complexes of niobium and tantalum Lindqvist-type anions, $[\text{M}_6\text{O}_{19}]^{8-}$, with

organometallic $[\text{RhCp}^*]^{2+}$ fragments, were reported by Abramov group.⁷¹ Recently, Blanchard group have described the synthesis of a new organometallic derivative of POMs, $(\text{TBA})_3[\alpha\text{-H}_2\text{PW}_{11}\text{O}_{39}\{\text{Rh}^{\text{III}}\text{Cp}^*(\text{OH}_2)\}]$, presenting an accessible coordination site on the Rh^{III} center.⁷² Furthermore, in 2021, four organometallic RhCp^* - and IrCp^* -containing 20-Tungstobismuthates(III) and -Antimonates(III) were reported by Kortz group.⁷³

1.6 Catalysis

The hydrogenation of arenes provides a direct and retrosynthetically simple route towards saturated carbo- and heterocycles. This is an important industrial process with a wide range of applications ranging from the production of functional materials, important intermediates in organic synthesis, and pharmaceuticals to the improvement of diesel fuel quality.⁷⁴ Metals, especially noble metals and their nanoparticles, have been found to be highly effective catalysts in this area. The reduction of noble metal salts and the decomposition/reduction of organometallic compounds are both common methods for forming noble metal nanoparticles.⁷⁵ In both cases, the resulting nanoparticles are typically stabilized by ligands or capping groups such as polymers, dendrimers, ionic liquids, and surfactants, in order to prevent uncontrolled aggregation. Recently, the anionic template-assisted method was used to synthesize a series of silver nanocrystals (NCs) with different sizes and shapes.⁷⁶ However, these methods do not allow for an elegant control over the size and shape of the resulting nanoparticles. Therefore, our aim has been to design and synthesize discrete noble metal-based oxo clusters having a particular size, shape, and nuclearity, and subsequently loading them onto stable and catalytically inert supports with high surface area.

Chapter II Experimental Details

2.1 Instrumentations

2.1.1 Single-Crystal X-Ray Diffraction

Data for crystals were collected at 100 K on a Bruker D8 APEX II CCD single-crystal diffractometer equipped with kappa geometry (graphite monochromator, $\lambda_{\text{Mo K}\alpha} = 0.71073$ Å) by using APEX III software package,⁷⁷ except for **KNa-Pt₃W₁₁**, **KNa-Pt^{II}₂W₅**, **KNa-Pt^{III}₂W₅** and **K-Pt₄As₈(dehy)** which were collected at 100 K on a Rigaku XtaLAB Synergy, Dualflex, HyPix single-crystal diffractometer equipped with kappa geometry (graphite monochromator, $\lambda_{\text{Mo K}\alpha} = 0.71073$ Å) by using CrysAlis^{Pro} software package.⁷⁸ The crystals were mounted in a Hampton cryoloop with paratone-N oil. Multi-scan absorption corrections were applied using the SADABS⁷⁹ and ABSPACK⁸⁰ program, respectively. The structures were solved by direct methods with the aid of successive difference Fourier maps, and were refined against all data using the APEX III software in conjunction with SHELXL-2014.⁸¹ The hydrogen atoms of the organic groups and hydroxyl groups were placed in calculated positions and refined using a riding model and the remaining non-hydrogen atoms were refined with anisotropic displacement parameters. The H atoms of the crystal waters were not located. Refinements were conducted by full-matrix least squares against |F| using all data. Images of the crystal structures were generated by Diamond, version 3.2 (software copyright, Crystal Impact GbR). Some of the lattice water molecules were too disordered and thus the disagreeable reflections were removed by the SQUEEZE command in PLATON.⁸²

2.1.2 Fourier Transform Infrared (FT-IR) Spectroscopy

By virtue of characteristic metal–oxygen vibrations, FT-IR spectroscopy provides valuable structural information of every polyanion, especially in the fingerprint region (1000 to 400 cm^{-1}). All the spectra were recorded on KBr disks using a Nicolet-Avatar 370 spectrometer between 400 and 4000 cm^{-1} . The abbreviations used in the thesis to assign the peak intensities are as follows: s = strong, m = medium, and w = weak.

2.1.3 Elemental and Thermogravimetric Analyses

The elemental analyses were performed by Zentrallabor, Technische Universität Hamburg (TUHH), Am Schwarzenberg-Campus 1, 21073 Hamburg (heavy atoms) and Analytische Laboratorien, Industriepark Kaiserau (Haus Heidbruch), 51789 Lindlar, Germany (CHN). The K and Na analyses were performed in house by atomic absorption (AA) spectroscopy carried out on a Varian SpectrAA 220 spectrometer.

In order to evaluate the thermal stability of obtained polyanions, thermogravimetric analyses were carried out on a TA Instruments SDT Q600 thermobalance with a 100 mL min^{-1} flow of nitrogen, with the temperature being ramped from 20 – 500 $^{\circ}\text{C}$ at a rate of 5 $^{\circ}\text{C min}^{-1}$.

2.1.4 Nuclear Magnetic Resonance (NMR) Spectroscopy

The solution stability of all the polyanions was examined by multinuclear NMR spectroscopy after redissolution of their alkali metal salts in $\text{H}_2\text{O}/\text{D}_2\text{O}$. The corresponding NMR spectra were recorded on a 400 MHz JEOL ECX instrument at room temperature or by heating, using 5-mm tubes for ^1H , ^{13}C , ^{31}P and ^{195}Pt with respective resonance frequencies of 399.78 MHz (^1H), 100.71 MHz (^{13}C), 162.14 MHz (^{31}P) and 85.94 MHz

(^{195}Pt). The chemical shifts are reported with respect to the references $\text{Si}(\text{CH}_3)_4$ (^1H and ^{13}C), 85% H_3PO_4 (^{31}P) and Na_2PtCl_6 (^{195}Pt).

2.1.5 Electro-spray-Ionization Mass Spectrometry (ESI-MS)

To better assess the solution behavior of as-synthesized compounds, High-resolution ESI-MS spectra were recorded using a Bruker Daltonics Q-TOF Impact instrument employing both negative and positive electro-spray ionization modes. MicrOTOF Focus mass spectrometer (Bruker Daltonics) was fitted with an ESI source and external calibration was achieved with 10 mL of 0.1M sodium formate solution. The instrument ion source and tubing were rinsed with methanol. The calibration was carried out using the enhanced quadratic calibration mode. All ESI-MS measurements were performed in both negative and positive ion modes. Samples were measured as direct infusions at a concentration of 100 $\mu\text{g}/\text{mL}$ in deionized water at a flow rate of 180 $\mu\text{L}/\text{min}$. The spectral simulations were carried out in Data Analysis 4.1 (Bruker Daltonics, Bremen).

2.1.6 X-ray photoelectron spectroscopy (XPS)

The oxidation states of atoms in compound were ascertained using X-ray photoelectron spectroscopy (XPS) measurements. The samples were dispersed in acetone and spin-coated onto the as prepared substrates at a rotation speed of 1000 rpm. The ultra-high vacuum vessel, which had a vacuum pressure of $\sim 1 \times 10^{-8}$ mbar, was equipped with a water-cooled X-ray gun with a double Mg/Al anode (Specs XR 50) and a hemispherical electron analyzer (Specs Phoibos 100). Mg $K\alpha_{1,2}$ radiation ($E = 1253.6$ eV) was used as a source of excitation. The photoelectrons were detected in the large area lens mode and fixed analyzer

transmission at a pass energy of 50 eV. The measured data were analyzed using the CASA-XPS software. The positions of the peaks were in the expected regions.

2.1.7 Powder X-ray diffraction (PXRD)

Powder X-ray diffraction data were acquired on a Rigaku Miniflex 600 (Rigaku Corporation, Tokyo, Japan) using a primary beam Cu K α radiation ($\lambda = 1.541838 \text{ \AA}$) at 40 kV and 15 mA. The instrument scanning 2θ range was from 5 to 50° in steps of 0.02°, with a scan speed of 5 ° min⁻¹.

2.1.8 Sorption Measurements

N₂-adsorption (physisorption) measurements for surface area and pore size analysis were performed at 77 K on a Quantachrome NOVA 4000e surface area and pore size analyzer and a Quantachrome Autosorb-1 analyzer (Figure 3.6). Samples were placed in 9 mm Quantachrome cells and degassed under vacuum at 100 °C for 16 hours prior to measurements. The surface area was estimated using the Brunauer–Emmett–Teller (BET) theory and pore size was determined using Barrett-Joyner-Halenda (BJH) method.

2.1.9 Batch Reactor

Hydrogenation reactions were also performed in a 100 mL Parr 5500 stainless steel high-pressure compact reactor coupled with Parr 4848 reactor controller, allowing operation at high temperature (up to 350 °C) and pressure (up to 180 bar). In a typical reaction, the reactor was loaded with 50 mL substrate solution and 50 mg of the supported catalyst (noble metal loading is always indicated). The reactor was purged with pure H₂ prior to each reaction. The progress of the reaction was followed by monitoring the drop in

hydrogen pressure. The reaction mixture was analyzed using a GC-FID from Shimadzu after each reaction.

2.1.10 Gas chromatography (GC)

Gas chromatography (GC) analysis was performed in a Shimadzu GC-2010 equipped with a flame ionization detector (FID) in order to measure the substrate conversion and selectivity of the obtained products via a HP-5 column (15 m × 0.25 mm, I.D. 0.25 μ m) with the carrier gas being He.

2.1.11 Bond Valence Sum (BVS) Calculations

To determine the oxidation states of incorporated metal ions as well as the protonation states of oxygen ligands in obtained polyanions, bond valence sum (BVS) calculations were performed with a program copyrighted by Chris Hormillosa & Sean Healy and distributed by I. D. Brown.⁸³

2.2 Synthesis of $(\text{RhC}_5\text{Me}_5\text{Cl}_2)_2$ and POM Precursors

All the mentioned POM precursors in the thesis were synthesized according to the published procedures and the identity of the products was confirmed by NMR and FT-IR spectroscopy. The amount of crystal water present in each compound was determined by thermogravimetric analysis.

2.2.1 Synthesis of $(\text{RhCp}^*\text{Cl}_2)_2$

The RhCp^* dimers were synthesized according to the published procedures.⁸⁴ In a 50 mL round bottom flask, a sample of 1.0 g of $\text{RhCl}_3 \cdot x\text{H}_2\text{O}$ (Sigma-Aldrich) was dissolved in 30 mL of methanol followed by the addition of 690 μL of 1,2,3,4,5-pentamethylcyclopentadiene (Cp^*H). The flask was connected to a condenser and flushed with nitrogen for about 5 min, then refluxed at 73 °C in an oil bath for 48 hours during which the setup was constantly flushed with nitrogen. After cooling to room temperature, the solution was filtered to isolate a red microcrystalline material. The filtrate was concentrated to about 5 mL on a rotary evaporator and some additional product crystallized out during the evaporation. The obtained crystals were then added to the previously filtered material and the combined batch was washed with 10 mL of diethyl ether and dried under air. (Yield: 95% based on Rh)

2.2.2 $\text{Na}_9[\text{A-}\alpha\text{-As}^{\text{V}}\text{W}_9\text{O}_{34}] \cdot 18\text{H}_2\text{O}$

To a solution of $\text{Na}_2\text{WO}_4 \cdot 2\text{H}_2\text{O}$ (45 g, 136 mmol) in H_2O (40 mL), $\text{Na}_2\text{HAsO}_4 \cdot 7\text{H}_2\text{O}$ (4.7 g, 15 mmol) and 8.7 mL of pure acetic acid were successively added. The solid which precipitated gradually was filtered, washed with ethanol and air-dried with aspiration. Yield: 38 g (90% based on W).⁸⁵

2.3 Synthesis of Mesoporous Supports

2.3.1 Synthesis of SBA15

A modified synthetic procedure was used to synthesize the Santa Barbara Amorphous-15 (SBA15).⁸⁶ In a typical synthesis, 120.0 g of Pluronic® P123 (Mn ~ 5,800, Sigma Aldrich) stirred in a mixture of 3.6 L of water and 100 ml of 37% HCl until complete dissolution (~ 4 hours). To this solution, 270 mL of TEOS were added dropwise. The resulting solution was stirred in a water bath for 16 hours at 36 °C, and then aged at 95 °C under static conditions for 3 days. The white precipitate was collected by filtration, dried in air for 2 days followed by calcination at 550 °C under air for 6 hours with a heating rate of 1 °C min⁻¹ to remove the template.

2.3.2 Synthesis of Aminopropyl-Modified SBA15 (SBA15-aps)

SBA15 (33.0 g) and (3-Aminopropyl)triethoxysilane (18 mL) were refluxed for 5 hours in 1 L of toluene and filtered at room temperature. The resulting white powder was dried at 100 °C for 5 hours.

Chapter III Polyoxo-noble-metalates

polyoxopalladates(II) represent a significant subclass of the polyoxo-noble-metalate family and are continually developing. No platinum analogues of polyoxopalladates(II) have been reported to date, except the first polyoxoplatinate $[\text{Pt}^{\text{III}}_{12}\text{O}_8(\text{SO}_4)_{12}]^{4-}$. The polyoxoaurates $\text{Au}^{\text{III}}_4\text{As}_4\text{O}_{20}]^{8-}$ and $[\text{Au}^{\text{III}}_4\text{Se}_4\text{O}_{20}]^{4-}$ exhibit tetrameric structure. It becomes apparent that the polyoxoplatinate and polyoxoaurate chemistry has been stagnant ever since the reports of the early members. However, by now no polyoxoanion containing both platinum(IV) and gold(III) centers has been reported. As a part of our ongoing research interests to expand the polyoxo-noble-metalates system, in this chapter, 6 novel polyoxo-noble-metalates are presented in an effort to push the area to a higher synthetic and analytical level.

3.1 Pt^{IV} -containing hexaplatinate(II) and hexapalladate(II)

In this work, the first Pt^{IV} -containing discrete polyoxoplatinate(II) $[\text{Pt}^{\text{IV}}\text{Pt}^{\text{II}}_6\text{O}_6(\text{AsO}_2(\text{CH}_3)_2)_6]^{2-}$ (**Pt7**) and polyoxopalladate(II) $[\text{Pt}^{\text{IV}}\text{Pd}^{\text{II}}_6\text{O}_6(\text{AsO}_2(\text{CH}_3)_2)_6]^{2-}$ (**PtPd6**) have been prepared and characterized in the solid-state (single-crystal XRD, FT-IR spectroscopy, elemental and thermogravimetric analyses), in solution (multinuclear (^1H , ^{13}C , ^{195}Pt) NMR), and in the gas phase (ESI-MS spectroscopy). Catalytic studies were performed on **Pt7** supported on SBA15-apts for *o*-xylene hydrogenation at 300 °C and 90 bar H_2 pressure and indicated excellent activity and recyclability with low activation temperature.

3.1.1 Synthesis

KNa[Pt^{IV}Pt^{II}₆O₆(AsO₂(CH₃)₂)₆]·NaNO₃·NaAsO₂(CH₃)₂·21H₂O (KNa-Pt₇)

H₂Pt(OH)₆ (9 mg, 0.03 mmol) was dissolved in 0.1 mL of 1 M NaOH. This solution was added to 2 mL of 2 M sodium dimethylarsinate buffer (pH 7) containing K₂PtCl₄ (75 mg, 0.18 mmol), and stirred for 1 h at 80 °C. After two weeks, red block-shaped crystals were collected by filtration and washed with 96% ethanol. Yield: 9 mg (10% with respect to H₂Pt(OH)₆ as limiting reagent). Elemental Analysis: Calculated (%) for **KNa-Pt₇**: Pt 46.00, As 17.67, K 1.32, Na 2.32, C 5.66, H 2.85, N 0.47. Found (%): Pt 46.00, As 18.40, K 1.38, Na 2.28, C 5.13, H 2.52, N 0.43. FT-IR (KBr/cm⁻¹): 3600–3300 (s) [ν(O–H) of H₂O], 3003–2922 (w) [ν(C–H) methyl groups of cacodylate], 1633 (m) [H₂O bending fundamental mode δ], 1383 (s) [δ(C–H) methyl groups of cacodylate], 1267 (m) [δ_{in-plane}(O–H)], 1056 (w) [ν_{sym}(N–O) of NO₃⁻], 898 (w) [δ_{out-of-plane}(O–H)], 794–604 (s) [ν(Pt–O)], 505 (m) [ν(As–C)].

Na₂[Pt^{IV}Pd^{II}₆O₆(AsO₂(CH₃)₂)₆]·2NaNO₃·9H₂O (Na-PtPd₆)

H₂Pt(OH)₆ (9 mg, 0.03 mmol) was dissolved in 0.1 mL of 1 M NaOH. This solution was added to 2 mL of 2 M sodium dimethylarsinate buffer (pH 7) containing Pd(NO₃)₂ (43 mg, 0.18 mmol), and stirred for 1 h at 80 °C. After ten days, red needle-shaped crystals were collected by filtration and washed with 96% ethanol. Yield: 30 mg (47% with respect to H₂Pt(OH)₆ as limiting reagent). Elemental Analysis: Calculated (%) for **Na-PtPd₆**: Pt 9.16, Pd 29.98, As 21.11, Na 4.32, C 6.77, H 2.56, N 1.32. Found (%): Pt 8.90, Pd 29.80, As 21.70, Na 4.11, C 7.13, H 2.28, N 1.01. FT-IR (KBr/cm⁻¹): 3600–3300 (s) [ν(O–H) of H₂O], 3007–2853 (w) [ν(C–H) of methyl groups of cacodylate], 1639 (m) [H₂O bending

fundamental mode δ], 1384 (s) [$\delta(\text{C-H})$ of the methyl groups of cacodylate], 1268 (m) [$\delta_{\text{in-plane}}(\text{O-H})$], 1050 (w) [$\nu_{\text{sym}}(\text{N-O})$ of NO_3^-], 904 (w) [$\delta_{\text{out-of-plane}}(\text{O-H})$], 806–581 (s) [$\nu(\text{Pt-O})$, $\nu(\text{Pd-O})$], 514–491 (m) [$\nu(\text{As-C})$].

KNa-Pt₇@SBA15-apts

The **KNa-Pt₇** (20 mg, 0.0067 mmol) was dissolved in 100 mL of deionized water followed by the slow addition of 380 mg of the SBA15-apts to the resulting orange coloured solution under stirring. The quantities of the **KNa-Pt₇** and support were taken such that the resultant composite material would have a ~5 wt% Pt-loading. After refluxing for 2 h, the mixture was filtered under vacuum and the residue was washed three times with deionized water and air-dried. The filtrate was found to be colourless, which indicated quantitative loading. The dried **KNa-Pt₇@SBA15-apts** composite material was then calcined at 250 °C for 4 h (heating rate = 0.5 °C/min) in order to obtain the calcined pre-catalyst that was eventually reduced in situ under H_2 inside the Parr compact reactor to generate the catalyst for the hydrogenation of arenes.

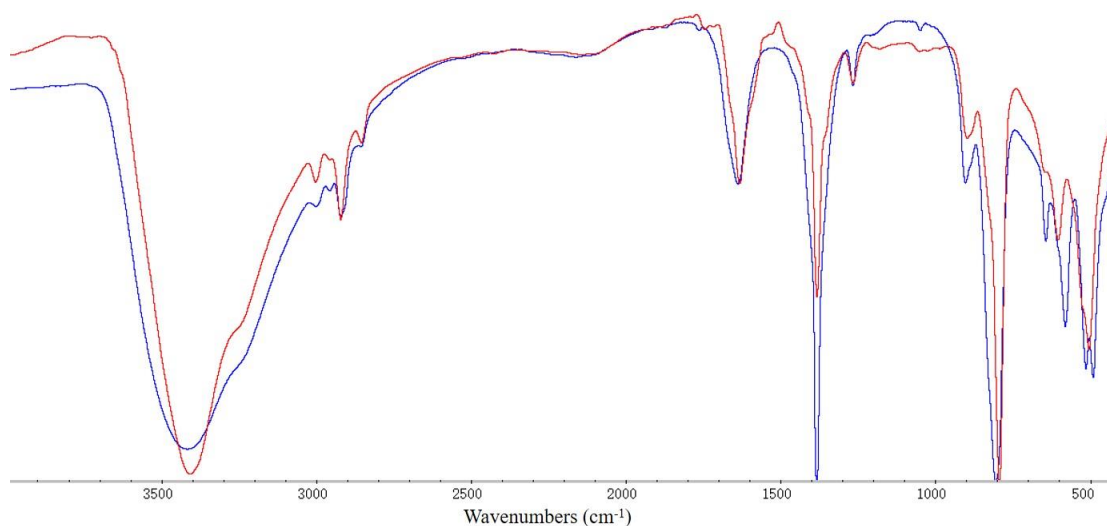


Figure 3.1. FT-IR spectrum of **KNa-Pt₇** (red) and **Na-PtPd₆** (blue).

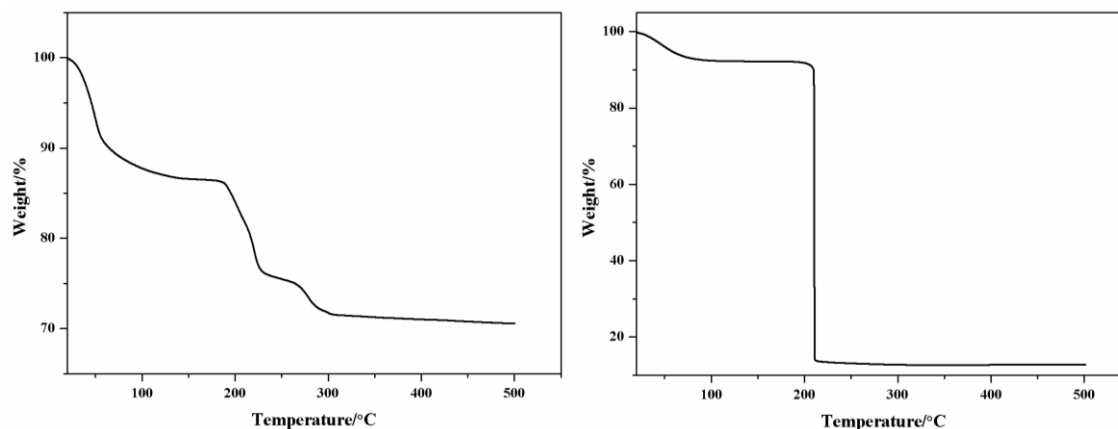


Figure 3.2. Thermograms of **KNa-Pt₇** (left) and **Na-PtPd₆** (right) from room temperature to 500 °C under N₂ atmosphere.

3.1.2 Single-Crystal XRD Data

Table 3.1. Crystal data and structure refinement for **KNa-Pt₇** and **Na-PtPd₆**.

Compound	KNa-Pt₇	Na-PtPd₆
empirical formula ^a	KNa ₃ Pt ₇ As ₇ C ₁₄ H ₈₄ O ₄₄ N	Na ₄ PtPd ₆ As ₆ C ₁₂ H ₅₄ O ₃₃ N ₂
fw, ^a g mol ⁻¹	2968.86	2129.64
crystal system	Orthorhombic	Triclinic
space group	Pcca	P1
<i>a</i> (Å)	26.8981(9)	6.71005(9)
<i>b</i> (Å)	13.4671(4)	15.14730(18)
<i>c</i> (Å)	19.6627(7)	15.2445(2)
α (°)	90	62.3352(13)
β (°)	90	86.3984(12)
γ (°)	90	88.6937(11)
<i>V</i> (Å ³)	7122.6(4)	1369.56(3)
<i>Z</i>	4	1
<i>D_c</i> (g cm ⁻³)	2.499	2.532
abs coeff, mm ⁻¹	16.603	8.171
F(000)	4768	971

θ range for data collection, deg	2.206 to 26.477	2.680 to 25.027
completeness to Θ_{\max}	99.8 %	99.9%
index ranges	-33 \leq h \leq 33, -16 \leq k \leq 16, -22 \leq l \leq 24	-7 \leq h \leq 7, -18 \leq k \leq 18, -18 \leq l \leq 18
reflns collected	56395	91736
indep reflns	7294	9526
$R(\text{int})$	0.1190	0.0851
abs corn	Semi-empirical from equivalents	Semi-empirical from equivalents
data/restraints/param	7294/18/302	9526 / 3 / 575
GOF on F^2	1.020	1.046
$R_1, {}^b wR_2^c$ [$I > 2\sigma(I)$]	0.0465, 0.1188	0.0339, 0.0922
$R_1, {}^b wR_2^c$ (all data)	0.0860, 0.1356	0.0353, 0.0934
Absolute structure parameter	/	0.479(6)
Largest diff peak and hole, e \AA^{-3}	1.533 and -2.517	3.133 and -2.588

^aThe entries are the actual formula units and weights as obtained from bulk elemental analysis.
^b $R_1 = \frac{\sum ||F_o| - |F_c||}{\sum |F_o|}$. ^c $wR_2 = \frac{[\sum w(F_o^2 - F_c^2)^2 / \sum w(F_o^2)^2]}{1/2}$.

3.1.3 Bond Valence Sum Calculations

In **KNa-Pt₇** and **Na-PtPd₆**, the BVS values for the central Pt atoms are 3.992 and 3.867, respectively. In **KNa-Pt₇**, the BVS values for the six surrounding Pt atoms range from 1.990 to 1.943. In **Na-PtPd₆**, the BVS values for the six surrounding Pd atoms range from 2.030 to 2.183. The BVS values for different types of μ_3 -bridging oxygens are presented in Tables 3.2. These values show that these oxygens are not protonated and therefore the central Pt ion is in the 4+ oxidation state and the surrounding Pt and Pd ions are in the 2+ oxidation state, respectively.

Table 3.2. BVS values for μ_3 -bridging oxygen atoms in **KNa-Pt₇** and **Na-PtPd₆**.

μ_3 -O	Bond distance(Å)	BVS value	μ_3 -O	Bond distance(Å)	BVS value
KNa-Pt₇					
O1	Pt1-O1 (2.0336)	1.682	O3	Pt3-O4 (2.0307)	1.680
	Pt2-O1 (2.0253)			Pt4-O4 (2.0151)	
	Pt3-O1 (2.0064)			Pt1-O4 (2.0243)	
O2	Pt2-O2 (1.9984)	1.697			
	Pt4-O2 (2.0262)				
	Pt1-O2 (2.0314)				
Na-PtPd₆					
O1	Pd1-O1 (2.0736)	1.699	O4	Pd3-O4 (1.9815)	1.826
	Pd6-O1 (1.9911)			Pd4-O4 (1.9708)	
	Pt1-O1 (2.0393)			Pt1-O4 (2.0618)	
O2	Pd1-O2 (1.9885)	1.866	O5	Pd4-O5 (1.9864)	1.850
	Pd2-O2 (1.9928)			Pd5-O5 (1.9820)	
	Pt1-O2 (2.0124)			Pt1-O5 (2.0326)	
O3	Pd2-O3 (2.0078)	1.773	O6	Pd5-O6 (1.9953)	1.721
	Pd3-O3 (1.9921)			Pd6-O6 (2.0301)	
	Pt1-O3 (2.0486)			Pt1-O6 (2.0570)	

3.1.4 Results and Discussion

3.1.4.1 Solid-State Structure

Single-crystal XRD studies revealed that **Pt₇** crystallizes as a mixed potassium-sodium salt, $\text{KNa}[\text{Pt}^{\text{IV}}\text{Pt}^{\text{II}}\text{O}_6(\text{AsO}_2(\text{CH}_3)_2)_6] \cdot \text{NaNO}_3 \cdot \text{NaAsO}_2(\text{CH}_3)_2 \cdot 21\text{H}_2\text{O}$ (**KNa-Pt₇**), in the orthorhombic space group Pcca and **PtPd₆** crystallizes as a sodium salt, $\text{Na}_2[\text{Pt}^{\text{IV}}\text{Pd}^{\text{II}}\text{O}_6(\text{AsO}_2(\text{CH}_3)_2)_6] \cdot 2\text{NaNO}_3 \cdot 9\text{H}_2\text{O}$ (**Na-PtPd₆**), in the triclinic space group P1, respectively. The symmetry unit of solid-state interaction of polyanions are showed in

Figure 3.3. Both novel polyanions **Pt₇** and **PtPd₆** are isostructural, displaying a central distorted Pt^{IV}O₆ octahedron surrounded by a ring of six square-planar MO₄ (M = Pt^{II}, Pd^{II}) units with six terminal dimethylarsinate (also known as cacodylate, cac) ligands, resulting in a disk-shaped structure with idealized D_{3d} symmetry (Figure 3.4). All seven metal centers in both polyanions are coplanar forming a regular Pt^{IV}-centered M₆ hexagon (M = Pt^{II}, Pd^{II}) with metal-metal distances Pt^{II}...Pt^{II} 3.065-3.129 Å and Pt^{IV}...Pt^{II} 3.083-3.094 Å in **Pt₇** and Pd^{II}...Pd^{II} 3.016-3.103 Å; Pt^{IV}...Pd^{II}: 3.047-3.076 Å in **PtPd₆**, respectively. The octahedral coordination environment of the central Pt^{IV} ions is formed exclusively by μ₃-oxo groups and the Pt^{IV}-O bond distances are in the range of 2.023–2.033 Å in **Pt₇**, and in the range of 2.012–2.063 Å in **PtPd₆**. The square-planar coordination environments of the Pt^{II} and Pd^{II} ions in **Pt₇** and **PtPd₆**, respectively, are formed by two μ₃-oxo groups and two cacodylate oxygens (Pt^{II}-O: 1.998–2.071 Å; Pd^{II}-O: 1.972–2.095 Å). The average Pt^{IV}-O bond length in **Pt₇** of 2.029 Å and in **PtPd₆** of 2.042 Å is comparable with that of 2.01 Å observed in [H₃PtW₆O₂₄]⁵⁻.³⁵ Bond valence sum (BVS) calculations suggest no protonation for any of the oxygen atoms in **Pt₇** and **PtPd₆** (Tables 3.2).

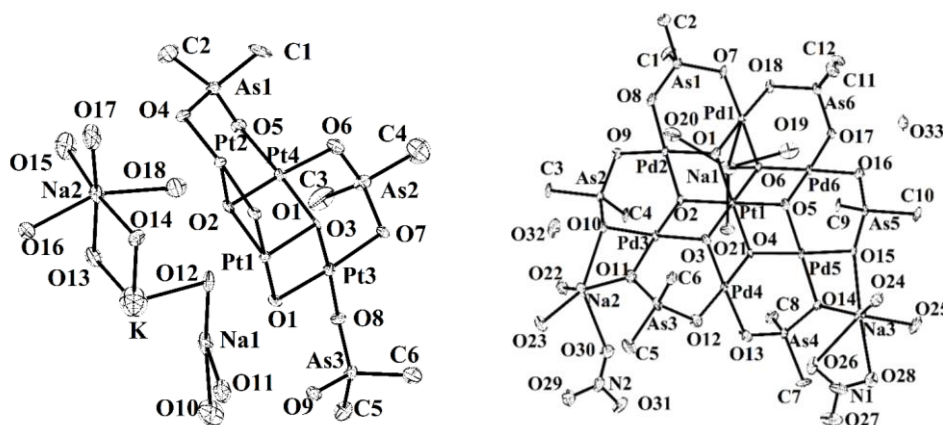


Figure 3.3. The symmetry unit of solid-state interaction of polyanions with Na⁺ and K⁺ counter cations in **Pt₇** (left) and Na⁺ counter cations in **PtPd₆** (right), respectively (50% probability ellipsoids).

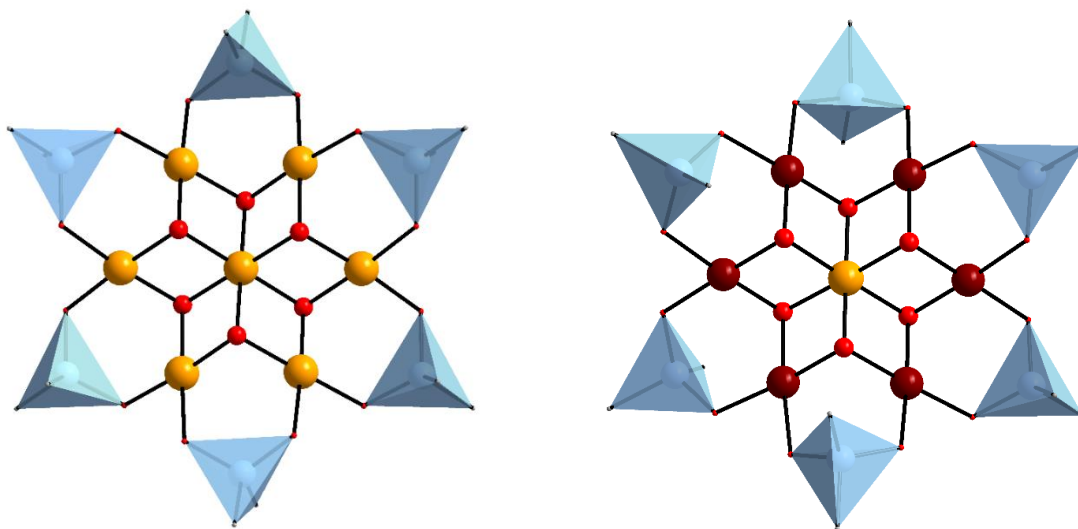


Figure 3.4. Structural representation of **Pt₇** (left) and **PtPd₆** (right). Color code: Pt (orange), Pd (dark red), O (red), C (gray), {(CH₃)₂AsO₂} (blue tetrahedra), hydrogens omitted for clarity.

3.1.4.2 Multinuclear NMR Study

To complement our solid-state XRD results on **Pt₇** and **PtPd₆** with solution studies, we performed ¹H, ¹³C and ¹⁹⁵Pt NMR measurements on **KNa-Pt₇** and **Na-PtPd₆** redissolved in H₂O/D₂O. The ¹H (D₂O) NMR spectrum of sodium cacodylate (Na-cac) exhibits sharp peaks at 4.70 and 1.41 ppm, respectively, corresponding to the protons of the crystal water molecules and cacodylate methyl groups, respectively (Figure 3.5a). The ¹H (D₂O) NMR spectra of **Pt₇** and **PtPd₆** exhibit the expected two peaks at 2.36 and 1.60 ppm for **Pt₇** and 2.38 and 1.60 ppm for **PtPd₆**, respectively, corresponding to the two structurally and hence magnetically inequivalent cacodylate methyl groups (Figure 3.5a). The small peak at 1.64 ppm for **Pt₇** corresponds to the methyl groups of co-crystallized cacodylate (Figure 3.6). On the other hand, the small peak at 1.62 ppm for **PtPd₆** can be assigned to free cacodylate, which is formed *in situ* by partial decomposition of **PtPd₆**. This observation is further supported by the time-dependent ¹H spectrum of **PtPd₆** (Figure 3.7). The ¹H NMR

spectrum of **Pt₇** remained unchanged even for two months, which indicates the high solution stability of this polyanion (Figure 3.8).

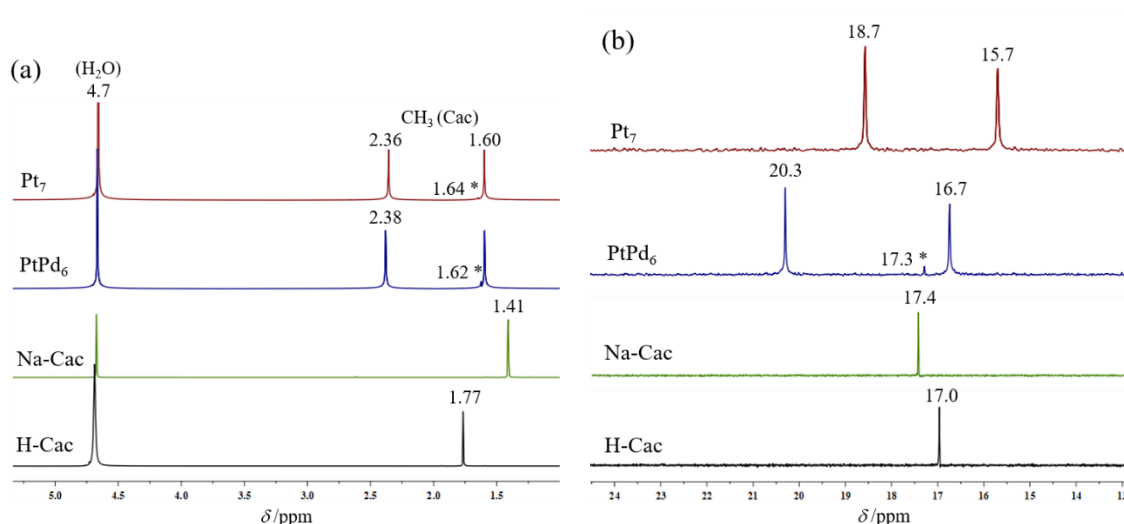


Figure 3.5. ¹H (a) and ¹³C (b) NMR spectra (D₂O) of **Pt₇** and **PtPd₆** compared to spectra of the references cacodylic acid (H-cac) and sodium cacodylate (Na-cac). The * represents free cacodylate ions.

The ¹³C (D₂O) NMR spectrum of Na-cac exhibits a narrow peak at 17.4 ppm, whereas the ¹³C (D₂O) NMR spectrum of **Pt₇** exhibits peaks at 18.7 and 15.7 ppm, corresponding to the two crystallographically inequivalent cacodylate methyl groups (Figure 3.5b). For **PtPd₆**, the expected two signals were observed with chemical shift values of 20.3 and 16.7 ppm, respectively. In analogy to the ¹H NMR spectrum, there is also a small peak at 17.3 ppm for this compound. The ¹⁹⁵Pt spectrum of **Pt₇** shows a broad signal at 727 ppm (Figure 3.9), which is assigned to Pt^{II}. On the other hand, we could not observe any signal for the Pt^{IV} centers for the low concentration. However, the ¹⁹⁵Pt NMR spectrum of **PtPd₆** revealed the expected singlet at 4080 ppm, which is unequivocally due to the central Pt^{IV} ion (Figure 3.9). The chemical shift of ¹⁹⁵Pt NMR of polyanions **Pt₇** and **PtPd₆** were confirmed by DFT calculations (*vide infra*). In any case, the combination of ¹H and ¹³C NMR spectra is fully

consistent with the solid-state structures of **Pt₇** and **PtPd₆**, providing clear evidence for the presence of the polyanion in solution.

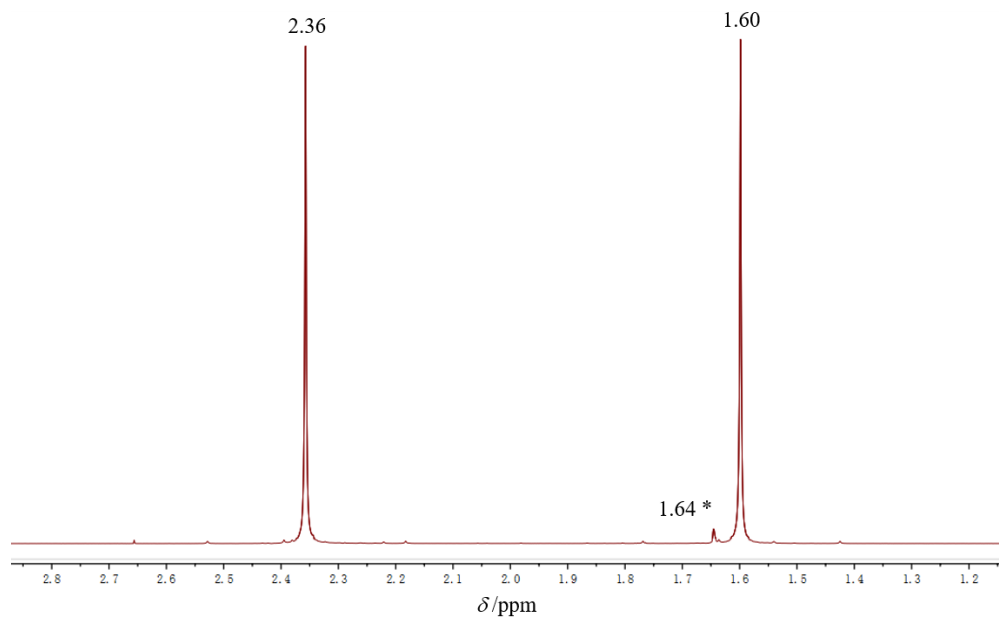


Figure 3.6. Enlarged ^1H spectrum (D_2O) of **KNa-Pt₇**.

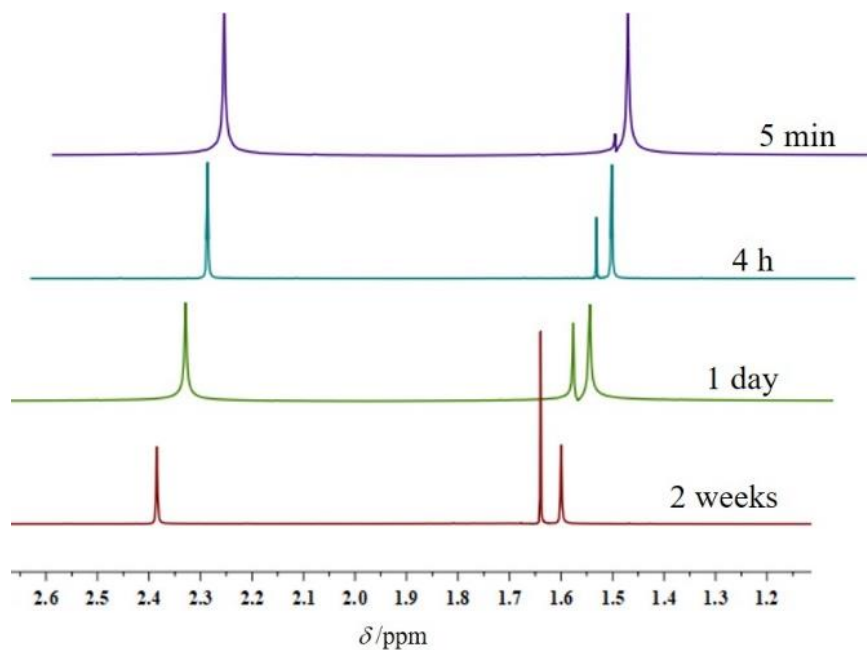


Figure 3.7. Time dependent ^1H spectra (D_2O) of **Na-PtPd₆**.

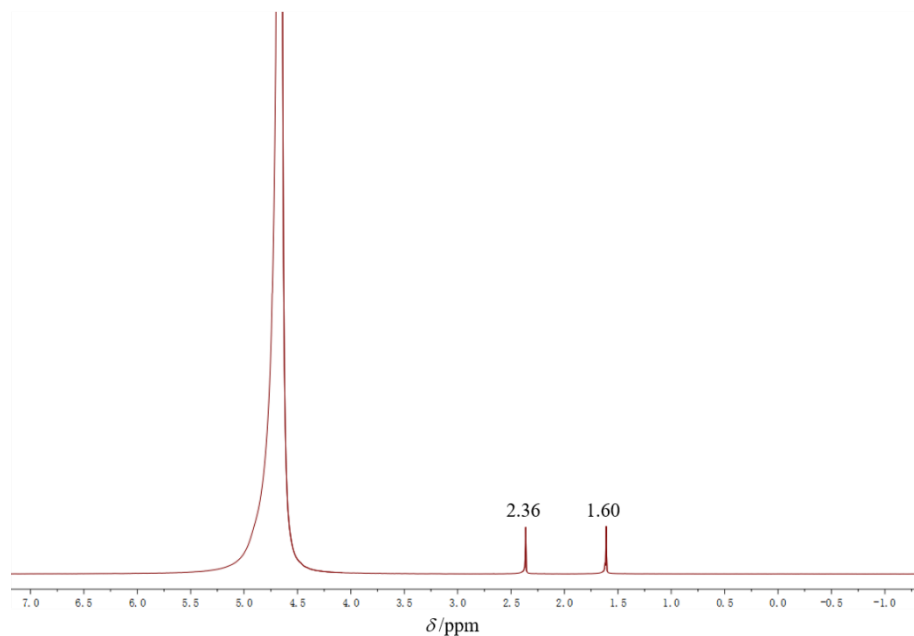


Figure 3.8. ^1H spectrum (D_2O) of KNa-Pt_7 after 2 months.

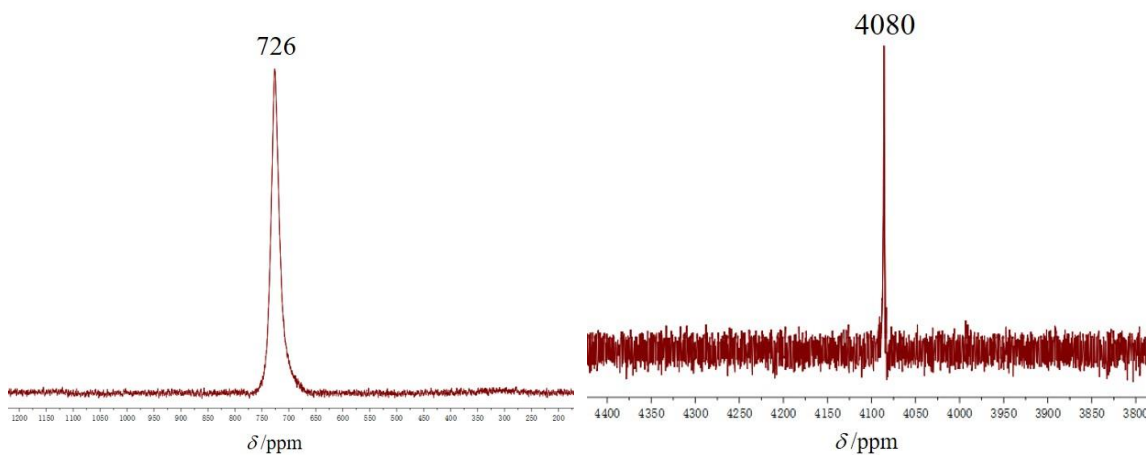


Figure 3.9. ^{195}Pt NMR spectra of KNa-Pt_7 (left) and Na-PtPd_6 (right).

3.1.4.3 ESI-MS Analysis

ESI-mass spectra of KNa-Pt_7 and Na-PtPd_6 were acquired from aqueous solutions in the negative ion mode. For Pt_7 , two groups of signals centered around m/z 1141 and 2284 were observed (Figure 3.10). As a starting point for spectra assignment, we assumed the presence of the core structure $[\text{Pt}^{\text{IV}}\text{Pt}^{\text{II}}_6\text{O}_6(\text{AsO}_2(\text{CH}_3)_2)_6]^{2-}$ (Pt_7) as established by XRD, and the

observed isotope pattern is in full agreement with this structure. The signal centered around m/z 1141 can be assigned to a doubly-charged species based on the spacing of the isotope peaks (Figure 3.11). The simulated mass spectrum is in good agreement with the experimentally observed spectrum. The signal centered at around m/z 2284 can be assigned to a singly-charged ion accompanied by a proton, suggesting that the charge of the oxo-cluster is reduced from 2- to 1- (Figure 3.11). For the structural analogue **PtPd₆**, one signal was observed in the negative ion mode centered at m/z 875 with isotope patterns expected for the structure (Figure 3.12). Following spectral simulations, we assigned these signals to the doubly-charged species $[\text{Pt}^{\text{IV}}\text{Pd}^{\text{II}}_6\text{O}_6(\text{AsO}_2(\text{CH}_3)_2)_6]^{2-}$ (**PtPd₆**) (Figure 3.12).

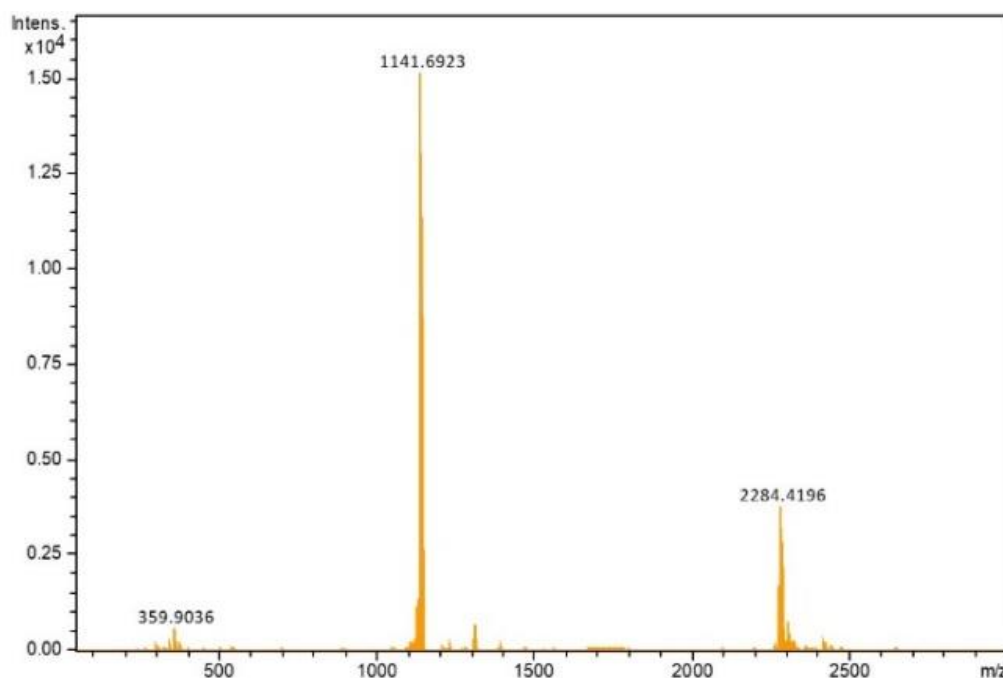


Figure 3.10. ESI-MS spectrum (full scan) of an aqueous solution of **KNa-Pt₇** in the negative-ion mode.

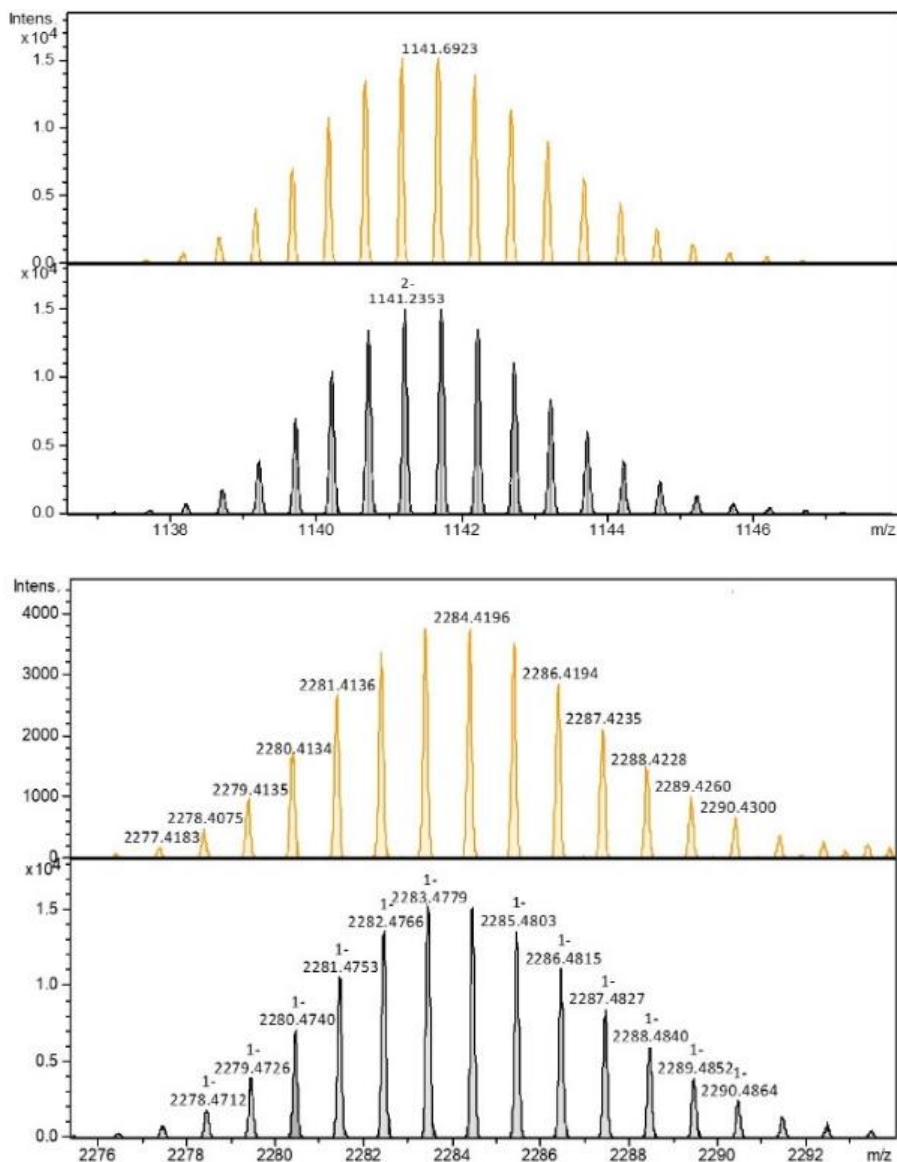


Figure 3.11. Left: Simulated (bottom panel) and experimental ESI-MS spectrum (top panel) of a doubly charged $[Pt_7O_6((CH_3)_2AsO_2)_6]^{2-}$ ion (expanded view); right: Simulated (bottom panel) and experimental ESI-MS spectrum (top panel) of a singly charged $[HPT_7O_6((CH_3)_2AsO_2)_6]^-$ ion (expanded view).

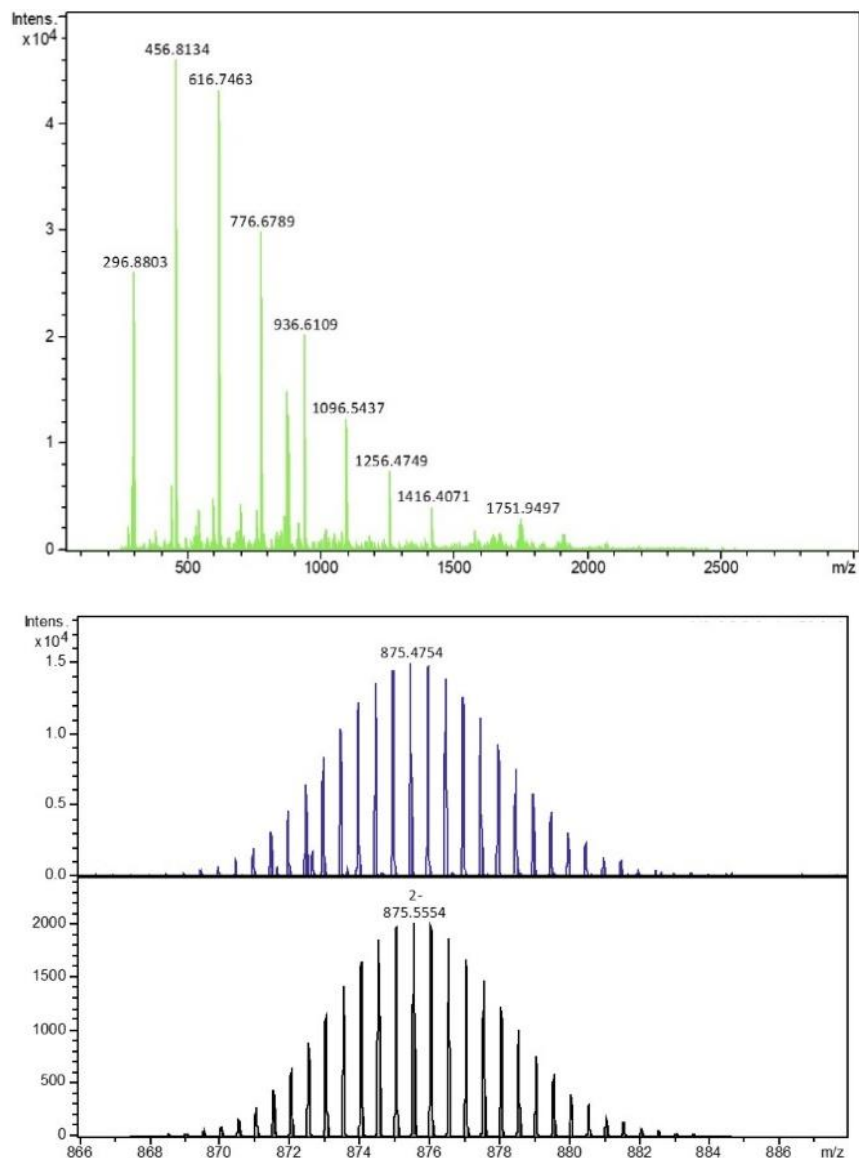


Figure 3.12. Left: ESI-MS spectrum (full scan) of an aqueous solution of **Na-PtPd₆** in the negative-ion mode; Right: Simulated (bottom panel) and experimental ESI-MS spectrum (top panel) of a doubly charged $[\text{PtPd}_6\text{O}_6((\text{CH}_3)_2\text{AsO}_2)_6]^{2-}$ ion (expanded view).

3.1.4.4 XPS Spectroscopy

X-ray photoelectron spectroscopy (XPS) measurements were performed on both **KNa-Pt₇** and **Na-PtPd₆** in order to ascertain the oxidation states of Pt and Pd. Both **Pt₇** and **PtPd₆** exhibited a Pt $4f_{7/2}$ band at ~ 74.9 eV, which is typical for Pt in the 4+ oxidation state. The XPS spectrum of **Pt₇** exhibited characteristic $4f_{7/2}$ peaks at ~ 72.5 eV and ~ 74.9 eV with a

ratio of 6 :1, indicating that Pt is present in the 2+ and 4+ oxidation states, respectively (Figure 3.13). The XPS spectrum of **PtPd₆** exhibited the characteristic Pd 3d_{5/2} band at 337.2 eV, which is typical for Pd in the 2+ oxidation state (Figure 3.14). These observations were also corroborated by bond valence sum (BVS) calculations on Pt and Pd in **Pt₇** and **PtPd₆**, which indicated that the central Pt ion is in the 4+ oxidation state and the surrounding Pt and Pd ions are in the 2+ oxidation state.

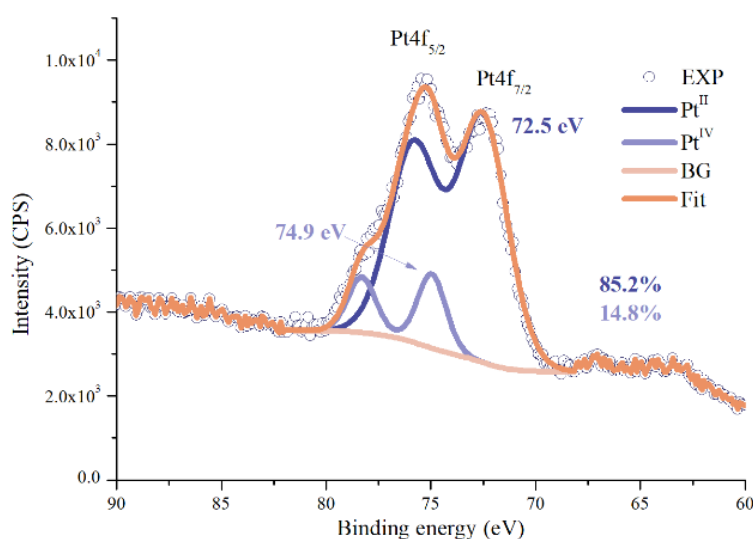


Figure 3.13. X-ray photoelectron spectra and fits for Pt 4f_{7/2} and 4f_{5/2} doublet of **KNa-Pt₇**.

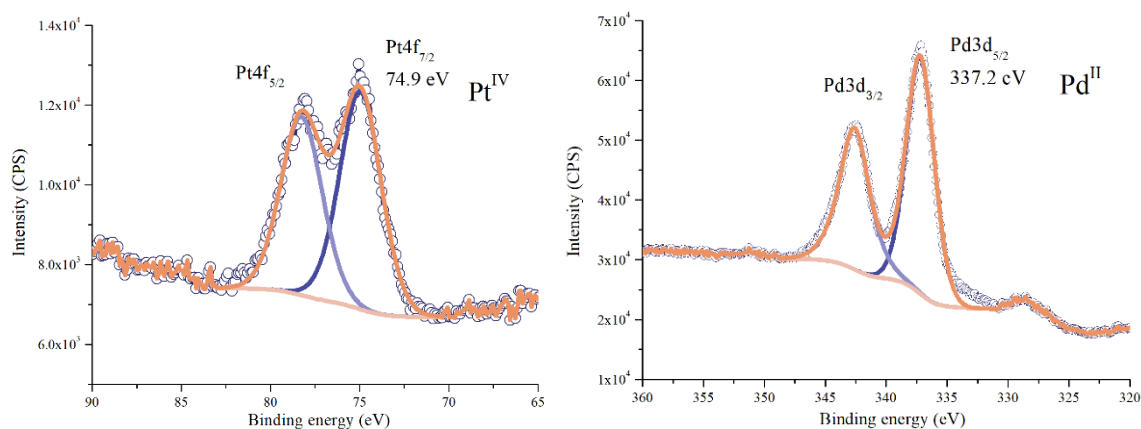


Figure 3.14. X-ray photoelectron spectra and fits for Pt 4f_{7/2} and 4f_{5/2} doublet of **Na-PtPd₆** (top), and Pd 3d_{5/2} and 3d_{3/2} doublet of **Na-PtPd₆** (bottom).

3.1.4.5 Computational Study

The structures of the anions **Pt₇** and **PtPd₆** have been computationally optimized using Density Functional Theory (DFT) methods (B3LYP⁸⁷ and OPBE⁸⁸) together with the basis sets 6-31g(d,p)⁸⁹ for light atoms (H, O and C) and LANL2DZ⁹⁰ with corresponding Effective Core Potentials for the heavier elements (Pt, Pd and As), the aqueous environment has been simulated through a continuum model, namely PCM,⁹¹ as implemented in Gaussian.⁹² The geometries obtained for **Pt₇** were compared with the available crystal structures, a root-mean-square deviation (RMSD) of 0.24 and 0.22 Å (without hydrogens) was found respectively using B3LYP and OPBE functionals, indicating that both functionals provide geometries similar to the crystal structures (note calculations are in aqueous solution). To simulate the ¹⁹⁵Pt NMR spectra of these two anions, ADF⁹³ calculations with different functionals together with the TZ2P⁹⁴ basis set, relativistic spin-orbit ZORA,⁹⁵ simulation of the water environment with COSMO⁹⁶ and Gaussian nuclear distribution model⁹⁷ were run on the previously optimized structures, and the selected results are presented in Table 3.3. Computationally derived NMR chemical shifts (δ_{cal}) are strongly dependent on the methodology used.^{98, 22a, 55} For **Pt₇** and **PtPd₆** the best results compared to experiment were achieved using SSB-D⁹⁹ and OPBE methods on B3LYP geometries, similarly to previously reported results⁵⁵ on similar systems. Predicted NMR shifts show errors from few ppm to few hundreds of ppm. However, the difference on the NMR chemical shifts of Pt^{IV} in **PtPd₆** and the average of the six Pt^{II} in **Pt₇** shows only a small error. This difference of the two signals is 3408 ppm with SSB-D and 3548 ppm with OPBE, which are both close to the experimentally measured difference of 3354 ppm. This suggests that the predicted signal for Pt^{IV} in **Pt₇** should appear in the range above 4080 and

below 4500 ppm, whereas the Pt^{II} signals in this type of complex should appear around 700 ppm. It can be concluded that the assignments of the experimental ¹⁹⁵Pt NMR chemical shifts described in this work are correct.

Table 3.3. Computationally predicted NMR chemical shifts (δ_{calc}) in ppm for **Pt₇** and **PtPd₆** using different methods.^a

Compound	PtPd₆	Pt₇		
Metal center	Pt ^{IV}	Pt ^{II}	Pt ^{IV}	Pt^{IV} - Pt^{II}^b
SSB-D/B3LYP ^c	3854	446	4057	3408
SSB-D/OPBE ^c	4415	802	4696	3613
OPBE/B3LYP ^c	4307	759	4538	3548
BP86/B3LYP ^c	4503	895	4628	3763
<i>Experimental</i>	<i>4080</i>	<i>726</i>	<i>---</i>	<i>3354</i>

^a All chemical shifts δ_{calc} (in ppm) correspond to differences between the predicted ¹⁹⁵Pt NMR shielding for indicated species and NMR shielding of ¹⁹⁵Pt NMR reference PtCl₆²⁻ both at the same level of theory.

^b Difference between the averaged signal of the unique Pt^{IV} in the **PtPd₆** anion and the signal of the six Pt^{II} nuclei in the **Pt₇** anion.

^c Notation Method1/Method2 corresponds to: Method 1 is the method used for NMR calculations in ADF, Method 2 is the method used for geometry optimization in Gaussian.

Table 3.4. Cartesian Coordinates of computationally optimized structures for **Pt₇** and **PtPd₆** anions (Ångström, Å)

B3LYP optimized structures							
Pt₇ (E= -2704.39024651 hartree)			PtPd₆ (E= -2749.86031087 hartree)				
C	11.51219	6.239557	18.44955	C	11.39559	6.498758	18.34859
As	10.50165	5.096236	17.26097	As	10.45199	5.235408	17.22419
C	10.91647	3.241424	17.66648	C	10.96543	3.438359	17.7616
O	8.176254	5.478381	14.59704	Pd	9.873097	4.526939	14.14562
O	8.852169	5.422103	17.57968	O	8.152834	5.508683	14.57717
Pt	6.914744	4.663864	13.12553	Pd	7.500233	4.47664	16.19603
O	5.089541	5.628471	13.52218	O	8.790046	5.473892	17.51617
O	2.182657	5.88283	12.62032	Pt	6.914316	4.663366	13.12523
As	1.597772	5.544079	14.19216	O	5.124642	5.661876	13.52186
C	0.18277	6.821166	14.52109	Pd	3.955518	4.799657	12.10487
O	4.007069	3.545437	16.92919	O	2.259894	5.920341	12.62311
As	5.109231	3.721234	18.22578	As	1.673971	5.680136	14.20487
C	4.570963	2.426579	19.55789	C	0.360642	7.068432	14.5199

Chapter III Polyoxo-noble-metalates

O	7.092346	5.969835	8.407972	Pd	4.546458	4.64399	15.17685
As	8.720354	5.606762	8.025285	O	4.035215	3.475189	16.84168
C	9.258767	6.901622	6.69345	As	5.122597	3.572353	18.15025
O	11.0918	3.563482	10.8006	C	4.611103	2.18297	19.39877
As	12.23139	3.78237	12.05904	Pd	6.328489	4.850115	10.0545
C	13.6459	2.504751	11.73011	O	7.069297	6.028457	8.487547
O	5.653247	3.849397	11.65387	As	8.706296	5.755584	8.100259
O	7.567455	5.650409	11.38869	C	9.217179	7.146487	6.853178
O	8.739777	3.69909	12.72889	Pd	9.282223	4.682889	11.07361
O	2.737441	5.763643	15.45039	O	10.99651	3.510461	10.80274
O	6.26214	3.677434	14.86258	As	12.15469	3.646564	12.04574
O	2.807023	3.840724	10.57302	C	13.46801	2.258277	11.73059
As	3.327892	4.23187	8.990302	O	5.675785	3.818082	11.67328
C	2.912962	6.086949	8.586048	O	7.558418	5.694587	11.42924
O	4.977381	3.906242	8.671427	O	8.70397	3.664952	12.72855
O	9.822914	5.781609	9.32173	O	2.832361	5.816689	15.44762
O	11.64623	3.44368	13.63078	O	6.270259	3.632169	14.82127
O	11.02251	5.486292	15.67804	O	2.861444	3.797617	10.62434
O	6.737465	3.358743	17.84365	As	3.37676	4.091196	9.026359
C	0.857935	3.748354	14.26124	C	2.862789	5.888262	8.489435
C	8.851441	3.824467	7.262627	O	5.038676	3.853014	8.73421
C	4.977342	5.503759	18.98777	O	9.793478	5.852009	9.409041
C	12.97198	5.577788	11.99033	O	11.56851	3.405951	13.62736
C	2.317425	3.089276	7.800959	O	10.9674	5.528601	15.62618
H	11.2369	6.022412	19.48314	O	6.759352	3.2981	17.7629
H	12.57877	6.058012	18.30561	C	0.781473	3.956177	14.32458
H	11.28078	7.280277	18.21729	C	8.896938	4.037435	7.208476
H	0.43681	3.574013	15.25338	C	4.933184	5.29146	19.04043
H	0.077853	3.653919	13.50313	C	13.04733	5.370492	11.92656
H	1.661099	3.036951	14.06437	C	2.433304	2.827959	7.901691
H	-0.24495	6.642815	15.50926	H	11.12643	6.327214	19.39234
H	0.600778	7.828078	14.47644	H	12.47132	6.367917	18.21826
H	-0.59001	6.708497	13.75848	H	11.10979	7.510557	18.05628
H	5.640752	5.571441	19.8524	H	0.355056	3.841589	15.32319
H	5.276204	6.227479	18.22822	H	-0.01078	3.908382	13.57479
H	3.945376	5.685281	19.29461	H	1.513219	3.167667	14.14135
H	5.232548	2.497683	20.42291	H	-0.0688	6.943576	15.51548
H	3.542254	2.627233	19.86237	H	0.853663	8.039537	14.45064
H	4.638473	1.427856	19.12362	H	-0.42668	7.000936	13.76688
H	10.342	2.603759	16.99327	H	5.58771	5.31744	19.91396
H	10.64679	3.033318	18.70398	H	5.214903	6.081959	18.34298
H	11.98563	3.07608	17.5189	H	3.894635	5.423396	19.35055
H	1.25081	3.270234	7.945426	H	5.261989	2.224677	20.27389
H	2.592279	3.30758	6.767488	H	3.57343	2.33192	19.70275
H	2.549346	2.048423	8.032094	H	4.715542	1.213875	18.90805
H	8.187795	3.757364	6.398125	H	10.4371	2.718859	17.13399

H	8.552582	3.100489	8.021924	H	10.69578	3.28537	18.80845
H	9.883279	3.64278	6.955446	H	12.0433	3.319463	17.63461
H	13.75202	5.671771	12.74854	H	1.357549	2.958707	8.031925
H	13.39329	5.752099	10.99826	H	2.702564	2.999716	6.858003
H	12.1691	6.289513	12.18721	H	2.71914	1.816121	8.193829
H	3.486987	6.724105	9.260119	H	8.24267	4.011797	6.334737
H	3.183129	6.295982	7.548865	H	8.615535	3.246136	7.905156
H	1.8437	6.251978	8.73324	H	9.935657	3.906417	6.898523
H	14.07389	2.683109	10.74206	H	13.83933	5.418119	12.67663
H	14.41857	2.616955	12.49289	H	13.4741	5.485201	10.92811
H	13.22747	1.498004	11.77449	H	12.31558	6.159032	12.10967
H	10.28738	6.700793	6.388766	H	3.390896	6.607774	9.117218
H	8.597003	6.830891	5.828543	H	3.132237	6.041672	7.442603
H	9.1916	7.900272	7.127956	H	1.784893	6.006711	8.616612
Pt	9.326223	4.676608	11.04055	H	13.89759	2.383351	10.7351
Pt	9.925286	4.527493	14.16508	H	14.25523	2.325594	12.48373
Pt	7.513271	4.48679	16.25082	H	12.97496	1.287162	11.79956
Pt	4.50324	4.650833	15.21052	H	10.25495	6.998315	6.549141
Pt	3.904085	4.799758	12.08601	H	8.566385	7.105302	5.977962
Pt	6.316257	4.84148	10.00037	H	9.112243	8.115054	7.34483

OPBE optimized structures

Pt₇ (E= -2705.17432490 hartree)

C	11.47118	6.121321	18.42001
As	10.42179	5.043911	17.18433
C	10.79332	3.162327	17.56194
O	8.159759	5.492543	14.58296
O	8.77158	5.449789	17.53036
Pt	6.914664	4.663749	13.12555
O	5.115941	5.646567	13.52137
O	2.261141	5.908973	12.59224
As	1.705035	5.496465	14.18138
C	0.224131	6.712078	14.52491
O	4.013904	3.521851	16.84438
As	5.146666	3.770679	18.13293
C	4.592372	2.537361	19.533
O	7.042362	5.992429	8.474761
As	8.682854	5.556934	8.118349
C	9.237036	6.790147	6.718138
O	10.99777	3.53721	10.78393
As	12.1244	3.831255	12.0699
C	13.60539	2.61576	11.72633
O	5.669511	3.834983	11.66813
O	7.56194	5.674447	11.41721
O	8.713415	3.680988	12.72978
O	2.83166	5.790437	15.46738
O	6.267403	3.653089	14.83389

PtPd₆ (E= -2750.69303880 hartree)

C	11.4185	6.365309	18.32927
As	10.40688	5.184731	17.15538
C	10.8495	3.345255	17.65431
Pd	9.83157	4.503789	14.12603
O	8.148858	5.519401	14.55793
Pd	7.496901	4.483092	16.15243
O	8.744183	5.52071	17.47217
Pt	6.914275	4.664213	13.12559
O	5.154073	5.688683	13.52662
Pd	3.997078	4.824284	12.12495
O	2.328995	5.997216	12.60185
As	1.756223	5.653898	14.19288
C	0.349696	6.956994	14.53884
Pd	4.584516	4.647498	15.15179
O	4.041913	3.443528	16.77509
As	5.153666	3.618279	18.08314
C	4.619807	2.290848	19.40529
Pd	6.331962	4.844293	10.09885
O	7.02074	6.04374	8.529012
As	8.674681	5.710244	8.167727
C	9.207786	7.039237	6.846866
Pd	9.243756	4.680834	11.09925
O	10.92541	3.478238	10.7825
As	12.07189	3.674072	12.05753

O	2.842653	3.830109	10.64305	C	13.47839	2.370972	11.71139
As	3.407529	4.283605	9.066867	O	5.679871	3.808681	11.69341
C	3.035853	6.165159	8.689259	O	7.549365	5.711353	11.44912
O	5.05772	3.877664	8.720822	O	8.674349	3.639669	12.72445
O	9.815607	5.805928	9.406911	O	2.902491	5.849776	15.4681
O	11.56827	3.418693	13.65902	O	6.279099	3.617209	14.8021
O	10.98665	5.49744	15.60816	O	2.870661	3.797965	10.69423
O	6.787124	3.335164	17.7765	As	3.422825	4.140448	9.095399
C	1.010892	3.670216	14.24077	C	2.980192	5.978999	8.593154
C	8.804944	3.741572	7.40414	O	5.08578	3.804359	8.779961
C	5.024716	5.586035	18.84717	O	9.786365	5.884394	9.475859
C	12.81849	5.657523	12.01047	O	11.49945	3.330679	13.64867
C	2.358128	3.20617	7.831208	O	10.95806	5.530063	15.55676
H	11.18415	5.874784	19.44717	O	6.807349	3.283664	17.72204
H	12.53448	5.909575	18.26924	C	0.936113	3.878387	14.26083
H	11.27037	7.178403	18.22088	C	8.858553	3.950289	7.332234
H	0.590678	3.490816	15.23597	C	4.970382	5.37884	18.91755
H	0.232391	3.569975	13.47715	C	12.89219	5.449493	11.98926
H	1.832952	2.977642	14.04225	C	2.412158	2.957558	7.923032
H	-0.19456	6.500003	15.51385	H	11.13359	6.171465	19.36829
H	0.599063	7.739578	14.49192	H	12.48841	6.177	18.19457
H	-0.5434	6.570866	13.75736	H	11.18744	7.402444	18.06753
H	5.692717	5.665252	19.71129	H	0.509316	3.726296	15.25766
H	5.324638	6.290207	18.06676	H	0.148526	3.827369	13.50172
H	3.988881	5.769354	19.15151	H	1.702975	3.125232	14.06012
H	5.256276	2.648849	20.39617	H	-0.07958	6.771179	15.52856
H	3.561569	2.762426	19.82447	H	0.785098	7.960399	14.50454
H	4.654977	1.516135	19.14496	H	-0.42587	6.861626	13.7721
H	10.21796	2.546016	16.86623	H	5.623488	5.420118	19.79555
H	10.49944	2.950687	18.59546	H	5.260683	6.146915	18.19547
H	11.86655	2.988426	17.43022	H	3.926507	5.517984	19.21757
H	1.294803	3.417402	7.98247	H	5.276879	2.363935	20.27767
H	2.644646	3.453196	6.804028	H	3.582805	2.476325	19.70282
H	2.559484	2.149104	8.02988	H	4.705794	1.296111	18.95729
H	8.136813	3.662252	6.540131	H	10.29573	2.658369	17.00846
H	8.505269	3.037365	8.184606	H	10.56897	3.188158	18.70102
H	9.840753	3.558418	7.099606	H	11.92695	3.19736	17.52658
H	13.59703	5.75778	12.77404	H	1.34209	3.144985	8.057757
H	13.23864	5.836906	11.01524	H	2.69667	3.150466	6.883737
H	11.99643	6.3501	12.20901	H	2.644272	1.920955	8.185952
H	3.609971	6.781513	9.385957	H	8.205798	3.909406	6.45396
H	3.331127	6.377204	7.656219	H	8.567937	3.181855	8.053818
H	1.962359	6.338596	8.819501	H	9.902557	3.811266	7.032629
H	14.02412	2.827989	10.73744	H	13.68008	5.500507	12.74805
H	14.37287	2.756928	12.49395	H	13.31862	5.601347	10.99223
H	13.23053	1.58823	11.75917	H	12.12552	6.202811	12.19013

H	10.26796	6.565271	6.426924	H	3.534126	6.667009	9.237666
H	8.573317	6.67829	5.854875	H	3.260686	6.134193	7.546148
H	9.174122	7.811454	7.105914	H	1.902772	6.127262	8.720673
Pt	9.281532	4.677239	11.07435	H	13.90759	2.556787	10.72165
Pt	9.871547	4.524299	14.14672	H	14.254	2.466371	12.47808
Pt	7.500076	4.482871	16.19599	H	13.04303	1.367547	11.74573
Pt	4.547902	4.65042	15.17689	H	10.24522	6.855303	6.549869
Pt	3.957779	4.803242	12.10448	H	8.551355	6.966086	5.97401
Pt	6.329235	4.844681	10.05512	H	9.120283	8.033468	7.295695

3.1.4.6 Catalytic Study

The efficacy of the porous silica-supported **Pt₇** has been investigated as a heterogeneous precatalyst in the hydrogenation of *o*-xylene (Figure 3.15). In a typical catalytic reaction, 50 mg of the catalyst (0.005 mmol Pt content) was introduced into a 100 mL stainless-steel high-pressure Parr Compact reactor and 50 mL of a 0.5 M solution of the monocyclic arenes in n-hexane was added. The catalyst was then reduced *in situ* under H₂ (~50 bar) at 250 °C and stirred for 1 min. And subsequently the reaction was started by increasing the temperature to 300 °C and stirring the reaction mixture at 1000 rpm keeping the initial H₂ pressure at ~90 bar. Instead of using milder H₂ pressures, a high reaction pressure of ~90 bar was used in order to drive the reaction forward using the Le Châtelier's principle. The progress of the reaction was followed by monitoring the consumption of H₂ (pressure decrease) and gas chromatography (GC) analysis and the completion of the reaction was correlated with no further decrease in the H₂ pressures. Recyclability experiments on the catalyst were performed by filtering off and drying the used catalyst and utilizing it again in subsequent catalytic cycles under the same reaction conditions.

The *o*-xylene was chosen as a model substrate to study the efficacy of the **KNa-Pt₇@SBA15-apts** catalyst because the reaction rate for *o*-xylene was the slowest among the monocyclic arenes (*p*-xylene > *m*-xylene > *o*-xylene).¹⁰⁰ For the catalytic studies, **KNa-**

Pt₇ was used as the precursor, and the supported precatalyst **KNa-Pt₇@SBA15-apts** was obtained by dissolving **KNa-Pt₇** in water and slowly adding the 3-aminopropyltriethoxysilane (apts)-modified SBA15 (SBA15-apts) to the stirred solution, which was subsequently refluxed for 2 h (Pt loading \approx 5 wt %). The mixture was filtered, and the residue was washed multiple times with deionized water, air-dried, and subsequently calcined at 250 °C for 4 h (heating rate = 0.5 °C/min) in order to obtain the precatalyst **KNa-Pt₇@SBA15-apts** that was eventually reduced *in situ* under H₂ inside the Parr reactor, thereby generating the actual catalyst for the hydrogenation of arenes. It was found that for *o*-xylene as the substrate, the reaction was complete in \sim 10 min with a \sim 96% conversion and a *cis/trans* ratio (*S_{c/t}*) of 67:29, which is opposite of the selectivity of the favored *trans*-1,2-DMCH with Pd-based catalysts (Table 3.5).

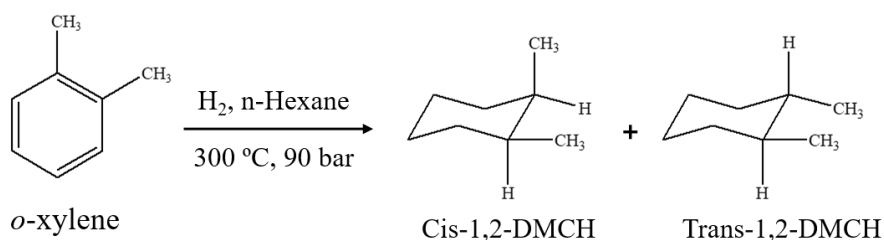


Figure 3.15. Schematic representation of the catalytic hydrogenation of *o*-xylene using the catalyst **KNa-Pt₇@SBA15-apts**.

Such observations are also in line with those reported for *o*-xylene hydrogenation over supported Pd and Ni and Pt catalysts.¹⁰¹ The nature of the catalyst and the operation conditions have a strong effect on the product stereoselectivity, like temperature, metal dispersion.¹⁰² *O*-xylene is believed to adsorb parallel to the surface of metals because of the interaction between π -electrons in the aromatic ring and the unoccupied d-metal orbitals.¹⁰³ To reduce the repulsive effect, the two methyl substituents in *o*-xylene should be oriented away from the surface, and consequently *cis*-DMCH should be obtained. Hence,

the cis stereoisomer is the kinetically favored product. While the cis stereoisomer is thermodynamically favored.^{102a} The increased selectivity to trans-isomer as a function of temperature and increased metal dispersion has intensively been explained by roll-over mechanism proposed by Inuone group,¹⁰⁴ where the model well explained the exchange of hydrogen atoms on both sides of cyclopentane molecule (over Pd catalysts). Therefore, the cis/trans ratio of the final product is opposite for the Pt-based and Pd-based catalysts.

Table 3.5. *o*-xylene hydrogenation at 300 °C and 90 bar H₂ pressure using different supported catalyst materials (support = SBA15-apts).

Pre-Catalyst	M loading (mmol)	Activation Method	Reaction Time (min)	Conversion (%)	Selectivity (S _{c/t})	References
KNa-Pt ₇	0.005	250 °C air calcination (4 h)	10	~96 (1 st cycle) ~99 (2 nd cycle) ~100 (3 rd cycle)	S _{c/t} = 67/29 S _{c/t} = 66/33 S _{c/t} = 65/35	This work
Pd ₄₀ -SiW ₁₂	0.009	250 °C air calcination (4 h)	55	~99	37/63	27b
Pd ₁₃ As ₈	0.01	Chemical reduction by hydrazine, 650 °C air calcination (4.5 h)	960	~100	40/60	105
Pd ₁₃ Se ₈	0.01	550 °C air calcination (4.5 h)	50	~100	43/57	
NiPd ₁₂ Se ₈	0.01	550 °C air calcination (4.5 h)	25	~100	40/60	
Pd _{15.4} P ₁₀	0.01	550 °C air calcination (4.5 h)	15	~100	40/60	
Na ₁₀ [Pt ₃ S ₂ (SO ₃) ₆]	0.006	425 °C air calcination (1 h)	150	~100 (150 °C) ~100 (350 °C)	70/30 75/25	55
Pt/Al ₂ O ₃	0.002	500 °C air calcination (12 h)	180	27.4 (250 °C)	—	106
Silicalite-1@Pt/α-Al ₂ O ₃	0.1	500 °C air calcination (4 h)	240	80.7 (200 °C)	—	107
Pt/C ₁₂ MCM-41	0.013	300 °C H ₂ reduction (2 h)	120	38 (110 °C)	25/13	108

The reaction of arenes with SBA15-apts alone did not show any hydrogenation activity.

The catalyst was also found to be recyclable up to 3 consecutive reaction cycles with a slightly increase in the reaction conversion (Table 3.5). Also, N₂ sorption measurements

were performed on the precatalyst before and after loading/calcination and after catalysis in order to investigate the effect on the surface area (Figure 3.16, Table 3.6). We found that both the surface area and pore volume of the SBA15 support (434 m²/g and 0.691 cc/g) decrease after modification with apts (377 m²/g and 0.535 cc/g), as expected.

Table 3.6. Variation of the surface area and pore size of the prepared materials after modification, **Pt₇** immobilization, calcination and after catalysis.

Materials	Surface Area (m ² /g)	Pore Volume (cc/g)
SBA15	434	0.619
SBA15-apts	377	0.535
Pt₇ @SBA15-apts (1 wt% Pt-basis)	300	0.500
Pt₇ @SBA15-apts (1 wt% Pt-basis) calcined at 250 °C	333	0.518
Pt₇ @SBA15-apts (1 wt% Pt-basis) calcined at 250 °C and after catalysis	255	0.500

Immobilization of **KNa-Pt₇** on the modified SBA15 further decreases the surface area and pore volume, which indicates that the pores are partially blocked upon loading, as expected. These values increase again upon calcination due to loss of the aminopropyl arms from the silica surface. After catalysis, there is a subsequent decrease in the surface area and pore volume, probably due to partial blocking of the pores by the Pt nanoparticles. The ¹H NMR spectrum of the filtrate obtained after loading the **KNa-Pt₇** on the modified SBA15 support only exhibited one peak at 4.7 ppm, corresponding to water, confirming that during the loading process the **Pt₇** polyanion has been adsorbed quantitatively into the pores of the SBA-15 (Figure 3.17). The activity of **KNa-Pt₇** as a heterogeneous hydrogenation precatalyst has been compared with the other Pt-based catalysts, and various

polyoxopalladates (POPs) supported on SBA15-apts (Table 3.5). **KNa-Pt₇@SBA15-apts** has the distinct advantage of requiring a much lower activation temperature with excellent activity and recyclability.

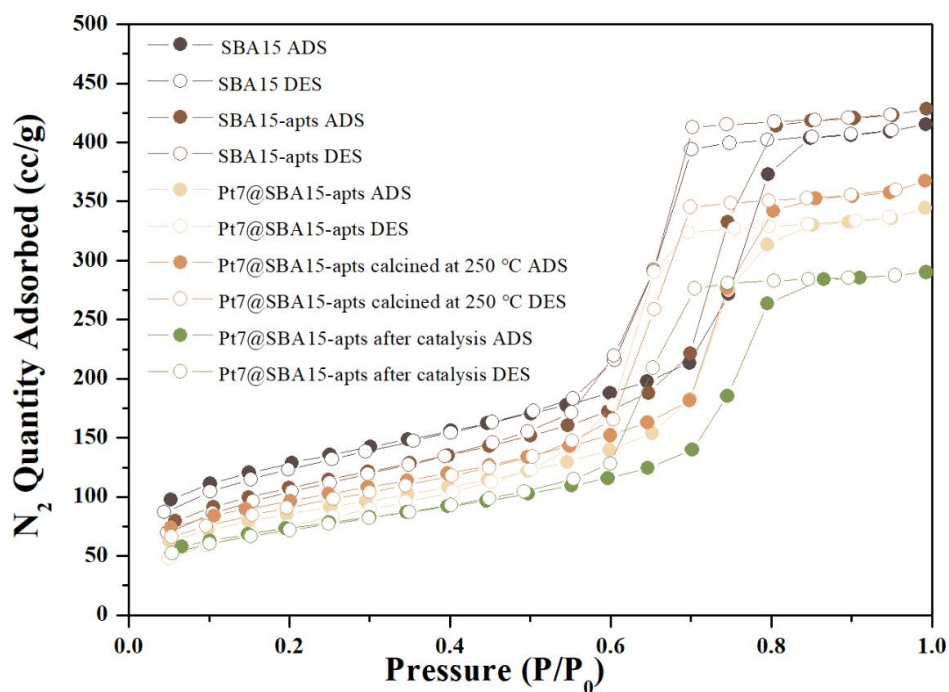


Figure 3.16. N₂ sorption isotherms of the SBA15 support before and after modification, after immobilization with **KNa-Pt₇** and after calcination and catalysis.

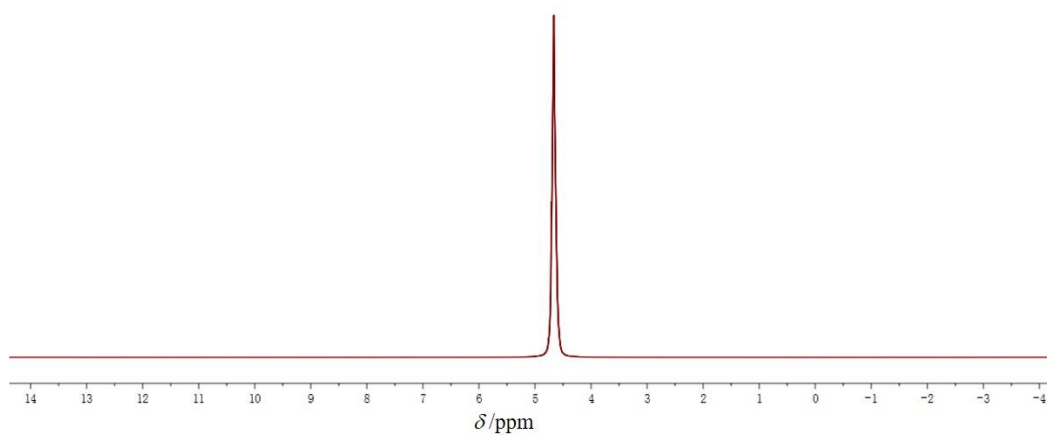


Figure 3.17. ¹H spectrum of the filtrate obtained after immobilizing **KNa-Pt₇** on the modified SBA15 support.

3.1.5 Conclusions

In summary, the first mixed-valent polyoxo-platinate(IV,II) **Pt₇** and the first Pt^{IV}-containing polyoxopalladate(II) **PtPd₆** as discrete inorganic oxo complexes by using simple open beaker and aqueous solution synthetic conditions have been synthesized and structurally characterized. Both polyanions **Pt₇** and **PtPd₆** were fully characterized in the solid state and the oxidation states of the noble metal ions were unequivocally identified. The solution (¹H, ¹³C and ¹⁹⁵Pt NMR) and gas phase studies also support the existence of the two polyanions. In fact, **Pt₇** was shown to be stable in solution for several months, which provides much potential for further studies and applications, e.g. in the catalytic or biomedical directions. The **Pt₇** polyanion supported on porous silica can be an effective heterogeneous catalyst for the hydrogenation of arenes. This work can be considered as a synthetic breakthrough in polyoxoplatinate (POPt) and platinum-containing polyoxopalladate (POPd) chemistry, and besides performing catalytic studies (e.g. hydrogenation of olefins using the novel polyanions homogeneously or as bottom up precursors for supported noble metal nanoparticles) the synthesis of more derivatives of this family of polyoxo-noble-metalates in the future is also the aim.

3.2 Au(III)-containing noble metal-oxo clusters

3.2.1 Synthesis

$\text{Na}[\text{Pt}^{\text{IV}}_2\text{Au}^{\text{III}}_3\text{O}_6(\text{AsO}_2(\text{CH}_3)_2)_6] \cdot \text{NaCl} \cdot \text{NaNO}_3 \cdot 6\text{H}_2\text{O}$ (**Na-Pt₂Au₃**)

$\text{H}[\text{AuCl}_4]$ (0.061 g, 0.18 mmol) was dissolved in 1.5 mL aqueous sodium cacodylate buffer (2 M, adjust pH to 7 by adding 68% HNO_3), leading to an orange solution. Then $\text{H}_2\text{Pt}(\text{OH})_6$ (0.036 g, 0.12 mmol) was dissolved in 0.4 mL 1M NaOH solution, and added to the resulting orange solution while heating at 80 °C. During the dropwise addition of $\text{H}_2\text{Pt}(\text{OH})_6$, the color of the reaction mixture changed from orange to orange-red. The obtained solution was stirred at 80 °C for 30 min. Slow evaporation of the filtrate at room temperature in an open vial resulted in yellow hexagonal crystals within 2 days. The obtained crystals **Na-Pt₂Au₃** were collected after 5 days by filtration and air dried for 2 days. Yield: 0.085 g (68% based on Au). Upon rehydration, **Na-Pt₂Au₃** can be fully transformed to the crystalline phase in the mother liquor **Na-Pt₂Au₃(a)** (see main text for details). Polyanion **Pt₂Au₃** can also be synthesized using the reagents in stoichiometric ratio in water (instead of cacodylate buffer), but the yield was only 35%. FT-IR (KBr, cm^{-1}): 3529–3143 (s) [$\nu(\text{O-H})$ of H_2O], 3000–2800 (w) [$\nu(\text{C-H})$ of methyl groups of cacodylate], 1597 (m) [H_2O bending fundamental mode δ], 1381 (m) [$\delta(\text{C-H})$ of the methyl groups of cacodylate], 913 (w) [$\delta_{\text{out-of-plane}}(\text{O-H})$], 803 (s) [$\nu(\text{Au-O})$], 679–646 (w) [$\nu(\text{Pt-O})$], 566–452 (m) [$\nu(\text{As-C})$]. Elemental analysis (%) calcd for **Na-Pt₂Au₃**: Au 27.18, Pt 17.95, As 20.68, Na 3.17, Cl 1.63, N 0.64, C 6.63, H 2.23; found: Au 26.80, Pt 18.90, As 20.80, Na 3.35, Cl 2.60, N 0.73, C 6.65, H 2.18.

K[Pt^{IV}₂Au^{III}₃O₆(AsO₂(CH₃)₂)₆]·KCl·KAsO₂(CH₃)₂·18H₂O (K-Pt₂Au₃)

H[AuCl₄] (0.061 g, 0.18 mmol) was dissolved in 1.5 mL aqueous cacodylic acid buffer (2 M, adjust pH to 7 by adding solid KOH), leading to an orange solution. Then H₂Pt(OH)₆ (0.036 g, 0.12 mmol) was dissolved in 0.4 mL 1 M KOH solution, and added to the orange solution while heating at 80 °C. During the dropwise addition of H₂Pt(OH)₆, the color of the reaction mixture changed from orange to orange-red. The obtained solution was stirred at 80 °C for 30 min. Slow evaporation of the filtrate at room temperature in an open vial resulted in yellow rod-shaped crystals within 1 month. The obtained crystals were collected by filtration and dried in air. Yield: 0.068 g (46% based on Au). FT-IR (KBr pellet, cm⁻¹): 3407 (s) [ν(O–H) of H₂O], 3019–2924 (w) [ν(C–H) of methyl groups of cacodylate], 1668–1643 (m) [H₂O bending fundamental mode δ], 1411 (m) [δ(C–H) of the methyl groups of cacodylate], 915 (w) [δ_{out-of-plane}(O–H)], 810 (s) [ν(Au–O)], 702–648 (w) [ν(Pt–O)], 523 (m) [ν(As–C)]. Elemental analysis (%) calcd for **K-Pt₂Au₃**: Au 23.51, Pt 15.53, As 20.87, K 4.67, C 6.69, H 2.13; found: Au 23.50, Pt 15.70, As 20.60, K 4.37, C 6.62, H 2.60.

Na₂[Pd^{II}₁₀Au^{III}₄O₁₂(AsO₂(CH₃)₂)₁₀]·17H₂O (Na-Au₄Pd₁₀)

H[AuCl₄] (0.034 g, 0.1 mmol) was dissolved in 3 mL aqueous sodium cacodylate buffer (2 M, adjust pH to 7 by adding 68% HNO₃), leading to an orange solution. Then Pd(NO₃)₂ (0.057 g, 0.25 mmol) was added to the resulting orange solution. The obtained deep-red solution was stirred at 80 °C for 60 min. Slow evaporation of the filtrate at room temperature in an open vial resulted in dark red rod-like crystals within 2 days. Then decant the supernatant and the rod crystals were washed with 96% ethanol ((Pd₇²⁹ determined by FT-IR and single crystal XRD, yield: 20% (based on Pd)). Later, slow evaporation of the supernatants leads to formation of dark red blocky crystals **Na-Au₄Pd₁₀** within two

weeks, which were collected by filtration. yield: 5% (based on Pd). FT-IR (KBr, cm^{-1}): 3500–3200 (s) [$\nu(\text{O-H})$ of H_2O], 3013–2920 (w) [$\nu(\text{C-H})$ of methyl groups of cacodylate], 1638 (m) [H_2O bending fundamental mode δ], 1384 (m) [$\delta(\text{C-H})$ of the methyl groups of cacodylate], 1264 (w) [$\delta_{\text{in-plane}}(\text{O-H})$], 916-890 (w) [$\delta_{\text{out-of-plane}}(\text{O-H})$], 803 (s) [$\nu(\text{Au-O})$], 649 (m) [$\nu(\text{Pd-O})$], 518 (m) [$\nu(\text{As-C})$].

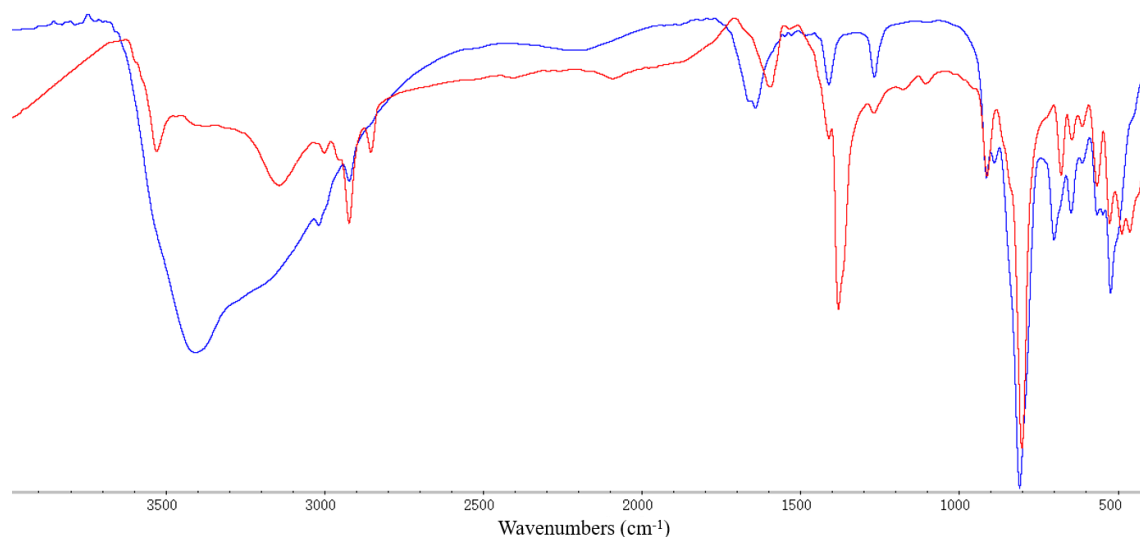


Figure 3.18. FT-IR spectra of $\text{Na-Pt}_2\text{Au}_3$ (red) and $\text{K-Pt}_2\text{Au}_3$ (blue).

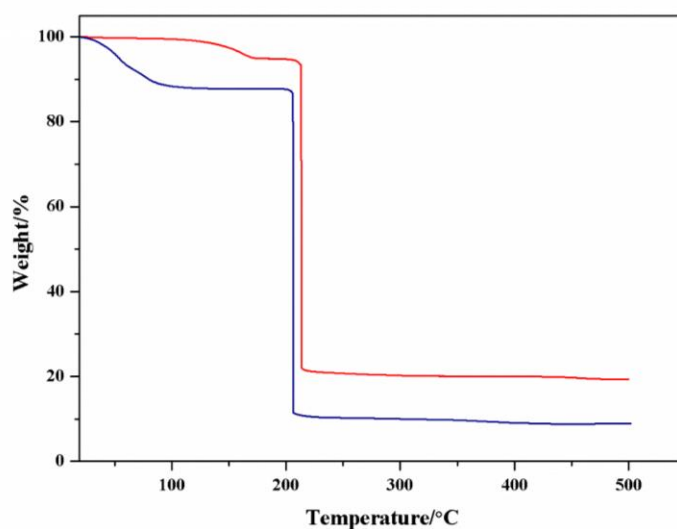


Figure 3.19. Thermograms of $\text{Na-Pt}_2\text{Au}_3$ (red) and $\text{K-Pt}_2\text{Au}_3$ (blue) from room temperature to 500 °C under N_2 .

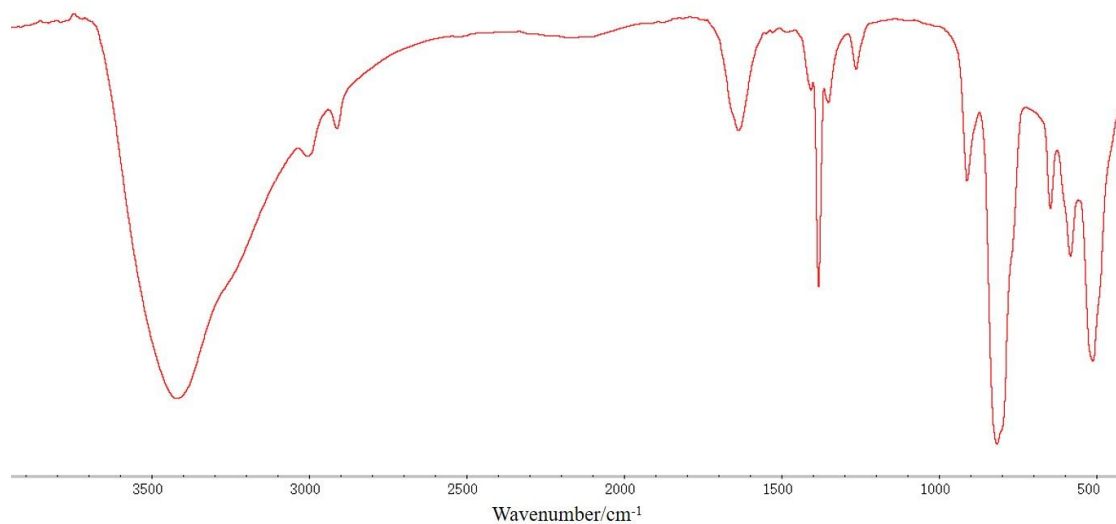


Figure 3.20. FT-IR spectrum of **Pd₇** from 400–4000 cm⁻¹ on KBr pellets.

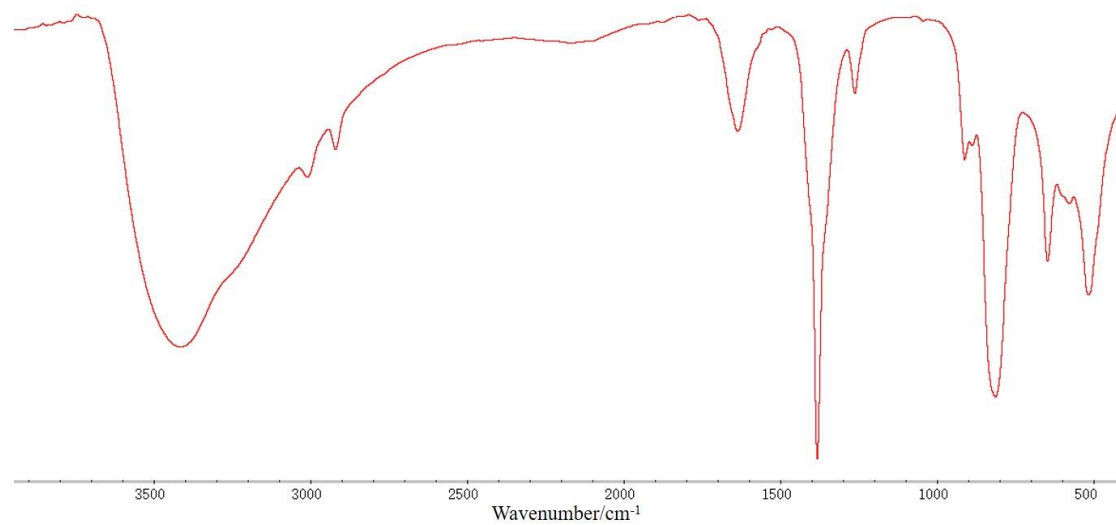


Figure 3.21. FT-IR spectrum of **Na-Au₄Pd₁₀** from 400–4000 cm⁻¹ on KBr pellets.

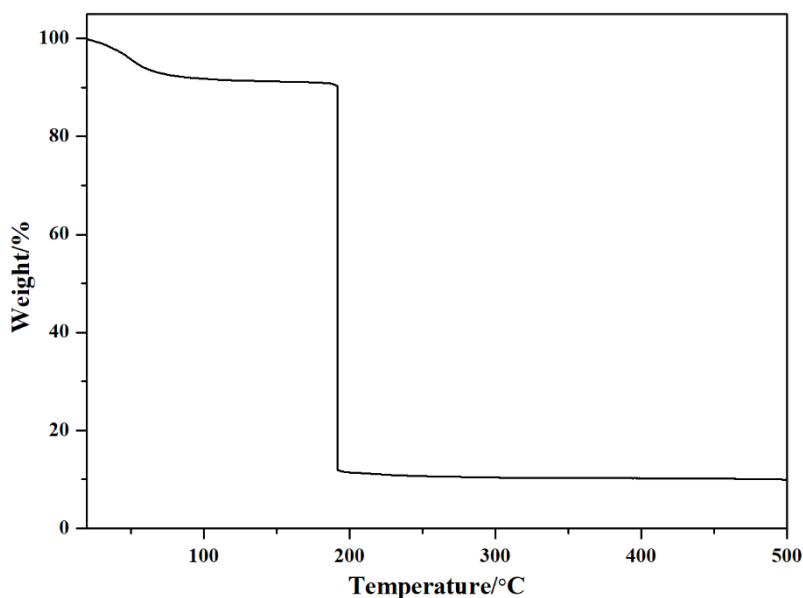


Figure 3.22. Thermograms of **Na-Au₄Pd₁₀** from room temperature to 500 °C under N₂.

3.2.2 Single-Crystal XRD Data

The solvent masking was done using the SQUEEZE command of Platon,⁸² the results of which have been added to the CIF files in the section titled “SQUEEZE RESULTS”. From the calculations, it can be seen that the solvent accessible void of the crystal structure **Na-Pt₂Au₃(a)** is $\sim 739 \text{ \AA}^3$, and the electron count in the solvent accessible void is ~ 291 . Considering $Z = 2$, this roughly comes out to be around 14 H₂O molecules, which is larger as compared to what is observed from TGA analysis and elemental analysis (this air-dried material actually corresponds to the compound **Na-Pt₂Au₃**). This is typically due to the facile removal of the lattice water molecules (converting **Na-Pt₂Au₃(a)** to **Na-Pt₂Au₃**), which has been carefully studied using SXRD, PXRD and TGA. Similarly, for **K-Pt₂Au₃**, a solvent accessible void of $\sim 148 \text{ \AA}^3$ was observed, and the electron count in the solvent accessible void to be ~ 90 . Considering $Z = 2$, this roughly comes out to be around 5 H₂O molecules. If we add this to the 11 H₂O molecules already assigned from XRD, we get 16 lattice H₂O molecules, which is very close to what is observed from TGA analysis and

elemental analysis (~18 lattice H₂O molecules). For **Na-Pt₂Au₃(a)**, two Au positions are disordered within the structure due to thermal motion, with partial occupancies of 47:3. For **K-Pt₂Au₃**, two As positions of free cacodylate ions are disordered within the structure due to thermal motion, with partial occupancies of 80:20. The disorder on the Au atom in **Na-Pt₂Au₃(a)** has been modelled by using the PART function and allowing for free refinement of the occupancies of the disordered atoms as well as their thermal parameters. This indicated a ~6% disorder on the Au atom. Based on our observations from PXRD studies, we seem to form a mixture of two closely related crystalline phases differing in the amounts of lattice water molecules (**Na-Pt₂Au₃** and **Na-Pt₂Au₃(a)**). Even a slight exposure to air results in the removal of some of the lattice water molecules, which may lead to the observed disorder in the Au atoms as such a phase change appears to be facile.

Table 3.7. Crystal data and structure refinement for **Na-Pt₂Au₃**, **Na-Pt₂Au₃(a)**, **K-Pt₂Au₃** and **Na-Au₄Pd₁₀**.

Compound	Na-Pt₂Au₃	Na-Pt₂Au₃(a)	K-Pt₂Au₃	Na-Au₄Pd₁₀
empirical formula	Na ₃ Pt ₂ Au ₃ As ₆ C ₁₂ H ₄₈ O ₂₇ NCl ^a	Na ₃ Pt ₂ Au ₃ As ₆ C ₁₂ H ₃₆ O ₂₇ NCl	K ₃ Pt ₂ Au ₃ As ₇ C ₁₄ H ₇₈ O ₃₈ Cl ^a	NaPd ₅ Au ₂ As ₅ C ₁₀ H ₃₀ O ₁₈
fw, g mol ⁻¹	2173.51 ^a	2161.44	2513.00 ^a	1761.86
crystal system	Hexagonal	Hexagonal	Triclinic	Triclinic
space group	P $\bar{6}$	P6 ₃ /m	P $\bar{1}$	P $\bar{1}$
<i>a</i> (Å)	10.933(3)	10.9156(7)	13.5559(16)	12.910(2)
<i>b</i> (Å)	10.933(3)	10.9156(7)	14.1105(16)	14.335(2)
<i>c</i> (Å)	20.585(5)	26.8948(18)	16.6726(19)	14.431(2)
<i>α</i> (°)	90	90	75.614(3)	62.125(3)
<i>β</i> (°)	90	90	66.913(3)	71.102(4)
<i>γ</i> (°)	120	120	85.534(3)	73.751(4)
<i>V</i> (Å ³)	2130.9(12)	2775.2(4)	2841.1(6)	2207.0(6)
<i>Z</i>	1	2	2	2
<i>D_c</i> (g cm ⁻³)	1.684	2.587	2.790	2.651

abs coeff, mm ⁻¹	10.817	16.612	17.013	12.391
θ range for data collection, deg	3.667 to 24.850	3.719 to 26.382	2.970 to 25.790	1.626 to 27.460
completeness to Θ_{\max}	99.2%	99.5%	99.6%	99.8%
index ranges	-12 \leq h \leq 12, -12 \leq k \leq 12, -20 \leq l \leq 24	-13 \leq h \leq 12, -13 \leq k \leq 13, -33 \leq l \leq 33	-16 \leq h \leq 16, -17 \leq k \leq 17, -18 \leq l \leq 20	-16 \leq h \leq 16, -18 \leq k \leq 18, -18 \leq l \leq 18
reflns collected	22878	36290	33904	28170
indep reflns	2531	1944	10846	10055
$R(\text{int})$	0.1073	0.0735	0.0896	0.0944
abs corrn	Semi-empirical from equivalents	Semi-empirical from equivalents	Semi-empirical from equivalents	Semi-empirical from equivalents
data/restraints/param	2531 / 57 / 84	1944 / 0 / 98	10846 / 33 / 632	10055 / 12 / 389
GOF on F^2	1.061	0.891	0.969	1.057
$R_1, {}^b wR_2^c$ [$I > 2\sigma(I)$]	0.0606, 0.1538	0.0274, 0.0685	0.0490, 0.1077	0.0688, 0.2111
$R_1, {}^b wR_2^c$ (all data)	0.0713, 0.1632	0.0331, 0.0723	0.0785, 0.1212	0.1046, 0.2513
Largest diff peak and hole, e \AA^{-3}	5.723 and -3.135	1.407 and -1.045	2.442 and -2.096	4.811 and -5.087

^aThe values are the actual formula units and weights as obtained from bulk elemental analysis.

^b $R_1 = \sum ||F_o| - |F_c|| / \sum |F_o|$. ^c $wR_2 = [\sum w(F_o^2 - F_c^2)^2 / \sum w(F_o^2)^2]^{1/2}$.

3.2.3 Bond Valence Sum Calculations

In **Na-Pt₂Au₃** and **Na-Pt₂Au₃(a)**, the BVS values for the independent gold atom are 2.911 and 2.592, and the values for the independent platinum atom are 3.798 and 4.348, respectively. The BVS values for different types of μ_2 -bridging oxygens are presented in Table 3.8. These values show that these oxygens are not protonated and therefore polyanion **Pt₂Au₃** is a true gold(III)-platinum(IV) oxo species. In **K-Pt₂Au₃**, the BVS values for the three gold atoms range from 2.609 to 2.665, and the values for the two platinum atoms are 4.209 and 4.228, respectively, supporting the +3 oxidation state of gold and +4 oxidation state of platinum in polyanion **Pt₂Au₃**. In **Na-Au₄Pd₁₀**, the BVS values for the two gold atoms are 2.413 and 2.760, respectively, and the values for the five palladium atoms range from 2.114 to 2.265, supporting the +3 oxidation state of

gold and +2 oxidation state of palladium in polyanion $\text{Au}_4\text{Pd}_{10}$. The BVS values for different types of μ_3 -bridging oxygens in $\text{Na-Au}_4\text{Pd}_{10}$ are presented in Table 3.9.

Table 3.8. BVS values for μ_2 -bridging oxygen atoms in $\text{Na-Pt}_2\text{Au}_3$, $\text{Na-Pt}_2\text{Au}_3(\mathbf{a})$, and $\text{K-Pt}_2\text{Au}_3$.

Compound	$\mu_2\text{-O}$	BVS value
$\text{Na-Pt}_2\text{Au}_3$	Au – O2 – Pt	1.433
$\text{Na-Pt}_2\text{Au}_3(\mathbf{a})$	Au – O1 – Pt	1.498
$\text{K-Pt}_2\text{Au}_3$	Au1 – O1 – Pt2	1.494
	Au1 – O3 – Pt1	1.492
	Au2 – O5 – Pt1	1.476
	Au2 – O7 – Pt2	1.470
	Au3 – O9 – Pt2	1.558
	Au3 – O10 – Pt1	1.509

Table 3.9. BVS values for μ_3 -bridging oxygen atoms in $\text{Na-Au}_4\text{Pd}_{10}$.

$\mu_3\text{-O}$	Bond distance(Å)	BVS value	$\mu_3\text{-O}$	Bond distance(Å)	BVS value
O1	Pd1-O1 (1.9984)	1.714	O5	Au1-O5 (2.0010)	1.739
	Pd2-O1 (2.0106)			Pd4-O5 (2.0063)	
	Au1-O1 (2.0264)			Pd3-O5 (2.0120)	
O2	Pd1-O1 (1.9915)	1.674	O6	Au1-O6 (2.0007)	1.703
	Pd2-O1 (2.0322)			Pd5-O6 (2.0190)	
	Au1-O1 (2.0392)			Pd4-O6 (2.0259)	
O7	Au2-O7 (1.9572)	1.805	O8	Au2-O8 (1.9530)	1.814
	Pd3-O7 (2.0053)			Pd5-O8 (2.0048)	
	Pd1-O7 (2.0244)			Pd2-O8 (2.0239)	

3.2.4 Results and Discussion

3.2.4.1 Solid-State Structure

The first example of a discrete mixed platinum(IV)-gold(III) oxoanion, $[\text{Pt}^{\text{IV}}_2\text{Au}^{\text{III}}_3\text{O}_6((\text{CH}_3)_2\text{AsO}_2)_6]^-$ (Pt_2Au_3 , see Figure 3.23), which was synthesized in aqueous medium at 80 °C and isolated as a hydrated sodium salt,

$\text{Na}[\text{Pt}^{\text{IV}}_2\text{Au}^{\text{III}}_3\text{O}_6((\text{CH}_3)_2\text{AsO}_2)_6] \cdot \text{NaCl} \cdot \text{NaNO}_3 \cdot 6\text{H}_2\text{O}$ (**Na-Pt₂Au₃**) or a potassium salt, $\text{K}[\text{Pt}^{\text{IV}}_2\text{Au}^{\text{III}}_3\text{O}_6((\text{CH}_3)_2\text{AsO}_2)_6] \cdot \text{KCl} \cdot \text{KAsO}_2(\text{CH}_3)_2 \cdot 18\text{H}_2\text{O}$ (**K-Pt₂Au₃**) in good yield. The symmetry units of solid-state interaction of polyanion **Pt₂Au₃** are showed in Figure 3.24. The polyanion **Pt₂Au₃** was prepared by reaction of $\text{H}_2[\text{Pt}(\text{OH})_6]$ with hydrogen tetrachloroaurate $\text{H}[\text{AuCl}_4]$ in a pH 7 sodium dimethylarsinate buffer, resulting in a rapid color change (the initial orange solution color becomes orange-red). It is well known that an acidification of a $[\text{Au}(\text{OH})_4]^-$ solution leads to the formation of insoluble $\text{Au}(\text{OH})_3$, and that chloride ions do not compete with OH^- for Au^{III} in neutral or slightly alkaline solutions (pH 7.0 to 8.5).¹⁰⁹ In this case, the *in situ* formed tetrahydroxogold(III) ion $[\text{Au}(\text{OH})_4]^-$ (or a closely related derivative) reacts smoothly with $[\text{Pt}(\text{OH})_6]^{2-}$ in the presence of cacodylate ions, which act as capping groups, thereby terminating the condensation process.

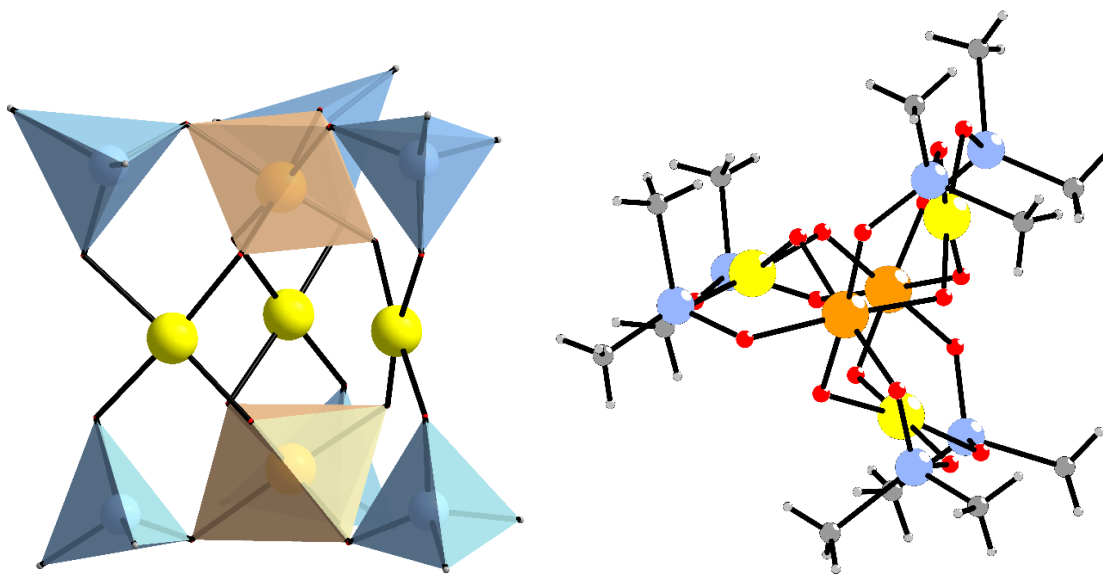


Figure 3.23. Combined ball-and-stick/polyhedral representation and Ball-and-stick representation (side view) of **Pt₂Au₃**. Color code: {PtO₆} orange octahedra, {(CH₃)₂AsO₂} blue tetrahedra, Au yellow, Pt orange, As sky blue, O red, C grey. Hydrogen atoms omitted for clarity.

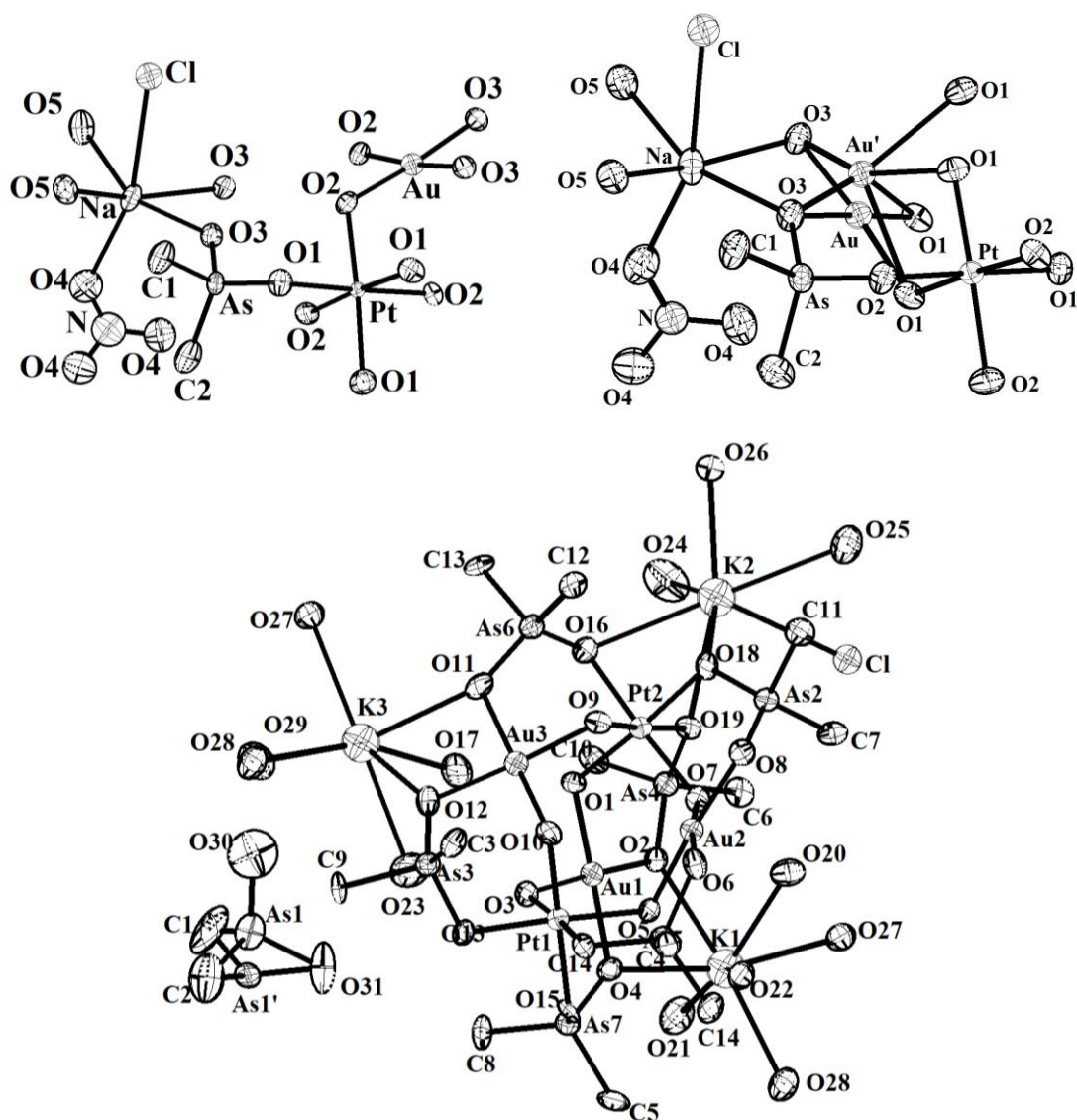


Figure 3.24. The symmetry unit of solid-state interaction of polyanion **1** with Na^+ counter cations in $\text{Na-Pt}_2\text{Au}_3$ (top left) and $\text{Na-Pt}_2\text{Au}_3(\text{a})$ (top right), as well as K^+ counter cations in $\text{K-Pt}_2\text{Au}_3$ (bottom), respectively (50% probability ellipsoids). Hydrogen atoms omitted for clarity.

The polyanion Pt_2Au_3 possesses a waterwheel structure with two Pt ions linked by three square-planar coordinated Au ions and terminally coordinated by six cacodylate ligands, resulting in an assembly with C_{3h} symmetry (Figure 3.23). In $\text{K-Pt}_2\text{Au}_3$, the average Au–O bond lengths are 1.953(9) Å for the oxo ligands and 2.017(9) Å for the oxygen atoms of the cacodylate fragments. Bond valence sum (BVS) calculations showed no protonation

for any bridging oxygen atoms (Table 3.6). The average Au–O bond lengths in **K-Pt₂Au₃** (1.986 ± 0.010 Å) are comparable to those in other known gold(III)-oxo complexes, such as the square-planar Au₂O₂ core of [Au₂{N₂C₁₀H₇(CH₂CMe₃)-6}₂(μ-O)₂][PF₆]₂ ($1.976(3)$ and $1.961(3)$ Å),¹¹⁰ the SrAu₂(CH₃COO)₈ (1.979 ± 0.008) Å,¹¹¹ or the polyoxoaurate Au₄As₄ (1.980 ± 0.023 Å),³³ and quite a bit shorter than the Au–O distance in dimethylgold(III) hydroxide (2.154 ± 0.148) Å.¹¹² The Au⋯Au distance in **K-Pt₂Au₃** (3.973 ± 0.070 Å) is significantly longer than in Au₄As₄ (3.246 ± 0.024 Å). The Pt–O bond lengths around the octahedrally coordinated Pt centers are quite regular, ranging from $1.960(9)$ to $2.063(9)$ Å. The same applies for the sodium salt **Na-Pt₂Au₃**. The three Au ions in **1** are located in the same plane and exhibit a slightly distorted square-planar coordination. The oxo ligands bridging to the platinum centers are situated on both sides of this {Au₃} plane, while all O–As–O bridges connect a Pt and an Au atom. In the solid-state lattice of **Na-Pt₂Au₃**, the polyanions are surrounded by a belt of six Na⁺ ions, three NO₃⁻ ions, and three Cl⁻ ions, resulting in a supramolecular 2D layer with a hexagonal pattern (Figure 3.25).

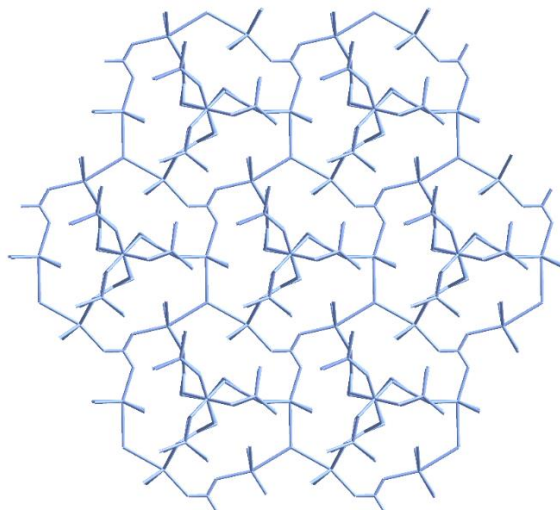


Figure 3.25. Solid state structure of **Na-Pt₂Au₃** highlighting the supramolecular 2D

layered plane.

Single-crystal X-ray analysis revealed that the polyanion **Au₄Pd₁₀** comprises 10 square-planar oxo-coordinated Pd^{II} ions and 4 square-planar oxo-coordinated Au^{III} ions, which can be subdivided in a central cube shaped [Pd₄O₄((CH₃)₂AsO₂)₂] unit, connected to two tetrameric bowl shaped [AuPd₃O₄((CH₃)₂AsO₂)₄] units by two square-planar coordinated gold atoms on each side, resulting in a mixed palladium(II)-gold(III) oxoanion [Pd^{II}₁₀Au^{III}₄O₁₂(AsO₂(CH₃)₂)₁₀]²⁻ (**Au₄Pd₁₀**) (Figure 3.26). The symmetry unit of solid-state interaction of polyanion **Au₄Pd₁₀** is showed in Figure 3.27. In **Na-Au₄Pd₁₀**, the average Au^{III}-O bond lengths are 1.967(6) Å for the oxo ligands linked to central cube [Pd₄O₄((CH₃)₂AsO₂)₂] unit and 2.017(3) Å for the oxygen atoms from the [AuPd₃O₄((CH₃)₂AsO₂)₄] unit. The Pd-O distances range from 1.991(5) to 2.059(1) Å. To the best of our knowledge, this is the second example of mixed gold-palladium polyoxo-noble-metalate, except for [NaAu^{III}₄Pd^{II}₈O₈(AsO₄)₈]¹¹⁻³⁰.

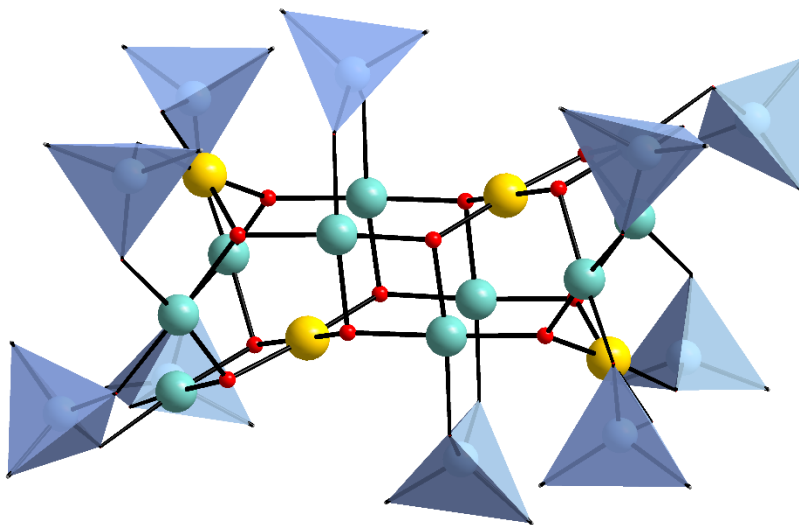


Figure 3.26. Combined ball-and-stick/polyhedral representation and Ball-and-stick representation (side view) of **Au₄Pd₁₀**. Color code: {(CH₃)₂AsO₂} blue tetrahedra, Pd green, Au yellow. Hydrogen atoms omitted for clarity.

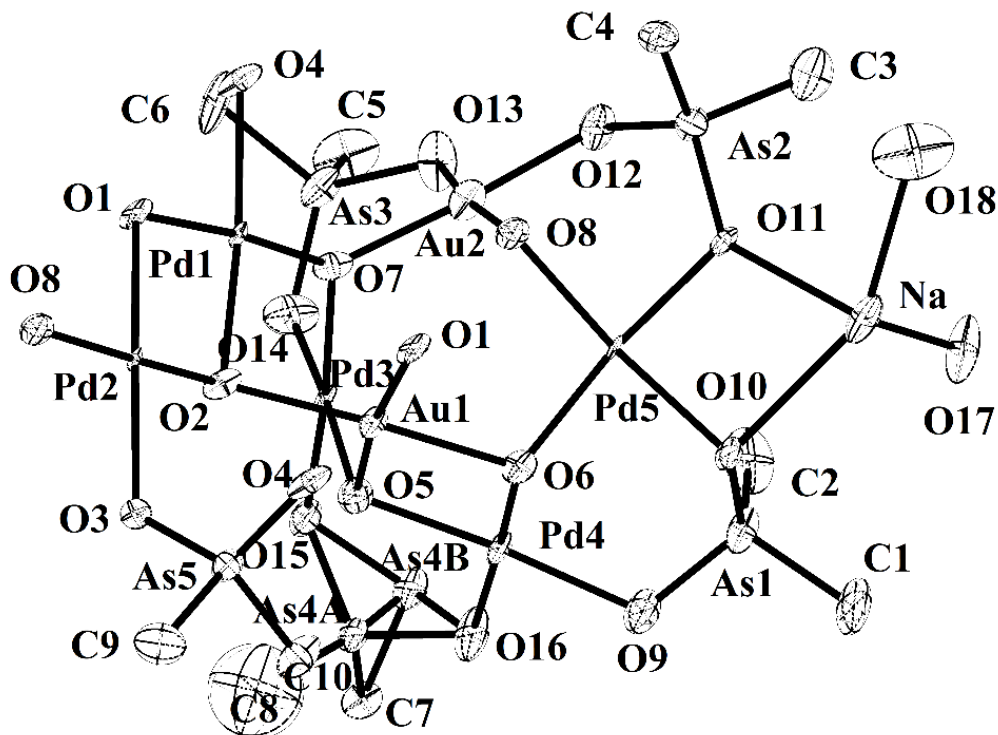


Figure 3.27. The symmetry unit of solid-state interaction of polyanion $\text{Au}_4\text{Pd}_{10}$ with Na^+ counter cations in $\text{Na-Au}_4\text{Pd}_{10}$ (50% probability ellipsoids). Hydrogen atoms omitted for clarity.

3.2.4.2 Multinuclear NMR Study

To complement our solid-state XRD results on Pt_2Au_3 with solution studies, we performed ^1H , ^{13}C and ^{195}Pt NMR measurements on $\text{Na-Pt}_2\text{Au}_3$ and $\text{K-Pt}_2\text{Au}_3$ redissolved in $\text{H}_2\text{O}/\text{D}_2\text{O}$. The ^1H NMR spectrum of the reference Na-Cac in water exhibits sharp peaks at 4.7 and 1.4 ppm, respectively, corresponding to the protons of the cacodylate methyl groups and crystal water molecules. On the other hand, the ^1H NMR spectrum of $\text{Na-Pt}_2\text{Au}_3$ exhibits peaks at 2.1 and 1.7 ppm that correspond to the two structurally and hence magnetically inequivalent cacodylate methyl groups (Figure 3.28). The ^1H NMR spectrum of $\text{K-Pt}_2\text{Au}_3$ exhibits three distinct peaks at 2.1, 1.7, and 1.6 ppm, respectively. The two downfield signals belong to Pt_2Au_3 , whereas the peak at 1.6 ppm corresponds to the methyl

protons of free cocrystallized cacodylate ions. We also investigated the pH stability of polyanion **Pt₂Au₃** by NMR and the pH-dependent ¹H NMR spectra show that polyanion **Pt₂Au₃** is stable at pH 2 to 10 (Figure 3.29).

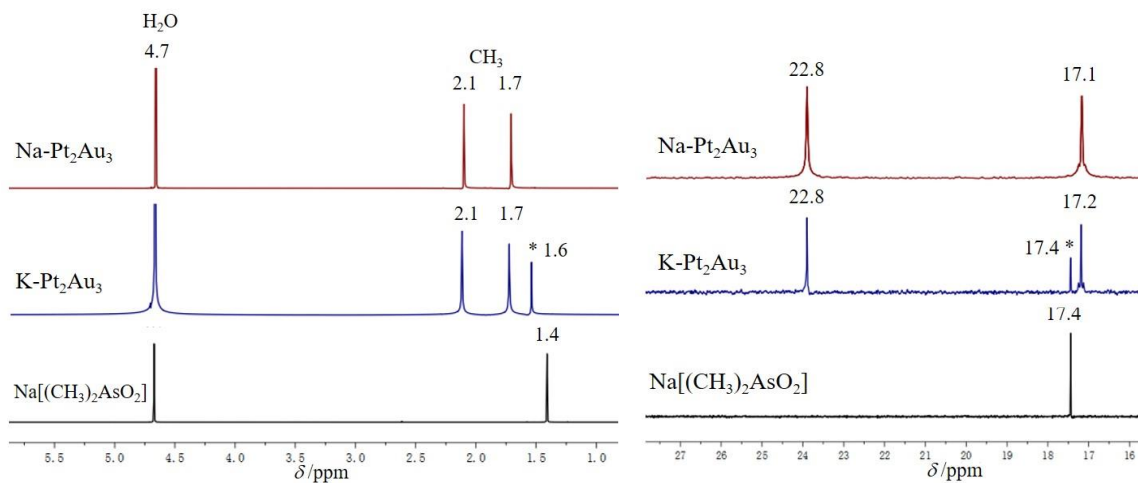


Figure 3.28. ¹H (left) and ¹³C (right) NMR spectra of **Na-Pt₂Au₃** and **K-Pt₂Au₃** dissolved in H₂O/D₂O compared to spectra of the sodium cacodylate reference.

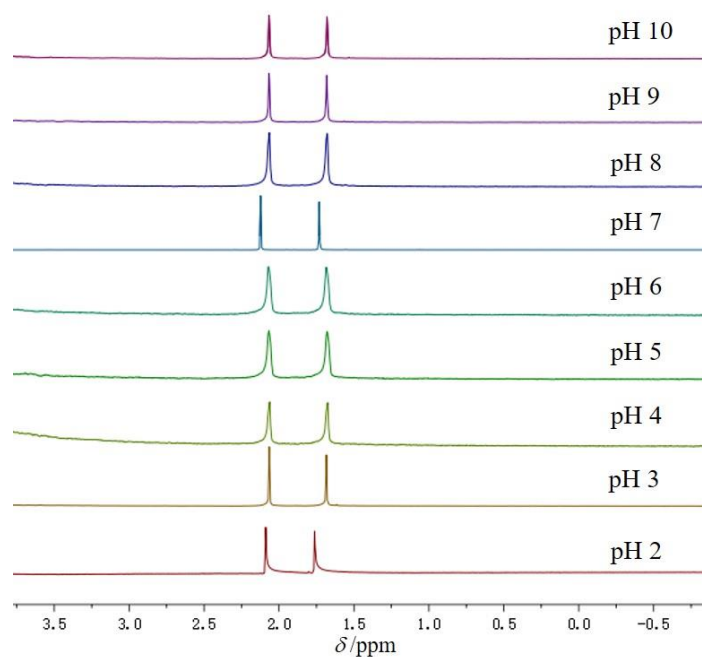


Figure 3.29. pH-dependent ¹H NMR spectra (D₂O/H₂O) of **Na-Pt₂Au₃**.

The ^{13}C NMR spectrum of **Na-Pt₂Au₃** exhibits peaks at 22.8 and 17.1 ppm that correspond to the two structurally inequivalent cacodylate methyl groups (Figure 3.28). The ^{13}C NMR spectrum of Na-Cac exhibits a narrow peak at 17.3 ppm. The ^{13}C NMR spectrum of **K-Pt₂Au₃** exhibits three distinct sharp peaks (in analogy to its ^1H NMR spectrum) at 22.8, 17.2, and 17.4 ppm corresponding to the methyl groups of the two structurally inequivalent cacodylate methyl groups of **1** and free cocrystallized cacodylate ions, respectively.

Next, ^{195}Pt NMR measurements were performed on **Na-Pt₂Au₃** and **K-Pt₂Au₃** redissolved in water. This technique had been applied earlier for the platinum(IV)-containing decavanadate $[\text{H}_2\text{Pt}^{\text{IV}}\text{V}_9\text{O}_{28}]^{5-}$, exhibiting a clean signal at $\delta = 3832$ ppm.⁴³ We located the expected singlet for **Na-Pt₂Au₃** and **K-Pt₂Au₃** at 3140 and 3142 ppm, respectively (Figure 3.30). The corresponding ^{195}Pt NMR signal for the precursor $\text{H}_2[\text{Pt}(\text{OH})_6]$ appeared more downfield at 3294 ppm. We also performed time and temperature dependent ^{195}Pt NMR measurements on fresh synthesis solutions of **Na-Pt₂Au₃** (Figure 3.31). After stirring at room temperature for 10 min and 40 min there are two peaks at 3316 and 3142 ppm, respectively, corresponding to the reagent $\text{H}_2\text{Pt}(\text{OH})_6$ and polyanion **Pt₂Au₃**. However, after heating at 40 °C for 30 min, the spectrum exhibits only a narrow peak at 3141 ppm, indicating that **Pt₂Au₃** is formed cleanly as the only product during the reaction procedure, suggesting a reaction yield of essentially 100%, which is extremely rare in POM chemistry. The combination of ^1H , ^{13}C , and ^{195}Pt NMR is fully consistent with the solid-state structure of **K-Pt₂Au₃** and **Na-Pt₂Au₃** and hence provides unequivocal evidence for the presence of polyanion **Pt₂Au₃** also in solution.

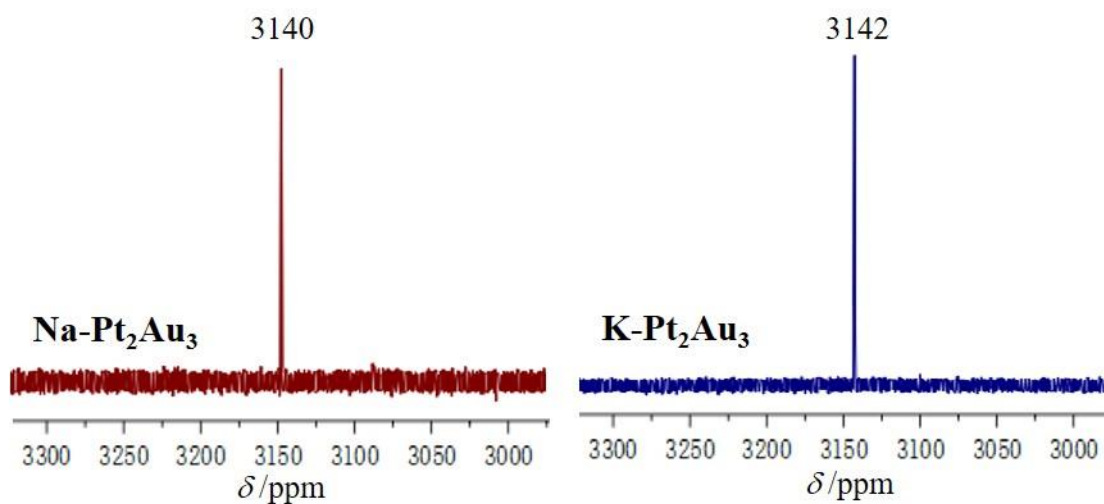


Figure 3.30. ^{195}Pt NMR spectra of $\text{Na-Pt}_2\text{Au}_3$ and $\text{K-Pt}_2\text{Au}_3$ dissolved in $\text{H}_2\text{O}/\text{D}_2\text{O}$.

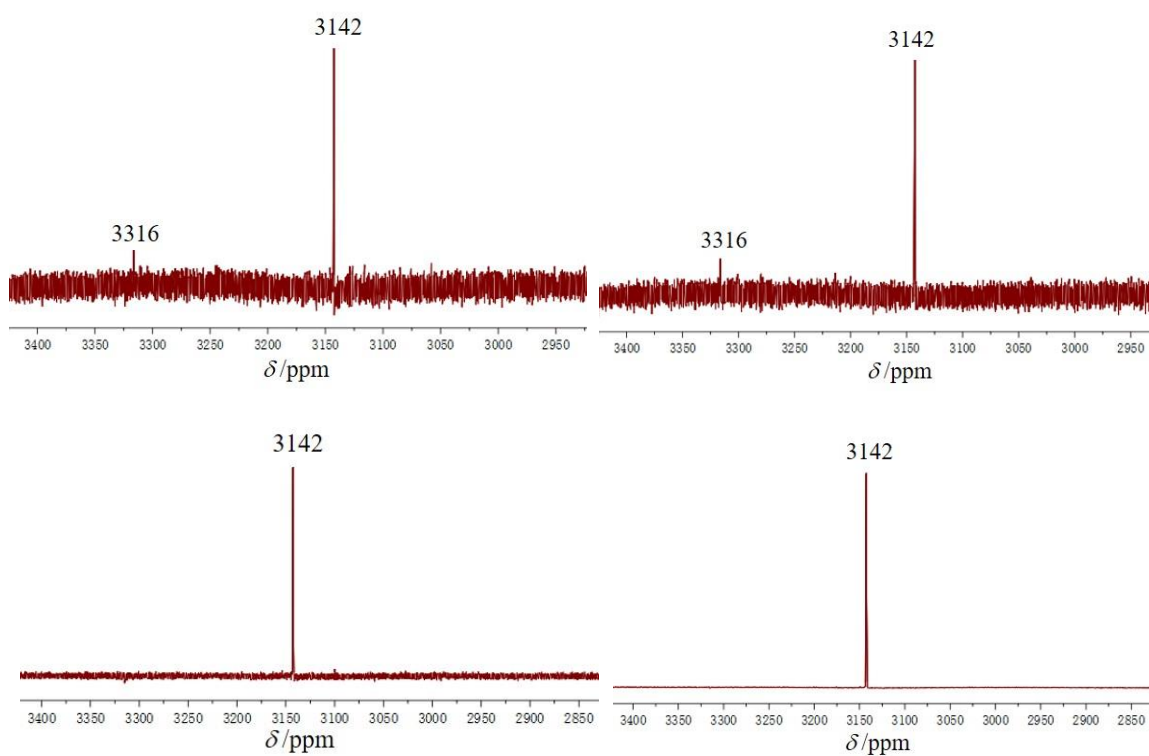


Figure 3.31. ^{195}Pt NMR spectra of fresh synthesis solutions of $\text{Na-Pt}_2\text{Au}_3$ after stirring at room temperature for 10 min (top left, 4510 scans) and for 40 min (top right, 3018 scans), as well as at 40 °C for 30 min (bottom left, 3052 scans) and the same solution after a longer measurement time (bottom right, 126693 scans).

3.2.4.3 ESI-MS Analysis

Furthermore, the sodium and potassium salts of polyanion **Pt₂Au₃** were investigated by ESI-MS in the positive and negative ion modes (Figure 3.32). In the negative ion mode, signals centered around m/z 1898.55 were observed for both **Na-Pt₂Au₃** and **K-Pt₂Au₃**. These could be clearly assigned to the singly-charged title polyanion $[\text{Pt}^{\text{IV}}_2\text{Au}^{\text{III}}_3\text{O}_6((\text{CH}_3)_2\text{AsO}_2)_6]^-$ (**Pt₂Au₃**), see Figure 3.33. In the positive ion mode spectrum of **Na-Pt₂Au₃**, a main group of signals was observed centered around m/z 983.75, corresponding to a doubly-charged species with an elemental composition of $[\text{Na}_3\text{Pt}_2\text{Au}_3\text{O}_6(\text{AsO}_2(\text{CH}_3)_2)_6]^{2+}$ (Figure 3.34). The isotope distribution was fully confirmed by comparison of the experimental spectrum to a simulated spectrum. Thus, the ESI-MS spectra of **Na-Pt₂Au₃** and **K-Pt₂Au₃** corroborate the solid-state structural analysis and show that polyanion **Pt₂Au₃** is structurally intact in solution, even under ESI conditions. Additional MS assignments for **Na-Pt₂Au₃** and **K-Pt₂Au₃** are summarized in Table 3.10.

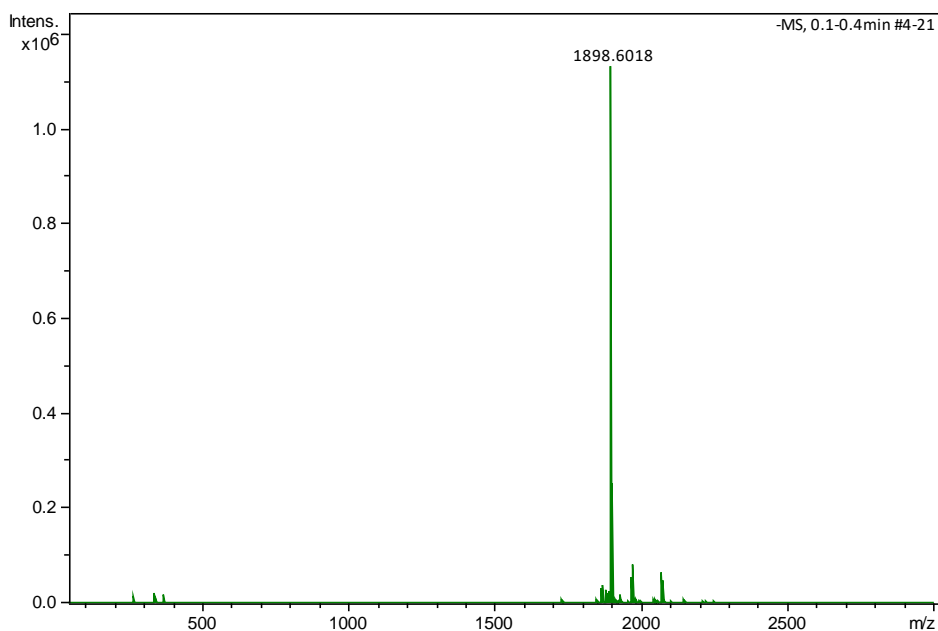


Figure 3.32. ESI-MS spectrum (full scan) for aqueous solutions of **Na-Pt₂Au₃** in the negative-ion mode (identical result for **K-Pt₂Au₃**).

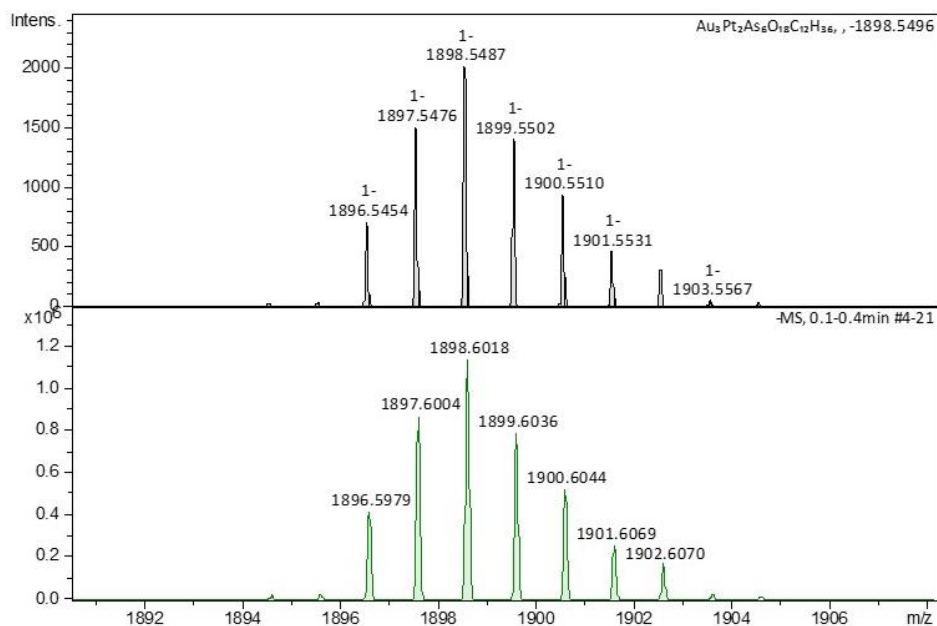


Figure 3.33. Simulated ESI-MS spectrum of $\text{Na-Pt}_2\text{Au}_3$ and $\text{K-Pt}_2\text{Au}_3$ in negative-ion mode (top) and experimental ESI-MS spectrum (bottom) of the singly-charged polyanion Pt_2Au_3 (expanded view).

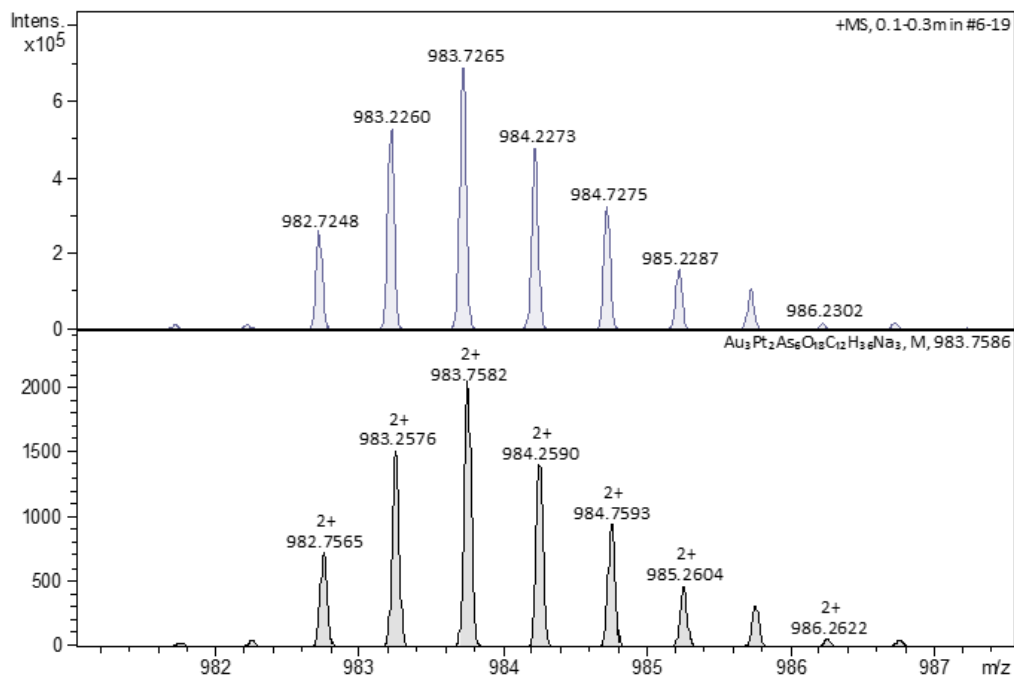


Figure 3.34. Simulated ESI-MS spectrum of $\text{Na-Pt}_2\text{Au}_3$ in positive-ion mode (bottom) and experimental ESI-MS spectrum (top) of the doubly-charged $[\text{Na}_3\text{Pt}_2\text{Au}_3\text{O}_6(\text{AsO}_2(\text{CH}_3)_2)_6]^{2+}$ ion (expanded view).

Table 3.10. Peak assignments of the ESI-MS spectra of **Na-Pt₂Au₃** and **K-Pt₂Au₃**.

Na[Pt ₂ Au ₃ O ₆ (AsO ₂ (CH ₃) ₂) ₆]·NaCl·NaNO ₃ ·6H ₂ O (Na-Pt₂Au₃)		
Formula	Target Mass (amu)	Measured Mass (amu)
[Pt ₂ Au ₃ O ₆ (AsO ₂ (CH ₃) ₂) ₆] ⁻	1898.9887	1898.7804
[Na ₂ Pt ₂ Au ₃ O ₆ (AsO ₂ (CH ₃) ₂) ₆] ⁺	1944.9682	1944.4715
[Na ₃ Pt ₂ Au ₃ O ₆ (AsO ₂ (CH ₃) ₂) ₆] ²⁺	983.979	983.7274
K[Pt ₂ Au ₃ O ₆ (AsO ₂ (CH ₃) ₂) ₆]·KCl·KAsO ₂ (CH ₃) ₂ ·18H ₂ O (K-Pt₂Au₃)		
Formula	Target Mass (amu)	Measured Mass (amu)
[Pt ₂ Au ₃ O ₆ (AsO ₂ (CH ₃) ₂) ₆] ⁻	1898.9887	1898.8694
[K ₂ Pt ₂ Au ₃ O ₆ (AsO ₂ (CH ₃) ₂) ₆] ⁺	1977.1853	1976.4124
[K ₃ Pt ₂ Au ₃ O ₆ (AsO ₂ (CH ₃) ₂) ₆] ²⁺	1008.1418	1007.6855

3.2.4.4 Powder XRD Study

Single-crystal-to-single-crystal (SCSC) transformations constitute solid-state phase transitions induced by external stimulus, such as light, heat, guest, and mechanochemical forces.¹¹³ While SCSC transformations in metal-organic frameworks (MOFs) and coordination polymers (CPs) are well-documented, reports on SCSC transformations at the discrete clusters remain scarce. Such transformations in discrete clusters are challenging because they usually involve the breakage and formation of chemical bonds, as well as the rearrangement of structures in the solid state, which can destroy the crystalline state of the molecules. To our knowledge, only five other thermally induced processes have been described, involving high-, room- and low temperature polymorphic transitions¹¹⁴ or structural variations by dehydration.¹¹⁵

Na-Pt₂Au₃ undergoes a reversible single-crystal-to-single-crystal (SCSC) transformation in the solid state upon rehydration and dehydration, where rehydration was achieved by keeping the sample in an atmosphere of water vapor at room temperature and dehydration

was achieved by air drying for one day. The polyanion Pt_2Au_3 crystallizes in the centrosymmetric space group $P6_3/m$ when in the mother liquor ($\text{Na-Pt}_2\text{Au}_3(\text{a})$), but after air drying for one day, it transforms to the non-centrosymmetric space group $P\bar{6}$ ($\text{Na-Pt}_2\text{Au}_3$). The two crystal structures show the exact same polyanion as confirmed by single-crystal XRD, but the unit cell volume shrinks significantly from 2775.2(4) to 2130.9(12) \AA^3 upon air-drying for a day, and the packing arrangement is significantly different, because the layer sequence is AAA in $\text{Na-Pt}_2\text{Au}_3$ and ABA in $\text{Na-Pt}_2\text{Au}_3(\text{a})$ (Figure 3.35).

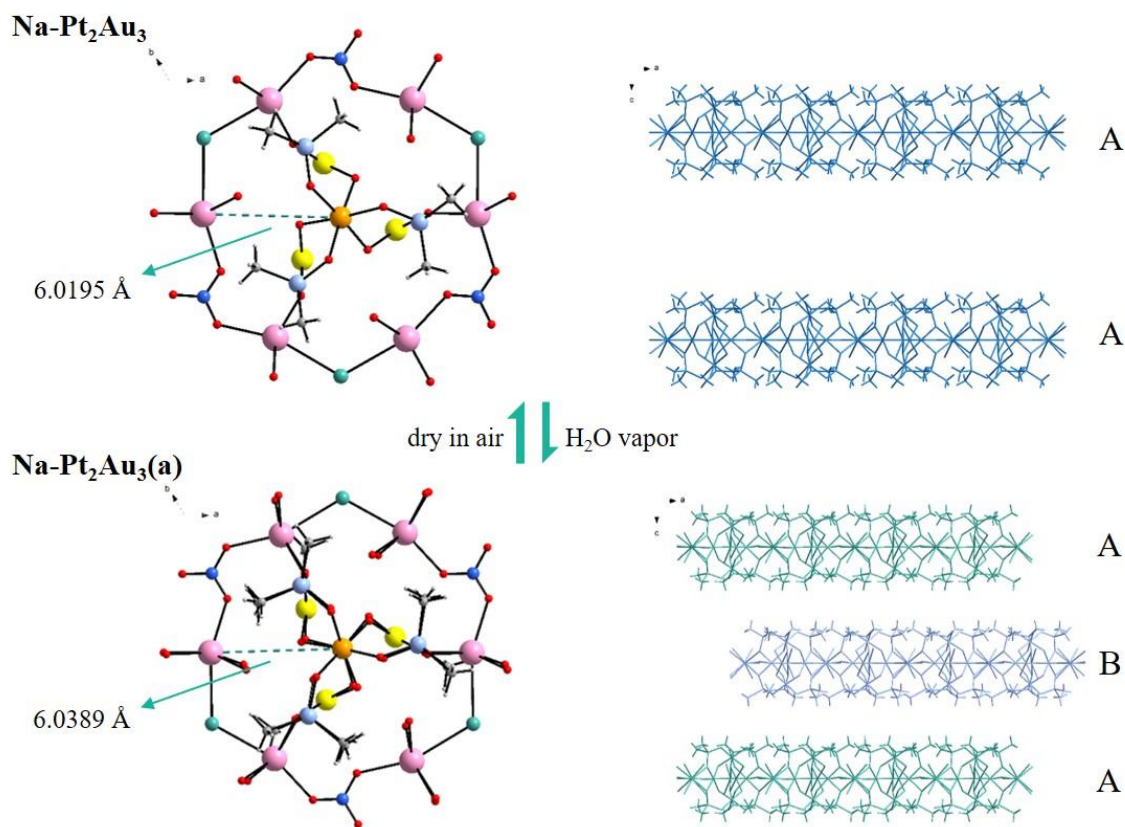


Figure 3.35. The fully reversible SCSC transition of $\text{Na-Pt}_2\text{Au}_3$ to $\text{Na-Pt}_2\text{Au}_3(\text{a})$. Left: ball-and-stick representation; right: packing diagrams for $\text{Na-Pt}_2\text{Au}_3$ (AA mode) and $\text{Na-Pt}_2\text{Au}_3(\text{a})$ (AB mode). Color code: Au yellow, Pt orange, O red, C grey, N blue, As light blue, Cl light green, Na pink, H light grey.

The structural transformation of $\text{Na-Pt}_2\text{Au}_3(\text{a})$ to $\text{Na-Pt}_2\text{Au}_3$ upon dehydration by air drying was also confirmed by powder-XRD (PXRD) measurements (Figure 3.36 and 3.37),

due to significantly different stacking of the 2D layers. A pure phase of **Na-Pt₂Au₃(a)** is obtained in the crystals in the mother liquor, but after drying in air for one day, a transformation to the new phase **Na-Pt₂Au₃** occurs. After 2 days, a completely pure phase of **Na-Pt₂Au₃** is observed. The transformation from **Na-Pt₂Au₃** to **Na-Pt₂Au₃(a)** is fully reversible during a rehydration and dehydration process. Rehydration of **Na-Pt₂Au₃** in the presence of water vapor at room temperature results in **Na-Pt₂Au₃(a)** within half an hour. The rehydration behavior of **Na-Pt₂Au₃** was also demonstrated by thermogravimetric analysis (TGA) and infrared spectroscopy (FT-IR) on **Na-Pt₂Au₃** (Figures 3.38 and 3.39).

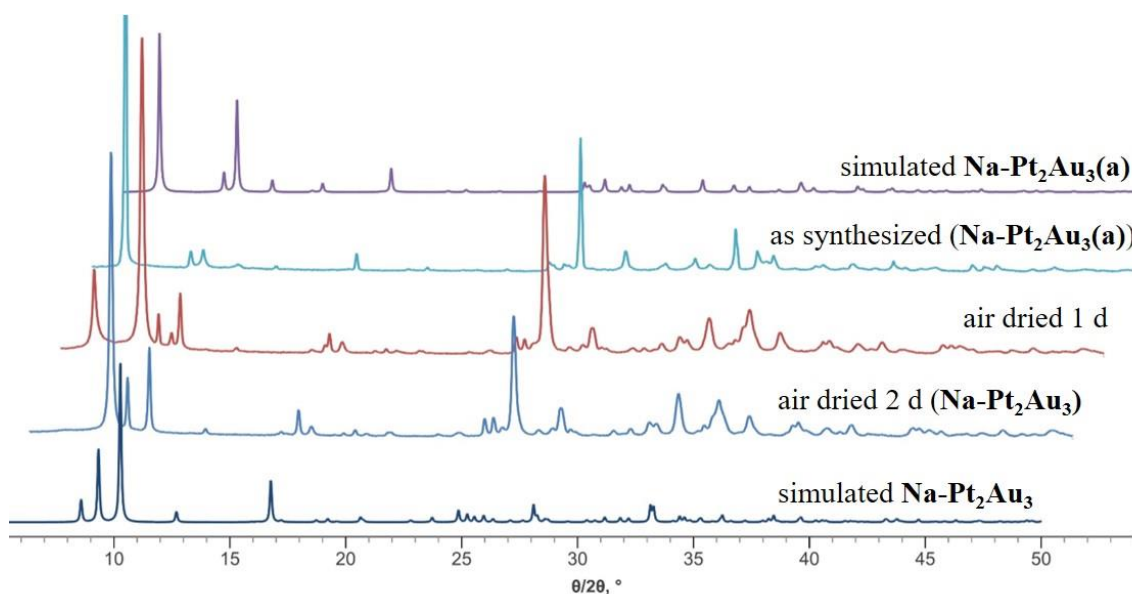


Figure 3.36. Experimental and simulated PXRD patterns of **Na-Pt₂Au₃(a)** and **Na-Pt₂Au₃** during a dehydration process by air drying (simulated diffraction patterns derived from single-crystal data).

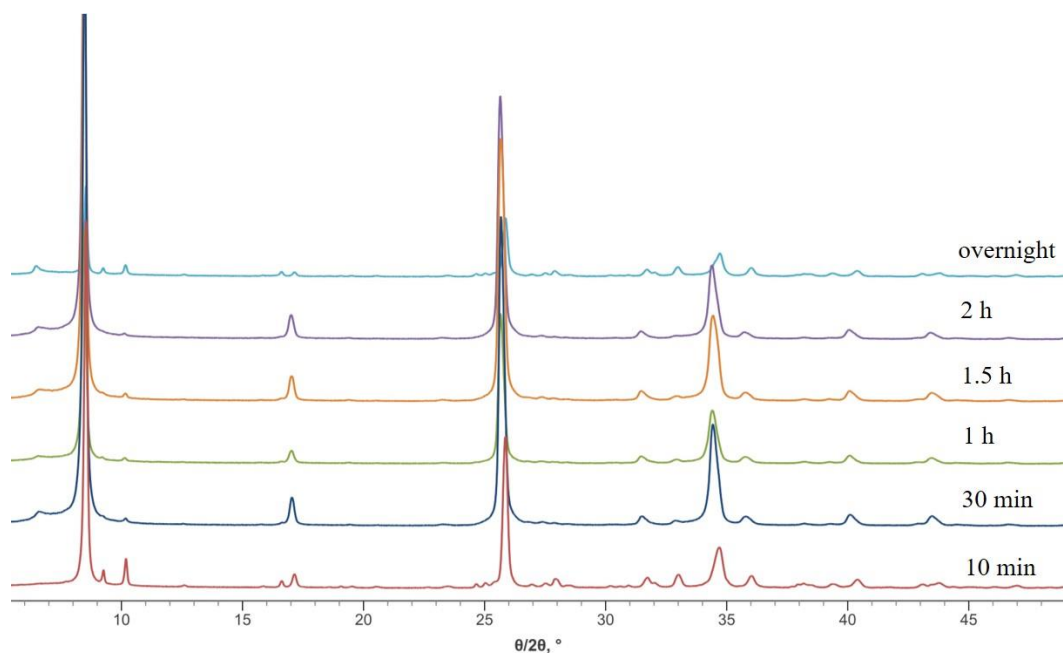


Figure 3.37. PXRD patterns for Na-Pt₂Au₃ in the presence of water vapor for different periods of time at RT.

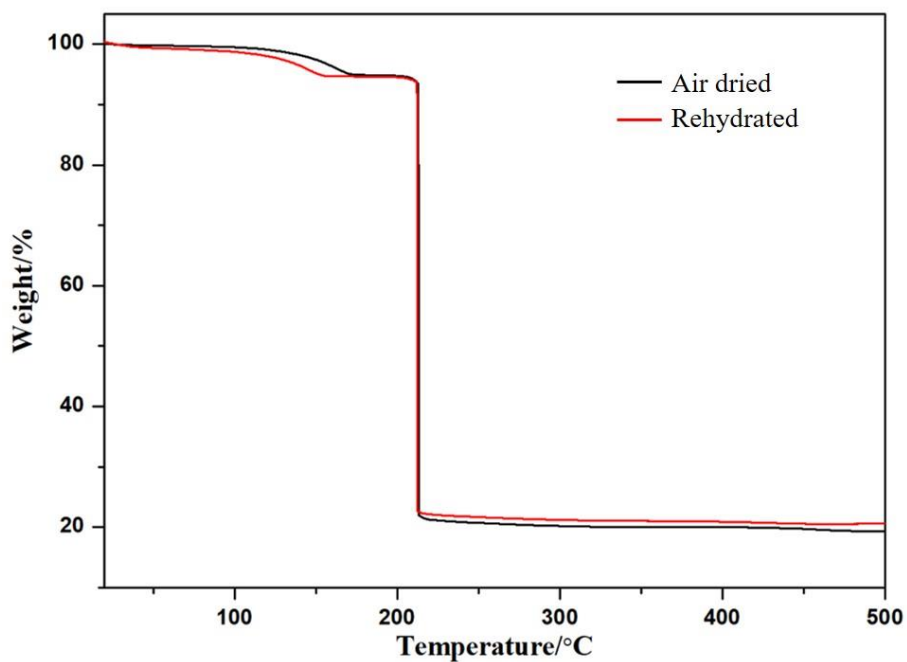


Figure 3.38. Thermograms of air-dried and partially rehydrated (several hours) Na-Pt₂Au₃ from room temperature to 500 °C under N₂ atmosphere. Complete rehydration of the bulk material Na-Pt₂Au₃ results in partial dissolution.

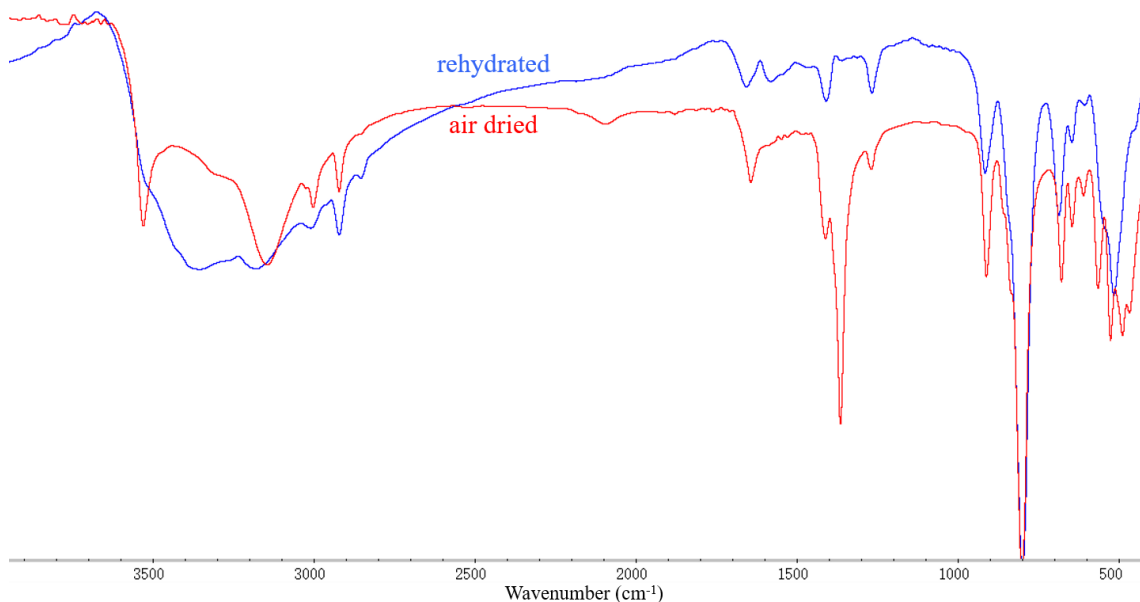


Figure 3.39. FT-IR spectra of air-dried and rehydrated **Na-Pt₂Au₃** from 400–4000 cm^{-1} on KBr pellets.

3.2.4.5 Light irradiation

We have also investigated the stability of solid **Na-Pt₂Au₃** under blue light ($\lambda = 450\text{-}480$ nm, blue LED lamp LED PAR30, E-27). The PXRD spectra revealed that the crystal structure maintains a high degree of crystallinity up to at least 4 h (Figure 3.40). Regarding solutions of **Na-Pt₂Au₃** in water upon irradiation with blue light, ^1H NMR revealed that the free cacodylate signal at 1.6 ppm gradually increased from the original 0% to 2, 3, 6, 14, 17 and 20% after 5, 15, 30, 60, 120 and 240 min, respectively (Figure 3.40). Without irradiation, ^1H NMR demonstrated that there is only a 2% decomposition of **Na-Pt₂Au₃** after 1 day (Figure 3.41).

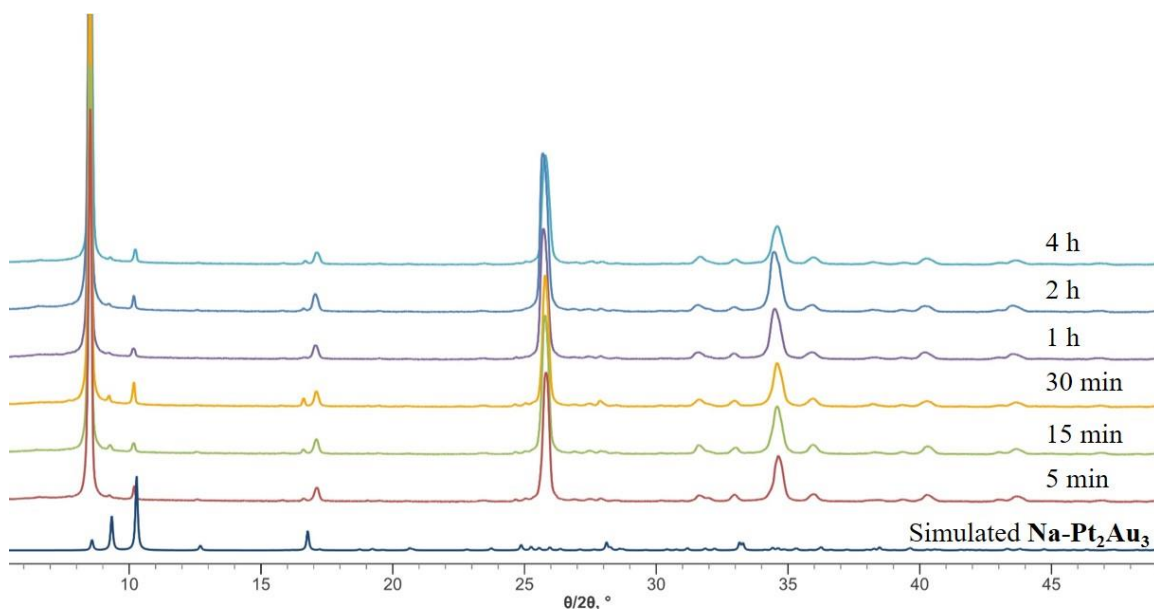


Figure 3.40. Time-dependent PXRD spectra of **Na-Pt₂Au₃** under blue light irradiation.

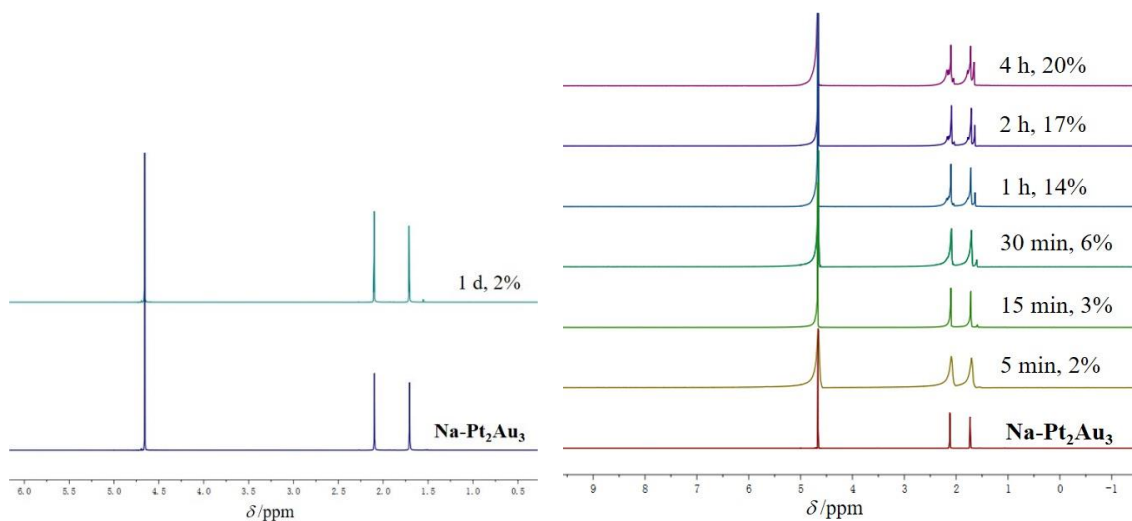


Figure 3.41. Time-dependent ^1H NMR spectra of **Na-Pt₂Au₃** without (left) and with (right) blue light irradiation.

3.2.5 Conclusions

We have synthesized and structurally characterized the first discrete mixed gold-platinum-oxoanion $[\text{Pt}^{\text{IV}}_2\text{Au}^{\text{III}}_3\text{O}_6((\text{CH}_3)_2\text{AsO}_2)_6]^-$ (**Pt₂Au₃**) by using simple one-pot open-beaker techniques. The ^{195}Pt NMR spectrum of redissolved solid 1 in water demonstrates solution stability, which provides much potential for further applications of **Pt₂Au₃** in catalysis and

biomedicine. The reversible single-crystal-to-single-crystal transformation of **Na-Pt₂Au₃(a)** to **Na-Pt₂Au₃** upon dehydration and rehydration is of particular interest, as concern solid state applications (sorption etc). The polyanion **Pt₂Au₃** merges the areas of polyoxoplatinate and polyoxoaurate chemistry and pushes the area of polyoxo-noble-metalate chemistry to a higher synthetic and analytical level. Further studies in this area are ongoing.

3.3 Sc(III) and Zn(II)-containing 16-palladium(II)-oxo cluster

3.3.1 Synthesis

4[Pd₁₆O₂₄(OH)₈((CH₃)₂As)₈]·NaSc((CH₃)₂As)₄(H₂O)₂·xH₂O (Sc-Pd₁₆)

Sc(NO₃)₃ (7 mg, 0.03 mmol) and Pd(NO₃)₃ (43 mg, 0.18 mmol) were dissolved in 4 mL aqueous sodium cacodylate buffer (0.5 M, adjust pH to 7 by adding 68% HNO₃), and stirred at RT for 1 day leading to deep-red solution. Slow evaporation of the filtrate at room temperature in an open vial resulted in dark red crystals after 45 days. But the yield is too low to collect sample for elemental analysis. FT-IR (KBr, cm⁻¹): 3414–3241 (s) [ν(O–H) of H₂O], 3003–2924 (w) [ν(C–H) of methyl groups of cacodylate], 1617 (m) [H₂O bending fundamental mode δ], 1408 (m) [δ(C–H) of the methyl groups of cacodylate], 1269 (w) [δ_{in-plane}(O–H)], 906 (w) [δ_{out-of-plane}(O–H)], 828–645 (s) [ν(Pd–O)], 503 (m) [ν(As–C)].

4[Pd₁₆O₂₄(OH)₈((CH₃)₂As)₈]·Na₂Zn((CH₃)₂As)₄·xH₂O (Zn-Pd₁₆)

The compound was prepared by exactly the same procedure as **Sc-Pd₁₆**, but with Zn(NO₃)₂ (6 mg, 0.03 mmol) instead of Sc(NO₃)₃. Dark dark red crystals were obtained. But the yield is too low to collect sample for elemental analysis. FT-IR (KBr pellet, cm⁻¹): 3500–3200 (s) [ν(O–H) of H₂O], 3001–2921 (w) [ν(C–H) of methyl groups of cacodylate], 1639 (m) [H₂O bending fundamental mode δ], 1408–1386 (m) [δ(C–H) of the methyl groups of cacodylate], 1265 (w) [δ_{in-plane}(O–H)], 903 (w) [δ_{out-of-plane}(O–H)], 829–647 (s) [ν(Pd–O)], 586–499 (m) [ν(As–C)].

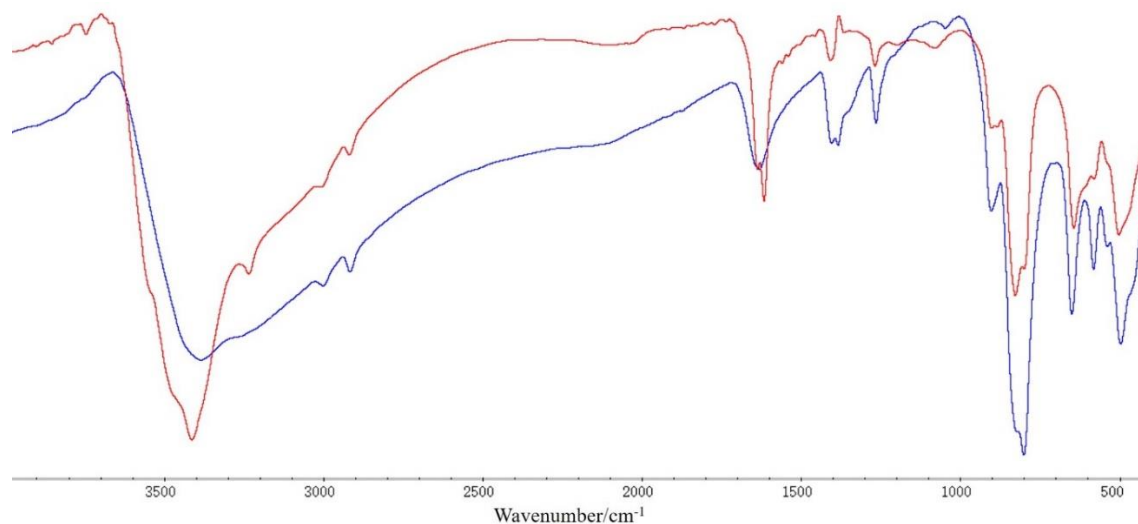


Figure 3.42. FT-IR spectra of **Sc-Pd₁₆** (red) and **Zn-Pd₁₆** (blue) from 400–4000 cm^{-1} on KBr pellets.

3.3.2 Single-Crystal XRD Data

Table 3.11. Crystal data and structure refinement for **Sc-Pd₁₆** and **Zn-Pd₁₆**.

Compound	Sc-Pd₁₆	Zn-Pd₁₆
empirical formula	$\text{Na}_{10}\text{Pd}_{64}\text{ScAs}_{36}\text{C}_{72}\text{H}_{216}\text{O}_{160}$	$\text{Na}_8\text{Pd}_{64}\text{ScAs}_{36}\text{C}_{72}\text{H}_{216}\text{O}_{160}$
fw, g mol^{-1}	13408.14	13398.44
crystal system	Tetragonal	Tetragonal
space group	$I4_1/a$	$I4_1/a$
a (Å)	39.276(3)	39.205(3)
b (Å)	39.276(3)	39.205(3)
c (Å)	22.279(2)	22.283(2)
α (°)	90	90
β (°)	90	90
γ (°)	90	90
V (Å ³)	34367(6)	34250(7)
Z	4	4
D_c (g cm^{-3})	2.598	2.598
abs coeff, mm^{-1}	6.795	6.866
θ range for data collection, deg	1.466 to 20.884	1.469 to 20.892

completeness to Θ_{\max}	99.7%	99.6%
index ranges	-39 \leq h \leq 39, -38 \leq k \leq 38, -23 \leq l \leq 23	-39 \leq h \leq 38, -39 \leq k \leq 39, -22 \leq l \leq 21
reflns collected	132540	153891
indep reflns	9060	9027
$R(\text{int})$	0.1347	0.1495
abs corrn	Semi-empirical from equivalents	Semi-empirical from equivalents
data/restraints/param	9060 / 7 / 780	9027 / 1 / 787
GOF on F^2	1.160	1.131
$R_1,^a wR_2^b$ [$I > 2\sigma(I)$]	0.0844, 0.2264	0.0903, 0.2394
$R_1,^a wR_2^b$ (all data)	0.1541, 0.3190	0.1512, 0.3232
Largest diff peak and hole, $e \text{ \AA}^{-3}$	3.927 and -2.997	4.743 and -3.728

$^a R_1 = \sum ||F_o| - |F_c|| / \sum |F_o|$. $^b wR_2 = [\sum w(F_o^2 - F_c^2)^2 / \sum w(F_o^2)]^{1/2}$.

3.3.3 Bond Valence Sum Calculations

In **Sc-Pd₁₆**, the BVS values for the independent Pd atom range from 2.039 to 2.345. And the values for the independent Pd atom In **Zn-Pd₁₆** range from 1.996 to 2.349. The BVS values for different types of bridging oxygens are presented in Table 3.12.

Table 3.12. BVS values for μ_2 - and μ_4 -bridging oxygen atoms in **Sc-Pd₁₆** and **Zn-Pd₁₆**.

Sc-Pd ₁₆					
μ_2 -O	Bond distance(Å)	BVS value	μ_2 -O	Bond distance(Å)	BVS value
O1	Pd9–O1 (2.0111)	1.081	O21	Pd9–O21 (2.0064)	1.092
	Pd13–O1 (2.0281)			Pd11–O21 (2.0250)	
O5	Pd10–O5 (2.0185)	1.068	O25	Pd13–O25 (2.0216)	1.074
	Pd12–O5 (2.0297)			Pd2–O25 (2.0228)	
O28	Pd16–O28 (2.0014)	1.124	O26	Pd15–O26 (1.9872)	1.104
	Pd12–O28 (2.0087)			Pd10–O26 (2.0379)	
O29	Pd11–O29 (2.0019)	1.072	O33	Pd15–O33 (2.0127)	1.084

	Pd3–O29 (2.0446)			Pd16–O33 (2.0281)	
μ_4-O	Bond distance(Å)	BVS value	μ_4-O	Bond distance(Å)	BVS value
O6	Pd14–O6 (2.0044)	2.192	O11	Pd1–O11 (1.9979)	2.154
	Pd5–O6 (2.0085)			Pd9–O11 (2.0172)	
	Pd11–O6 (2.0197)			Pd8–O11 (2.0320)	
	Pd15–O6 (2.0263)			Pd12–O11 (2.0377)	
O7	Pd4–O7 (2.0028)	2.180	O14	Pd5–O14 (1.9726)	2.163
	Pd8–O7 (2.0164)			Pd7–O14 (2.0109)	
	Pd13–O7 (2.0214)			Pd3–O14 (2.0392)	
	Pd12–O7 (2.0260)			Pd15–O14 (2.0566)	
O8	Pd1–O8 (1.9923)	2.179	O16	Pd4–O16 (1.9631)	2.269
	Pd2–O8 (2.0109)			Pd16–O16 (1.9912)	
	Pd10–O8 (2.0226)			Pd6–O16 (2.0278)	
	Pd9–O8 (2.0427)			Pd13–O16 (2.0288)	
O10	Pd2–O10 (1.9549)	2.232	O17	Pd6–O17 (1.9744)	2.192
	Pd14–O10 (1.9999)			Pd7–O17 (2.0171)	
	Pd11–O10 (2.0407)			Pd16–O17 (2.0276)	
	Pd10–O10 (2.0427)			Pd3–O17 (2.0424)	
Zn-Pd₁₆					
μ_2-O	Bond distance(Å)	BVS value	μ_2-O	Bond distance(Å)	BVS value
O2	Pd8–O2 (1.9819)	1.103	O11	Pd8–O11 (2.0130)	1.103
	Pd3–O2 (2.0281)			Pd11–O11 (2.0118)	
O3	Pd5–O3 (2.0151)	1.078	O25	Pd13–O25 (2.0216)	1.074
	Pd11–O3 (2.0226)			Pd2–O25 (2.0228)	
O4	Pd2–O4 (2.0036)	1.081	O26	Pd15–O26 (1.9872)	1.104
	Pd4–O4 (2.0366)			Pd10–O26 (2.0379)	
O5	Pd12–O5 (1.9971)	1.136	O33	Pd15–O33 (2.0127)	1.084
	Pd4–O5 (2.0055)			Pd16–O33 (2.0281)	
μ_4-O	Bond distance(Å)	BVS value	μ_4-O	Bond distance(Å)	BVS value

O12	Pd15–O12 (1.9559)	2.172	O23	Pd9–O23 (1.9911)	2.144
	Pd16–O12 (2.0147)			Pd2–O23 (2.0142)	
	Pd11–O12 (2.0451)			Pd1–O23 (2.0165)	
	Pd12–O12 (2.0657)			Pd5–O23 (2.0741)	
O18	Pd5–O18 (1.9936)	2.194	O24	Pd10–O24 (1.9666)	2.235
	Pd1–O18 (2.0006)			Pd6–O24 (1.9770)	
	Pd7–O18 (2.0296)			Pd4–O24 (2.0319)	
	Pd13–O18 (2.0350)			Pd3–O24 (2.0625)	
O19	Pd9–O19 (1.9650)	2.178	O27	Pd13–O27 (1.9679)	2.260
	Pd10–O19 (2.0313)			Pd11–O27 (1.9989)	
	Pd3–O19 (2.0330)			Pd15–O27 (2.0002)	
	Pd2–O19 (2.0435)			Pd7–O27 (2.0505)	
O22	Pd14–O22 (1.9906)	2.212	O28	Pd16–O28 (1.9950)	2.159
	Pd6–O22 (2.0062)			Pd14–O28 (1.9984)	
	Pd8–O22 (2.0163)			Pd12–O28 (2.0434)	
	Pd4–O22 (2.0331)			Pd8–O28 (2.0469)	

3.3.4 Results and Discussion

3.3.4.1 Solid-State Structure

Single-crystal X-ray analysis revealed that both **Sc-Pd₁₆** and **Zn-Pd₁₆** crystallize in the tetragonal space group $I4_1/a$ (Table 3.11), and their asymmetric units consist of 1/4 Sc^{III} and Zn^{II} ions, respectively, along with one **Pd₁₆** unit which was reported by Kortz group.^{27a} The **Pd₁₆** comprises 16 square-planar oxo-coordinated palladium-(II) ions, which can be subdivided in a central $[\text{Pd}_8\text{O}_8(\text{OH})_8]^{8-}$ square-antiprismatic unit, encircled by a cyclic $[\text{Pd}_8\text{O}_{16}((\text{CH}_3)_2\text{As})_8]^{8+}$ unit, resulting in the neutral, discrete metal oxo cluster **Pd₁₆** (Figure 3.42). The **Pd₁₆** has idealized D_{4d} point group symmetry with the C_4 principal rotation axis passing through the central $[\text{Pd}_8\text{O}_8(\text{OH})_8]^{8-}$ square-antiprismatic unit. Bond valence sum

(BVS) calculations on the μ_2 -OH groups yields values of 1.068–1.136 (Table 3.12), confirming that these oxygens are monoprotonated. Therefore, in the solid state, the molecular clusters are composed of four **Pd**₁₆ units, and one octahedral coordinated Sc^{III} ion with four cacodylate ligands and two water ligands and tetrahedral coordinated Zn^{II} ion with four cacodylate ligands, respectively, which are linked to each other through weak C–H···O hydrogen bonds (Figure 3.43).

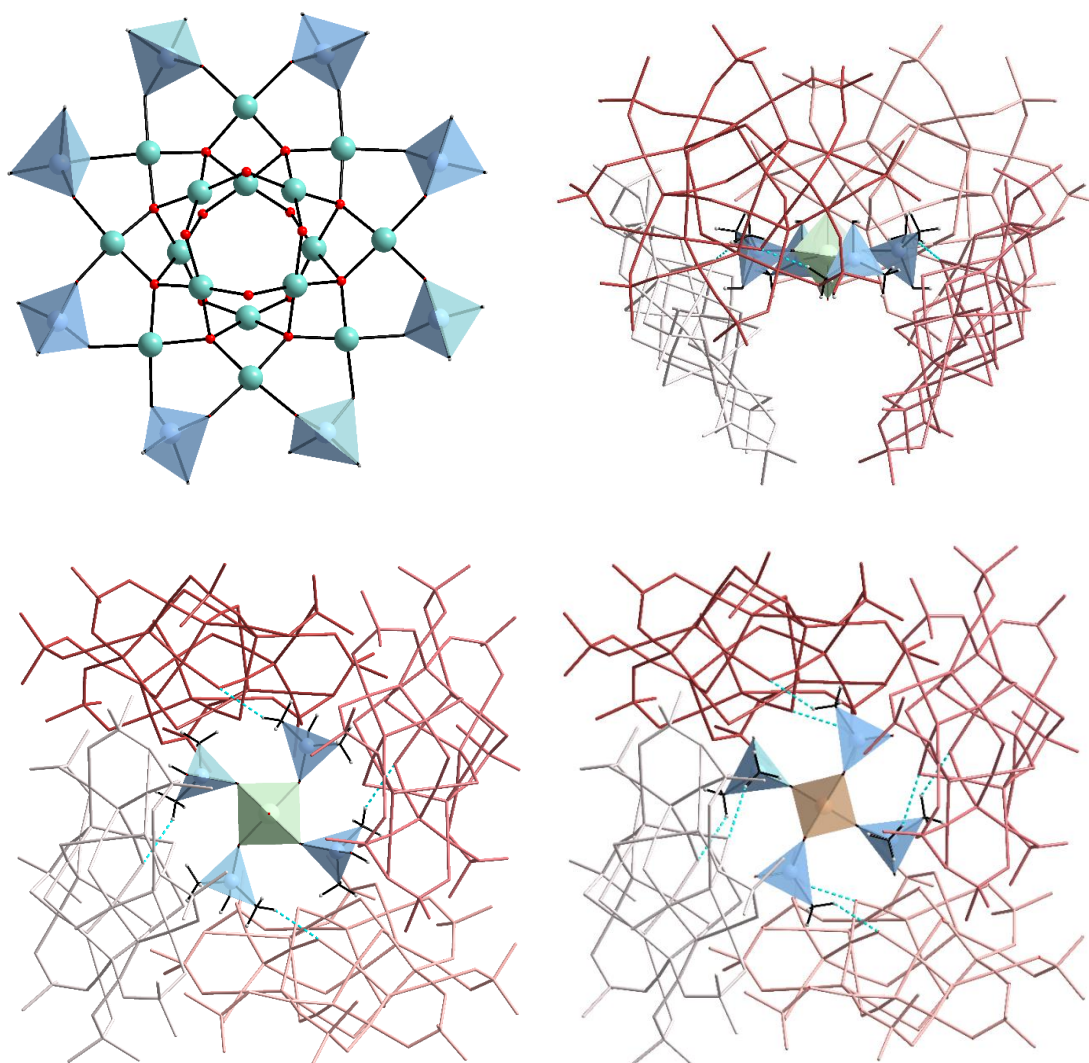


Figure 3.43. Structural representation of the disk-shaped **Pd**₁₆ (top left), view of H-bond interaction in **Sc-Pd**₁₆ (top right (along *b* axis) and bottom left (along *c* axis)) and **Zn-Pd**₁₆ (bottom right (along *c* axis)). Color code: Pd green, O (red), H grey, {(CH₃)₂AsO₂} blue tetrahedra, {ScO₆} green octahedra, {ZnO₄} orange tetrahedron.

3.3.5 Conclusions

Two $M \cdot (Pd_{16})_4$ type palladium oxo clusters incorporating 3d Sc^{III} and Zn^{II} as guest metal M have been prepared. Further structural characterization needs to be studied. Without forming internal coordination mode via metal–oxo interactions, such results confirm that, the guest metal ions can be introduced via host-guest interaction.

Chapter IV Platinum(II/III) Isopolytungstates

The coordination chemistry of platinum has a long history and can be regarded as classics, but surprisingly little is known about coordination of Pt(IV) or Pt(II) to polyoxometalates (POM). Moreover, some reports on supposedly Pt-coordinated POM remain controversial.¹¹⁶ Hence the preparation and reliable characterization of Pt-containing POM (this is also more or less true for other noble metals) still remains a considerable challenge. To further extend the research of this area, in this chapter, three new platinum(II/III) isopolytungstate, $[\text{Pt}_3\text{W}_{11}\text{O}_{41}]^{10-}$ (**Pt₃W₁₁**), $[\text{Pt}^{\text{II}}_2\text{W}_5\text{O}_{18}((\text{CH}_3)_2\text{AsO}_2)_2]^{4-}$ (**Pt^{II}₂W₅**), $[\text{Pt}^{\text{III}}_2\text{W}_5\text{O}_{18}((\text{CH}_3)_2\text{AsO}_2)_4]^{4-}$ (**Pt^{III}₂W₅**), and one dimeric Pt(III) compound $\{[\text{Pt}^{\text{III}}_2((\text{CH}_3)_2\text{AsO}_2)_5]^+\}_n$ (**Pt₂**) are presented. The hydrated salts of all three compounds were characterized in the solid state by single-crystal XRD, FT-IR spectroscopy, elemental and thermogravimetric analyses. Their aqueous solution behaviors of **Pt^{II}₂W₅** were studied by multinuclear (¹H, ¹³C and ¹⁹⁵Pt) NMR.

4.1 Synthesis

K₃Na₇[Pt₃W₁₁O₄₁]·16H₂O (KNa-Pt₃W₁₁) and **Na₂K₂[Pt^{II}₂W₅O₁₈((CH₃)₂AsO₂)₂]·9H₂O (KNa-Pt^{II}₂W₅)**

K₂PtCl₄ (41.5 mg, 0.1 mmol) and Na₂WO₄ (33.0 mg, 0.1 mmol) were added in aqueous sodium cacodylate buffer (2 mL, 0.5 M, adjust pH to 7 by adding 68% HNO₃), then stirred for 20 min at 80 °C. The initial orange-red solution colour first becomes light brown and then changes to deeper brown. Colorless and grey greenish crystals which is paratungstate came out overnight, then filtrated after 2 days. After several days, dark red block crystals

(**KNa-Pt₃W₁₁**, yield: 2% (based on Pt)) and grey-greenish crystals were obtained. Then decant the supernatant and the crystals were washed with 2 M sodium cacodylate buffer and finally with 96% ethanol. Since the crops of **KNa-Pt₃W₁₁** crystals practically always contained crystalline grey-greenish crystals, we can mechanically separate them under a microscope (relatively easy because of the different color). Anal. Calcd (%) for **KNa-Pt₃W₁₁**: Pt 15.28, W 52.80, K 3.06, Na 4.2. Found: Pt 16.30, W 50.60, K 3.07, Na 3.79. FT-IR (KBr/cm⁻¹): 3600–3200(s) [ν(O–H) of structural H₂O], 1622 (m) [δ(O–H) of H₂O], 1380 (w) [δ_{in-plane}(O–H)], 933 (m) [ν(W–O (terminal))], 890–768 (m) [ν(W–O (bridging))], 713 (m) [ν(Pt–O)], 497 (w) [ν(Pt–O)]. Later, slow evaporation of the supernatants leads to formation of red rod crystals **KNa-Pt^{II}W₅**, within 2 d, which were collected by filtration (**Method 1**). yield: 14% (based on Pt). Anal. Calcd (%) for **KNa-Pt^{II}W₅**: Pt 18.08, W 42.60, As 6.94, K 3.62, Na 2.13, C 2.23, H 1.40. Found: Pt 19.00, W 42.40, As 7.62, K 3.56, Na 2.46, C 2.77, H 1.39. FT-IR (KBr/cm⁻¹): 3600–3200(s) [ν(O–H) of structural H₂O], 3026–2853 (w) [ν(C–H) of methyl groups of cacodylate], 1629 (m) [δ(O–H) of H₂O], 1384 (s) [δ(C–H) methyl groups of cacodylate], 1271 (w) [δ_{in-plane}(O–H)], 925 (m) [ν(W–O (terminal))], 863 (m) [ν(W–O (bridging))], 802 (s) [ν(As–O–Pt)], 700–514 (s) [ν(Pt–O)], 406 (m) [ν(As–C)].

Method 2 for **KNa-Pt^{II}W₅**: K₂PtCl₄ (16.6 mg, 0.04 mmol) and Na₂WO₄ (33.0 mg, 0.1 mmol) were added in aqueous sodium cacodylate buffer (2 mL, 1 M, adjust pH to 7 by adding 68% HNO₃), then stirred for 20 h at RT, then stirred for another 30 min at 80 °C. slow evaporation of the orange solution leads to formation of colorless block and orange rod crystals within 2 weeks. Red-orange crystals were collected by filtration. Yield: 10%

(based on Pt). This material is identical to that produced by **Method 1** as based on FT-IR and single crystal XRD.

Na₂K₂[Pt^{III}₂W₅O₁₈((CH₃)₂AsO₂)₄·xH₂O (KNa-Pt^{III}₂W₅)

KNa-Pt^{III}₂W₅ (30 mg, 0.01 mmol) were added in aqueous sodium cacodylate buffer (1.5 mL, 0.5 M, adjust pH to 7 by adding 68% HNO₃), then stirred at 80 °C for 20 min. Slow evaporation of the orange solution leads to formation of orange rod (**KNa-Pt^{II}₂W₅**) and red cube crystals (**KNa-Pt^{III}₂W₅**) within one week. The yield of **KNa-Pt^{III}₂W₅** is very low, thus we can't collect the sample for elemental analysis. FT-IR (KBr/cm⁻¹): 3600–3200(s) [ν(O–H) of structural H₂O], 3026–2936 (w) [ν(C–H) of methyl groups of cacodylate], 1629 (m) [δ(O–H) of H₂O], 1405 (s) [δ(C–H) methyl groups of cacodylate], 1274 (w) [δ_{in-plane}(O–H)], 964–935 (m) [ν(W–O (terminal))], 862 (m) [ν(W–O (bridging))], 802 (s) [ν(As–O–Pt)], 700–514 (s) [ν(Pt–O)], 400 (m) [ν(As–C)].

4[Pt^{III}₂((CH₃)₂AsO₂)₅]·2[PtCl₄]·Na₂[PtCl₄]·xH₂O (Pt₂)

K₂PtCl₄ (75 mg, 0.18 mmol) and Mn(OAc)₃ (9 mg, 0.03 mmol) were added in aqueous sodium cacodylate buffer (2 mL, 1 M, adjust pH to 7 by adding 68% HNO₃), then stirred for 3 h at 80 °C. Slow evaporation of the red solution leads to formation of red rod crystals (**Pt**) within 2 months. The yield of **Pt₂** is very low, thus we can't collect the sample for elemental analysis. FT-IR (KBr/cm⁻¹): 3500–3200(s) [ν(O–H) of structural H₂O], 3000–2900 (w) [ν(C–H) of methyl groups of cacodylate], 1624 (m) [δ(O–H) of H₂O], 1405 (s) [δ(C–H) methyl groups of cacodylate], 1286 (w) [δ_{in-plane}(O–H)], 806 (s) [ν(As–O–Pt)], 701–519 (s) [ν(Pt–O)], 427 (m) [ν(As–C)].

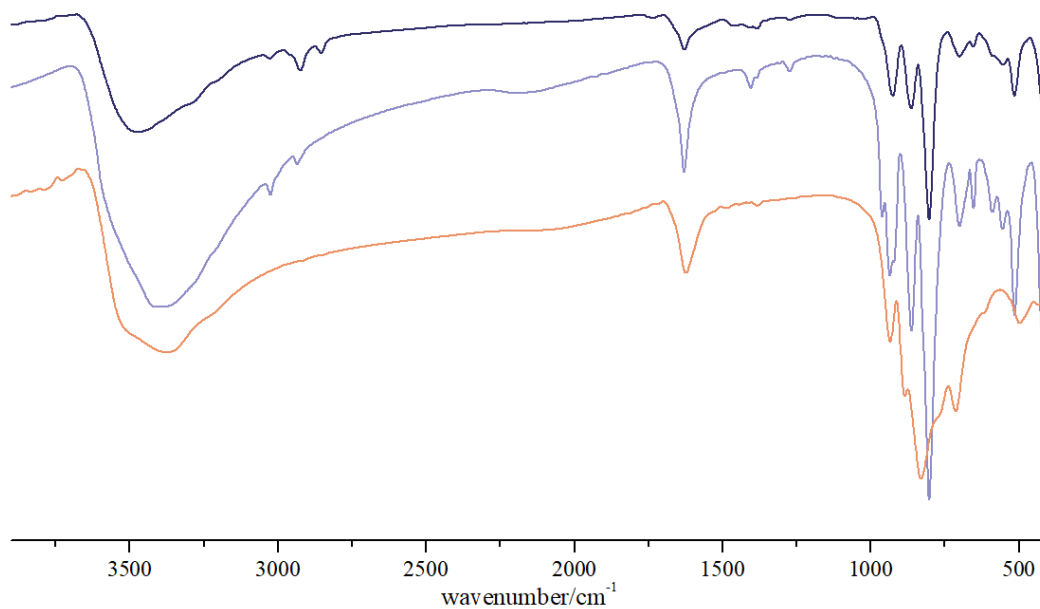


Figure 4.1. FT-IR spectra of **KNa-Pt₃W₁₁** (orange), **KNa-Pt^{II}₂W₅** (blue) and **KNa-Pt^{III}₂W₅** (purple).

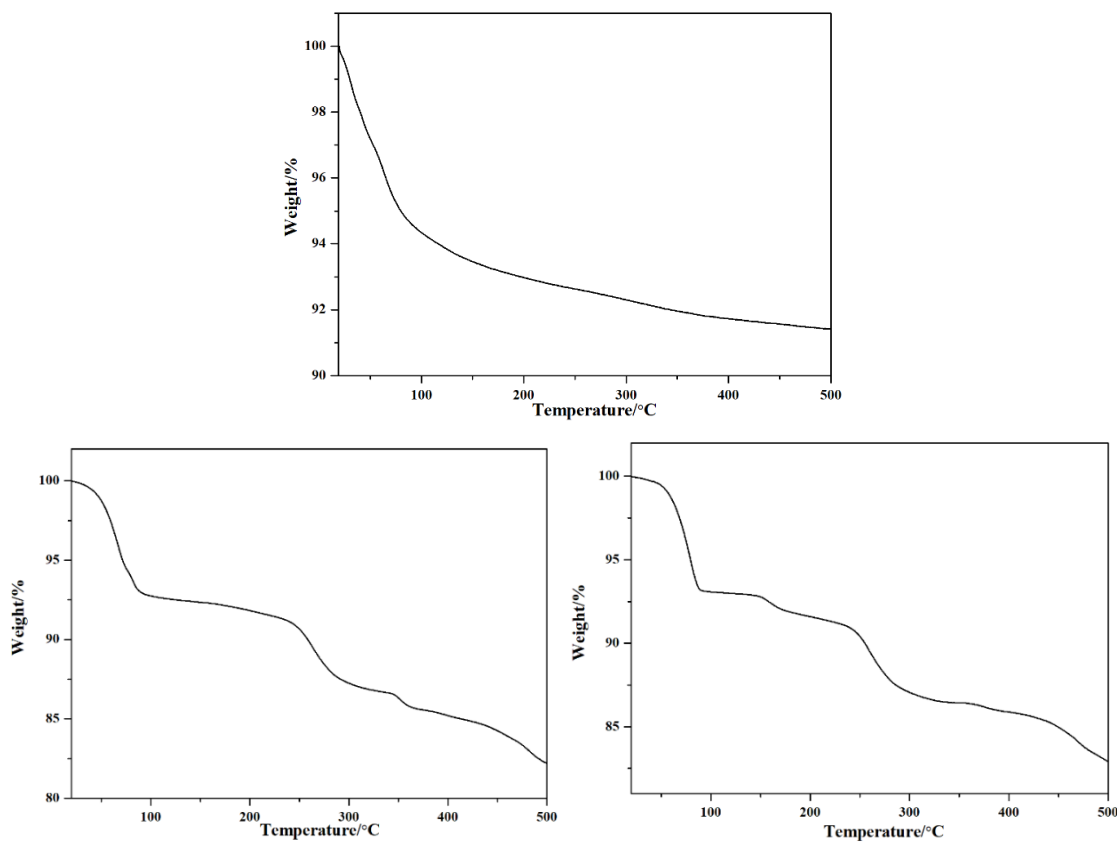


Figure 4.2. Thermograms of **KNa-Pt₃W₁₁** (top), **KNa-Pt^{II}₂W₅** (bottom left) and **KNa-Pt^{III}₂W₅** (bottom right) from room temperature to 500 °C under N₂ atmosphere.

4.2 Single-Crystal XRD Data

Table 4.1. Crystal data and structure refinement for **KNa-Pt₃W₁₁**, **KNa-Pt^{II}₂W₅**, **KNa-Pt^{III}₂W₅** and **Pt₂**.

Compound	KNa-Pt₃W₁₁	KNa-Pt^{II}₂W₅	KNa-Pt^{III}₂W₅	Pt₂
empirical formula	K ₃ Na ₇ Pt ₃ W ₁₀ O ₁₆ H ₃₂ ^a	K ₂ Na ₂ Pt ₂ W ₅ As ₂ O ₃₁ C ₄ H ₃₀ ^a	K ₂ Na ₂ Pt ₂ W ₅ As ₄ O ₃ 7C ₈ H ₂₄	Na ₂ Pt ₁₁ As ₂₀ Cl ₁₂ O ₄₂ C ₄₀ H ₁₂₀
fw, g mol ⁻¹	3829.92 ^a	2157.64 ^a	2445.56	5389.12
crystal system	Triclinic	Monoclinic	Monoclinic	Monoclinic
space group	P $\bar{1}$	P2/n	C2/c	P2 ₁ /n
<i>a</i> (Å)	12.6266(3)	16.9228(3)	17.2840(3)	20.9500(11)
<i>b</i> (Å)	13.6378(4)	11.8389(2)	11.6921(2)	11.0222(5)
<i>c</i> (Å)	17.5633(4)	17.8814(3)	22.3889(4)	32.2968(13)
α (°)	82.104(2)	90	90	90
β (°)	82.452(2)	93.2993(17)	93.0538(14)	102.515(3)
γ (°)	64.519(3)	90	90	90
<i>V</i> (Å ³)	2695.47(13)	3576.56(12)	4518.08(13)	7280.6(6)
<i>Z</i>	1	4	4	2
<i>D_c</i> (g cm ⁻³)	4.459	4.003	3.595	2.458
abs coeff, mm ⁻¹	31.401	25.999	22.056	15.314
F(000)	3102	3776	4344	4880
θ range for data collection, deg	2.349 to 25.026	2.411 to 25.025	2.318 to 31.677	1.292 to 26.400
completeness to Θ_{\max}	99.9 %	99.9 %	99.9 %	99.9 %
index ranges	-15 ≤ <i>h</i> ≤ 15, -16 ≤ <i>k</i> ≤ 16, -20 ≤ <i>l</i> ≤ 20	-19 ≤ <i>h</i> ≤ 20, -14 ≤ <i>k</i> ≤ 14, -21 ≤ <i>l</i> ≤ 21	-24 ≤ <i>h</i> ≤ 24, -16 ≤ <i>k</i> ≤ 16, -32 ≤ <i>l</i> ≤ 33	-26 ≤ <i>h</i> ≤ 21, -13 ≤ <i>k</i> ≤ 12, -40 ≤ <i>l</i> ≤ 37
reflns collected	31292	25593	57273	61624
indep reflns	9501	6320	6818	14874
<i>R</i> (int)	0.0616	0.0463	0.0406	0.1130
abs corrn	Semi-empirical from equivalents	Semi-empirical from equivalents	Semi-empirical from equivalents	Semi-empirical from equivalents

data/restraints/param	9501 / 30 / 658	6320 / 0 / 443	6818 / 6 / 281	14874 / 36 / 604
GOF on F^2	1.039	1.064	1.099	1.030
$R_1, {}^b wR_2^c$ [$I > 2\sigma(I)$]	0.0487, 0.1304	0.0300, 0.0726	0.0295, 0.0630	0.0665, 0.1658
$R_1, {}^b wR_2^c$ (all data)	0.0595, 0.1384	0.0336, 0.0739	0.0361, 0.0651	0.1031, 0.1827
Largest diff peak and hole, $e \text{ \AA}^{-3}$	4.389 and -3.800	1.922 and -2.000	7.618 and -2.147	6.813 and -3.797

^aThe entries are the actual formula units and weights as obtained from elemental analysis.

^b $R_1 = \sum ||F_o| - |F_c|| / \sum |F_o|$. ^c $wR_2 = [\sum w(F_o^2 - F_c^2)^2 / \sum w(F_o^2)^2]^{1/2}$.

4.3 Bond Valence Sum Calculations

The BVS values for the W atoms range from 5.749 to 6.236. In **KNa-Pt^{II}₂W₅**, the BVS values for two Pt atoms are 2.080 and 2.073, respectively. In **KNa-Pt^{III}₂W₅**, the BVS values for Pt atom is 3.292. In **Pt₂**, the BVS values for Pt atoms range from 3.098 to 3.211.

4.4 Results and Discussion

4.4.1 Solid-State Structure

A new tri-Pt(II)-containing isopolyoxotungstate $[\text{Pt}_3\text{W}_{11}\text{O}_{41}]^{10-}$ (**Pt₃W₁₁**) was synthesized by reaction of K_2PtCl_4 with $\text{Na}_2\text{WO}_4 \cdot 2\text{H}_2\text{O}$ in aqueous medium with rapid colour change overnight (the initial orange-red solution colour first changes to brown and then becomes deeper). Slow evaporation of the solution leads to formation of gray-greenish and dark red blocky crystals (Figure 4.3), which were separated by fractional crystallization. The hydrated salts of **Pt₃W₁₁** was isolated as a mixed potassium-sodium salt, $\text{K}_3\text{Na}_7[\text{Pt}_3\text{W}_{11}\text{O}_{41}] \cdot 16\text{H}_2\text{O}$ (**KNa-Pt₃W₁₁**). After collecting the **Na-Pt₃W₁₁** crystals, a new di-Pt(II)-containing isopolyoxotungstate $[\text{Pt}^{\text{II}}_2\text{W}_5\text{O}_{18}((\text{CH}_3)_2\text{AsO}_2)_2]^{4-}$ (**Pt^{II}₂W₅**) was obtained from the filtration, forming red rod-like crystals. The hydrated salts of **Pt^{II}₂W₅**

was isolated as a mixed potassium-sodium salt, $\text{K}_2\text{Na}_2[\text{Pt}^{\text{II}}_2\text{W}_5\text{O}_{18}((\text{CH}_3)_2\text{AsO}_2)_2] \cdot 9\text{H}_2\text{O}$ ($\text{KNa-Pt}^{\text{II}}\text{W}_5$). Then another di-Pt(III)-containing isopolyoxotungstate $[\text{Pt}^{\text{III}}_2\text{W}_5\text{O}_{18}((\text{CH}_3)_2\text{AsO}_2)_4]^{4-}$ ($\text{Pt}^{\text{III}}_2\text{W}_5$) was synthesized by reaction of $\text{KNa-Pt}^{\text{II}}\text{W}_5$ with $\text{Na}(\text{CH}_3)_2\text{AsO}_2$ in aqueous medium, forming red cuboid crystals. The hydrated salts of $\text{Pt}^{\text{III}}_2\text{W}_5$ was isolated as a mixed potassium-sodium salt, $\text{K}_2\text{Na}_2[\text{Pt}^{\text{III}}_2\text{W}_5\text{O}_{18}((\text{CH}_3)_2\text{AsO}_2)_4] \cdot x\text{H}_2\text{O}$ ($\text{KNa-Pt}^{\text{III}}_2\text{W}_5$). The symmetry units of solid-state interaction of polyanion with Na^+ and K^+ counter cations are shown in Figure 4.4 and 4.5.

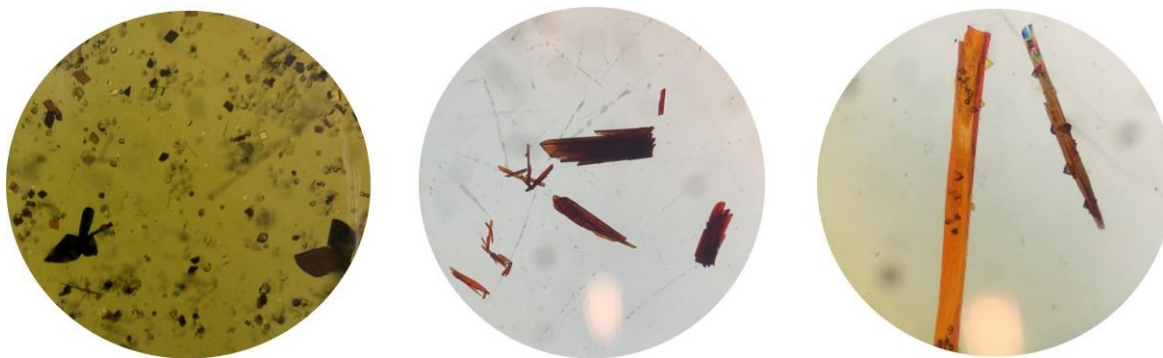


Figure 4.3. Crystal shape of $\text{KNa-Pt}_3\text{W}_{11}$, $\text{KNa-Pt}^{\text{II}}_2\text{W}_5$ and $\text{KNa-Pt}^{\text{III}}_2\text{W}_5$ (small cube crystals) from left to right.

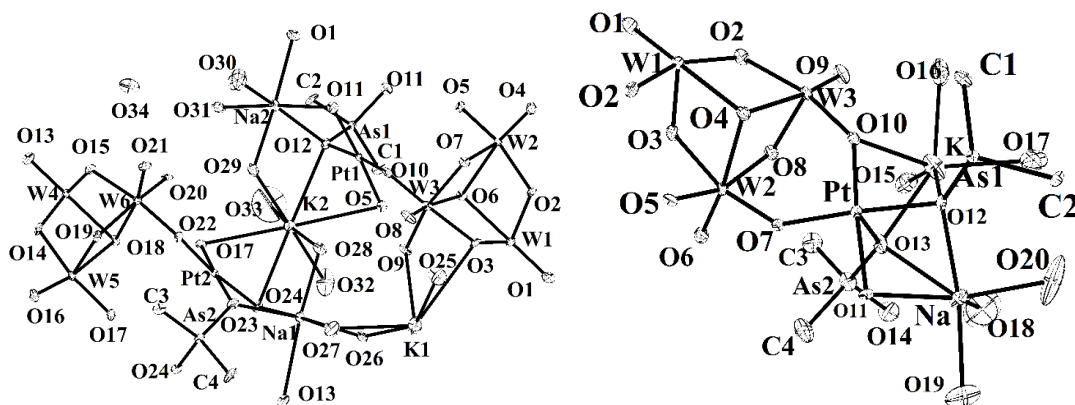


Figure 4.4. The symmetry unit of solid-state interaction of polyanion with Na^+ and K^+ counter cations in $\text{KNa-Pt}^{\text{II}}_2\text{W}_5$ (top) and $\text{KNa-Pt}^{\text{III}}_2\text{W}_5$ (bottom). (50% probability ellipsoids).

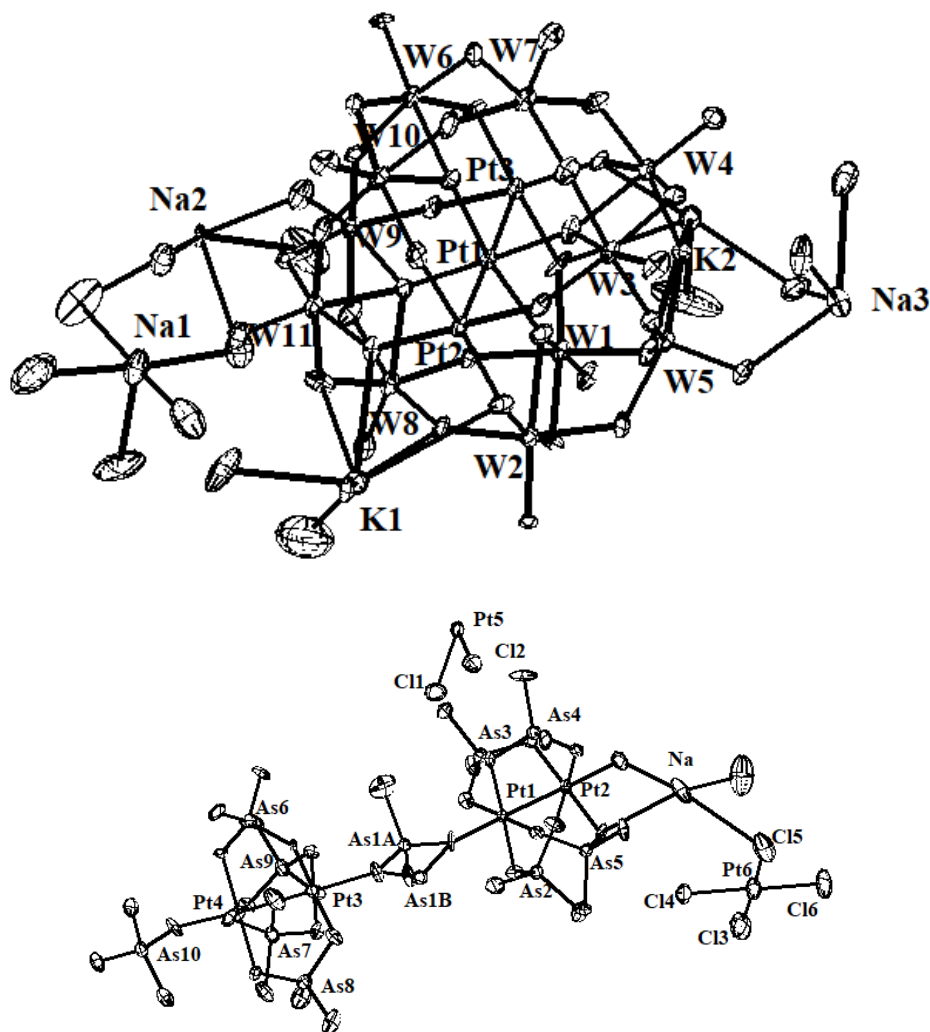


Figure 4.5. The symmetry unit of solid-state interaction of polyanion with Na^+ and K^+ counter cations in $\text{KNa-Pt}_3\text{W}_{11}$ (top), Na^+ and Cl^- counter ions in Pt_2 (bottom). (50% probability ellipsoids).

The cluster Pt_3W_{11} crystallized in the triclinic lattice with space group $P\bar{1}$. This is a unique complex, first of this type in the chemistry of polyoxotungstates. The $[\text{Pt}_3\text{W}_{11}\text{O}_{41}]^{10-}$ polyanion encapsulated by metal-oxo $\{\text{W}_{11}\text{O}_{41}\}$ ring constructed by one corner-sharing W_3O_{13} groups, two corner-sharing WO_5 groups and three corner-sharing W_2O_{10} groups (Figure 4.6). Three W_2O_{10} groups and two $\{\text{WO}_5\}$ square-pyramids are alternating. A linear $\{\text{Pt}_3\text{O}_{12}\}$ triad is located on the central axis of the $\{\text{W}_{11}\text{O}_{41}\}$ ring, indicating that the

$\{\text{Pt}_3\text{O}_{12}\}$ unit may induce an inter templating effect, resulting in an assembly with C_s symmetry, is also believed to be a driving force for the formation of square-pyramidal $\{\text{WO}_5\}$ moiety. The W_3O_{13} group consists of three edge-sharing WO_6 octahedra. The central Pt atom is coordinated by four oxygen atoms from three $\{\text{W}_3\text{O}\}$ and one $\{\text{W}_2\text{O}\}$ corners. The other two Pt atoms are each coordinated by four oxygen atoms from three $\{\text{W}_3\text{O}\}$ and one $\{\text{W}_2\text{O}\}$ terminals. The Pt–Pt bonds in Pt_3W_{11} are contracted to some 2.636(2) and 2.674(4) Å, suggesting metal–metal bonding interactions between the three Pt atoms.¹¹⁷ The Pt···O distances between $[\text{Pt}_3\text{W}_{11}\text{O}_{41}]^{10-}$ polyanions are 2.368(1) and 2.630(1) Å, which are shortest distances of the fifth position found by now. In the solid state, the $\{\text{Pt}_3\text{W}_{11}\text{O}_{41}\}$ units bridge each other via two pairs of weak Pt–O bonds consistent with [4+1] coordination geometry forming a zig-zag chain (Figure 4.7).

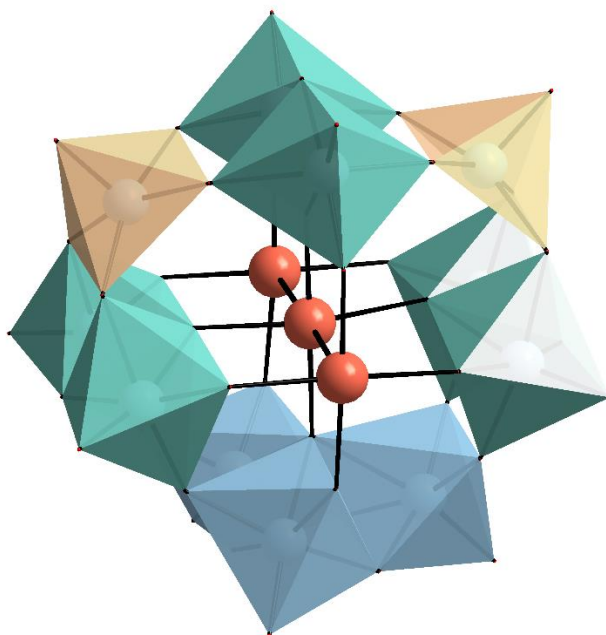


Figure 4.6. Combined polyhedral/ball-and-stick representation of $[\text{Pt}_3\text{W}_{11}\text{O}_{41}]^{10-}$ polyanion. Pt red, $\{\text{WO}_6\}$ blue and green octahedra, $\{\text{WO}_5\}$ orange square-pyramids.

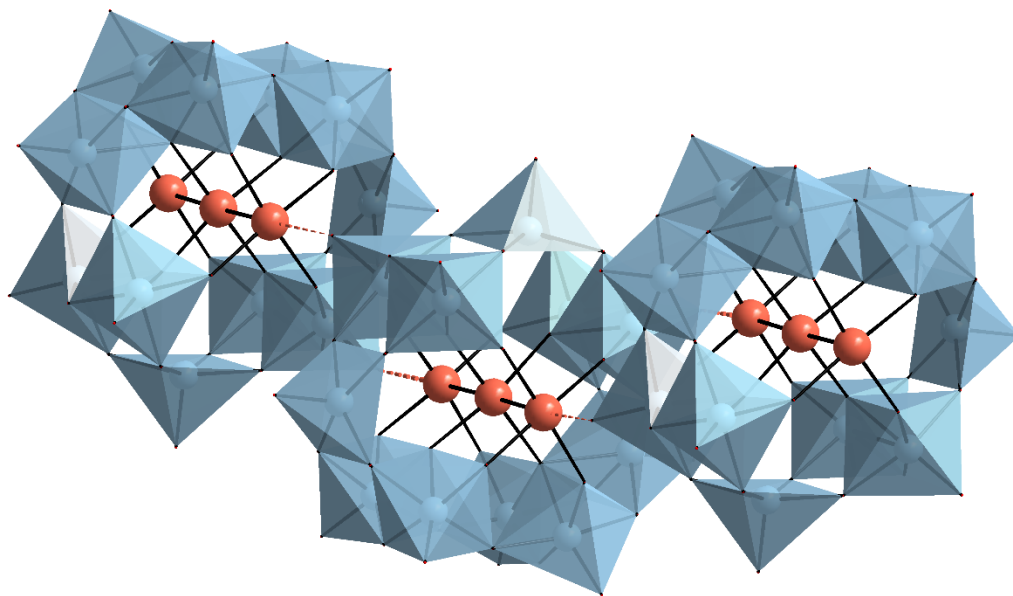


Figure 4.7. Combined polyhedral/ball-and-stick representation of $\{[\text{Pt}_3\text{W}_{11}\text{O}_{41}]^{10-}\}_n$ chain. Pt red, $\{\text{WO}_6\}$ and $\{\text{WO}_5\}$ blue octahedra.

In platinum(II) chemistry, it is well-known that the number of coordination five complexes is generally less common compared to coordination four complexes. The reason is related to the well-known tendency of this d^8 ion to form a favorable square-planar geometry (sp) maintaining the coordinative unsaturation. Nevertheless, it is possible to obtain five-coordinate complexes through a rational design of the coordination environment, mainly based on the steric destabilization of the sp geometry, like cisplatin and its second-generation derivatives,¹¹⁸ which mainly with halides,¹¹⁹ pseudohalides,¹²⁰ hydride,¹²¹ hydrocarbyl¹²² or organometal fragments¹²³) and neutral (nitrogen-¹²⁴ or sulfurcontaining ligands).¹²⁵ Whereas, no structures of five-coordinated complexes with oxygen atoms occupying the five positions in the coordination sphere were found. By contrast several examples were found of the metal complexes containing the oxygen atom located inside the coordination sphere or outside but at a short distance from the metal centre (range $\text{Pt}\cdots\text{O}$ 2.734–3.275 Å,¹²⁶ significantly longer than those found for Pt_3W_{11}) suggesting a

weak bonding interaction between the metal center and the oxygen atom, consistent with a [4+1] coordination.

In the crystal structure of $\text{Pt}^{\text{II}}\text{W}_5$, the centrosymmetric $[\text{Pt}^{\text{II}}_2\text{W}_5\text{O}_{18}((\text{CH}_3)_2\text{AsO}_2)_2]^{4-}$ anions comprise two platinum(II) ions in the square-planar environment; each Pt(II) coordinates two chelating cacodylate ligands and $\{\text{W}_5\text{O}_{18}\}^{6-}$ anion with monolacunary Lindquist structure by two terminal oxygen atoms (Figure 4.8). A minor distortion in the Pt(II) environment is required to coordinate neighbouring oxygen atoms of POM ligands. In $\text{Pt}^{\text{II}}\text{W}_5$, the O–Pt–O angles are 86.7(3)–91.8(3)°, the larger angles corresponding to bonding to the $\{\text{W}_5\text{O}_{18}\}$ moiety. And the diagonal angles are 173.0(3)–176.8(3)°. The distances Pt–O vary in the range of 1.970(7)–2.044(7) Å. The Pt atoms are spaced by 2.983(8) Å, which is by 0.15 Å shorter than the Pt···Pt separation of 3.13 Å reported for $[\text{Pt}_2(\text{W}_5\text{O}_{18})_2]^{8-}$.⁴² This distance should be regarded as nonbonding.

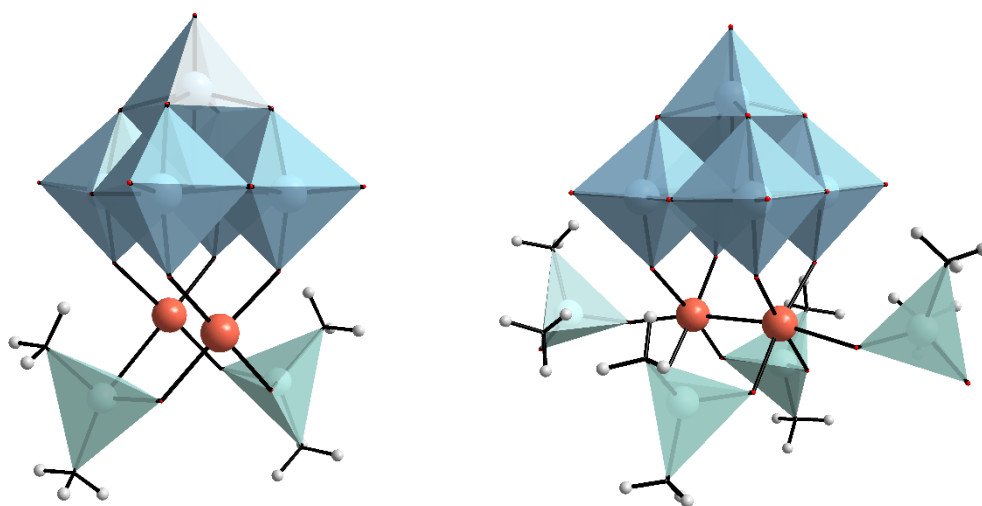


Figure 4.8. Combined polyhedral/ball-and-stick representation of $[\text{Pt}^{\text{II}}_2\text{W}_5\text{O}_{18}((\text{CH}_3)_2\text{AsO}_2)_2]^{4-}$ anion (left) and $[\text{Pt}^{\text{III}}_2\text{W}_5\text{O}_{18}((\text{CH}_3)_2\text{AsO}_2)_4]^{4-}$ anion (right). Pt red, $\{\text{WO}_6\}$ blue octahedra, $\{(\text{CH}_3)_2\text{AsO}_2\}$ green tetrahedra.

In **Pt^{III}₂W₅**, the centrosymmetric [Pt^{III}₂W₅O₁₈((CH₃)₂AsO₂)₄]⁴⁻ anions also comprise two platinum(II) ions coordinated with two chelating cacodylate ligands and W₅O₁₈⁶⁻ anion (Figure 4.8). But each Pt atom has an extra monodentate cacodylate ligand leading to square-pyramidal coordination symmetry with direct Pt–Pt bonding (2.642(4) Å), which is common in {Rh₂} and {Pt₂} dimers, each Rh^{II} or Pt^{III} center typically binds to four equatorial ligands and one axial ligand.¹²⁷ The O–Pt–O angles are 79.8(2)–91.7(2)°, the larger angles corresponding to bonding to the {W₅O₁₈} moiety. The diagonal angles are 171.51(2)–172.51(2)°, which are smaller than that in **Pt^{II}₂W₅**. Additionally, the O–Pt–Pt–O bonds are not colinear, with value of 169.6(1)° for the angles at Pt atom due to the steric crowding by the polyoxometalate ligand. The distances Pt–O vary in the range of 1.978(4)–2.157(5) Å, the longest distance corresponding to bonding to the mono-dentate cacodylate ligand. In the solid state, the discrete anions are surrounded by K⁺ and Na⁺ cations, which coordinate both oxygen atoms of cacodylate ligands as well as of solvate water molecules. And we also synthesized the dumbbell **Pt₂** with cacodylate ligands. In contrast to the discrete anions in **Pt^{III}₂W₅**, the monodentate (CH₃)₂AsO₂⁻ ions are connected to further **Pt₂⁺** ions in a chelating way leading to chains of the composition {[Pt^{III}₂((CH₃)₂AsO₂)₅]⁺]_n (Figure 4.9). The lacunary Lindqvist pentatungstate has typical geometric characteristics; W=O, W–μ-O and W–μ₅-O bond lengths are 1.719(6)–1.786(8), 1.802(4)–2.009(4) and 2.229(7)–2.3541(8) Å, respectively, being in good agreement with the [Pt₂(W₅O₁₈)₂]⁸⁻. Powder X-ray diffraction (PXRD) studies on **KNa-Pt^{II}₂W₅** indicated that the compounds were crystalline and pure as evidenced from the fact that the PXRD spectra of freshly prepared samples matched well with the simulated PXRD spectra (calculated from the SC-XRD data, see Figure 4.10).

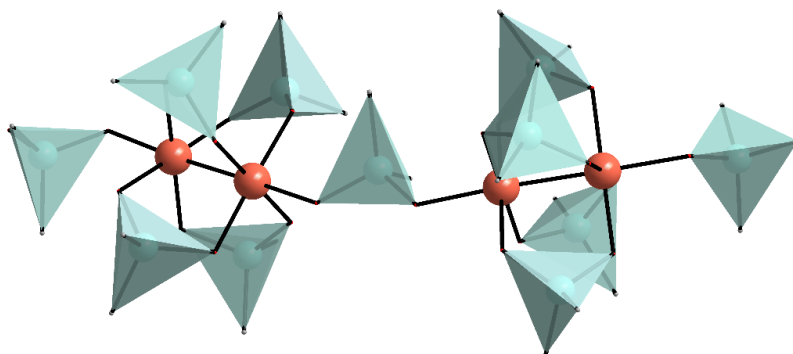


Figure 4.9. Combined polyhedral/ball-and-stick representation of $\{[\text{Pt}^{\text{III}}_2((\text{CH}_3)_2\text{AsO}_2)_5]^+\}_n$ chain. Pt red, $\{(\text{CH}_3)_2\text{AsO}_2\}$ green tetrahedra.

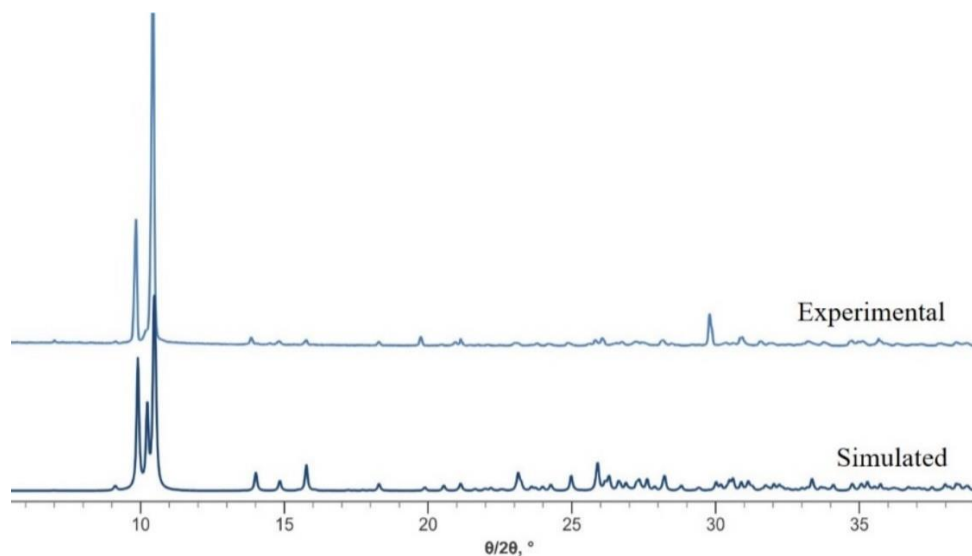


Figure 4.10. Simulated and experimental PXRD patterns of $\text{KNa-Pt}^{\text{II}}_2\text{W}_5$ upon dehydration and rehydration. (simulated diffraction pattern derived from single-crystal data).

4.4.2 Multinuclear NMR Study

To complement the solid-state XRD results on $\text{Pt}^{\text{II}}_2\text{W}_5$ with solution studies, ^1H , ^{13}C and ^{195}Pt NMR measurements were performed on $\text{KNa-Pt}^{\text{II}}_2\text{W}_5$ redissolved in $\text{H}_2\text{O}/\text{D}_2\text{O}$. The ^1H NMR spectrum of sodium cacodylate (Na-cac) exhibits sharp peaks at 4.7 and 1.4 ppm, respectively, corresponding to the protons of the crystal water molecules and cacodylate methyl groups, respectively. The ^1H NMR spectra of $\text{Pt}^{\text{II}}_2\text{W}_5$ exhibit the expected two

peaks at 1.8 and 1.6 ppm, corresponding to the two structurally and hence magnetically inequivalent cacodylate methyl groups (Figure 4.11). The ^1H NMR spectrum of $\text{Pt}^{\text{II}}_2\text{W}_5$ remained unchanged even for 5 days, which indicates the high solution stability of this polyanion. The ^{13}C NMR spectrum of Na-cac exhibits a narrow peak at 17.4 ppm, whereas the ^{13}C NMR spectrum of $\text{Pt}^{\text{II}}_2\text{W}_5$ exhibits peaks at 19.4 and 16.6 ppm, corresponding to the two crystallographically inequivalent cacodylate methyl groups (Figure 4.11).

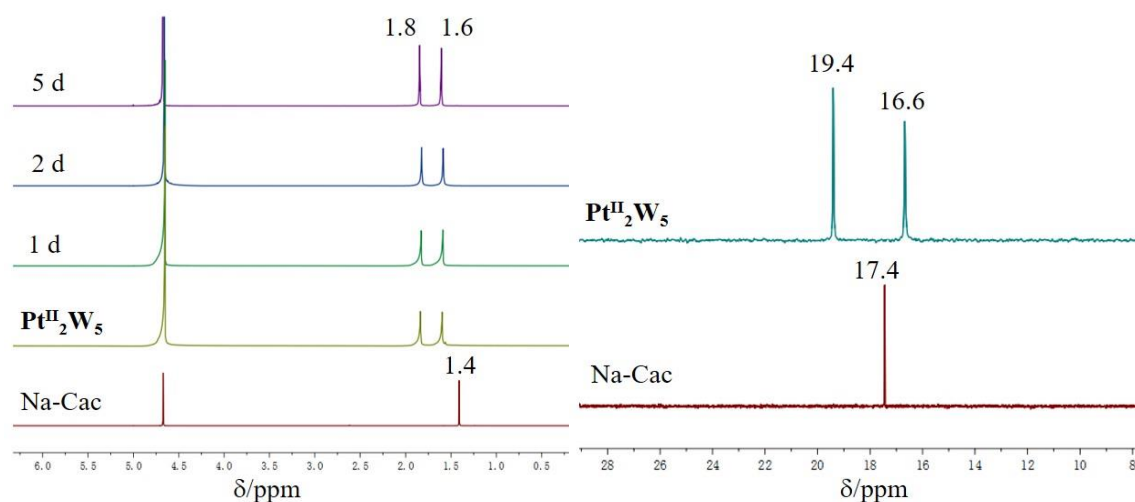


Figure 4.11. Time-dependent ^1H (left) and ^{13}C (right) NMR spectra ($\text{H}_2\text{O}/\text{D}_2\text{O}$) of $\text{Pt}^{\text{II}}_2\text{W}_5$ compared to spectra of the reference sodium cacodylate (Na-Cac).

Next, we performed ^{195}Pt NMR measurements on $\text{KNa-Pt}^{\text{II}}_2\text{W}_5$ redissolved in water (Figure 4.12). We located the expected singlet for $\text{KNa-Pt}^{\text{II}}_2\text{W}_5$ at 610 ppm. The corresponding ^{195}Pt NMR signal for the precursor K_2PtCl_4 appeared more upfield at -1616 ppm. In 1996, Kuznetsova et al. observed a ^{195}Pt NMR singlet of an aqueous reaction of $[\text{PW}_{11}\text{O}_{39}]^{7-}$ with $[\text{PtCl}_4]^{2-}$ at -1179 ppm.¹²⁸ In 2011, Lefebvre and co-workers reported a ^{195}Pt NMR chemical shift of -3962 ppm for a DMSO solution of the $[\text{SiW}_{12}\text{O}_{40}]^{4-}$ Keggin ion with $[\text{Pt}^{\text{II}}(\text{CH}_3)(\text{COD})]^+$ moieties grafted on its surface.¹²⁹ Later, Kato and co-workers observed the broad signals of ^{195}Pt NMR spectra of Pt^{II} -incorporating POMs [α -

$\text{PW}_{11}\text{O}_{39}(\text{cis-Pt}(\text{NH}_3)_2)_2]^{3-40, 130}$ and $[\text{PW}_{11}\text{O}_{39}\{\text{cis-Pt}^{\text{II}}(\text{Me}_2\text{ppz})\}]^{5-}$ ($\text{Me}_2\text{ppz} = N, N'$ -dimethylpiperazine).⁴⁷ By now, no Pt(II)-containing solid POM showed discernible ^{195}Pt NMR peaks under all conditions studied, likely due to severe chemical shift anisotropy of four-coordinate Pt^{II} species. Importantly, this is the first report on the successful use of ^{195}Pt NMR in Pt(II)-containing POM.

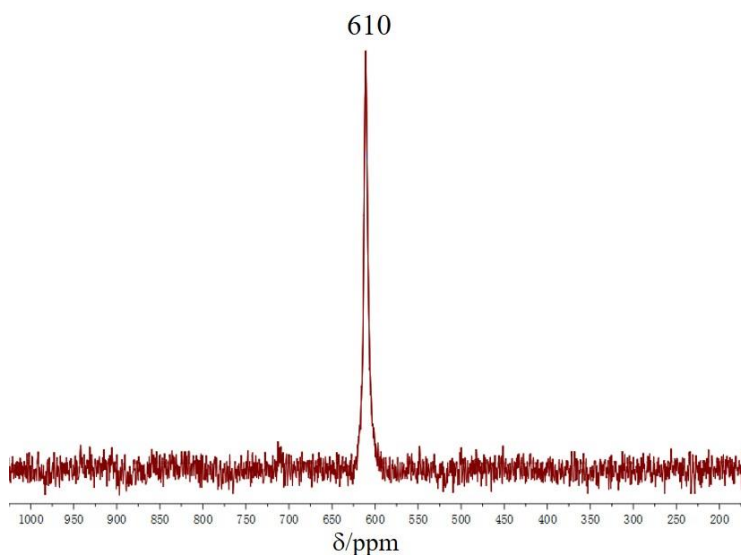


Figure 4.12. ^{195}Pt NMR spectrum ($\text{H}_2\text{O}/\text{D}_2\text{O}$) of $\text{Pt}^{\text{II}}_2\text{W}_5$.

4.5 Conclusions

Three new platinum(II/III) isopolytungstate: $[\text{Pt}_3\text{W}_{11}\text{O}_{41}]^{10-}$ (Pt_3W_{11}), $[\text{Pt}^{\text{II}}_2\text{W}_5\text{O}_{18}((\text{CH}_3)_2\text{AsO}_2)_2]^{4-}$ ($\text{Pt}^{\text{II}}_2\text{W}_5$), $[\text{Pt}^{\text{III}}_2\text{W}_5\text{O}_{18}((\text{CH}_3)_2\text{AsO}_2)_4]^{4-}$ ($\text{Pt}^{\text{III}}_2\text{W}_5$), have been synthesized in aqua media and characterized by ^1H , ^{13}C and ^{195}Pt NMR spectra. The polyoxoanion $[\text{Pt}_3\text{W}_{11}\text{O}_{41}]^{10-}$ consists of three $\{\text{W}_3\text{O}_{13}\}$ and one $\{\text{W}_2\text{O}_{10}\}$ fragments connected by three Pt atoms forming linear $\{\text{Pt}_3\text{O}_{12}\}$ triad involved in direct Pt–Pt bonding (2.64 to 2.68 Å). The distance between the metal and the oxygen from neighbouring Pt_3W_{11} cluster ($\text{Pt}\cdots\text{O}$ distances, 2.34 and 2.65 Å), consistent with [4+1] coordination for outer platinum centers in compound, showing a weak bonding interaction. The polyoxoanion

Pt^{II}₂W₅ and **Pt^{III}₂W₅** both consists of one lacunary Lindqvist fragments {W₅O₁₈}⁶⁻ coordinated by two Pt(II) in square planar coordination and two Pt(III) in square-pyramidal coordination with direct Pt–Pt bonding (2.64 Å), respectively. This work is the first report on the successful use of ¹⁹⁵Pt NMR in Pt(II)-containing POM.

Chapter V Platinum(II/IV) Arsenate(III) Clusters

Representatives of oxidoarsenates(V) are well known. However, representatives of oxidoarsenates(III) are comparatively scarce. Although, the classical coordination chemistry of platinum has a long history and is replete with interesting compounds, only limited work has been reported on the cluster of Pt^{IV} or Pt^{II}. although many oxide compounds that contain AsO₃³⁻ ions have been prepared, and most metal ions in such types of compounds are transition- and rare-earth-metal ions, nearly nothing is known about the platinum. In particular, the only known compound is the arsenoplatinum, [Pt(μ -NHC(CH₃)O)₂ClAs(OH)₂] with Pt–As = 2.27 Å.⁵⁹ While exploring systems containing platinum and arsenic in aqua media, the first two full inorganic discrete platinum arsenate(III) clusters: [Pt^{IV}(As₃O₆)₂]²⁻ (**PtAs₆**) and [Pt^{II}₄(H₂AsO₃)₆(HAsO₃)₂]²⁻ (**Pt₄As₈**), have been synthesized in aqua media. And a platinum arsenate(III) heteropolytungstate [Pt₂As₆W₄O₂₈]¹⁰⁻ (**Pt₂As₆W₄**) has been synthesized in aqua media and characterized by ¹⁹⁵Pt NMR.

5.1 Synthesis

Na₂[Pt(As₃O₆)₂]·7H₂O (**Na-PtAs₆**)

H₂Pt(OH)₆ (50 mg, 0.167 mmol) and As₂O₃ (100 mg, 0.9 mmol) were added in 3 mL of 1 M NaOH and stirred for 1 h at 80 °C. Yellowish blocky crystals came out overnight, and after 3 days crystals were collected by filtration. Yield: 50% based on Pt. Anal. Calcd (%) for **PtAs₆**: Pt 19.34, As 44.56, Na 4.56. Found: Pt 18.94, As 44.63, Na 4.31. FT-IR (KBr/cm⁻¹): 3451(s) [ν (O–H) of structural H₂O], 3363–3267 (s) [ν (O–H) of absorbed H₂O],

1633 (m) [$\delta(\text{O-H})$ of H_2O], 998 (w) [$\nu(\text{As-O-Pt})$], 773 (s) [$\nu(\text{As-O})$], 625–598 (s) [$\nu_{\text{as}}(\text{AsO}_3^{3-})$], 531–512 (s) [$\nu(\text{Pt-O})$, $\nu(\text{As-O-As})$].

$\text{K}_2[\text{Pt}_4(\text{H}_2\text{AsO}_3)_6(\text{HAsO}_3)_2] \cdot 5\text{H}_2\text{O}$ (K-Pt₄As₈)

$\text{K}_2\text{Pt}(\text{NO}_2)_4$ (45.7 mg, 0.1 mmol) and As_2O_3 (20 mg, 0.1 mmol) were added in 1 mL of 0.5 M H_2SO_4 and stirred for 20 min at 80 °C with copious evolution of brown gas. Yellowish blocky crystals came out overnight, and after 3 days crystals were collected by filtration. Yield: 70% based on Pt. Anal. Calcd (%) for **Pt₄As₈**: Pt 40.10, As 30.80, K 4.02. Found: Pt 40.62, As 29.75, K 4.15. FT-IR ($\text{KBr}/\text{cm}^{-1}$): 3600–3300 (s) [$\nu(\text{O-H})$ of H_2O and hydroxyl], 2916–2366 (s) [$\nu(\text{O-H})$ of unit $\text{Pt-O-As}(\text{OH})_2$], 1627 (m) [$\delta(\text{O-H})$ of hydroxyl], 1408 (s) [$\delta_{\text{in-plane}}(\text{O-H})$], 1220 (m) [$\delta(\text{As-OH})$], 810(s) [$\gamma(\text{O-H})$, $\nu_{\text{as}}(\text{As-O})$], 723 (s) [$\nu_{\text{s}}(\text{As-O})$, $\nu(\text{Pt-As})$], 550–508 (m) [$\nu(\text{Pt-O})$].

$\text{Na}_{10}[\text{Pt}_2\text{As}_6\text{W}_4\text{O}_{28}] \cdot 18\text{H}_2\text{O}$ (Na-Pt₂As₆W₄)

Method 1: K_2PtCl_4 (41.5 mg, 0.1 mmol) and Na_2WO_4 (66.0 mg, 0.2 mmol) were added in 2 mL of 0.5 M NaAsO_2 solution and adjusted pH to 8 by 1 M NaOH , then stirred for 30 min at room temperature. Yellowish rod crystals came out after one week and were collected by filtration. Yield: 50% based on Pt. Anal. Calcd (%) for **Pt₂As₆W₄**: Pt 15.14, W 28.53, As 17.44, Na 8.92. Found: Pt 15.40, W 29.00, As 16.80, Na 8.40. FT-IR ($\text{KBr}/\text{cm}^{-1}$): 3436(s) [$\nu(\text{O-H})$ of structural H_2O], 1670–1636 (m) [$\delta(\text{O-H})$ of H_2O], 1384 (s) [$\delta_{\text{in-plane}}(\text{O-H})$], 937 (m) [$\nu(\text{W-O (terminal)})$], 886 (m) [$\nu(\text{As-O-Pt})$], 782 (s) [$\nu(\text{As-O})$], 648 (s) [$\nu(\text{W-O (bridging)})$], 516–458 (s) [$\nu(\text{Pt-O})$, $\nu(\text{As-O-As})$]. **Method 2.** The same polyanion can also be synthesized using a stoichiometric procedure in water as follows: K_2PtCl_4 (41.5 mg, 0.1 mmol), Na_2WO_4 (32.9 mg, 0.1 mmol) and NaAsO_2 (38.0 mg, 0.3 mmol) were added in 2 mL H_2O and stirred at 70 °C for 20 min. Yellow rod crystals came

out overnight, and after 3 days crystals were collected by filtration. Yield: 53% based on Pt. This material is identical to that produced by **Method 1** as based on FT-IR and single crystal XRD.

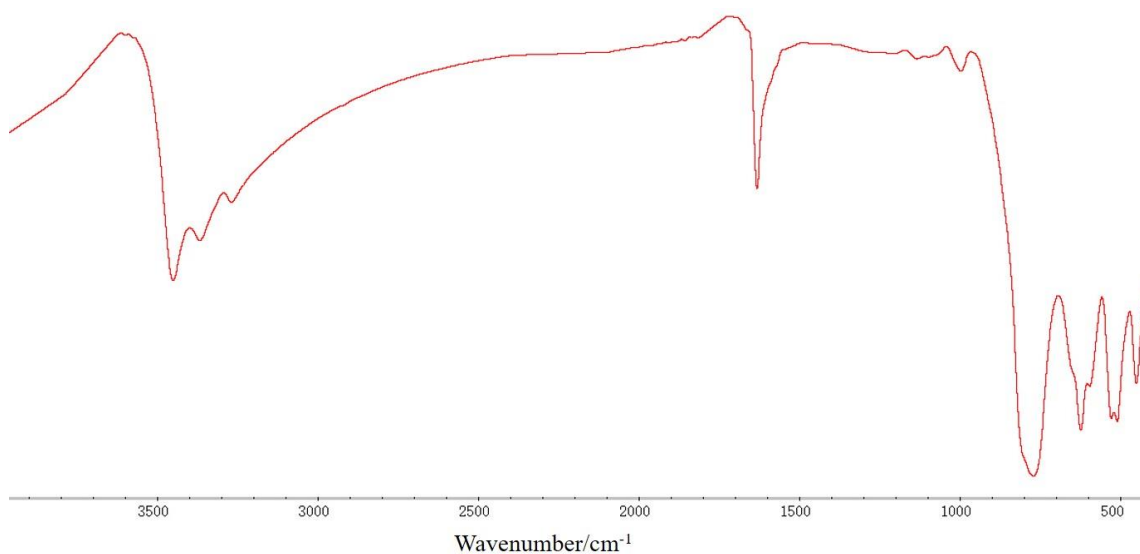


Figure 5.1. FT-IR spectrum of Na-PtAs₆.

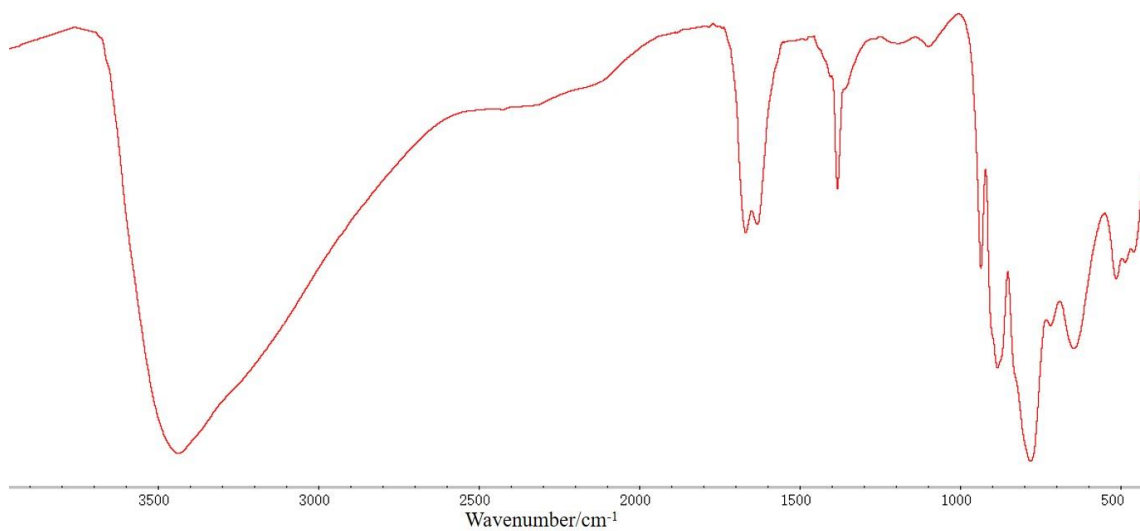


Figure 5.2. FT-IR spectrum of Na-Pt₂As₆W₄.

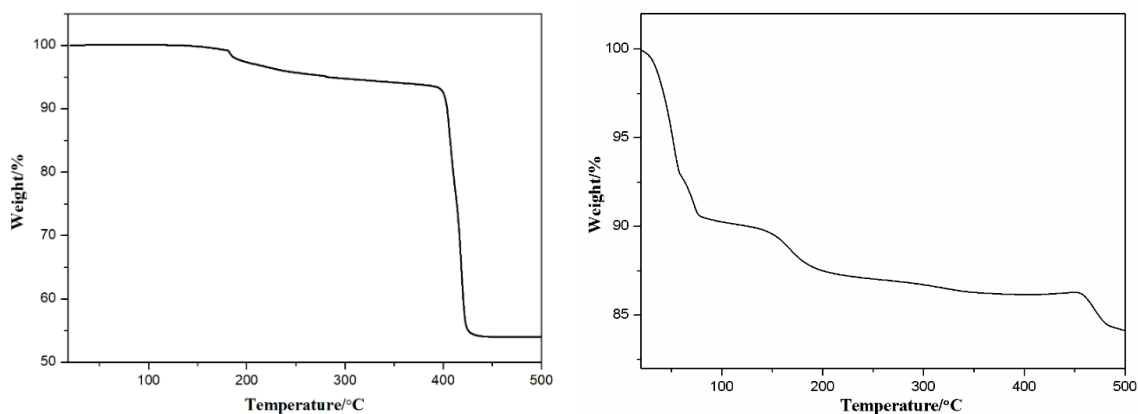


Figure 5.3. Thermograms of **Na-PtAs₆** (left) and **Na-Pt₂As₆W₄** (right) from room temperature to 500 °C under N₂ atmosphere.

5.2 Single-Crystal XRD Data

Table 5.1. Crystal data and structure refinement for **Na-PtAs₆**, **K-Pt₄As₈**, **K-Pt₄As₈ (dehy)** and **Na-Pt₂As₆W₄**.

Compound	Na-PtAs₆	K-Pt₄As₈	K-Pt₄As₈ (dehy)	Na-Pt₂As₆W₄
empirical formula	Na ₂ PtAs ₆ O ₂₀ H ₁₆ ^a	K ₂ Pt ₄ As ₈ O ₅₃ H ₁₄ ^a	KPt ₄ As ₈ O ₂₄	Na ₁₀ Pt ₂ As ₆ W ₄ O ₄₆ H ₃₆ ^a
fw, g mol ⁻¹	1026.70 ^a	1946.05 ^a	1802.82	2577.20 ^a
crystal system	Triclinic	Tetragonal	Tetragonal	Triclinic
space group	P $\bar{1}$	P4/nnc	P4/nnc	P $\bar{1}$
<i>a</i> (Å)	6.704(3)	19.3248(7)	16.7915(3)	8.607(3)
<i>b</i> (Å)	7.034(3)	19.3248(7)	16.7915(3)	12.765(4)
<i>c</i> (Å)	8.177(3)	16.9569(7)	18.0190(4)	13.030(4)
α (°)	100.415(8)	90	90	117.519(8)
β (°)	101.514(8)	90	90	97.633(8)
γ (°)	104.523(8)	90	90	90.295(8)
<i>V</i> (Å ³)	354.8(3)	6332.5(5)	5080.5(2)	1254.7(7)
<i>Z</i>	1	4	8	1
<i>D_c</i> (g cm ⁻³)	4.281	3.838	4.714	3.375
abs coeff, mm ⁻¹	23.904	26.067	32.562	18.803
F(000)	410	6460	6296	1133

θ range for data collection, deg	3.248 to 27.418	1.490 to 25.054	2.261 to 25.020	3.073 to 26.419
completeness to Θ_{\max}	99.8 %	99.9 %	99.9 %	99.8 %
index ranges	-8 \leq h \leq 8, -9 \leq k \leq 9, -10 \leq l \leq 10	-22 \leq h \leq 23, -23 \leq k \leq 22, -20 \leq l \leq 20	-19 \leq h \leq 19, -19 \leq k \leq 19, -20 \leq l \leq 21	-10 \leq h \leq 10, -15 \leq k \leq 15, -16 \leq l \leq 16
reflns collected	6444	54917	40868	21401
indep reflns	1614	2825	2257	5120
$R(\text{int})$	0.0591	0.1529	0.0590	0.1458
abs corn	Semi-empirical from equivalents	Semi-empirical from equivalents	Semi-empirical from equivalents	Semi-empirical from equivalents
data/restraints/param	1614 / 0 / 106	2825 / 145 / 176	2257 / 147 / 168	5120 / 144 / 313
GOF on F^2	1.054	1.093	1.065	1.024
$R_1, {}^b wR_2^c$ [$I > 2\sigma(I)$]	0.0288, 0.0721	0.0795, 0.1752	0.0805, 0.2246	0.0554, 0.1181
$R_1, {}^b wR_2^c$ (all data)	0.0336, 0.0742	0.1093, 0.1987	0.0935, 0.2383	0.1075, 0.1398
Largest diff peak and hole, $e \text{ \AA}^{-3}$	2.100 and -2.247	3.525 and -3.097	6.745 and -3.477	2.350 and -3.236

^aThe entries are the actual formula units and weights as obtained from elemental analysis.

^b $R_1 = \Sigma||F_o| - |F_c||/\Sigma|F_o|$. ^c $wR_2 = [\Sigma w(F_o^2 - F_c^2)^2/\Sigma w(F_o^2)^2]^{1/2}$.

5.3 Bond valence sum calculations.

Table 5.2. Bond valence sum values for different types of bridging oxygen atoms and terminal oxygen atoms for **K-Pt₄As₈** and **Na-Pt₂As₆W₄**.

O	Bond distance(\AA)	BVS value	O	Bond distance(\AA)	BVS value
K-Pt₄As₈					
O1	Pt2-O1 (2.076)	1.750	O8	Pt1-O8 (2.066)	1.770
	As1-O1 (1.688)			As3-O8 (1.686)	
O10	Pt2-O10 (2.077)	1.703	O11	Pt1-O11 (2.070)	1.652
	As4-O10 (1.701)			As4-O11 (1.719)	
O2	As1-O2 (1.722)	1.198	O6	As2-O6 (1.709)	1.174
O3	As1-O3 (1.737)	1.089	O7	As3-O7 (1.765)	1.008
O4	As2-O4 (1.562)	1.848	O9	As3-O9 (1.704)	1.257

O5	As2-O4 (1.805)	0.958	O12	As4-O9 (1.711)	1.234
Na-Pt₂As₆W₄					
O3	As2-O3 (1.777)	1.99	O6	W1-O6 (2.194)	1.74
	As3-O3 (1.807)			As1-O6 (1.701)	
O7	W2-O7 (2.209)	1.79	O8	W1-O8 (1.981)	2.03
	As1-O7 (1.681)			As2-O8 (1.727)	
O11	W1-O11 (1.949)	1.84	O12	As3-O12 (1.731)	2.05
	W2-O11 (1.947)			As3-W2 (1.965)	
O1	Pt1-O1 (2.088)	1.57			
	W1-O1 (2.105)				
	W2-O1 (2.143)				

5.4 Results and Discussion

5.4.1 Solid-State Structure

We have discovered first two full inorganic discrete platinum arsenate(III) clusters: $[\text{Pt}^{\text{IV}}(\text{As}_3\text{O}_6)_2]^{2-}$ (**PtAs₆**), $[\text{Pt}^{\text{II}}_4(\text{H}_2\text{AsO}_3)_6(\text{HAsO}_3)_2]^{2-}$ (**Pt₄As₈**), and one platinum arsenate(III) heteropolytungstate $[\text{Pt}_2\text{As}_6\text{W}_4\text{O}_{28}]^{10-}$ (**Pt₂As₆W₄**). Single-crystal XRD studies revealed that **PtAs₆** crystallizes as a sodium salt, $\text{Na}_2[\text{Pt}(\text{As}_3\text{O}_6)_2] \cdot 7\text{H}_2\text{O}$ (**Na-PtAs₆**), in the triclinic space group $P\bar{1}$, **Pt₄As₈** crystallizes as a potassium salt, $\text{K}_2[\text{Pt}_4(\text{H}_2\text{AsO}_3)_6(\text{HAsO}_3)_2] \cdot 5\text{H}_2\text{O}$ (**K-Pt₄As₈**), in the Tetragonal space group $P4/nnc$, and **Pt₂As₆W₄** crystallizes as a sodium salt, $\text{Na}_{10}[\text{Pt}_2\text{As}_6\text{W}_4\text{O}_{28}] \cdot 18\text{H}_2\text{O}$ (**Na-Pt₂As₆W₄**), in the triclinic space group $P\bar{1}$, respectively. The symmetry unit of solid-state interaction of polyanion with Na^+ and K^+ counter cations are shown in Figure 5.4.

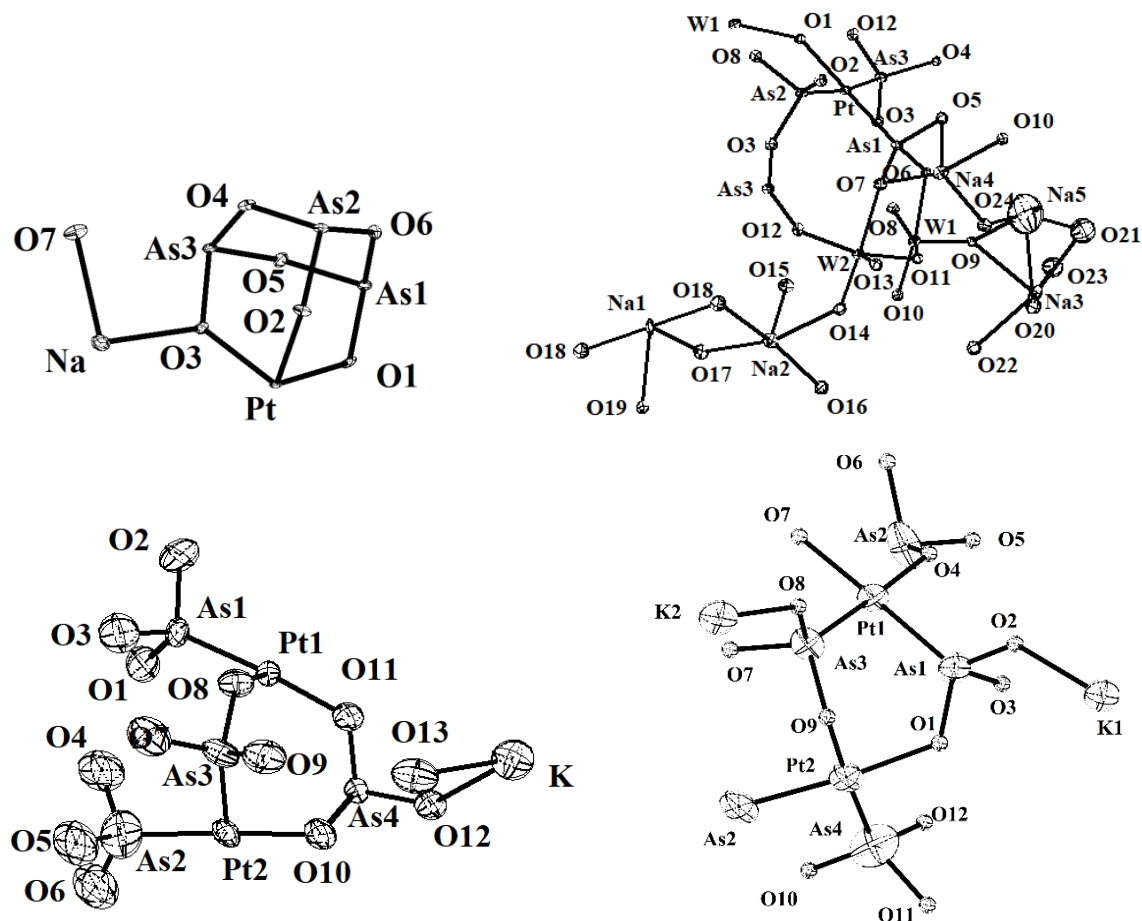


Figure 5.4. The symmetry unit of solid-state interaction of polyanion with Na^+ counter cations in Na-PtAs_6 (top left) and $\text{Na-Pt}_2\text{As}_6\text{W}_4$ (top right), as well as K^+ counter cations in $\text{K-Pt}_4\text{As}_8$ (bottom left) and $\text{K-Pt}_4\text{As}_8$ (dehy) (bottom right), respectively (50% probability ellipsoids).

In cluster PtAs_6 , the central Pt atom in this complex is in an ideal octahedral environment coordinated by two As_3O_6 aggregates through three O atoms, generating a ten-membered ring PtAs_3O_6 (Figure 5.5). It comprises three crystallographically independent As(III) sites both possessing distorted tetrahedral environments when taking into account the stereochemically active lone pair. The trivalent ones usually contain ψ -tetrahedral AsO_3^{3-} groups because of the $4s^2$ -configuration. The cyclic $[\text{As}_3\text{O}_6]^{3-}$ anion is formed by three vertex-linked AsO_3 trigonal pyramids. The average Pt–O bond distance is 2.022(4) Å. The $[\text{Pt}(\text{As}_3\text{O}_6)_2]^{2-}$ anion is remarkable for that it is the only arsenate(III) of platinum. The

similar structure of $[\text{As}_3\text{O}_6]^{3-}$ is cyclic thioarsenate anion $[\text{As}_3\text{S}_6]^{3-}$.¹³¹ In the solid-state structure of **PtAs₆**, three terminal O atoms of the $[\text{As}_3\text{O}_6]^{3-}$ units are oriented toward the same side of the $[\text{As}_3\text{O}_3]$ ring. The anions are arranged in a tripod-like manner along the *b* axis with opposite orientations in neighboring tripods. The connectivity of the Na–O bonds leads to a 3D framework consisting of $[\text{Na}_2\text{Pt}(\text{As}_3\text{O}_6)_2]$ units (Figure 5.6), which interpenetrate the above-mentioned 3D framework by sharing both O vertices and O–O edges. The Na^+ cations are coordinated by seven oxygen atoms with Na–O distances in the range 2.421(6)–2.701(5) Å.

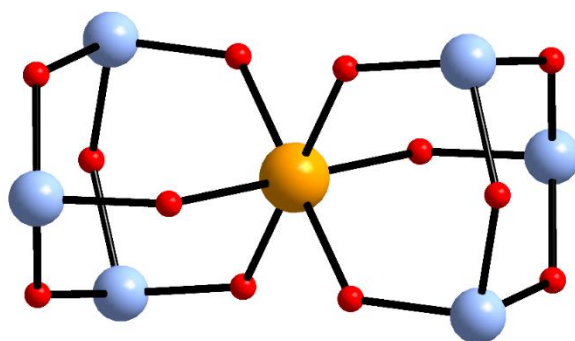


Figure 5.5. Ball-and-stick representation of $[\text{Pt}^{\text{IV}}(\text{As}_3\text{O}_6)_2]^{2-}$ polyanion. Pt orange, As light blue, O red.

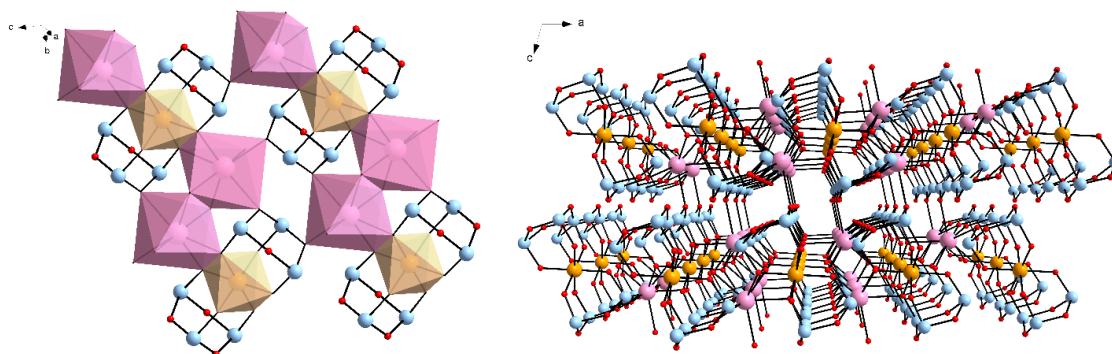


Figure 5.6. Crystal packing diagram of **PtAs₆**, showing the layered structure (left) and 3D framework (right) self-assembled by the $[\text{Pt}(\text{As}_3\text{O}_6)_2]^{2-}$ moieties via Na^+ ions. $\{\text{PtO}_6\}$ orange octahedra, $\{\text{NaO}_7\}$ pink polyhedra, As light blue, O red.

The cluster **Na-Pt₂As₆W₄** crystallized in $P\bar{1}$. The centrosymmetric $[\text{Pt}_2\text{As}_6\text{W}_4\text{O}_{28}]^{10-}$ anions comprise two platinum(II) ions in the square-planar environment. Each Pt(II) coordinates three AsO_3 ligands by apex As atoms and one $[\text{W}_2\text{O}_{10}]^{8-}$ ions by one $\mu_3\text{-O}$ atom (Figure 5.7). There are two types of AsO_3 pyramid ligands. Two AsO_3 units bind to one Pt atom by apex As atom and two W atoms by O atoms. Four AsO_3 ligands coordinate to one W atom and one Pt atom each employing one O atom and apex As atom, respectively. Two pairs of vertex-linked AsO_3 trigonal pyramids are sited on the opposite of Pt atoms. Two WO_6 octahedral share two by two an edge forming $[\text{W}_2\text{O}_{10}]^{8-}$ ion. The Pt atoms are spaced by 2.9797(9) Å.

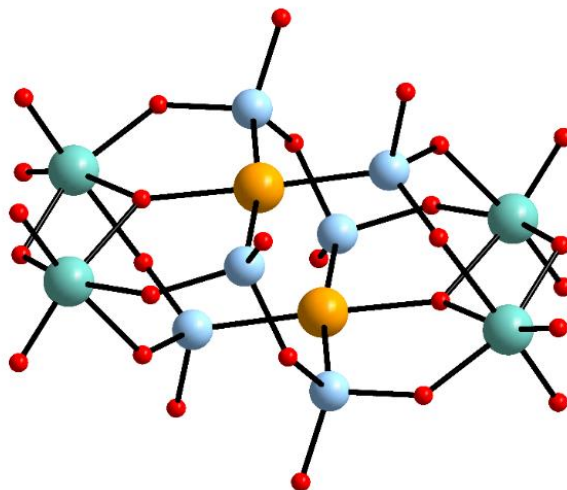


Figure 5.7. Ball-and-stick representation of $[\text{Pt}_2\text{As}_6\text{W}_4\text{O}_{28}]^{10-}$ polyanion. Pt orange, W green, As light blue, O red.

The first example of a fully inorganic arsenous acid platinum(II) cluster, $[\text{Pt}_4(\text{H}_2\text{AsO}_3)_6(\text{HAsO}_3)_2]^{2-}$ (**Pt₄Ass**) (Figure 5.8), is synthesized by heating $\text{K}_2\text{Pt}(\text{NO}_2)_4$ with As_2O_3 in 0.5 M H_2SO_4 at 80 °C for 20 min. It possesses an open cage structure with four square-planar coordinated Pt^{II} ions linked by six arsenite ligands. Each Pt atom is coordinated by two O atoms and two As atoms. There are three types of AsO_3 pyramid

ligands. Two AsO_3 units bind to three Pt atoms as μ_2 -1,2 κ O:3 κ As bridging ligands. The one remaining O atom is coordinated with K atom. Four AsO_3 ligands coordinate to two Pt atoms each employing one O atom and apex As atom. The remaining two ligands bind to one Pt atom each only employing the apex As atom, generating the novel $[\text{Pt}_4(\text{H}_2\text{AsO}_3)_6(\text{HAsO}_3)_2]^{2-}$ (**Pt₄As₈**) anionic cluster.

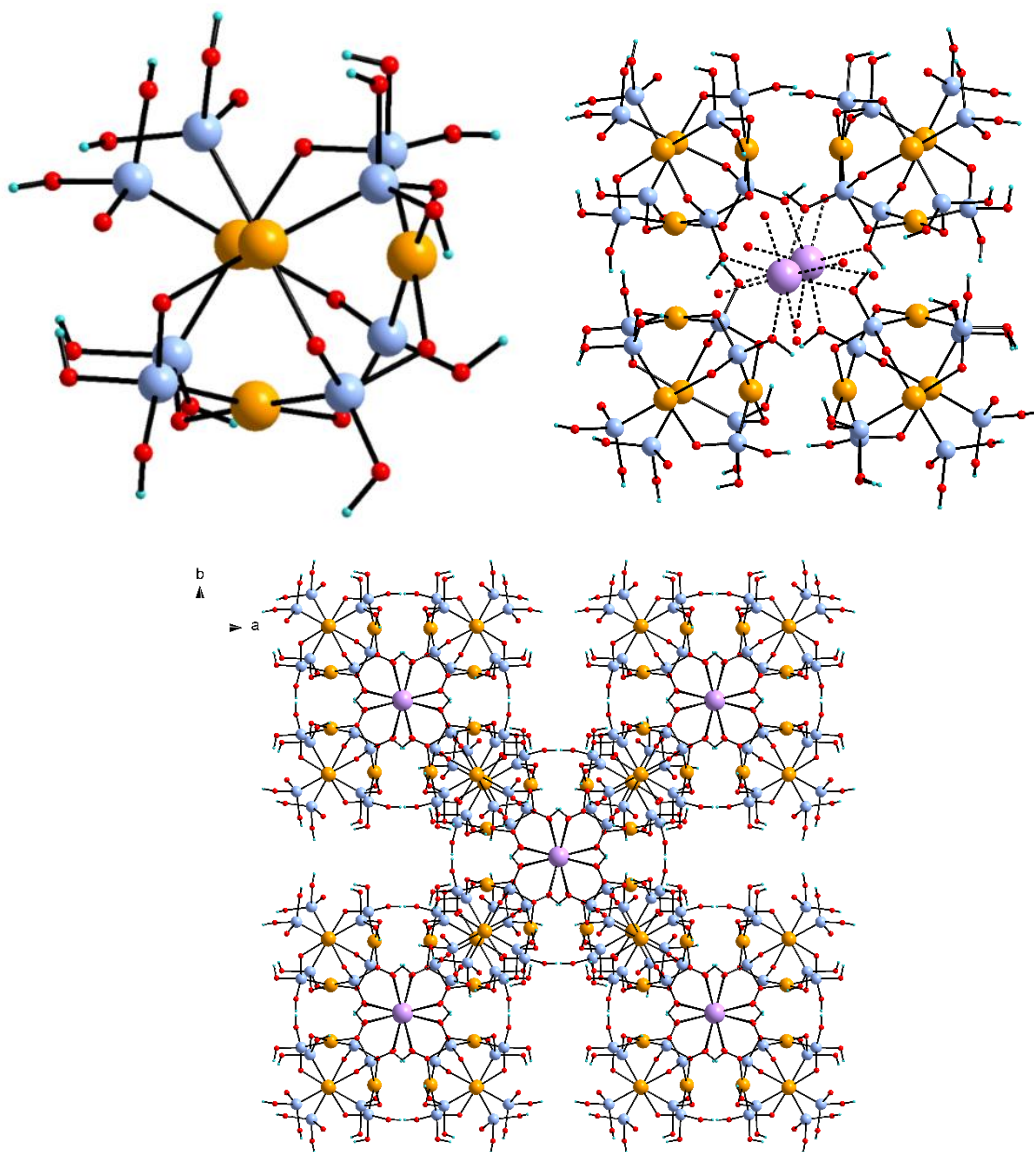


Figure 5.8. Ball-and-stick representation of $[\text{Pt}^{\text{II}}_4(\text{H}_2\text{AsO}_3)_6(\text{HAsO}_3)_2]^{2-}$ polyanion (left) and the $[\text{K}_2(\text{Pt}^{\text{II}}_4(\text{H}_2\text{AsO}_3)_6(\text{HAsO}_3)_2)]^{6-}$ fragment (middle). 3D lattice structure of **K-Pt₄As₈** (right). Color code: Pt orange, As light blue, K violet, O red, H sky blue.

In the solid-state structure, four **Pt₄As₈** tetramers are linked through two potassium cations, resulting in the kaleidoscope-shaped polyanion assembly $[\text{K}_2(\text{Pt}^{\text{II}}_4(\text{H}_2\text{AsO}_3)_6(\text{HAsO}_3)_2)_4]^{6-}$ (**K₂(Pt₄As₈)₄**). Each K atom lies on a 4-fold rotational axis and is connected to eight O atoms of four **Pt₄As₈** tetramers and four water molecules to form a coordination polyhedron in the shape of a slightly distorted square antiprism. This arrangement results in the polyanion **K₂(Pt₄As₈)₄** with idealized D_{4h} point-group symmetry. The K–O bond distances are 2.637 Å for the water ligands and 2.913 Å for the oxygen atoms of the arsenite groups. The As–O bond lengths appear to be normal for three dihydrogen arsenite group H_2AsO_3 , with two significantly longer As–OH bonds (1.723–1.758 Å) and one shorter As–O bonds (1.556–1.685 Å), whereas the bond lengths of the hydrogen arsenite group HAsO_3 are atypical: one shorter As–O bond of 1.704 Å, one somewhat longer As–OH bond of 1.711 Å, and one long As–O bond of 1.718 Å are observed.

Furthermore, the introduction of the protonized arsenite groups introduce strong hydrogen bonds in **K-Pt₄As₈**, which in turn leads to stronger intermolecular interactions in 3D space. Thus, each **K₂(Pt₄As₈)₄** unit with internal hydrogen bonding is linked to two others leading to a stable 3D hydrogen-bonded inorganic framework (HIF) (Figure 5.9 and 5.10). Hydrogen-bonded organic frameworks (HOFs)¹³² have received increasing attention and are expected to find applications in a wide range of fields. But the HOFs strategy can also be applied to inorganic materials.¹³³ The formation of a stable 3D framework in **K-Pt₄As₈** is accompanied by a higher isolated yield and crystallinity as well as aqueous insolubility.

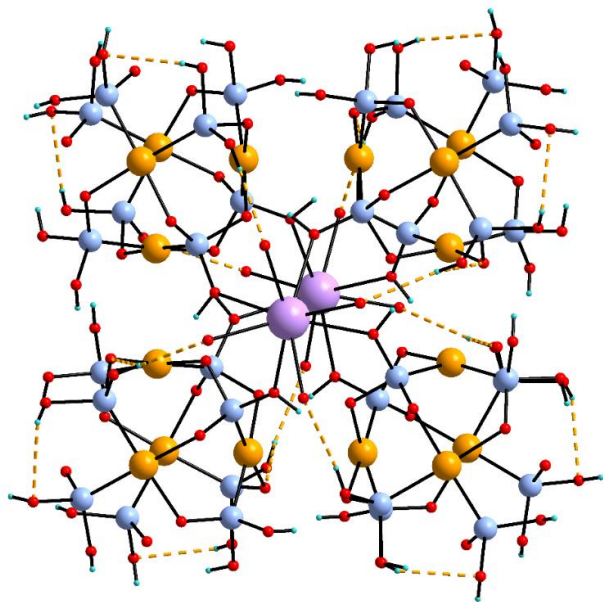


Figure 5.9. H-bond interactions (orange dotted bonds) within the $\text{K}_2(\text{Pt}_4\text{As}_8)_4$ fragment. Pt orange, As light blue, K violet, O red, H sky blue.

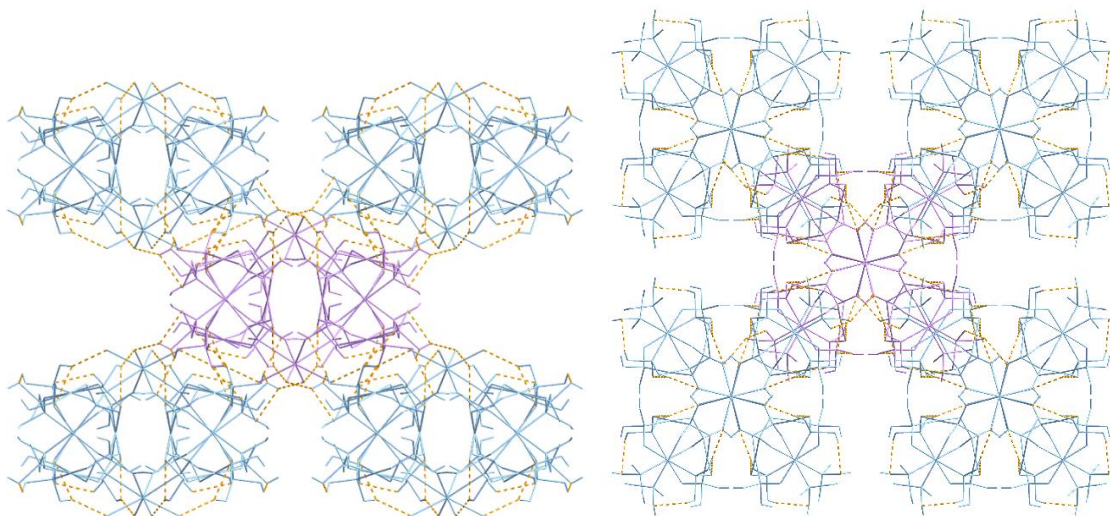


Figure 5.10. H-bond interactions (orange dotted bonds) in the $\text{K-Pt}_4\text{As}_8$ crystal packing along *b* and *c* axis.

We have identified three important factors governing the stacking in this series of compounds: interligand steric repulsions, interligand charge-transfer bonding, and Pt···Pt bonding. Although Pt_4As_8 is a discrete tetranuclear complex, it interacts with adjacent complexes by weak Pt···Pt stacking interactions to form a 1D chain (Figure 5.11 and Figure

5.12). The Pt···Pt separation of 3.446(2) Å is comparable with that of the mononuclear platinum complexes with aromatic ligands possessing a Pt···Pt interaction.¹³⁴ Square planar platinum(II) complexes often form linear-chain materials with striking spectroscopic properties. In these structures, the planar molecules stack with short Pt···Pt contacts (<3.5 Å), and the Pt···Pt···Pt chain is sometimes slightly zigzag: In analogy to hydrogen bonds, this weak bonding interaction between d⁸ metal centers is a potentially useful tool for the controlled assembly of molecules.

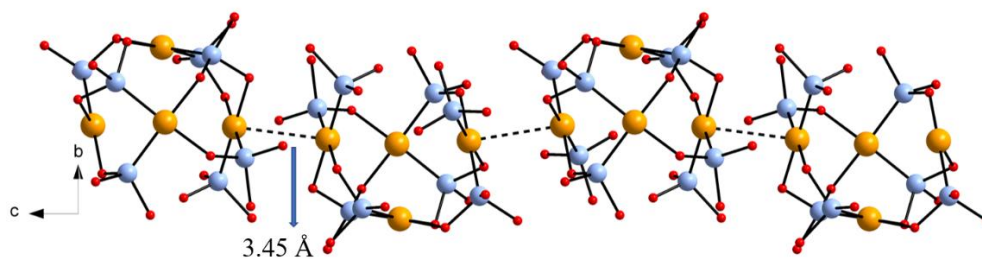


Figure 5.11. Crystal packing diagram of **Pt₄As₈**, Pt orange, As light blue, O red. H atoms are not shown.

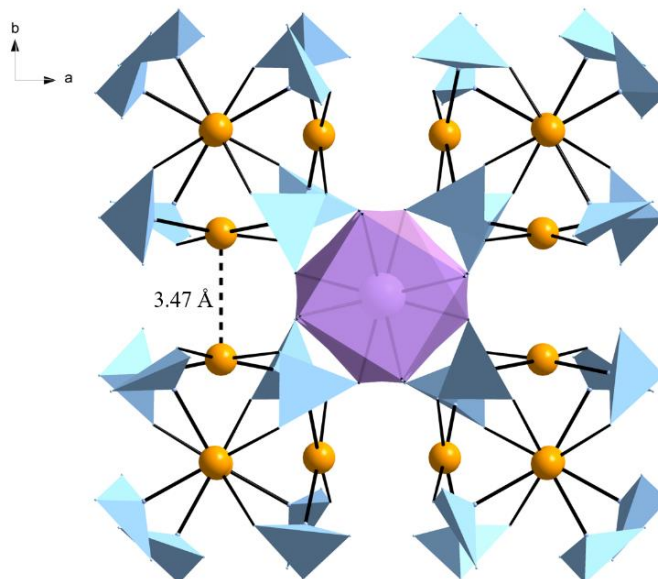


Figure 5.12. Pt···Pt distance in **K₂(Pt₄As₈)₄** fragment. {AsO₃} sky blue tetrahedra, {K₂O₈} purple polyhedral, Pt orange.

The closest precedents for the cluster **Pt₄As₈** are found in arsenious acid complex where the Pd^{II}¹³⁵ and Pt^{II}⁵⁹ centers bind directly to arsenous acid. In Pd^{II} and Pt^{II} complexes, As(OH)₃ is bound to the metal as a Lewis base with arsenic in a distorted tetrahedral and pyramidal environment, respectively. While As^{III} can act as either a Lewis base or a Lewis acid, in **Pt₄As₈** As^{III} acts simultaneously as a Lewis base (As→Pt) and as a Lewis acid (O→As). These multiple intramolecular interactions explain in part the strong Pt–As interaction (2.310(6)–2.316(3) Å) in **Pt₄As₈**. The bond valence sums (BVS) of the As and Pt atoms in **Pt₄As₈** are summarized in Table 5.3. The As₂ atom which only employs the apex As atom engaged in the Pt–As bond formation has a larger BVS than does other three As atoms (+4.06 vs. +3.70). It can be explained by the covalent character of Pt–As bond due to the interaction between hybridized *sp* orbitals of both As and Pt atoms, where part of the bonding density is polarized toward the positively charged arsenic atom leading to a more electropositive As³⁺ center.¹³⁶ A high electron transfer in the As→Pt direction taking place in the Pt–As mode, in agreement with its higher stability compared with the Pt–O mode (mainly because the bond in this case is coordinative).

Table 5.3. Bond valence sum values for Pt and As atoms for **K-Pt₄As₈**.

atom	Bond distance(Å)	BVS value	atom	Bond distance(Å)	BVS value
Pt1	O8 (2.064)	2.043	Pt2	O10 (2.073)	2.031
	O11 (2.070)			O1 (2.077)	
	As1 (2.312)			As1 (2.310)	
	As4 (2.316)			As4 (2.314)	
As1	O1 (1.686)	3.710	As2	O4 (1.558)	4.059
	O2 (1.716)			O5 (1.805)	
	O3 (1.730)			O6 (1.711)	
As3	O7 (1.764)	3.677	As4	O10 (1.704)	3.703
	O8 (1.685)			O11 (1.718)	

	O9 (1.697)			O12 (1.711)	
--	------------	--	--	-------------	--

5.4.2 ^{195}Pt NMR Study

^{195}Pt NMR spectroscopy reveals that the strong Pt–As interaction observed in the solid state persists in aqueous solution (Figures 5.13). We located the expected singlet for $\text{Pt}_2\text{As}_6\text{W}_4$ at -4118 ppm, which confirmed that Pt is in a 2+ oxidation state.

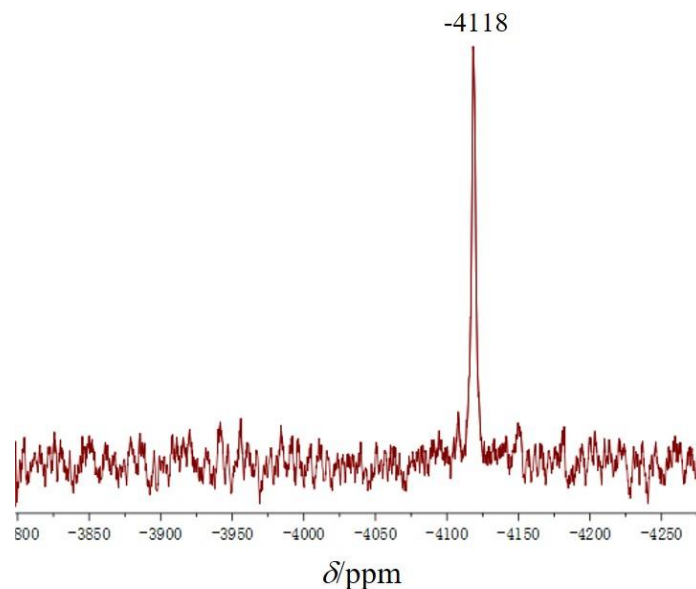


Figure 5.13. ^{195}Pt (D_2O) NMR spectra of $\text{Na-Pt}_2\text{As}_6\text{W}_4$.

5.4.3 Powder XRD Study

We discovered that $\text{K-Pt}_4\text{As}_8$ undergoes a reversible single-crystal-to-single-crystal (SCSC) transformation in the solid state upon rehydration and dehydration, where rehydration was achieved by keeping the sample in an atmosphere of water vapor at room temperature for overnight and dehydration was achieved by heating the compound at 80 °C for 5 h under vacuum. The polyanion Pt_4As_8 crystallizes in the centrosymmetric space group $P4/nnc$ when in the mother liquor or dry in air ($\text{K-Pt}_4\text{As}_8$), even after heating under vacuum, the space group keeps the same ($\text{K-Pt}_4\text{As}_8$ (dehy)). The two crystal structures show the exact same polyanion as confirmed by single-crystal XRD, but the unit cell

volume shrinks significantly from 6332.5(5) to 5080.5(2) Å³ upon heating, and the packing arrangement is noticeable different (Figure 5.14). In **K-Pt₄As₈**, four **Pt₄As₈** tetramers are linked through two potassium cations, resulting in discrete **K₂(Pt₄As₈)₄** fragment. Whereas in **K-Pt₄As₈ (dehy)**, each K atom is coordinated by eight **Pt₄As₈** tetramers resulting a high ordered packing arrangement in the 3D framework.

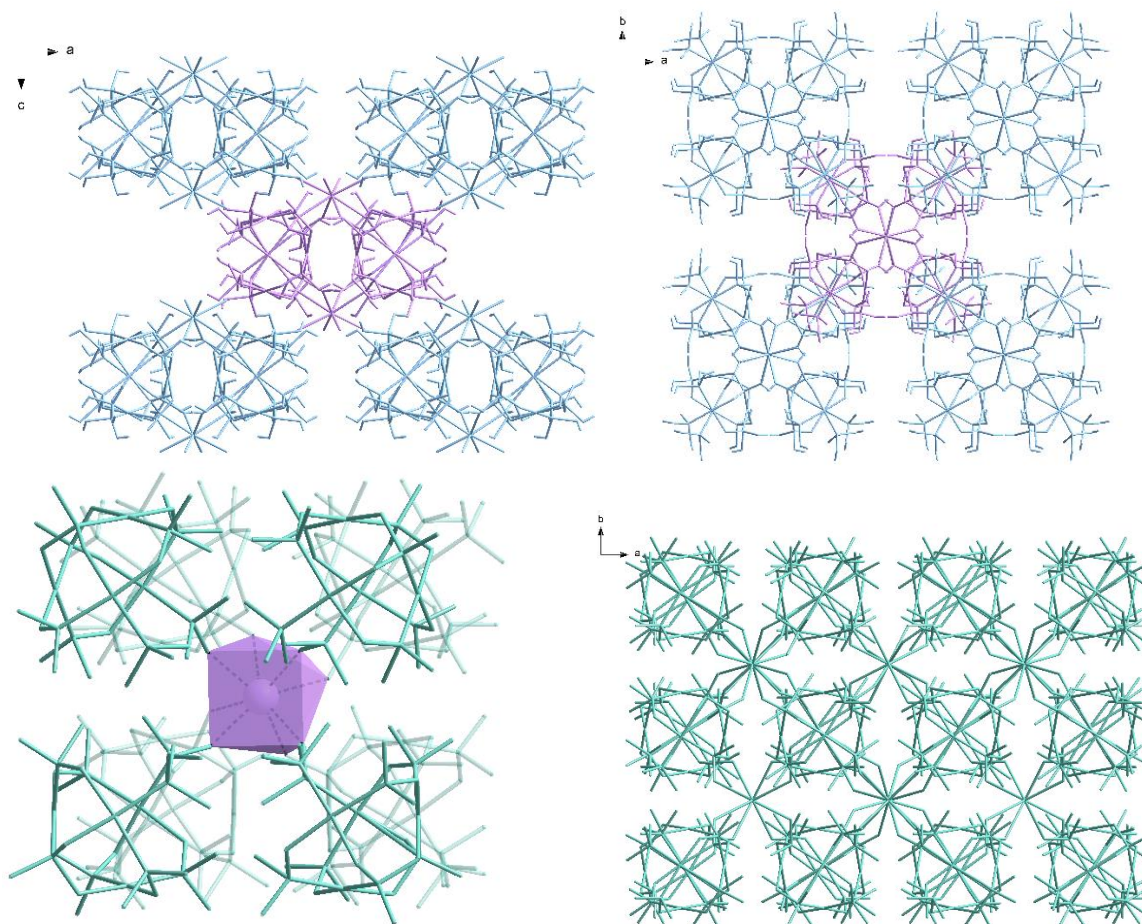


Figure 5.14. Top: Packing diagrams for **K-Pt₄As₈** (top) along *b* and *c* axis. Bottom: the $\{K(Pt_4(AsO_3)_8)_8\}$ fragment (left) and packing diagram (right) along *c* axis of **K-Pt₄As₈ (dehy)**. $\{KO_8\}$ purple polyhedron.

The structural transformation of **K-Pt₄As₈** to **K-Pt₄As₈ (dehy)** upon dehydration by heating was also confirmed by powder-XRD (PXRD) measurements (Figure 5.15). A pure phase of **K-Pt₄As₈** is obtained in the crystals when freshly prepared, but after heating at 80 °C

for 5 h, a transformation to the pure new phase **K-Pt₄As₈ (dehy)** occurs. The transformation from **K-Pt₄As₈** to **K-Pt₄As₈ (dehy)** is fully reversible during a rehydration and dehydration process. Rehydration of **K-Pt₄As₈ (dehy)** in the presence of water vapor at room temperature results in **K-Pt₄As₈** within overnight. If we keep the crystals **K-Pt₄As₈** air drying for two days, there is no new phase appeared. And if we heating at 70 °C for 5 h, we can observe the intermedial state with two phases (Figures 5.16). Thermogravimetric analysis (TGA) studies (Figure 5.17) and infrared spectroscopy (FT-IR) (Figures 5.18) on **K-Pt₄As₈** reiterated the stability of the compound upon dehydration and rehydration. Thus, the interaction of K⁺ ions and direct Pt–As bonding into the **K-Pt₄As₈** induces a drastic improvement in the stability and crystallinity of the compound due to the formation of stable extended supramolecular assembly.

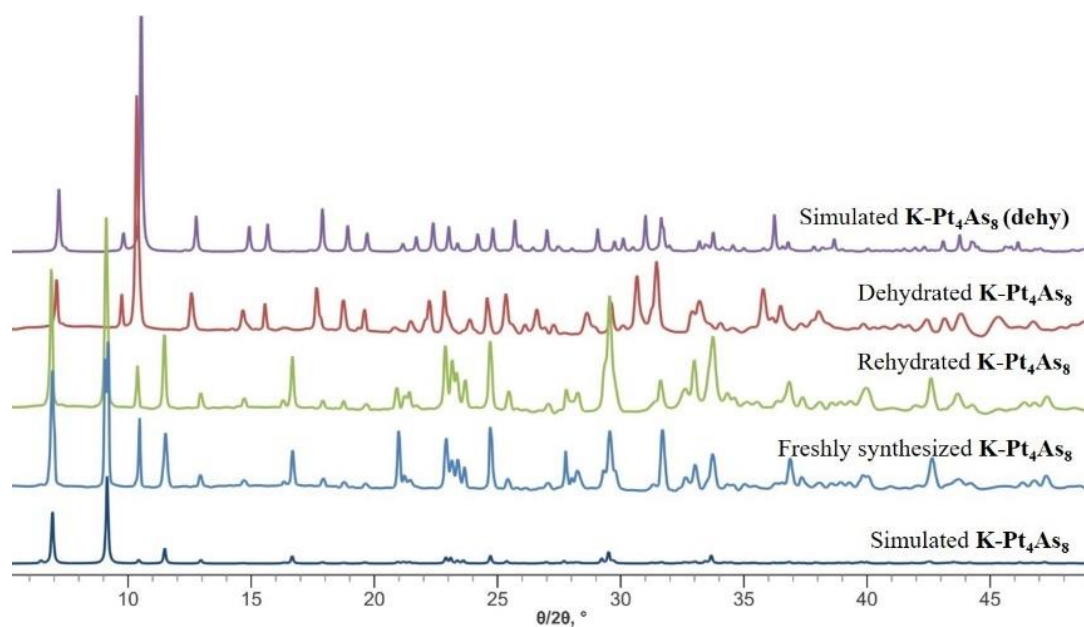


Figure 5.15. Simulated and experimental PXRD patterns (left) of **K-Pt₄As₈** and **K-Pt₄As₈ (dehy)** upon dehydration and rehydration. (simulated diffraction patterns derived from single-crystal data).

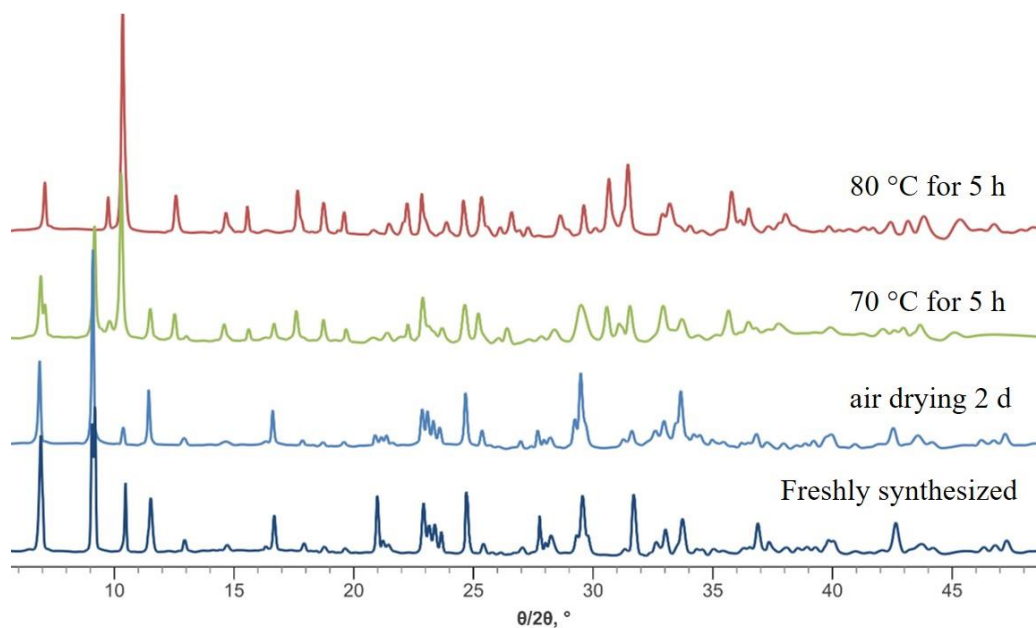


Figure 5.16. PXRD patterns $\text{K-Pt}_4\text{As}_8$ upon dehydration by air drying and heating.

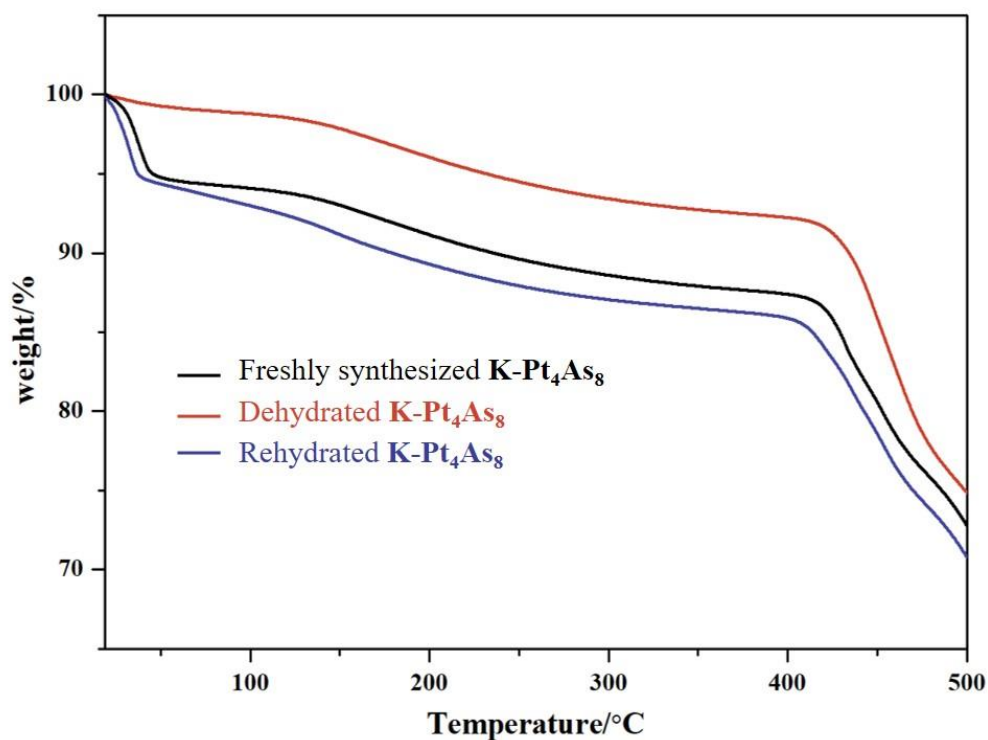


Figure 5.17. TGA curves of freshly prepared, dehydrated, and rehydrated compound $\text{K-Pt}_4\text{As}_8$.

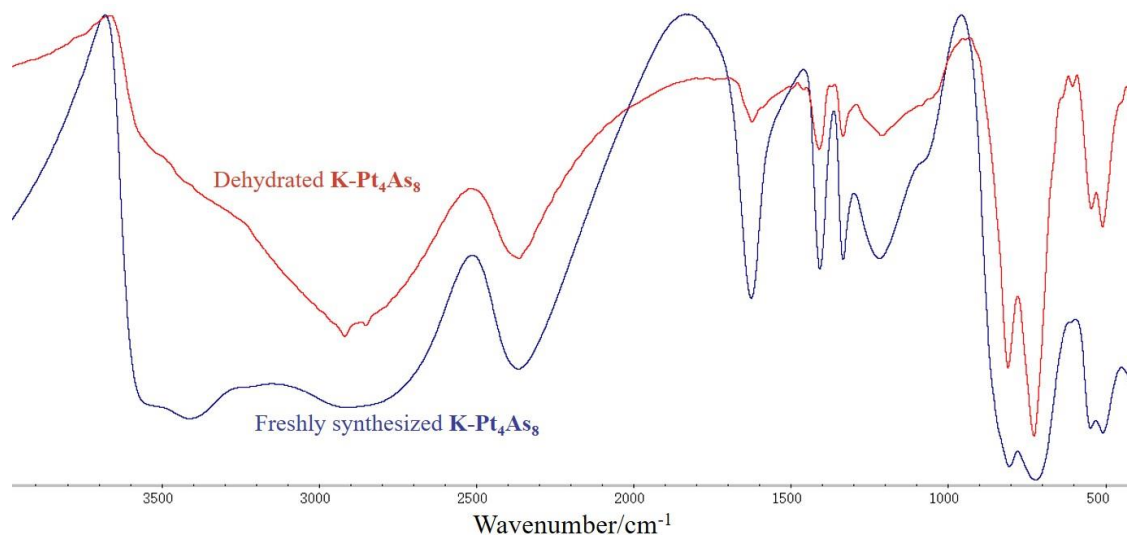


Figure 5.18. FT-IR spectrums of freshly synthesized and dehydrated **K-Pt₄As₈**.

5.4.4 XPS Study

X-ray photoelectron spectroscopy (XPS) measurements were performed on **K-Pt₄As₈** in order to ascertain the oxidation states of Pt and As. The cluster exhibited a Pt 4d_{5/2} band at ~316.6 eV, which is typical for Pt in a 2+ oxidation state (Figure 5.19 (left)). The XPS spectrum of As exhibited characteristic 3p peak at ~145.4 eV, indicating that As is in the 3+ oxidation state (Figure 5.19 (right)). The BVS of Pt²⁺ is calculated to be smaller than +2 (i.e., +0.86) by considering only the Pt–O bonds (Table 5.3). To come up with the BVS of +2 for Pt²⁺, the Pt–As bond should contribute the BVS of +0.57. On the basis of the BVS formula, $s = \exp[(r_0 - r)/B]$ with $s = 0.57$, $B = 0.37$ and $r = 2.31 \text{ \AA}$, we derive $r_0 = 2.11$ for the Pt²⁺–As³⁺ bond. A similar value of $r_0 = 1.99$ was extracted for the Fe²⁺–As³⁺ bond from the FeAs₆ octahedra in nanlingite.⁵⁸

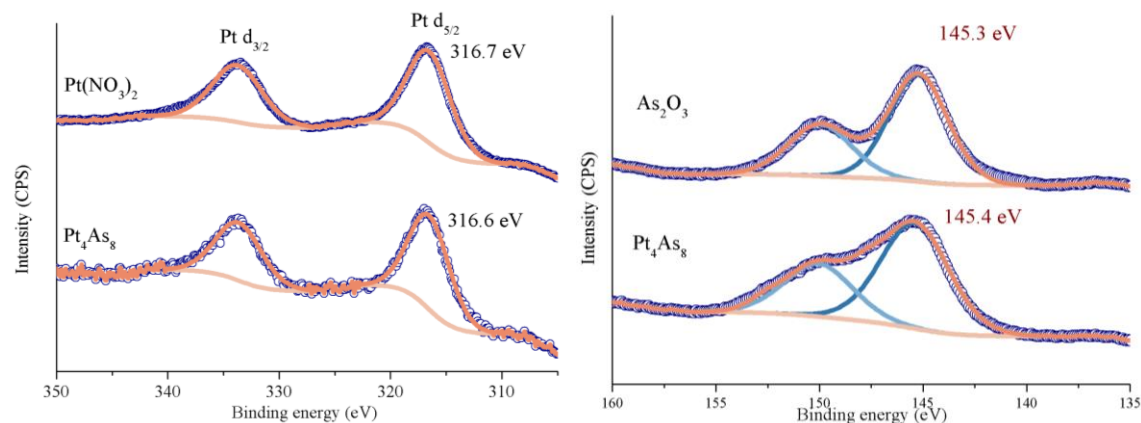


Figure 5.19. X-ray photoelectron spectra and fits for Pt d_{3/2} and d_{5/2} doublet (left) and As 3p doublet (right) of **Pt₄As₈**.

5.4.5 Infrared Spectroscopy Study

In FT-IR spectra of **K-Pt₄As₈** (Figure 5.20), the most intense bands are at 803 cm⁻¹ and 723 cm⁻¹, which most likely arise from $\gamma(\text{O-H}) + \nu_{\text{asym}}(\text{As-O})$ (803 cm⁻¹) and $\nu(\text{As-Pt}) + \nu_{\text{sym}}(\text{As-O})$ (723 cm⁻¹) vibrations, respectively. In the FT-IR spectrum of an aqueous solution of ATO (i.e., arsenous acid), As–O antisymmetric and symmetric stretches were observed at 800 cm⁻¹ and 750 cm⁻¹.¹³⁷ Upon complexation, a significant shift of these bands in the FT-IR spectra of **K-Pt₄As₈** toward lower frequencies is observed. Thus, the presence of this strong vibration at around 700 cm⁻¹ can be used to confirm that the AsO₃ pyramid is bound directly to platinum(II). To our knowledge, **Pt₄As₈** is the only cluster to contain arsenous acid moieties coordinated to the platinum(II) centers. Bands at 3558 cm⁻¹ and 3412 cm⁻¹ in the experimental spectrum of **K-Pt₄As₈** are assigned to asymmetric and symmetric stretching vibrations of the O–H groups. The bands at 2916 and 2316 cm⁻¹ are due to the two OH stretching frequencies of the unit Pt–O–As(OH)₂. The large separation of these bands occurs because of the coupling occurring through the heavy central atom. The band at 1627 cm⁻¹ is assigned to the bending vibration of O–H groups connecting As

atoms and K atoms. The sharp band observed at 1408 cm^{-1} is caused by in-plane bending vibration of O–H groups. The bending vibration of As–OH is at 1220 cm^{-1} as expected. The stretching vibration of Pt–O occurs in 544 and 508 cm^{-1} .

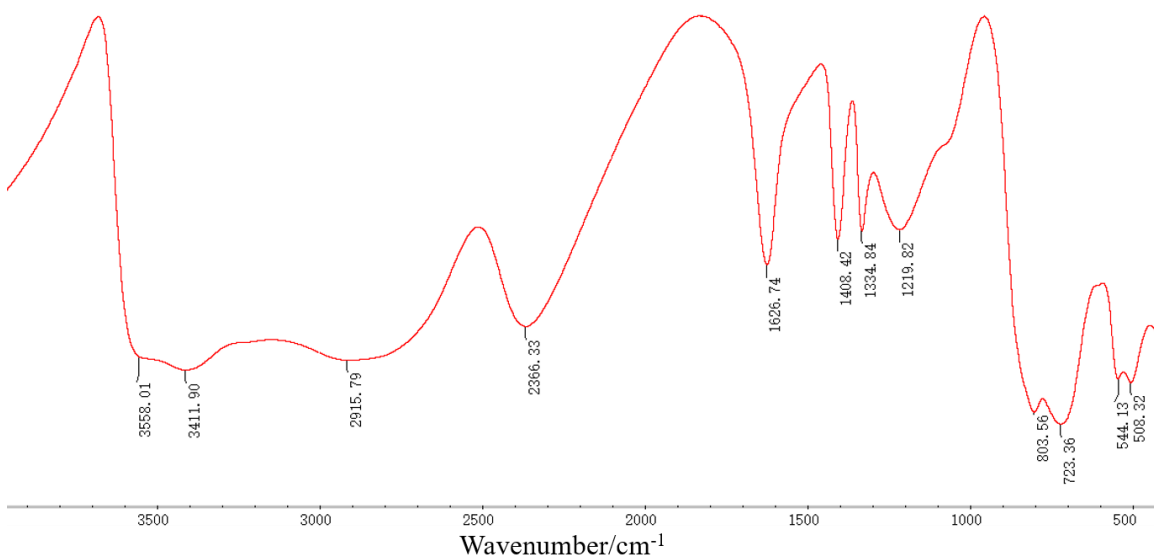


Figure 5.20. FT-IR spectrums of **K-Pt₄As₈**.

5.4.6 Conclusions

In summary, Clusters with arsenite ligands $[\text{Pt}^{\text{IV}}(\text{As}_3\text{O}_6)_2]^{2-}$ (**PtAs₆**) and $[\text{Pt}^{\text{II}}_4(\text{H}_2\text{AsO}_3)_6(\text{HAsO}_3)_2]^{2-}$ (**Pt₄As₈**) have been first prepared in aqueous solutions. And a platinum arsenate(III) heteropolytungstate $[\text{Pt}_2\text{As}_6\text{W}_4\text{O}_{28}]^{10-}$ (**Pt₂As₆W₄**) has been synthesized in aqua media and characterized by ^{195}Pt NMR. This result demonstrates that the coordination of AsO_3^{3-} anions to Pt^{II} ions with both As and O atoms can be achieved. The reversible single-crystal-to-single-crystal transformation of **K-Pt₄As₈** to **K-Pt₄As₈ (dehy)** upon dehydration and rehydration is of particular interest, as concern solid state applications (sorption etc). **Pt₄As₈** is expected to open a wide field of investigation for exotic platinum arsenate(III) cluster.

Chapter VI Organorhodium(III)-containing POMs

RhCp*-containing heteropolyoxotungstates: $[\text{Na}(\text{Rh}^{\text{III}}\text{C}_5\text{Me}_5)_4(\text{cis-As}^{\text{V}}_2\text{W}_{10}\text{O}_{42})]^{5-}$ (**Rh₄As₂W₁₀**) and $[\text{Na}(\text{Rh}^{\text{III}}\text{C}_5\text{Me}_5)_4(\text{tran-P}^{\text{V}}_2\text{W}_{10}\text{O}_{42})]^{5-}$ (**Rh₄P₂W₁₀**), were synthesized by reaction of $(\text{RhCp}^*\text{Cl}_2)_2$ with Na_2WO_4 in aqueous pH 7 Na_2HAsO_4 or Na_2HPO_4 solution at 70 °C. The two polyanions were structurally characterized in the solid state by single-crystal XRD, FT-IR, and TGA and in solution by ^{31}P and ^{13}C NMR.

6.1 Synthesis

Na₅[Na(Rh^{III}C₅Me₅)₄(cis-As^V₂W₁₀O₄₂)]·12H₂O (Na-Rh₄As₂W₁₀)

Method 1: A mixture of $(\text{RhCp}^*\text{Cl}_2)_2$ (10 mg, 0.0162 mmol) and $\text{Na}_9[\text{A-}\alpha\text{-As}^{\text{V}}\text{W}_9\text{O}_{34}]\cdot 18\text{H}_2\text{O}$ (46 mg, 0.0162 mmol) was dispersed in 3 mL 2 M sodium acetate solution (pH 8.8). The solution was heated for 30 min at 70 °C, then cooled to room temperature. Orange crystals were collected after two weeks. The yield: 30% (based on Rh).

Method 2: A mixture of $(\text{RhCp}^*\text{Cl}_2)_2$ (9 mg, 0.0125 mmol) and $\text{Na}_2\text{WO}_4\cdot 2\text{H}_2\text{O}$ (32.9 mg, 0.1 mmol) was dispersed in 2 mL 0.5 M Na_2HAsO_4 solution (pH 7). The solution was heated for 30 min at 70 °C, then cooled to room temperature. Orange crystals were collected after one week by filtration. The yield: 45% (based on Rh). Anal. Calcd (%) for **Na-Rh₄As₂W₁₀**: Rh 10.29, W 45.97, As 3.75, Na 2.87, C 12.01, H 2.29. Found: Rh 10.30, W 46.00, As 4.00, Na 2.70, C 11.96, H 2.61. FT-IR ($\text{KBr}/\text{cm}^{-1}$): 3600–3300 (s) [$\nu(\text{O-H})$ of H_2O], 3000–2900 (w) [$\nu(\text{C-H})$ of methyl groups], 1640 (m) [H_2O bending fundamental mode δ], 1451 (w) [$\nu(\text{C=C})$ of the Cp* groups], 1378 (s) [$\delta(\text{C-H})$ of the methyl groups],

1080–1014 (m) [$\nu(\text{W-O (terminal)})$], 931–716 (m) [$\nu(\text{W-O (bridging)})$], 609–506 [vibrational modes of Rh with Cp* groups].

$\text{Na}_5[\text{Na}(\text{Rh}^{\text{III}}\text{C}_5\text{Me}_5)_4(\text{trans-P}^{\text{V}}_2\text{W}_{10}\text{O}_{42})] \cdot 12\text{H}_2\text{O}$ (Na-Rh₄P₂W₁₀)

A mixture of $(\text{RhCp}^*\text{Cl}_2)_2$ (9 mg, 0.0125 mmol) and $\text{Na}_2\text{WO}_4 \cdot 2\text{H}_2\text{O}$ (32.9 mg, 0.1 mmol) was dispersed in 2 mL 0.5 M Na_2HPO_4 solution (pH 7). The solution was heated for 30 min at 70 °C, then cooled to room temperature. Orange crystals were collected after one week by filtration. The yield: 50% (based on Rh). Anal. Calcd (%) for **Na-2**: Rh 10.52, W 47.00, P 1.58, Na 2.94, C 12.28, H 2.35. Found: Rh 10.36, W 44.10, P 1.70, Na 2.70, C 11.87, H 2.35. FT-IR (KBr/ cm^{-1}): 3600–3300 (s) [$\nu(\text{O-H})$ of H_2O], 3000–2900 (w) [$\nu(\text{C-H})$ of methyl groups], 1635 (m) [H_2O bending fundamental mode δ], 1447 (w) [$\nu(\text{C=C})$ of the Cp* groups], 1380 (s) [$\delta(\text{C-H})$ of the methyl groups], 1081–1015 (m) [$\nu(\text{W-O (terminal)})$], 930–721 (m) [$\nu(\text{W-O (bridging)})$], 610–508 [vibrational modes of Rh with Cp* groups].

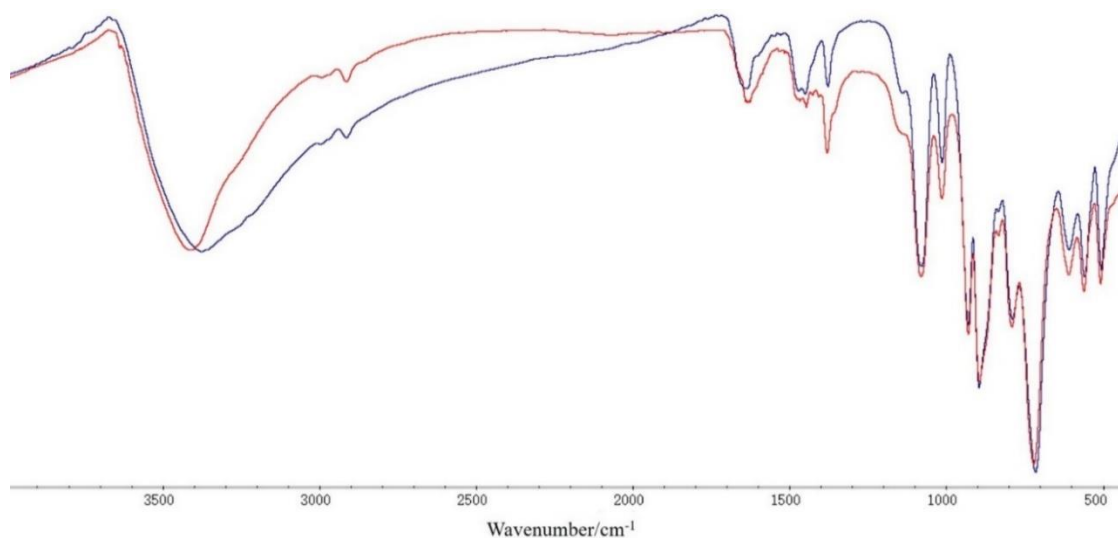


Figure 6.1. FT-IR spectra of **Na-Rh₄As₂W₁₀** (red) and **Na-Rh₄P₂W₁₀** (blue).

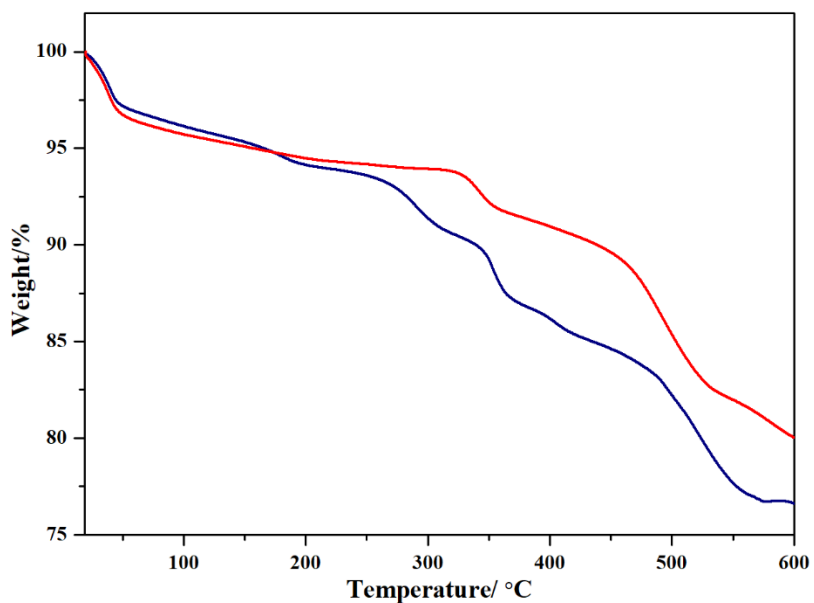


Figure 6.2. Thermograms of **Na-Rh₄As₂W₁₀** (red) and **Na-Rh₄P₂W₁₀** (blue) from room temperature to 500 °C under N₂ atmosphere.

6.2 Single-Crystal XRD Data

Table 6.1. Crystal data and structure refinement for **Na-Rh₄As₂W₁₀** and **Na-Rh₄P₂W₁₀**.

Compound	Na-Rh₄As₂W₁₀	Na-Rh₄P₂W₁₀
empirical formula ^a	Na ₆ Rh ₄ W ₁₀ As ₂ C ₄₀ H ₈₄ O ₅₄	Na ₆ Rh ₄ W ₁₀ P ₂ C ₄₀ H ₈₄ O ₅₄
fw, ^a g mol ⁻¹	3966.87	3878.97
crystal system	Monoclinic	Monoclinic
space group	P2 ₁ /n	P2 ₁ /c
<i>a</i> (Å)	14.2654(3)	18.483(2)
<i>b</i> (Å)	18.1929(4)	13.8800(18)
<i>c</i> (Å)	35.6075(9)	18.120(2)
<i>α</i> (°)	90	90
<i>β</i> (°)	90	106.324(3)
<i>γ</i> (°)	90	90
<i>V</i> (Å ³)	9241.2(4)	4461.1(10)
<i>Z</i>	4	2

D_c (g cm ⁻³)	2.617		2.757	
abs coeff, mm ⁻¹	13.868		13.690	
F(000)	6552		3346	
θ range for data collection, deg	1.538 to 27.676		1.863 to 23.345	
completeness to Θ_{\max}	100 %		99.4%	
index ranges	-18 \leq h \leq 18, -23 \leq k \leq 23, -46 \leq l \leq 46		-20 \leq h \leq 20, -15 \leq k \leq 15, -20 \leq l \leq 20	
reflns collected	100179		56877	
indep reflns	21368		6446	
R (int)	0.1395		0.0875	
abs corn	Semi-empirical equivalents	from	Semi-empirical equivalents	from
data/restraints/param	21368 / 60 / 910		6446 / 249 / 456	
GOF on F^2	1.072		1.740	
$R_1, {}^b wR_2^c$ [$I > 2\sigma(I)$]	0.1036, 0.2940		0.1175, 0.3754	
$R_1, {}^b wR_2^c$ (all data)	0.1759, 0.3490		0.1622, 0.4195	
Δ largest diff peak and hole, e \AA^{-3}	8.273 and -9.380		14.745 and -6.593	
^a The entries are the actual formula units and weights as obtained from bulk elemental analysis.				
^b $R_1 = \Sigma F_o - F_c / \Sigma F_o $. ^c $wR_2 = [\Sigma w(F_o^2 - F_c^2)^2 / \Sigma w(F_o^2)^2]^{1/2}$.				

6.3 Results and Discussion

6.3.1 Solid-State Structure

The tetra-Rh^{III}-containing heteropolytungstates $[\text{Na}(\text{Rh}^{\text{III}}\text{C}_5\text{Me}_5)_4(\text{cis-As}^{\text{V}}_2\text{W}_{10}\text{O}_{42})]^{5-}$ (**Rh₄As₂W₁₀**) and $[\text{Na}(\text{Rh}^{\text{III}}\text{C}_5\text{Me}_5)_4(\text{tran-P}^{\text{V}}_2\text{W}_{10}\text{O}_{42})]^{5-}$ (**Rh₄P₂W₁₀**; Figure 6.3) were synthesized by heating mixture of $(\text{RhCp}^*\text{Cl}_2)_2$ and Na_2WO_4 in a 1:8 molar ratio in aqueous Na_2HAsO_4 or Na_2HPO_4 solution (pH 7) at 70 °C for 30 min using conventional “open beaker” methods. The hydrated salts of **Na-Rh₄As₂W₁₀** and **Na-Rh₄P₂W₁₀** were isolated successively from the same mother liquor as bulk-pure materials,

$\text{Na}_5[\text{Na}(\text{Rh}^{\text{III}}\text{C}_5\text{Me}_5)_4\text{As}^{\text{V}}_2\text{W}_{10}\text{O}_{42}] \cdot 12\text{H}_2\text{O}$ (**Na-Rh₄As₂W₁₀**) and

$\text{Na}_5[\text{Na}(\text{Rh}^{\text{III}}\text{C}_5\text{Me}_5)_4\text{P}^{\text{V}}_2\text{W}_{10}\text{O}_{42}] \cdot 12\text{H}_2\text{O}$ (**Na-Rh₄P₂W₁₀**), in 45% and 50% yield, respectively.

Single-crystal XRD analysis revealed that **Rh₄As₂W₁₀** and **Rh₄P₂W₁₀** crystallize in the triclinic lattice with space group $P2_1/n$ and $P2_1/c$, respectively. Polyanions **Rh₄As₂W₁₀** and **Rh₄P₂W₁₀** are isomeric structures both exhibit V-shaped structure which is composed of two XW_5O_{22} ($\text{X} = \text{As}, \text{P}$) fragments linked *via* corners, in which there are two unique types of RhCp^* moieties. One type of RhCp^* moiety occupies the fourth vacant site of symmetrical pseudo-cuboidal halves arranged by three unique tungsten atoms in a trigonal plane, which thus complete a distorted pseudo-cubane ring. Each of the three oxygen atoms bonded to Rh atom form bridges to two tungsten atoms. For another type, RhCp^* moiety is bonded to the cluster *via* two cisoid terminal oxygen atoms over a face of the distorted cubic core and connect to X ($\text{X} = \text{As}, \text{P}$) atom by oxygen atom. These two oxygen atoms only form bridges to one tungsten atom. The cavity is occupied by a sodium ion, coordinated by eight oxygens of the inner $\{\text{O}_{10}\}$ polyhedron, with idealized C_s point group symmetry. The main difference between the two polyanions is the relative orientation of the two two XW_5O_{22} ($\text{X} = \text{As}, \text{P}$) fragments, either pointing in the same directions (cis isomer, **Rh₄As₂W₁₀**), or in opposite direction (tran isomer, **Rh₄P₂W₁₀**).

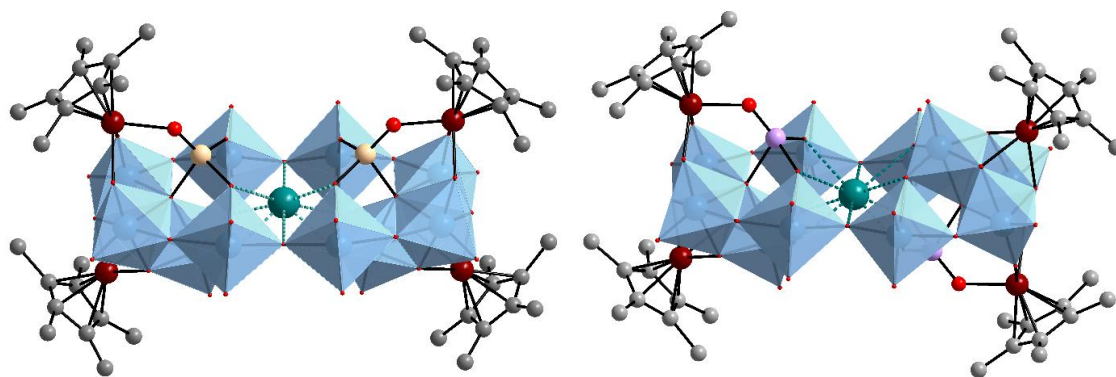


Figure 6.3. Polyhedral representation of the structure of **Rh₄As₂W₁₀** (left) and **Rh₄P₂W₁₀** (right). Color code: Rh (dark red), As (yellow), P (purple), Na (green), O (red), C (grey), WO₆ (blue octahedra).

6.3.2 Multinuclear NMR Study

To complement our solid-state XRD results on **Rh₄As₂W₁₀** and **Rh₄P₂W₁₀** with solution studies, we performed ¹³C NMR measurements on **Na-Rh₄As₂W₁₀** and **Na-Rh₄P₂W₁₀** redissolved in D₂O. ³¹P NMR measurement was also performed on **Rh₄P₂W₁₀**. The ¹³C NMR spectra of polyanions show the expected four peaks at 8.4, 8.0, 93.7 and 92.9 ppm for **Rh₄As₂W₁₀** and 8.4, 8.1, 93.5 and 92.8 ppm for **Rh₄P₂W₁₀** corresponding to the carbons of two structurally inequivalent the methyl groups and the Cp* rings, respectively (Figure 6.4). It is important to mention that the C-Rh coupling which is observed for the (RhCp*Cl₂)₂ was not observed when the monomer is coordinated to the POM. The absence of the C-Rh coupling is attributed to the fluxional behavior of the molecule. As shown in Figure 6.5, the ³¹P NMR spectrum of **Rh₄P₂W₁₀** in H₂O/D₂O exhibits an expected singlet at 2.3 ppm.

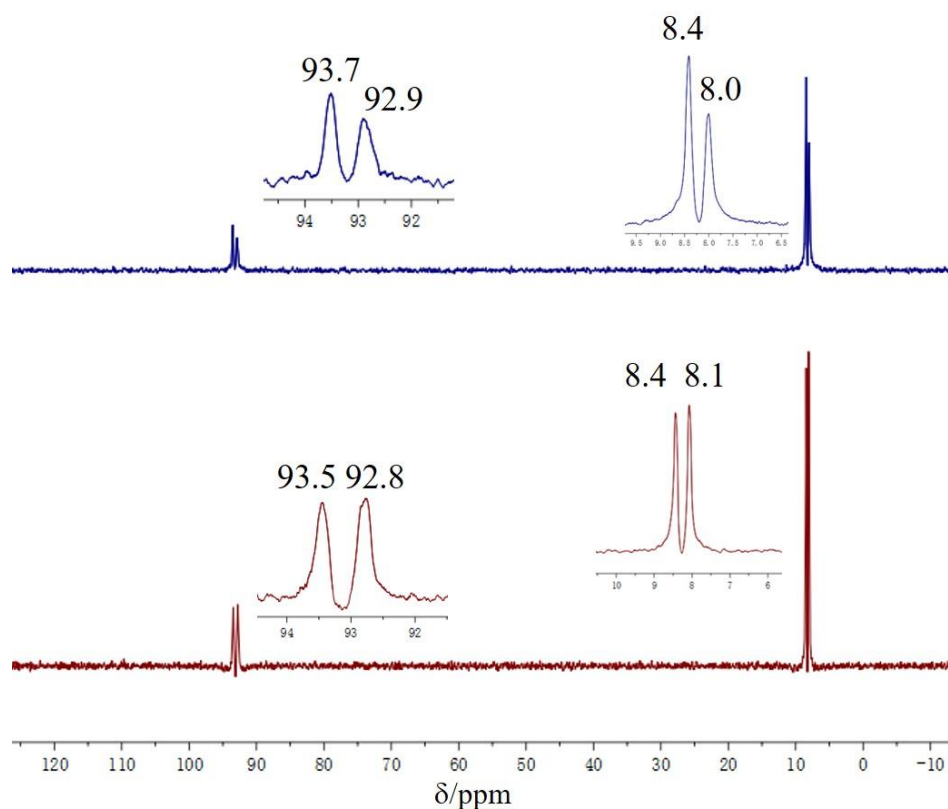


Figure 6.4. ^{13}C NMR spectra ($\text{H}_2\text{O}/\text{D}_2\text{O}$) of $\text{Rh}_4\text{As}_2\text{W}_{10}$ (top) and $\text{Rh}_4\text{P}_2\text{W}_{10}$ (bottom).

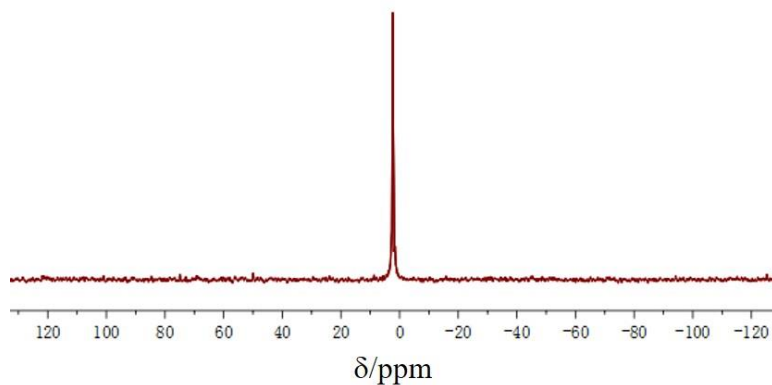


Figure 6.5. ^{31}P NMR spectra ($\text{H}_2\text{O}/\text{D}_2\text{O}$) of $\text{Rh}_4\text{P}_2\text{W}_{10}$.

6.4 Conclusions

In conclusion, two RhCp^* -containing heteropolyoxotungstates have been synthesized and structurally characterized. Both polyanions are composed of two equivalent $\text{AsW}_5\text{O}_{22}$ or

PW₅O₂₂ fragments linked *via* corners and a Na⁺ templating ion, and capped by four RhCp* units, resulting in a structure with idealized C_s point group symmetry.

Chapter VII Summery and Outlook

The work presented in this dissertation comprises three research projects, polyoxo-noble-metalates, noble metal-containing heteropoly- and isopoly- oxometalates and platinum(II/IV) arsenate(III) clusters. The obtained 16 novel compounds have been structurally characterized by a combination of solid-state techniques, such as single-crystal XRD, powder XRD, FT-IR spectroscopy, thermogravimetric, elemental analyses and XPS spectroscopy, and their solution stability was validated by multinuclear (e.g., ^1H , ^{13}C , ^{31}P , and ^{195}Pt) NMR and ESI-MS spectroscopy.

A total of 16 novel noble metal containing compounds have been discovered, associated with the main highlights as follows:

- Expand the family of polyoxoplatinates and polyoxopalladates by synthesizing the first mixed-valent polyoxoplatinate(IV,II) **Pt₇** and the first Pt^{IV}-containing polyoxopalladate(II) **PtPd₆** as discrete inorganic oxo complexes by using simple open beaker and aqueous solution synthetic conditions. In fact, **Pt₇** was shown to be stable in solution for several months, which provides much potential for further studies and applications, e.g. in the catalytic or biomedical directions.
- Synthesize and structurally characterize the first discrete mixed gold-platinum-oxoanion $[\text{Pt}^{\text{IV}}_2\text{Au}^{\text{III}}_3\text{O}_6((\text{CH}_3)_2\text{AsO}_2)_6]^-$ (**Pt₂Au₃**) by using simple one-pot open-beaker techniques. The ^{195}Pt NMR spectrum of redissolved solid **Pt₂Au₃** in water demonstrates solution stability, which provides much potential for further applications of **Pt₂Au₃** in catalysis and biomedicine. The reversible single-crystal-to-single-crystal transformation

of **Na-Pt₂Au₃(a)** to **Na-Pt₂Au₃** upon dehydration and rehydration is of particular interest, as concern solid state.

- Synthesize three new platinum(II/III) isopolytungstates: [Pt₃W₁₁O₄₁]¹⁰⁻ (**Pt₃W₁₁**), [Pt^{II}₂W₅O₁₈((CH₃)₂AsO₂)₂]⁴⁻ (**Pt^{II}₂W₅**), [Pt^{III}₂W₅O₁₈((CH₃)₂AsO₂)₄]⁴⁻ (**Pt^{III}₂W₅**) in aqua media. Exhibit a transformation from **Pt^{II}₂W₅** to **Pt^{III}₂W₅** involving single Pt^{III}-Pt^{III} bond.
- Prepare clusters with arsenite ligands [Pt^{IV}(As₃O₆)₂]²⁻ (**PtAs₆**) and [Pt^{II}₄(H₂AsO₃)₆(HAsO₃)₂]²⁻ (**Pt₄As₈**) in aqueous solutions, as well as a platinum arsenate(III) heteropolytungstate [Pt₂As₆W₄O₂₈]¹⁰⁻ (**Pt₂As₆W₄**) characterized by ¹⁹⁵Pt NMR. This result demonstrates that the coordination of AsO₃³⁻ anions to Pt^{II} ions with both As and O atoms can be achieved. The reversible single-crystal-to-single-crystal transformation of **K-Pt₄As₈** to **K-Pt₄As₈ (dehy)** upon dehydration and rehydration is of particular interest, as concern solid state applications (sorption etc).

The progress summarized above allows us to gain a deeper understanding of polyoxoplatinate, mixed polyoxo-noble metalates, noble metal containing POMs and platinum arsenate(III) chemistry. These polyanions enrich the class of metal-metal bonded and platinum containing compounds, especially can be considered as a synthetic breakthrough in polyoxoplatinate (POPt) and platinum-containing polyoxopalladate (POPd) chemistry. These discoveries allow us to shed light on design and preparation of desirable noble metal-based compounds as bottom-up precursors for supported noble metal nanoparticles.

The following work could be done as an outlook to future research: (i) synthesis of more derivatives of polyoxoplatinates and mixed polyoxo-noble-metalates; (ii) employ multifunctional ligands to provide a new path to synthesize novel polyoxoplatinates; (iii)

investigate the applications (e.g. catalysis, electrochemistry, HER) of obtained polyoxoplatinate, mixed gold-platinum-oxoanion and platinum containing POMs; (iv) expand the binary noble metal-based clusters by other precious metal ions, in order to produce innovative structures and interesting functionalities.

Appendix

Published Articles

1. Mixed Noble Metal-Oxo Clusters: Platinum(IV)-Gold(III) Oxoanion $[\text{Pt}^{\text{IV}}_2\text{Au}^{\text{III}}_3\text{O}_6((\text{CH}_3)_2\text{AsO}_2)_6]^-$
J. Zhang, S. Bhattacharya, A. B. Müller, L. Kiss, C. Silvestru, N. Kuhnert, U. Kortz, *Chem. Commun.*, **2023**. 59, 5918-5921.
2. Pt^{IV} -Containing Hexaplatinate(II) $[\text{Pt}^{\text{IV}}\text{Pt}^{\text{II}}_6\text{O}_6(\text{AsO}_2(\text{CH}_3)_2)_6]^{2-}$ and Hexapalladate(II) $[\text{Pt}^{\text{IV}}\text{Pd}^{\text{II}}_6\text{O}_6(\text{AsO}_2(\text{CH}_3)_2)_6]^{2-}$
J. Zhang, S. Bhattacharya, B. E. Khsara, T. Nisar, A. B. Müller, M. Besora, J. M. Poblet, V. Wagner, N. Kuhnert, U. Kortz, *Inorg. Chem.*, **2023**. (accepted)

Conferences

Oral Contributions

- Jiavao Zhang, Saurav Bhattacharya, Anja B. Müller, Levente Kiss, Cristian Silvestru, Nikolai Kuhnert, Ulrich Kortz. *Discovery of the First Platinum(IV)-Gold(III) Oxoanion: $[\text{Pt}^{\text{IV}}_2\text{Au}^{\text{III}}_3\text{O}_6((\text{CH}_3)_2\text{AsO}_2)_6]^-$* . The 7th Frontiers in Metal Oxide Cluster Science (FMOCS VII), April 11th – 14th, **2023**. Tarragona, Spain
- Jiavao Zhang, Saurav Bhattacharya, Anja B. Müller, Levente Kiss, Cristian Silvestru, Nikolai Kuhnert, Ulrich Kortz. *Discovery of the First Platinum(IV)-Gold(III) Oxoanion: $[\text{Pt}^{\text{IV}}_2\text{Au}^{\text{III}}_3\text{O}_6((\text{CH}_3)_2\text{AsO}_2)_6]^-$* . Chemisches Doktorandenkolloquium GDCh-Ortsverband Bremen WiSe, January 23rd, **2023**. Bremen, Germany

References

1. (a) M. T. Pope, *Heteropoly and Isopoly Oxometalates*. Springer-Verlag: Berlin, 1983; (b) V. W. Day, W. G. Klemperer, *Science*, **1985**, *228*, 533-541; (c) M. T. Pope, A. Müller, *Angew. Chem. Inr. Ed. Engl.*, **1991**, *30*, 34-48.
2. A. Müller, F. Peters, *Chem. Rev.*, **1998**, *98*, 239-271.
3. (a) J. J. Berzelius, *Annalen der Physik*, **1826**, *6*, 369-380; (b) L. Pauling, *J. Am. Chem. Soc.*, **1929**, *51*, 2868-2880; (c) J. F. Keggin, *Nature*, **1933**, *131*, 908-909; (d) J. F. Keggin, *Proc. Roy. Soc. A*, **1934**, *144*, 75-100.
4. (a) H. Wu, *J. Biol. Chem.*, **1920**, *43*, 189-220; (b) B. Dawson, *Acta Crystallogr.*, **1953**, *6*, 113-126.
5. (a) J. S. Anderson, *Nature*, **1937**, *140*, 850; (b) H. T. Evans-Jr, *J. Am. Chem. Soc.*, **1948**, *70*, 1291-1292; (c) H. Kondo, A. Kobayashi, Y. Sasaki, *Acta Crystallogr., Sect. C: Cryst. Struct. Commun.*, **1986**, *42*, 1115-1118.
6. (a) I. Lindqvist, *Arkiv foer Kemi*, **1953**, *5*, 247-250; (b) I. Lindqvist, B. Aronsson, *Arkiv foer Kemi*, **1954**, *7*, 49-52.
7. (a) R. D. Hall, *J. Am. Chem. Soc.*, **1907**, *29*, 5692-5714; (b) J. L. T. Waugh, D. P. Shoemaker, L. Pauling, *Acta Cryst.*, **1954**, *7*, 438-440.
8. R. Strandberg, *Acta Chem. Scand.*, **1973**, *27*, 1004-1018.
9. D. D. Dexter, J. V. Silverton, *J. Am. Chem. Soc.*, **1986**, *90*, 3589-3590.
10. (a) R. D. Peacock, T. J. R. Weakley, *J. Chem. Soc. A*, **1971**, 1836-1839; (b) J. Iball, J. N. Low, T. J. R. Weakley, *J. Chem. Soc., Dalton Trans.*, **1974**, 2021-2024; (c) T. Ozeki, M. Takahashi, T. Yamase, *Acta Crystallogr., Sect. C: Cryst. Struct. Commun.*, **1992**, *48*, 1370-1374; (d) M. Sugeta, T. Yamase, *Bull. Chem. Soc. Jpn.*, **1993**, *66*, 444-449.
11. (a) J. T. Rhule, C. L. Hill, D. A. Judd, *Chem. Rev.*, **1998**, *98*, 327-357; (b) I. V. Kozhevnikov, *Chem. Rev.*, **1998**, *98*, 171-198; (c) A. Müller, S. Roy, *Coord. Chem. Rev.*, **2003**, *245*, 153-166; (d) J. M. Clemente-Juan, E. Coronado, A. Gaita-Arino, *Chem. Soc. Rev.*, **2012**, *41* (22), 7464-7478; (e) L. Chen, W. L. Chen, X. L. Wang, Y. G. Li, Z. M. Su, E. B. Wang, *Chem. Soc. Rev.*, **2019**, *48* (1), 260-284.

References

12. (a) M. T. Pope, A. Müller, *Polyoxometalate Chemistry: From Topology via Self-Assembly to Applications*. Kluwer: Dordrecht: The Netherlands, 2001; (b) U. Kortz, A. Müller, J. van Slageren, J. Schnack, N. S. Dalal, M. Dressel, *Coord. Chem. Rev.*, **2009**, 253 (19-20), 2315-2327; (c) D. L. Long, R. Tsunashima, L. Cronin, *Angew. Chem. Int. Ed. Engl.*, **2010**, 49 (10), 1736-1758; (d) L. Cronin, A. Müller, *Chem. Soc. Rev.*, **2012**, 41 (22), 7333-7334.
13. T. Hori, S. Himeno, O. Tamada, *J. Chem. Soc., Dalton Trans.*, **1996**, 2083-2087.
14. J. Wang, P. Ma, J. Li, J. Niu, *Chem. Res. Chinese U.*, **2007**, 23, 263-267.
15. L. C. W. Baker, J. S. Figgis, *J. Am. Chem. Soc.*, **1970**, 92, 3794-3797.
16. (a) D. L. Kepert, *Inorg. Chem.*, **1969**, 8, 1556-1558; (b) M. T. Pope, *Inorg. Chem.*, **1976**, 15, 2008-2010.
17. (a) X. López, J. M. Poblet, *Inorg. Chem.*, **2004**, 43, 6863-6865; (b) X. López, J. J. Carbó, C. Bo, J. M. Poblet, *Chem. Soc. Rev.*, **2012**, 41, 7537-7371.
18. J. Lehmann, A. Gaita-Ariño, E. Coronado, D. Loss, *Nat. Nanotechnol.*, **2007**, 2, 312-317.
19. S. Bertaina, S. Gambarelli, T. Mitra, B. Tsukerblat, A. Müller, B. Barbara, *Nature*, **2008**, 453, 203-206.
20. X. Ma, H. Li, L. Chen, J. Zhao, *Dalton Trans.*, **2016**, 45 (12), 4935-60.
21. L. Vilà-Nadal, H. N. Miras, *Coordination Chemistry in Polyoxometalates and Metal Clusters*. In *Comprehensive Coordination Chemistry III*, Academic Press: Burlington, 2020.
22. (a) N. V. Izarova, N. Vankova, A. Banerjee, G. B. Jameson, T. Heine, F. Schinle, O. Hampe, U. Kortz, *Angew. Chem. Int. Ed. Engl.* **2010**, 49, 7807-7811; (b) M. Barsukova-Stuckart, N. V. Izarova, R. Barrett, Z. Wang, J. van Tol, H. W. Kroto, N. S. Dalal, B. Keita, D. Heller, U. Kortz, *Chem. Eur. J.* **2012**, 18, 6167-6171; (c) F. Xu, H. N. Miras, R. A. Scullion, D. L. Long, J. Thiel, L. Cronin, *Proc. Natl. Acad. Sci. U. S. A.*, **2012**, 109 (29), 11609-11612; (d) N. V. Izarova, M. T. Pope, U. Kortz, *Angew. Chem. Int. Ed. Engl.*, **2012**, 51 (38), 9492-9510; (e) P. Yang, Y. Xiang, Z. Lin, B. S. Bassil, J. Cao, L. Fan, Y. Fan, M. X. Li, P. Jimenez-Lozano, J. J. Carbo, J. M. Poblet, U. Kortz, *Angew. Chem. Int. Ed. Engl.* **2014**, 53, 11974-11978; (f) P. Yang, U. Kortz, *Acc. Chem. Res.*, **2018**, 51 (7), 1599-1608.

References

23. E. V. Chubarova, M. H. Dickman, B. Keita, L. Nadjjo, F. Miserque, M. Mifsud, I. W. C. E. Arends, U. Kortz, *Angew. Chem. Int. Ed. Engl.*, **2008**, *47* (49), 9542-9546.
24. N. V. Izarova, R. N. Biboum, B. Keita, M. Mifsud, I. W. Arends, G. B. Jameson, U. Kortz, *Dalton. Trans.*, **2009**, 9385-9387.
25. M. Barsukova-Stuckart, N. V. Izarova, G. B. Jameson, V. Ramachandran, Z. Wang, J. van Tol, N. S. Dalal, R. N. Biboum, B. Keita, L. Nadjjo, U. Kortz, *Angew. Chem. Int. Ed. Engl.*, **2011**, *50* (11), 2639-2642.
26. S. Bhattacharya, W. W. Ayass, D. H. Taffa, A. Schneemann, A. L. Semrau, S. Wannapaiboon, P. J. Altmann, A. Pöthig, T. Nisar, T. Balster, N. C. Burtch, V. Wagner, R. A. Fischer, M. Wark, U. Kortz, *J. Am. Chem. Soc.*, **2019**, *141*, 3385–3389.
27. (a) S. Bhattacharya, U. Basu, M. Haouas, P. Su, M. F. Espenship, F. Wang, A. Sole-Daura, D. H. Taffa, M. Wark, J. M. Poblet, J. Laskin, E. Cadot, U. Kortz, *Angew. Chem. Int. Ed. Engl.*, **2021**, *60* (7), 3632-3639; (b) S. Bhattacharya, X. Ma, A. S. Mougharbel, M. Haouas, P. Su, M. F. Espenship, D. H. Taffa, H. Jaensch, A. J. Bons, T. Stuerzer, M. Wark, J. Laskin, E. Cadot, U. Kortz, *Inorg. Chem.*, **2021**, *60* (22), 17339-17347.
28. S. Bhattacharya, A. Barba-Bon, T. A. Zewdie, A. B. Müller, T. Nisar, A. Chmielnicka, I. A. Rutkowska, C. J. Schurmann, V. Wagner, N. Kuhnert, P. J. Kulesza, W. M. Nau, U. Kortz, *Angew. Chem. Int. Ed. Engl.*, **2022**, *61* (25), e202203114.
29. X. Ma, S. Bhattacharya, T. Nisar, A. B. Müller, V. Wagner, N. Kuhnert, U. Kortz, *Chem. Commun.*, **2023**, *59* (7), 904-907.
30. N. V. Izarova, A. Kondinski, N. Vankova, T. Heine, P. Jager, F. Schinle, O. Hampe, U. Kortz, *Chem. Eur. J.*, **2014**, *20* (28), 8556-8560.
31. P. Yang, Y. Xiang, Z. Lin, Z. Lang, P. Jimenez-Lozano, J. J. Carbo, J. M. Poblet, L. Fan, C. Hu, U. Kortz, *Angew. Chem. Int. Ed. Engl.*, **2016**, *55* (51), 15766-15770.
32. M. Pley, M. S. Wickleder, *Angew. Chem. Int. Ed. Engl.*, **2004**, *43* (32), 4168-4170.
33. N. V. Izarova, N. Vankova, T. Heine, R. N. Biboum, B. Keita, L. Nadjjo, U. Kortz, *Angew. Chem. Int. Ed. Engl.*, **2010**, *49* (10), 1886-1889.
34. M. Delferro, C. Graiff, L. Elviri, G. Predieri, *Dalton. Trans.*, **2010**, *39* (19), 4479-4481.
35. U. Lee, A. Kobayashi, Y. Sasaki, *Acta Cryst.*, **1983**, *C39*, 817-819.
36. U. Lee, Y. Sasaki, *Chem. Lett.*, **1984**, 1297-1300.
37. U. Lee, H.-C. Joo, K.-M. Park, T. Ozeki, *Acta Cryst.*, **2003**, *C59*, 152-155.

References

38. V. W. Day, J. C. Goloboy, W. G. Klemperer, *Eur. J. Inorg. Chem.*, **2009**, 5079-5087.
39. M. Kato, C. N. Kato, *Inorg. Chem. Commun.*, **2011**, *14*, 982-985.
40. C. N. Kato, Y. Morii, S. Hattori, R. Nakayama, Y. Makino, H. Uno, *Dalton Trans.*, **2012**, *41*, 10021-10027.
41. C. M. Tourné, G. F. Tourné, F. Zonnevillle, *J. Chem. Soc. Dalton Trans.*, **1991**, 143-155.
42. M. N. Sokolov, S. A. Adonin, E. V. Peresyphkina, V. P. Fedin, *Dalton Trans.*, **2012**, *41* (39), 11978-11979.
43. U. Lee, H. C. Joo, K. M. Park, S. S. Mal, U. Kortz, B. Keita, L. Nadjo, *Angew. Chem. Int. Ed. Engl.*, **2008**, *47* (4), 793-796.
44. N. Vankova, T. Heine, U. Kortz, *Eur. J. Inorg. Chem.*, **2009**, *2009* (34), 5102-5108.
45. P. A. Abramov, C. Vicent, N. B. Kompankov, A. L. Gushchin, M. N. Sokolov, *Chem. Commun.*, **2015**, *51* (19), 4021-4023.
46. Z. Lin, N. V. Izarova, A. Kondinski, X. Xing, A. Haider, L. Fan, N. Vankova, T. Heine, B. Keita, J. Cao, C. Hu, U. Kortz, *Chem. Eur. J.*, **2016**, *22* (16), 5514-9.
47. C. N. Kato, S. Nagatani, T. Mizuno, *Eur. J. Inorg. Chem.*, **2018**, *2019* (3-4), 517-522.
48. F. Y. Yu, Z. L. Lang, L. Y. Yin, K. Feng, Y. J. Xia, H. Q. Tan, H. T. Zhu, J. Zhong, Z. H. Kang, Y. G. Li, *Nat. Commun.*, **2020**, *11* (1), 490.
49. (a) M. B. Hamida, M. S. Wickleder, *Z. Anorg. Allg. Chem.*, **2006**, *632* (14), 2195-2197; (b) S. Lösel, H. Hillebrecht, *Z. Anorg. Allg. Chem.*, **2008**, *634* (12-13), 2299-2302; (c) R. David, H. Kabbour, S. Colis, O. Mentre, *Inorg. Chem.*, **2013**, *52* (23), 13742-13750; (d) R. David, H. Kabbour, A. Pautrat, N. Touati, M. H. Whangbo, O. Mentre, *Angew. Chem. Int. Ed. Engl.*, **2014**, *53* (12), 3111-3114.
50. P. L. Smedley, D. G. Kinniburgh, *Appl. Geochem.*, **2002**, *17*, 517-568.
51. (a) P. A. O'Day, *Elements*, **2006**, *2* (2), 77-83; (b) J. Majzlan, P. Drahota, M. Filippi, *Reviews in Mineralogy and Geochemistry*, **2014**, *79* (1), 17-184.
52. (a) V. I. Privalov, V. V. Lapkin, V. P. Tarasov, Y. A. Buslaev, *Applied Magnetic Resonance*, **1990**, *1*, 445-456; (b) D. Min, R. D. Larsen, K. Emerson, E. H. Abbott, *Inorg. Chem.*, **1990**, *29* (1), 73-76.
53. P. Betz, A. Bino, *J. Am. Chem. Soc.*, **1988**, *110*, 902-903.

References

54. D. Vasilchenko, S. Berdugin, S. Tkachev, I. Baidina, G. Romanenko, O. Gerasko, S. Korenev, *Inorg. Chem.*, **2015**, *54* (10), 4644-4651.
55. A. Rajan, M. E. Mahmoud, F. Wang, S. Bhattacharya, A. S. Mougharbel, X. Ma, A. B. Müller, T. Nisar, D. H. Taffa, J. M. Poblet, N. Kuhnert, V. Wagner, M. Wark, U. Kortz, *Inorg. Chem.*, **2022**, *61* (30), 11529-11538.
56. T. Araki, P. B. Moore, *Am. Mineral.*, **1981**, *66*, 1263-1273.
57. F. Pertlik, *Monatsh. Chem.*, **1986**, *117*, 1257-1261.
58. Z. Yang, G. Giester, K. Ding, E. Tillmanns, *Eur. J. Mineral.*, **2011**, *23* (1), 63-71.
59. D. U. Miodragovic, J. A. Quentzel, J. W. Kurutz, C. L. Stern, R. W. Ahn, I. Kandela, A. Mazar, T. V. O'Halloran, *Angew. Chem. Int. Ed. Engl.*, **2013**, *52* (41), 10749-10752.
60. (a) P. J. Domaille, W. H. Knoth, *Inorg. Chem.*, **1983**, *22*, 818-822; (b) R. G. Finke, B. Rapko, P. J. Domaille, *Organometallics*, **1986**, *5*, 175-178.
61. K. Asakura, K. Kitamura-Bando, K. Isobe, H. Arakawa, Y. Iwasawa, *J. Am. Chem. Soc.*, **1990**, *112*, 3242.
62. K. Kitamura-Bando, K. Asakura, H. Arakawa, Y. Sugi, K. Isobe, Y. Iwasawa, *J. Chem. Soc., Chem. Commun.*, **1990**, 253.
63. C. J. Besecker, V. W. Day, W. G. Klemperer, M. R. Thompson, *J. Am. Chem. Soc.*, **1984**, *106*, 4125.
64. (a) D. J. Edlund, R. J. Saxton, D. K. Lyon, R. G. Finke, *Organometallics*, **1988**, *7*, 1962; (b) R. G. Finke, C. A. Green, B. Rapko, *Inorg. Synth.*, **1990**, *27*, 128; (c) R. G. Finke, D. K. Lyon, K. Nomiya, T. J. R. Weakley, *Acta Crystallogr.*, **1990**, *C46*, 1592.
65. K. Nomiya, C. Nozaki, A. Kano, T. Taguchi, K. Ohsawa, *J. Organomet. Chem.*, **1997**, *533*, 153-159.
66. (a) H. K. Chae, W. G. Klemperer, V. W. Day, *Inorg. Chem.*, **1989**, *28*, 1423; (b) Y. Hayashi, Y. Ozawa, K. Isobe, *Inorg. Chem.*, **1991**, *30*, 1025-1033.
67. (a) K. Nomiya, T. Hasegawa, *Chem. Lett.*, **2000**, *29*, 410-411; (b) K. Nomiya, Y. Sakai, Y. Yamada, T. Hasegawa, *Dalton Trans.*, **2001**, 52-56; (c) K. Nomiya, Y. Sakai, T. Hasegawa, *Dalton Trans.*, **2002**, 252-258.
68. V. Singh, P. Ma, M. G. Drew, J. Niu, J. Wang, G.-X. Jin, *Inorg. Chem.*, **2017**, *56*, 12520-12528.

References

69. K. Nishikawa, K. Kido, J. I. Yoshida, T. Nishioka, I. Kinoshita, B. K. Breedlove, Y. Hayashi, A. Uehara, K. Isobe, *Appl. Organomet. Chem.*, **2003**, *17*, 446-448.
70. V. Singh, P. Ma, M. G. Drew, J. Wang, J. Niu, *Dalton Trans.*, **2018**, *47*, 13870-13879.
71. P. A. Abramov, M. Sokolov, A. Virovets, S. Floquet, M. Haouas, F. Taulelle, E. Cadot, C. Vicent, V. Fedin, *Dalton Trans.*, **2015**, *44*, 2234-2239.
72. M. Girardi, D. Platzer, S. Griveau, F. Bedioui, S. Alves, A. Proust, S. Blanchard, *Eur. J. Inorg. Chem.*, **2019**, 387-393.
73. A. S. Mougharbel, S. Ahmedi, S. Bhattacharya, A. Rajan, U. Kortz, *ACS Omega*, 2021, *6*, 34494-34500
74. (a) M. P. Wiesenfeldt, Z. Nairoukh, T. Dalton, F. Glorius, *Angew. Chem. Int. Ed. Engl.*, **2019**, *58* (31), 10460-10476; (b) L. Zhang, M. Zhou, A. Wang, T. Zhang, *Chem. Rev.*, **2020**, *120* (2), 683-733; (c) C. Gao, F. Lyu, Y. Yin, *Chem. Rev.*, **2021**, *121* (2), 834-881.
75. (a) I. Chakraborty, T. Pradeep, *Chem. Rev.*, **2017**, *117* (12), 8208-8271; (b) Y. Du, H. Sheng, D. Astruc, M. Zhu, *Chem. Rev.*, **2020**, *120* (2), 526-622.
76. Q.-M. Wang, Y.-M. Lin, K.-G. Liu, *Acc. Chem. Res.*, **2015**, *48*, 1570-1579.
77. *APEX suite of crystallographic software, APEX 3, version 2015.5-2*. Bruker AXS Inc., Madison, Wisconsin, USA, 2015.
78. *CrysAlisPro Software System, Version 1.171.38.41*. Rigaku Oxford Diffraction.
79. SAINT, Version 7.56a and SADABS Version 2008/1, Bruker AXS Inc., Madison, Wisconsin, USA, 2008.
80. ABSPACK, SCALE. "Empirical absorption correction." *CrysAlis Pro-Software Package*, Rigaku Oxford Diffraction, 2022.
81. G. M. Sheldrick, "SHELXL-2014", University of Göttingen, Göttingen, Germany, 2014.
82. A. L. Spek, PLATON, A Multipurpose Crystallographic Tool, Utrecht University, Utrecht, The Netherlands, 2010.
83. I. D. Brown, D. Altermatt, *Acta Crystallogr.*, **1985**, *B41*, 244-247.
84. C. White, A. Yates, P. Maitlis, D. Heinekey, *Inorg. Synth.*, **1992**, *29*, 228-234.
85. R. Contant, R. Thouvenot, Y. Dromzée, A. Proust, P. Gouzerh, *J. Clust. Sci.*, **2006**, *17*, 317-331.

References

86. (a) D. Zhao, J. Feng, Q. Huo, N. Melosh, G. H. Fredrickson, B. F. Chmelka, G. D. Stucky, *Science*, **1998**, *279*, 548-552; (b) D. Zhao, Q. Huo, J. Feng, B. F. Chmelka, G. D. Stucky, *J. Am. Chem. Soc.*, **1998**, *120*, 6024-6036.
87. (a) C. Lee, W. Yang, R. G. Parr, *Phys. Rev. B*, **1988**, *37*, 785-789; (b) A. D. Becke, *J. Chem. Phys.* **1992**, *96*, 2155-2160.
88. (a) N. C. Handy, A. J. Cohen, *Mol. Phys.* **2001**, *99*, 403-412; (b) W.-M. Hoe, A. J. Cohen, N. C. Handy, *Chem. Phys. Lett.* **2001**, *341*, 319-328; (c) J. P. Perdew, K. Burke, M. Ernzerhof, *Phys. Rev. Lett.* **1996**, *77*, 3865-3868.
89. (a) W. J. Hehre, R. Ditchfield, J. A. Pople, *J. Chem. Phys.* **1972**, *56*, 2257-2261; (b) P. C. Hariharan, J. A. Pople, *Theor. Chem. Acc.* **1973**, *28*, 213-222; (c) M. M. Francl, W. J. Pietro, W. J. Hehre, J. S. Binkley, D. J. DeFrees, J. A. Pople, M. S. Gordon, *J. Chem. Phys.* **1982**, *77*, 3654-3665.
90. (a) P. J. Hay, W. R. Wadt, *J. Chem. Phys.* **1985**, *82*, 270-83; (b) W. R. Wadt, P. J. Hay, *J. Chem. Phys.* **1985**, *82*, 284-98.
91. E. Cancès, B. Mennucci, J. Tomasi, *J. Chem. Phys.* **1997**, *107*, 3032-3041.
92. Gaussian 16, Revision A.03, M. J. Frisch, G. W. Trucks, H. B. Schlegel, G. E. Scuseria, M. A. Robb, J. R. Cheeseman, G. Scalmani, V. Barone, G. A. Petersson, H. Nakatsuji, X. Li, M. Caricato, A. V. Marenich, J. Bloino, B. G. Janesko, R. Gomperts, B. Mennucci, H. P. Hratchian, J. V. Ortiz, A. F. Izmaylov, J. L. Sonnenberg, D. Williams-Young, F. Ding, F. Lipparini, F. Egidi, J. Goings, B. Peng, A. Petrone, T. Henderson, D. Ranasinghe, V. G. Zakrzewski, J. Gao, N. Rega, G. Zheng, W. Liang, M. Hada, M. Ehara, K. Toyota, R. Fukuda, J. Hasegawa, M. Ishida, T. Nakajima, Y. Honda, O. Kitao, H. Nakai, T. Vreven, K. Throssell, J. A. Montgomery, J. E. Peralta, F. Ogliaro, M. J. Bearpark, J. J. Heyd, E. N. Brothers, K. N. Kudin, V. N. Staroverov, T. A. Keith, R. Kobayashi, J. Normand, K. Raghavachari, A. P. Rendell, J. C. Burant, S. S. Iyengar, J. Tomasi, M. Cossi, J. M. Millam, M. Klene, C. Adamo, R. Cammi, J. W. Ochterski, R. L. Martin, K. Morokuma, O. Farkas, J. B. Foresman, D. J. Fox, Gaussian, Inc., Wallingford CT, 2016.
93. ADF 2019.306, SCM, Theoretical Chemistry, Vrije Universiteit, Amsterdam, The Netherlands, <http://www.scm.com>.
94. E. Van Lenthe, E. J. Baerends, *J. Comput. Chem.* **2003**, *24*, 1142-1156.

References

95. E. Van Lenthe, E. J. Baerends, J. G. Snijders, *J. Chem. Phys.* **1993**, *99* (6), 4597-4610.
96. C. C. Pye, T. Ziegler, *Theor. Chem. Acc.* **1999**, *101*, 396-408.
97. J. Autschbach, *Chem. Phys. Chem.* **2009**, *10*, 2274-2283.
98. (a) M. Pascual-Borràs, X. López, A. Rodríguez-Forteza, R. J. Errington, J. M. Poblet, *Chem. Sci.* **2014**, *5*, 2031; (b) A. Kondinski, N. Vankova, F. Schinle, P. Jäger, O. Hampe, U. Kortz, T. Heine, *Eur. J. Inorg. Chem.* **2014**, 3771-3778; (c) M. Pascual-Borràs, X. López, J. M. Poblet, *Phys. Chem. Chem. Phys.* **2015**, *17*, 8723.
99. M. Swart, M. Solà, F. M. Bickelhaupt, *J. Chem. Phys.* **2009**, *131*(9), 094103.
100. A. Stanislaus, B. H. Cooper, *Catal. Rev.: Sci. Eng.*, **1994**, *36* (1), 75-123.
101. (a) M. Viniegra, G. Córdoba, R. Gómez, *J. Mol. Catal.*, **1990**, *58*, 107; (b) R. A. Saymeh, H. M. Asfour, W. A. Tuaimen, *Asian J. Chem.*, **1997**, *9*, 350; (c) A. K. Neyestanaki, P. Mäki-Arvela, H. Backman, H. Karhu, T. Salmi, J. Väyrynen, D. Y. Murzin, *Journal of Molecular Catalysis A: Chemical*, **2003**, *193*, 237-250.
102. P. G. Menon, *Chem. Rev.*, **1994**, *94*, 1021-1046.
103. J. W. Peck, B. E. Koel, *J. Am. Chem. Soc.*, **1996**, *118*, 2708.
104. Y. Inuone, J. M. Herrmann, H. Schmidt, R. L. Burwell, J. B. Butt, J. B. Cohen, *J. Catal.*, **1978**, *53*, 401.
105. W. W. Ayass, J. F. Minambres, P. Yang, T. Ma, Z. Lin, R. Meyer, H. Jaensch, A. J. Bons, U. Kortz, *Inorg. Chem.*, **2019**, *58*, 5576-5582.
106. J. Wang, L. Huang, Q. Li, *Applied Catalysis A: General*, **1998**, *175*, 191-199.
107. Y. Wu, Y. Chai, J. Li, H. Guo, L. Wen, C. Liu, *Catal. Commun.*, **2015**, *64*, 110-113.
108. F. Letellier, J. Blanchard, K. Fajerwerg, C. Louis, M. Breysse, D. Guillaume, D. Uzio, *Catal. Lett.*, **2006**, *110*, 115-124.
109. (a) G. Jander, G. Krien, *Z. Anorg. Allg. Chem.*, **1960**, *304*, 154-163; (b) P. G. Jones, H. Rumpel, E. Schwarzmann, G. M. Sheldrick, *Acta Crystallogr., Sect. B.*, **1979**, *35*, 1435-1437; (c) D. Vlassopoulos, S. A. Wood, *Geochimica et Cosmochimica Acta*, **1990**, *54*, 3-12.
110. M. A. Cinellu, G. Minghetti, M. V. Pinna, S. Stoccoro, A. Zucca, M. Manassero, M. Sansoni, *J. Chem. Soc., Dalton Trans.*, **1998**, 1735-1741.
111. P. G. Jones, *Acta Crystallogr. Sect. C.*, **1984**, *40*, 804-805.

References

112. (a) M. G. Miles, G. E. Glass, R. S. Tobias, *J. Am. Chem. Soc.*, **1966**, *88*, 5738–5744; (b) G. E. Glass, J. H. Konnert, M. G. Miles, D. Britton, R. S. Tobias, *J. Am. Chem. Soc.*, **1968**, *90*, 1131–1138; (c) S. J. Harris, R. S. Tobias, *Inorg. Chem.*, **1969**, *8*, 2259–2264.
113. (a) A. Chaudhary, A. Mohammad, S. M. Mobin, *Cryst. Growth Des.*, **2017**, *17*, 2893–2910; (b) F. Hu, X. Bi, X. Chen, Q. Pan, Y. Zhao, *Chem. Lett.*, **2021**, *50* (5), 1015–1029; (c) E. Fernandez-Bartolome, A. Martinez-Martinez, E. Resines-Urien, L. Piñeiro-Lopez, J. S. Costa, *Coord. Chem. Rev.*, **2022**, *452*, 214281.
114. (a) S. Reinoso, M. H. Dickman, A. Praetorius, U. Kortz, *Acta Crystallogr.*, **2008**, *E64*, m614–m615; (b) L.-Z. Zhang, W. Gu, Z. Dong, X. Liu, B. Li, *CrystEngComm*, **2008**, *10* (10), 1318–1320.
115. (a) A. Iturrospe, L. San Felices, S. Reinoso, B. Artetxe, L. Lezama, J. M. Gutiérrez-Zorrilla, *Cryst. Growth Des.*, **2014**, *14* (5), 2318–2328; (b) L. Fernández-Navarro, A. Iturrospe, S. Reinoso, B. Artetxe, E. Ruiz-Bilbao, L. S. Felices, J. M. Gutiérrez-Zorrilla, *Cryst. Growth Des.*, **2020**, *20*, 3499–3509.
116. M. Tahmasebi, M. Mirzaei, A. Frontera, *Inorganica Chimica Acta*, **2021**, *523*, 120410.
117. A. Kondinski, *Nanoscale*, **2021**, *13*, 13574–13592.
118. (a) V. G. Albano, *Coord. Chem. Rev.*, **1994**, *133*, 67–114; (b) A. Annunziata, M. E. Cucciolito, R. Esposito, G. Ferraro, D. M. Monti, A. Merlino, F. Ruffo, *Eur. J. Inorg. Chem.*, **2019**, *2020*, 918–929.
119. (a) F. P. Fanizzi, F. P. Intini, L. Maresca, G. Natile, M. Lanfranchi, A. Tiripicchio, *J. Chem. Soc. Dalton Trans.*, **1991**, 1007–1015; (b) M. Benedetti, V. Lamacchia, D. Antonucci, P. Papadia, C. Pacifico, G. Natile, F. P. Fanizzi, *Dalton Trans.*, **2014**, *43*, 8826–8834.
120. (a) V. G. Albano, M. Monari, I. Orabona, A. Panunzi, F. Ruffo, *J. Am. Chem. Soc.*, **2001**, *123*, 4352–4353; (b) V. G. Albano, M. Monari, I. Orabona, A. Panunzi, G. Roviello, F. Ruffo, *Organometallics*, **2003**, *22*, 1223–1230.
121. (a) V. De Felice, A. De Renzi, F. Ruffo, D. Tesauro, *Inorg. Chim. Acta*, **1994**, *219*, 169–178; (b) V. G. Albano, C. Castellari, M. L. Ferrara, A. Panunzi, F. Ruffo, *J. Organomet. Chem.*, **1994**, *469*, 237–244.

References

122. (a) V. G. Albano, D. Braga, V. De Felice, A. Panunzi, A. Vitagliano, *Organometallics*, **1987**, *6*, 517-525; (b) M. E. Cucciolito, V. De Felice, A. Panunzi, A. Vitagliano, *Organometallics*, **1989**, *8*, 1180-1187.
123. (a) V. G. Albano, C. Castellari, V. De Felice, A. Panunzi, F. Ruffo, *J. Organomet. Chem.*, **1992**, *425*, 177-188; (b) V. G. Albano, C. Castellari, M. Monari, V. De Felice, M. L. Ferrara, F. Ruffo, *Organometallics*, **1995**, *14*, 4213-4221.
124. A. Sanchez, C. Castellari, A. Panunzi, A. Vitagliano, V. D. Felice, *J. Organomet. Chem.*, **1990**, *388*, 243-252.
125. L. Calvanese, M. E. Cucciolito, A. D'Amora, G. D'Auria, A. Esposito, R. Esposito, L. Falcigno, F. Ruffo, *Eur. J. Inorg. Chem.*, **2015**, *2015*, 4068-4075.
126. A. Romerosa, J. Suarez-Varela, M. A. Hidalgo, J. C. Avila-Rosón, E. Colacio, *Inorg. Chem.*, **1997**, *36*, 3784.
127. (a) F. A. Cotton, R. A. Walton, *Multiple Bonds Between Metal Atoms*. Wiley: New York, 1982; (b) M. N. Sokolov, V. S. Korenev, E. V. Peresyphkina, V. P. Fedin, *Russ. J. Coord. Chem.*, **2011**, *37*, 133-136.
128. N. I. Kuznetsova, L. G. Detusheva, L. I. Kuznetsova, M. A. Fedotov, V. I. Likholobov, *J. Mol. Catal. A: Chem.*, **1996**, *114*, 131-139.
129. N. Legagneux, E. Jeanneau, A. Thomas, M. Taoufik, A. Baudouin, A. de Mallmann, J.-M. Basset, F. Lefebvre, *Organometallics*, **2011**, *30*, 1783-1793.
130. M. Kato, C. N. Kato, *Inorg. Chem. Commun.*, **2011**, *14* (6), 982-985.
131. (a) J.-H. Chou, M. G. Kanatzidis, *Inorg. Chem.*, **1994**, *33* (24), 5372-5373; (b) J. A. Hanko, J.-H. Chou, M. G. Kanatzidis, *Inorg. Chem.*, **1998**, *37*, 1670-1671; (c) Y. Pan, Q. Jin, J. Chen, Y. Zhang, D. Jia, *Inorg. Chem.*, **2009**, *48* (12), 5412-5417; (d) C. Tang, F. Wang, W. Jiang, Y. Zhang, D. Jia, *Inorg. Chem.*, **2013**, *52* (19), 10860-10868.
132. (a) Z. Li, L.-Z. Wu, *Hydrogen Bonded Supramolecular Structures*. Springer: 2015; (b) I. Hisaki, C. Xin, K. Takahashi, T. Nakamura, *Angew. Chem. Int. Ed.*, **2019**, *58*, 11160-11170; (c) R.-B. Lin, Y. He, P. Li, H. Wang, W. Zhou, B. Chen, *Chem. Soc. Rev.*, **2019**, *48*, 1362-1389.
133. M. Igarashi, T. Nozawa, T. Matsumoto, F. Yagihashi, T. Kikuchi, K. Sato, *Nat. Commun.*, **2021**, *12*, 7025.

References

134. W. B. Connick, R. E. Marsh, W. P. Schaefer, H. B. Gray, *Inorg. Chem.*, **1997**, *36*, 913-922.
135. M. N. Sokolov, A. V. Virovets, D. N. Dybtsev, E. V. Chubarova, V. P. Fedin, D. Fenske, *Inorg. Chem.*, **2001**, *40*, 4816-4817.
136. D. Cortes-Arriagada, M. P. Oyarzun, L. Sanhueza, A. Toro-Labbe, *J. Phys. Chem. A.*, **2015**, *119*, 6909-6918.
137. (a) H. A. Szymanski, L. Marabella, J. Hoke, J. Harter, *Appl. Spectrosc.*, **1968**, *22*, 297-304; (b) J. Liu, H. Cheng, R. L. Frost, F. Dong, *Spectrochim. Acta. A. Mol. Biomol. Spectrosc.*, **2013**, *103*, 272-275.